NANYANG TECHNOLOGICAL UNIVERSITY
SINGAPORE

Study on the anisotropy and heterogeneity of microstructure and mechanical properties in additive manufactured Ti-6Al-4V parts by selective electron beam melting

KOK YIHONG

SCHOOL OF MECHANICAL AND AEROSPACE ENGINEERING

2018

Study on the anisotropy and heterogeneity of microstructure and mechanical properties in additive manufactured Ti-6Al-4V parts by selective electron beam melting

Kok Yihong

School of Mechanical and Aerospace Engineering

A thesis submitted to the Nanyang Technological University
In partial fulfillment of the requirement for the degree of
Doctor of Philosophy

2018

Abstract

Selective electron beam melting (SEBM) is a metal additive manufacturing (AM) technique that can produce high-quality metal parts with high strength and ductility. Due to the layer-by-layer approach and selective melting of the powder bed during the AM process, anisotropy and heterogeneity in the as-fabricated microstructure are challenges in the production of metal AM parts. An understanding of the formation mechanism that results in such microstructures in SEBM built Ti-6Al-4V is not yet fully understood.

This study thus aims to further the understanding of the anisotropy and heterogeneity within the as-fabricated microstructure of Ti-6Al-4V alloy for microstructural control and the development of new materials. The control of the microstructure and the development of new materials are important to enable more applications for SEBM-built parts.

Firstly, the phases within the as-built SEBM Ti-6Al-4V were studied and identified via phase characterisation techniques (e.g. TEM EDX, XRD and APT). Secondly, the influence of build geometry (e.g. thickness, height, and shape) on the microstructure and the mechanical properties were studied quantitatively via microstructural characterisation techniques (e.g. OM, SEM and TEM) and mechanical testing (e.g. Tensile test and Vickers microhardness). Lastly, the columnar grains within the as-built SEBM Ti-6Al-4V were studied as well. Numerical simulations to support the experimental observations and findings were also done via collaborations with other researchers.

The results showed that anisotropy and heterogeneity in the microstructure and mechanical properties indeed existed within the SEBM Ti-6Al-4V part. The phase transformation process that occurs during the fabrication process of SEBM-built Ti-6Al-4V was also shown. Differences in the build geometry thus terminated the phase transformation

process at various stages led to heterogeneity in its final mechanical properties. The columnar grain growth study showed that there existed strong texture intensity in the part with large cross sectional area that suggested competition between the columnar grains. Additionally, phenomenon of sub-columnar grain formation was also observed.

The study contributes to the scientific knowledge with regards to the phase and microstructural evolution that happens during the SEBM fabrication process. It can also be a useful reference guide on both microstructural control and development of new materials for SEBM process.

Acknowledgements

First and foremost, the author wishes to express sincere gratitude and appreciation to his supervisors, Associate Professor Tor Shu Beng and Associate Professor Loh Ngiap Hiang for their invaluable advice, help, and patience throughout his candidature. The author would like to express his immense gratitude to Dr. Tan Xipeng for his mentorship and invaluable guidance for this research. His dedication to the research has been a constant source of inspiration for the author. Appreciation is also extended to Dr. Fu Gang for being a member of the author's Thesis Advisory Committee.

The author would also like to thank Professor Chua Chee Kai for the opportunity in pursuing the research in the Singapore Centre for 3D Printing (SC3DP). The author is also grateful for the collaboration with SIMTech-NTU Joint Lab (3D Additive Manufacturing). The collaboration with Dr. Nai Mui Ling Sharon, Dr. Guglielmo Vastola, Dr. Pei Qing Xiang, Dr. He Zeming, Dr. Wang Pan and Dr. Srinivasan Raghavan were fruitful towards the research. The author also acknowledges the research funding received from these institutions.

In addition, I would also like to thank the following technical staff for their technical support and making my research experience a smooth and an enjoyable one: Mr. Chia Yak Khoong, Mr. Soh Beng Choon, Mr. Mack Wong, Mr. Tony Wee, Mr. Leong Kwok Phui, Ms. Yong Mei Yoke, Ms. Sandy Seah and Mr. Koh Wing Leong.

The author is also grateful to fellow group mates in the SEBM group, who have undertaken this enriching journey with him: Ms. Tan Yujun, Mr. Toh Wei Quan, Mr. Sun Zhongji, Mr. Shubham Chandra, Mr. Wang Cheng Cheng and Mr. Jing Wei. The weekly discussions provided different perspectives on the research throughout the duration of the time as a Ph.D. candidate.

The author would also like to express thanks to the other researchers and research students for all the fun and joy that we had in the last four years. Last but not the least, the author thanks his family, loved ones, and friends for their constant encouragement and understanding throughout the writing of this thesis.

List of publications

Throughout the course of this research, the author has written and contributed to several publications in international peer-reviewed journals and conference papers.

Peer-Reviewed Journal Papers

1. **Yihong Kok**, Xipeng Tan, Shubham Chandra, Pan Wang, Sharon Nai, Ngiap Hiang Loh, Shu Beng Tor. "Columnar grain growth in additive manufacturing of Ti-6Al-4V alloy by selective electron beam melting." In preparation.
2. **Yihong Kok**, Xipeng Tan, Pan Wang, Sharon Nai, Ngiap Hiang Loh, Erjia Liu, Shu Beng Tor. "Anisotropy and heterogeneity of microstructure and mechanical properties in metal additive manufacturing: a critical review." Under review.
3. **Yihong Kok**, Xipeng Tan, Ngiap Hiang Loh, Shu Beng Tor, Chee Kai Chua. "Geometry dependence of microstructure and microhardness for selective electron beam-melted Ti–6Al–4V parts." *Virtual and Physical Prototyping* 11 (2016): 1-9.
4. Xipeng Tan, **Yihong Kok**, Wei Quan Toh, Yu Jun Tan, Marion Descoins, Dominique Mangelinck, Shu Beng Tor, Kah Fai Leong, and Chee Kai Chua. "Revealing martensitic transformation and α/β interface evolution in electron beam melting three-dimensional-printed Ti-6Al-4V." *Scientific reports* 6 (2016).
5. Xipeng Tan, **Yihong Kok**; Yu Jun Tan, Marion Descoins, Dominique Mangelinck, Shu Beng Tor, Kah Fai Leong, Chee Kai Chua. "Graded microstructure and mechanical properties of additive manufactured Ti–6Al–4V via electron beam melting." *Acta Materialia* 97 (2015): 1-16.
6. Xipeng Tan, **Yihong Kok**, Yu Jun Tan, Guglielmo Vastola, Qing Xiang Pei, Gang Zhang, Yong-Wei Zhang, Shu Beng Tor, Kah Fai Leong, Chee Kai Chua. "An experimental and simulation study on building thickness dependent microstructure for electron beam melted Ti-6Al-4V." *Journal of Alloys and Compounds* 646 (2015): 303-309.
7. **Yihong Kok**, Xipeng Tan, Shu Beng Tor, Chee Kai Chua. "Fabrication and microstructural characterisation of additive manufactured Ti-6Al-4V parts by electron beam melting." *Virtual and Physical Prototyping* 10 (2015): 1-9.

Conference Papers

1. **Yihong Kok**, Xipeng Tan, Ngiap Hiang Loh, Shu Beng Tor, Chee Kai Chua. “Geometrical based characterization of complex Ti-6Al-4V parts fabricated by selective electron beam melting.” In the proceedings of 2nd International Conference on Progress in Additive Manufacturing 2016. May 2016, Singapore.
2. **Yihong Kok**, Shu Beng Tor, Ngiap Hiang Loh. "Comparison of Two Metallic Additive Manufacturing Technologies: Selective Laser Melting and Electron Beam Melting." In the proceedings of 1st International Conference on Progress in Additive Manufacturing 2014. May 2014, Singapore.
3. Xipeng Tan, **Yihong Kok**, Shu Beng. Tor, Chee Kai Chua. "Application of Electron Beam Melting (EBM) in Additive Manufacturing of an Impeller." In the proceedings of 1st International Conference on Progress in Additive Manufacturing 2014. May 2014, Singapore.

Table of Contents

List of figures

List of tables

List of abbreviations

α – Alpha phase

β – Beta phase

T_m – Melting temperature

Ø – Volume fraction of equiaxed grain

R – Solidification rate

N_0 – Nuclei density

R_p – Penetration range of electron

V – Electron acceleration voltage

ρ – Density

3D – Three-dimensional

AM - Additive manufacturing

APT – Atom Probe Tomography

ASTM – American Society for Testing and Materials

BCC – Body centred cubic

CAD – Computer aided design

CNC – Computerized Numerical Control

CAFD – Cellular Automata Fluid Dynamic

DED – Direct energy deposition

DMLS – Direct metal laser sintering

DF – Dark field

EBF3 – Electron beam free form fabrication

EDM – Electrical discharge machining

ELI – Extra low interstitial

FFF – Free foam fabrication

FE – Finite element

HAZ – Heat affected zone

HCP – Hexagonal closed packed

HT – Heat treated

HIP – Hot Iso-static Pressing

IPF – Inverse Pole Figures

ISO – International Organization for Standardization

LAM – Laser additive manufacturing

LENS – Laser engineered net shaping

LMD – Laser metal deposition

LF3 – Laser free-form fabrication

LOM – Laminated Object Manufacturing

OM – Optical microscopy

PBF – Powder Bed Fusion

RP – Rapid prototyping

RM – Rapid manufacturing

ROI – Region of interest

SAED – Selected area (electron) diffraction

SEBM – Selective electron beam melting

SEM – Scanning electron microscopy

SLM – Selective laser melting

SLS – Selective laser sintering

SR – Stress-relieved

SMD – Shaped metal deposition

TEM – Transmission electron microscopy

UAM – Ultrasonic Additive Manufacturing

XRD – X-ray diffraction

Chapter 1: Introduction

This chapter provides the research background and motivation, objectives and scope of the thesis. The thesis organization in the form of a brief outline of the contents is also presented at the end of the chapter.

1.1 Research Background

Metal additive manufacturing (AM), popularly known as metal three-dimensional (3D) printing, is a process of joining metallic materials (in powder, wire, sheet forms, etc.) to make objects from 3D models usually layer upon layer [1, 2]. Metal AM has the potential of revolutionizing how metallic items are designed and constructed in the digital industrial era [3-5]. Sales of metal AM systems have been increasing dramatically over the past few years [6]. Moreover, the AM technologies have become increasingly mature for industrial adoption [7]. Correspondingly, there is a clear boom in research interest in the area of metal AM, particularly in the last five years [8].

Most of the studies have stated the benefits of metal AM technology, while there are still some limitations such as anisotropy and heterogeneity in the microstructure and mechanical properties [9]. Anisotropy depicts a variety of orientation-dependent features in a material, while heterogeneity is defined as uniformity in its features. Recent studies have found that metal AM parts exhibited anisotropy and heterogeneity in microstructure and mechanical properties [10-14]. In practice, superior and consistent mechanical properties of metal AM parts are prerequisites for engineering applications [15, 16]. There have been extensive studies on the microstructure, mechanical properties, and processability of various metals and alloys in a variety of metal AM systems [9, 17]. In particular, the formation of anisotropic and

heterogeneous microstructure and its influence on mechanical properties are becoming hot research topics in metal AM field [15, 18, 19].

Metal AM parts usually undergo complex cyclic thermal history consisting of directional heat extraction, repeated melting and rapid solidification [20, 21], which would create anisotropic and heterogeneous microstructures that intrinsically differed from the metallic parts manufactured via conventional methods [12, 22]. As a result, anisotropic and heterogeneous properties may occur in metal AM parts. Also, AM defects such as pores, rough surfaces and lack of fusion layers, would also induce the anisotropic and heterogeneous properties of metal AM parts [18, 23]. Selective Electron beam melting (SEBM), a powder bed fusion metal AM technique that is discussed extensively in this thesis is no exception, especially since it operates at an elevated build temperature that is favorable for the formation of anisotropic and heterogeneous microstructures.

SEBM employs a focused electron beam to selectively melt a conductive metal powder bed directed by a computer aided design (CAD) model under a high vacuum. SEBM is capable of producing functional parts with excellent mechanical properties rapidly and energy-efficiently [1]. SEBM is a preferred AM technique for fabricating Ti-6Al-4V parts because of titanium's high affinity for oxygen. Ti-6Al-4V is the most common titanium alloy and one of the most important engineering materials. Due to its high strength-to-weight ratio, outstanding corrosion resistance and good biocompatibility, Ti-6Al-4V has great potential application in aerospace, marine & offshore, medical devices, etc [24]. Thus, Ti-6Al-4V is one of the most investigated AM material using the EBM technology [8, 25]. The other commonly investigated AM material are steel alloys [8].

It is known that columnar prior β grains would form in SEBM-built Ti-6Al-4V, which is attributed to the high thermal gradient and elevated built temperature of the SEBM process [26, 27]. Safdar et al. found that a transformed α/β microstructure consisting of Widmanstätten

α platelets and rod-like β phase was formed within the columnar prior β grains [27]. Much finer grains were found in SEBM-built Ti-6Al-4V compared to casting Ti-6Al-4V, owing to its very rapid cooling [28]. In general, the tensile properties of SEBM-built Ti-6Al-4V parts are comparable with that of wrought form and better than that of cast form [29].

However, there are still several controversies associated with anisotropic and heterogeneous microstructures of SEBM-built Ti-6Al-4V parts. Firstly, the knowledge and prediction of the exact amount of the different phases in the final SEBM-built part still encounter many open questions, including whether martensite will form or not during the SEBM process [30]. For example, recent investigations have clearly shown the formation of martensite in selective laser melting (SLM)-built Ti-6Al-4V samples [31] due to the higher cooling rates experienced in the SLM process compared to SEBM. Because the amount of martensite has a direct impact on the mechanical properties, including strength and fatigue resistance [32], the study on phase and microstructural evolution involved in the SEBM process is imperative.

Secondly, despite the rapid development of metal AM Ti-6Al-4V [33], the understanding of how the SEBM process affects the microstructure and mechanical properties of as-built Ti-6Al-4V components with complex geometries (e.g. build thickness, build height and build shape) is still at its early stage. Studies have reported that the columnar growth of grains along the build direction is a reason for the anisotropic mechanical properties regarding ductility [9]. But, few studies have investigated the microstructure selection mechanisms that governs the growth of such columnar grains during the SEBM of Ti-6Al-4V. An in-depth understanding of the anisotropic and heterogeneous microstructures of as-built Ti-6Al-4V would contribute to the knowledge regarding microstructural control in SEBM-built Ti-6Al-4V.

1.2 Research Motivation

A significant advantage of using the AM processes instead of conventional manufacturing processes is in their ability to fabricate geometries (e.g. hierarchical, multi-scale, lattice) that are not possible via conventional means. As such a comprehensive understanding of the metallurgical aspects of the SEBM process is important to aid in the design process of AM parts by understanding the material properties of an object based on its manufacturing process, geometry and orientation. The control of the material properties via its microstructure might also be possible. Additionally, anisotropy and heterogeneity in the microstructure of metal AM alloys is likely to be present in all AM processes due to the layer-by-layer process and the selective melting/deposition inherent in metal AM. As discussed in section 1.1, there is a lack of knowledge regarding the effect of the anisotropic and heterogeneous microstructure on the mechanical properties of SEBM-built material.

The decision to study Ti-6Al-4V titanium alloy is due to its usefulness in a variety of high-valued applications (e.g. medical implants, aerospace and marine components). Manufacturing titanium alloy via conventional manufacturing process (e.g. machining) is also difficult due to its high strength and chemical reactivity that significantly reduces the tool life in machining processes.

1.3 Research Objectives

The objectives of this study are to develop an in-depth understanding on the microstructure and mechanical properties of as-SEBM-built Ti-6Al-4Vparts and identify the issues of anisotropy and heterogeneity with the process. The study will be focused on the phase and microstructural evolution of Ti-6Al-4V that occurs during the SEBM process. This study would eventually contribute towards the understanding of microstructural control in SEBM fabricated metallic materials.

The study had the following objectives,

1. The identification of the phase constitution in the microstructure of the as-built SEBM Ti-6Al-4V alloy via phase characterisation techniques.
2. The study of the effects of build geometry (thickness, shape and height) on the microstructures and mechanical properties of the as-built SEBM Ti-6Al-4V alloy.
3. The study of the grain selection and competition mechanism that governs the columnar grain growth in the as-built SEBM Ti-6Al-4V alloy

1.4 Thesis Outline

- Chapter 1 introduces the background, motivation and objectives of this study.
- Chapter 2 reviews the literature on the metallurgy of titanium and titanium alloys as well as the fundamentals of solidification and phase transformation, major metal AM technologies and the reported anisotropic and heterogeneous microstructure, and mechanical properties in metal AM materials. It concluded with the scope of the research and a research road map to achieve the stated research objective.
- Chapter 3 describes the experimental procedures and equipment used in this study.
- Chapter 4 presents the results of the experiments regarding the phase identification and revealing the martensitic phase transformation during the SEBM processing of Ti-6Al-4V.
- Chapter 5 presents the results and discusses the influence of build geometry (e.g. build thickness, build height and build shape) on the anisotropic and heterogeneous microstructure and mechanical properties of SEBM-built Ti-6Al-4V.
- Chapter 6 presents the results of the columnar grain growth during the SEBM of Ti-6Al-4V and discusses on the grain selection mechanisms that govern its growth. The various phenomena such as layer banding and sub-columnar grain appearance is also discussed.
- Chapters 7 & 8 outline the conclusions based on the study and suggestions for future work.

Chapter 2: Literature Review

2.1 Introduction

Based on the research motivation and objectives, a literature review was undertaken to better understand more about Additive manufacturing in general and to build a good understanding of the current state of the art in additive manufactured titanium alloy. This chapter presents a review of published literature pertaining to this thesis. The first two sections contain the literature regarding the general metallurgy of titanium and its alloys as well as the fundamentals of solidification and phase transformation in metals. The Ti-6Al-4V titanium alloy is the focus of this study, and a comprehensive understanding of its metallurgy and the fundamentals of solidification and phase transformation would aid in the understanding of the study. The third section of this chapter presents the literature review on major metal AM processes. The SEBM technology employed in this study is described in greater detail. Applications regarding the use of AM titanium in the marine and offshore industry and the associated challenges are also discussed. The fourth section presents the literature review on the anisotropic and heterogeneous material properties for metal AM parts. Lastly, detailed research scope and roadmap to achieve the proposed research objectives are presented.

2.2 Metallurgy of titanium and titanium alloys

2.2.1 History of titanium

In 1791, William Gregor was the first to identify titanium as an unknown metallic substance in Ilmenite [34, 35]. Then Klaproth identified Rutile as an oxide of an unknown element which he named as titanium in 1795 and later identified ilmenite to be identical to titanium [34, 35]. In 1920, Matthew A. Hunter first produced pure titanium via a method that became known as the Hunter process [36]. However, the Hunter process was not effective for larger scale production of pure titanium [37]. During 1937 - 1970, W.J. Kroll developed a reduction process of titanium tetrachloride with magnesium in an inert environment to obtained pure titanium in a sponge-like form [38, 39]. In 1996 - 1997, George Z. Chen, Derek J. Fray and Tom W. Farthing developed a simpler process to obtain pure titanium and named it the FFC Cambridge process, named after their family names [40].

Titanium is a reactive metallic element with a high affinity for oxygen, nitrogen, and hydrogen. Therefore the melting of titanium is often done under an inert gas or vacuum environment [26, 41]. Despite the cost associated with maintaining such an environment when processing titanium with conventional manufacturing methods, its alloys are still of importance in industrial applications due to its high specific strength at elevated temperatures as shown in Figure 2.1.

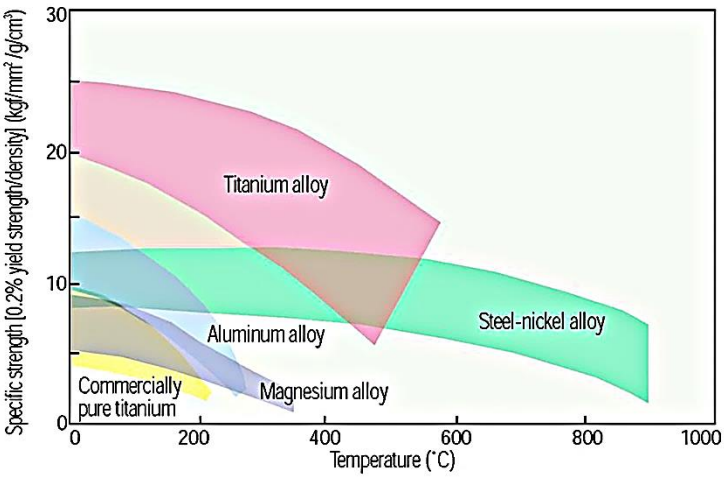

Figure 2.1 Comparison of specific 0.2% proof stress against temperature for light structural alloys [42, 43].

Figure 2.2 shows the United States of America's titanium industry shipments from 1950 to 2012 for the aerospace industry. It can be observed that the use of titanium in the aerospace industry has increased consistently over the years.

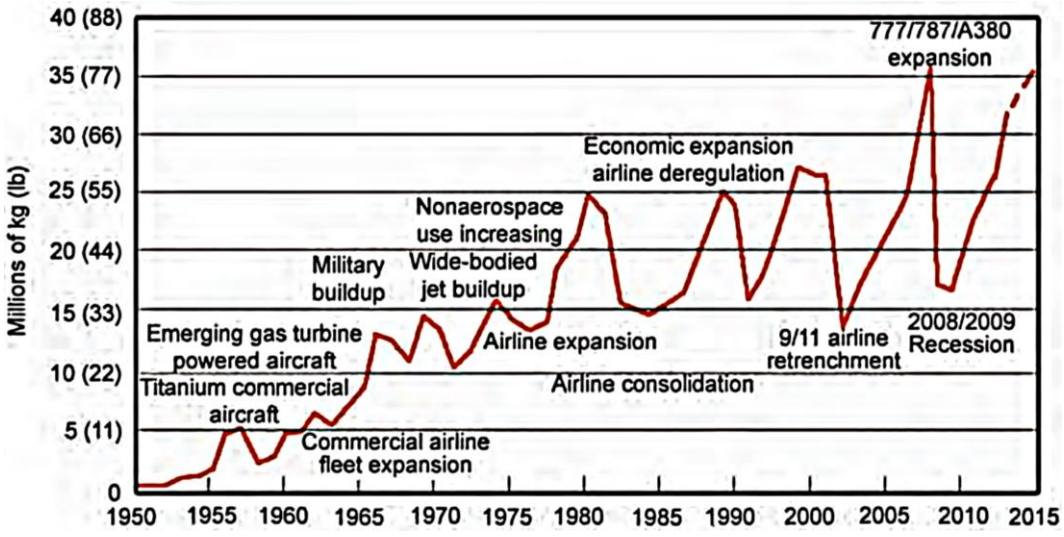

Figure 2.2 U.S. titanium industry shipments from 1950 to 2012 [44].

Recent development in the SEBM system has shown the suitability of the technology to process titanium material into various complex geometry such as an impeller [45]. It is hoped that new manufacturing methods such as the SEBM can lower the manufacturing cost of titanium alloys. Additively Manufactured titanium alloys have already been used in structural components in the aerospace and biomedical applications. There has also been interest to adopt AM titanium alloy in the marine industry due to it excellent corrosion resistance as mentioned by Mountford [46]. The lower manufacturing cost and the greater freedom in design of titanium parts brought about by metal AM would likely lead to the continual importance of titanium as a structural material in the future.

2.2.2 Titanium's crystal structure

The crystal structure is defined as the orderly manner in which atoms, ions or molecules are spatially arranged in a crystalline material. The crystal structure is important in determining the physical properties of a material such as cleavage/slip system. The crystal structure of titanium at ambient temperature and pressure is hexagonal close packed (HCP) with the lattice parameters a=0.295 nm, c=0.468 nm [44]. Additionally, the mechanical response of HCP metals is strongly dependent on the combination of deformation modes such as slip and twinning. Slip is possible on the pyramidal, prismatic and basal planes in the HCP crystal structure as shown in Figure 2.3 (a). At about 860 - 890^{o}C (the β transus temperature), the titanium undergoes an allotropic transform into a body-centered-cubic (BCC) crystal structure (with lattice parameters a = 0.332 nm) and is often referred to as β phase [44, 47]. The BCC crystal structure remains until the melting temperature of titanium at around 1670^{o}C [48]. In BCC crystals, slip predominantly occurs in the {110} planes as shown in Figure 2.3 (b).

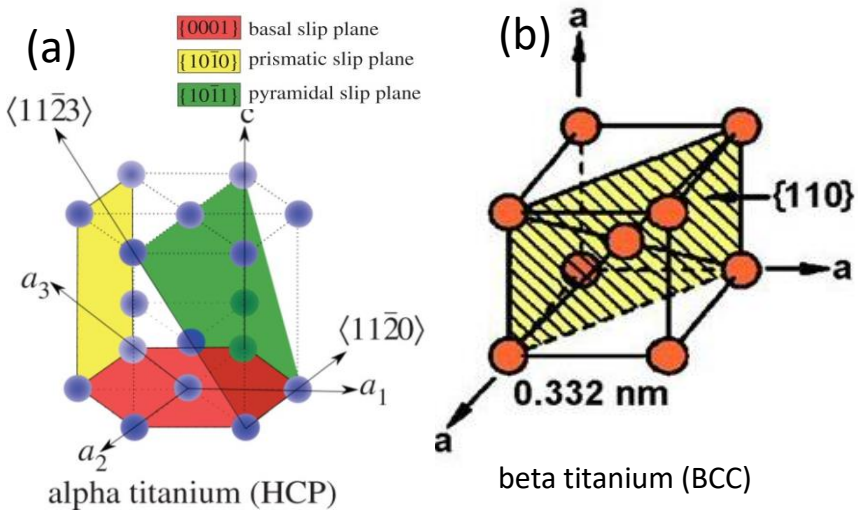

Figure 2.3 Schematics of the slip systems in HCP and BCC crystals; (a) Slip systems in HCP metals and alloys [49] (b) Slip systems in BCC metals and alloys [43].

The planes in the HCP structure shown in Figure 2.3 (a) are described by the Miller-Bravais four index notation (hkil), and the planes in the BCC structure shown in Figure 2.3 (b) are described by the Miller-Bravais three index notation (hkl). The four index Miller-Bravais notation can be expressed as a three index Miller-Bravais notation since i = - (h + k).

Due to the anisotropic nature of the HCP crystal structure, the elastic and hardness properties of titanium alloys are strongly dependent on the loading or deformation direction. Figure 2.4 shows a change in the unloading Young's modulus and the hardness of α-phase titanium alloy via nanoindentation with varying deformation direction [50]. The unloading Young's modulus and the hardness of α-phase titanium alloy are highest when the indentation is on the basal plane, and it is lowest when the indentation is on the prismatic plane. Additionally, it has been recognized that crystallographic texture has an influence on the microstructure evolution during the processing of metals such as the alpha/beta titanium alloy [51, 52]. As such the understanding of titanium's crystal structure would be important in comprehending the various material phenomenon that will be observed in the later experiments.

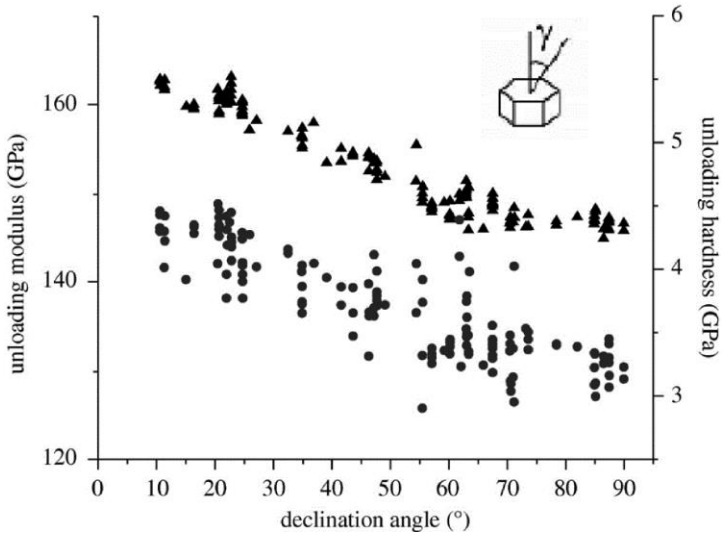

Figure 2.4 Variations in the unloading modulus and hardness with declination angle in HCP crystals; (Filled circles, unloading modules; filled triangles, unloading hardness) [50].

2.2.3 The effect of crystal lattice dimensions on the deformation of hcp metals

The effect of the crystal lattice dimensions on the deformation mode of HCP materials and titanium alloys is complex. Two important deformation modes in HCP metal materials are the slip and twinning[53]. Firstly the slip deformation mode will be discussed and then the twinning deformation mode. Slip deformation involves sliding of blocks of crystal over one other along specific crystallographic planes, called slip planes. The number of slip planes in hexagonal close packed (HCP) metals is less as compared to other crystal structures (e.g. BCC and FCC). Slip is possible on the pyramidal, prismatic and basal planes in the close-packed directions. A slip system is a combination of a slip direction and a slip plane. Four slip systems in the α phase are

1. $<11\bar{2}0>$ (0001), <a> on the basal plane
2. $<11\bar{2}0>$ {1010}, <a> on prismatic plane
3. <1120> {1011}, <a> on pyramidal plane
4. <1123> {1011}, <c+a> on pyramidal plane

Prior study have reported that the principal deformation mechanism in pure titanium is on the prismatic plane $\{00\bar{1}0\}$ along the slip direction of <1120> [54]. The activation of other slip planes may dependent on other factors such as the c/a ratio or stacking fault energy. The crystal structure of titanium at ambient temperature and pressure is close-packed hexagonal (α) with a c/a ratio of 1.587. Early studies report that chance for slip on the <a> basal slip system is decreased as the c/a ratio decreases [49].

Twinning deformation is said to occur when two separate crystals share some of the same crystal lattice points in a symmetrical manner. The plane of symmetry is called twinning plane. In the case of Ti-6Al-4V however, it is reported that slip is promoted and twinning is inhibited [55]. The presence of oxygen and/or Al is reported to suppress twinning by a study [54]. While a recent study reports that raising the aluminium content in titanium does slightly enhance twinning instead [53]. As such the effects of alloying elements on the deformation mode in titanium is still being investigated.

A recent study indicates that with the addition of oxygen interstitials, the pyramidal "<c+a>" slip is promoted to allow the grains in poly crystalline sample to undergo an arbitrary shape change [54, 56]. The pyramidal slip is known to have a critical resolved shear stress (CRSS) about 3–4 times that of prismatic "<a>" slip in typical titanium alloys [54]. The same study reports that alloying elements may reduce or improve the energies of individual stacking faults in α-Ti [56]. Thereby promoting slip on a particular slip plane.

In conclusion, the literature suggest that while the crystal lattice dimension, c/a ratio have an influence on the slip behaviour in HCP metal [49]. There have been a new study that indicate the energy in the various planes stacking faults has a role in determining the slip behaviour in HCP metals as well [56].

2.2.4 Alloying elements in titanium alloy

Alloying elements found in titanium alloys can be categorized based on their ability to increase or decrease the β transus temperature. Table 2.1 show some of such alloying elements that are commonly alloyed with titanium. Alloys which increase the β transus temperature are called β stabilizers and alloys which decrease the β transus temperature are referred to as α stabilizers. β stabilizers can be further sub-divided into isomorphous stabilizer and eutectoid stabilizer. The effect of α and β stabilizers has a significant effect on the titanium alloy as can be seen in Figure 2.5 (a, b, c). Another category of alloying elements has no influence on the β transus temperature and are found in both α and β phase (e.g. Zr and Sn) as shown in Figure 2.5 (d). Additionally, the addition of chromium as an alloying element can help improve the burn–resistance of titanium alloys in high temperature applications [47]. Lastly, titanium alloys being a two-phase alloy can also exist as a mixture of α + β phase with different microstructure morphology (e.g. lamellar and equiaxed).

Table 2.1 Major alloying elements effect on titanium [42, 57].

Effect	**Alloying Elements**
α-stabilizer	Al, Ga; interstitials: N, O, C
β-isomorphous	Mo, V, W Ta
β-eutectoid stabilizer	Cu, Mn, Cr, Fe, Ni, Co, Si; interstitial: H
Strengthening elements	Sn, Zr and Si (extensive solid solubility in α and β)

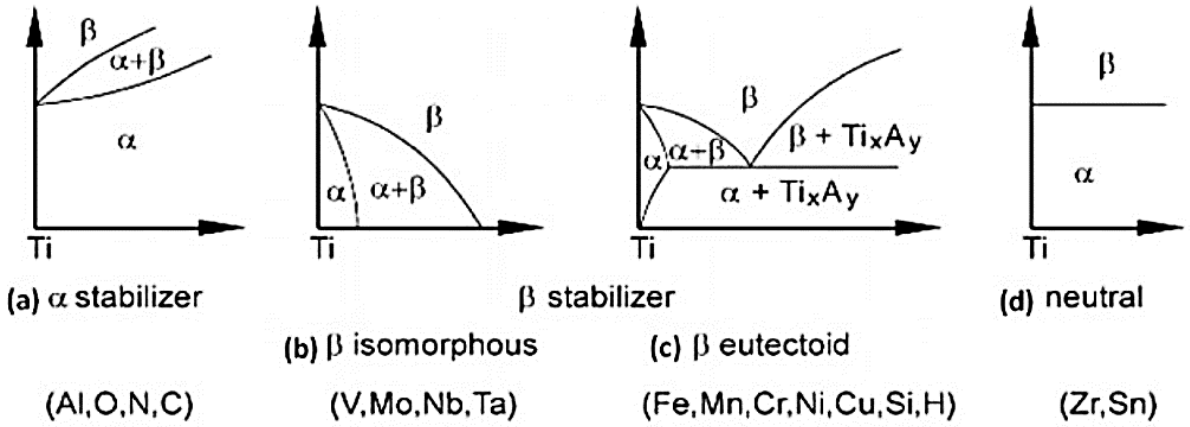

Figure 2.5 Phase diagrams corresponding to the different effect of alloying element on titanium; (a) α stabilizer (b) β isomorphous (c) β eutectoid (d) neutral [48].

2.2.4.1 α + β titanium alloys

Another category of titanium alloy is the α + β titanium alloy which has properties in between the α and β-titanium alloy as mentioned previously. These alloys thus have improved strength and formability as compared to fully α alloys. Such alloys contain α stabilizers with 4-6% of β stabilizers allowing the retention of the β phase at room temperature. The percentage of each phase retained is dependent upon the amount of the respective stabilizers alloyed with titanium. The most commonly studied α+β titanium alloy is the Ti-6Al-4V, which is the subject of this study. The pseudo-3D phase diagram of α + β titanium alloys is shown in Figure 2.6. The α-β transformation temperature of pure titanium is approximately 882^0C as well [58].

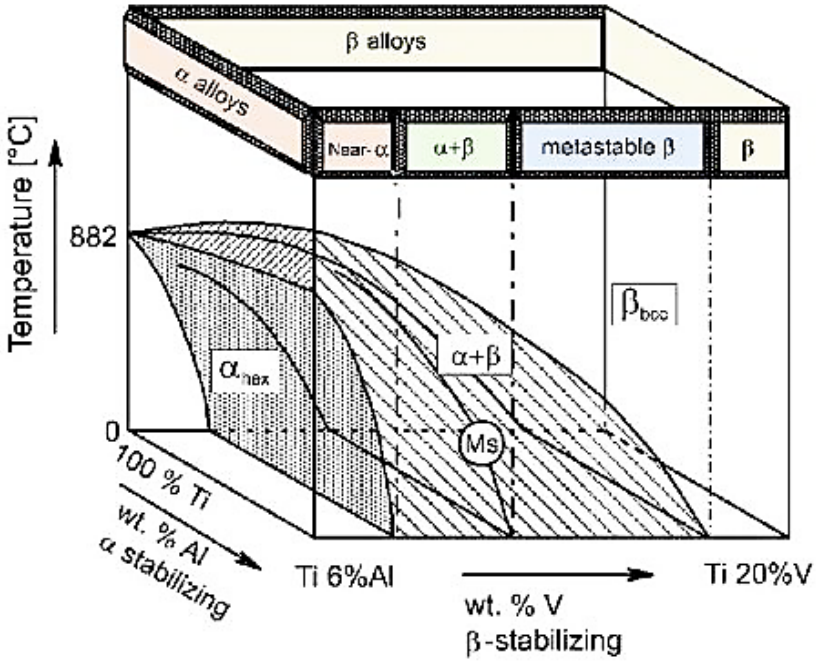

Figure 2.6 Schematic of the phase diagram in α/β titanium alloys [43].

Ti-6Al-4V alloy is the most widely used α + β titanium alloys due to its good mechanical properties (e.g. specific strength) and corrosion resistance. Table 2.2 shows some of the physical and mechanical properties of Ti-6Al-4V. The microstructure of Ti-6Al-4V can be modified via the appropriate application of heat treatment. Ti-6Al-4V contains a volume fraction of approximately 15% β-phase at a temperature of 800°C [48]. At ambient temperature, the alloy is predominantly in the α-phase and when it is heated to above the β-transus temperature the alloy is predominantly β-phase. Unfortunately, Ti-6Al-4V can only be used in applications where the operational temperature is below 300 °C due to its low creep performance [48]. The extra low interstitials (ELI) variety of Ti-6Al-4V yields better ductility properties with a slight reduction in its tensile properties. This is due to the lower oxygen content within the Ti-6Al-4V ELI alloy.

Table 2.2 Some physical and mechanical properties of Ti-6Al-4V alloy [59].

Property	Value
Density, g/cm3	4.43
Melting temperature, °C	1604-1660
Specific heat, J/kg · K	526.3
Thermal conductivity, W/m · K	6.7
Tensile strength, MPa	950
Tensile yield strength (0.2%), MPa	880
Elongation in tension, %	14
Charpy impact strength, J	17
Fatigue strength, MPa (Unnotched 10,000,000 Cycles)	510
Hardness (Rockwell C)	36

2.3 Fundamentals of solidification and phase transformation in metals and alloys

2.3.1 Solidification theory

Metal AM is a rapid melting and solidification process within a moving melt pool. The high cooling rate encountered in metal AM process leads to fine solidification microstructures that are not commonly producible via conventional processes such as forging or casting. But, the rapid melting and solidification can also lead to phenomena such as suppressed phase transformations, segregation, hot cracking and thermal residual stresses that are not desirable. Additionally, the unidirectional heat flow to the building substrate and thermal cycling that occurs due to the layer by layer process also add complexity to the understanding of the metal AM process. As such the fundamental understanding of the solidification theory and the phase transformation in conventionally produced titanium alloy must be understood to aid the investigation in this study. The solidification process controls the as-built microstructures which subsequently affect the macro-mechanical properties of the solidified material. An important aspect of the solidification process is the nucleation of new grains, grain growth, and the solid-state phase transformation phenomena.

Phase transition (liquid-solid) is present in everyday processes and can be observed via simple examples. However how phase transition happens in the molecular scale is less obvious.

The classical theory that describes this phenomenon is the classical nucleation theory. There are two modes of nucleation: (1) homogeneous nucleation and (2) heterogeneous nucleation. If a molten melt pool is cooled below its melting point (T_m), there is a driving force for solidification to take place due to the difference in molar free energy. It is expected that within a few Kelvins of the melting temperature the molten melt pool will immediately solidify into a solid phase. However, according to literature, it is theoretically possible to have undercooling of greater than 200 K for homogeneous nucleation though this is not observed [60-62]. Since the presence of impurities in the molten melt pool is hard to prevent, a more common mode of nucleation is heterogeneous. Thus, the barrier for solidification is reduced by the surface energies introduced by the impurities leading to a smaller undercooling. It is observed that homogenous nucleation does not take place under molten melt pool conditions [60, 61]. Typical undercooling of 1-2 K is reported in the nucleation of welding melt pools [63]. Figure 2.7 shows a illustration of possible solidification mechanisms within a local melt pool. It can be observed that nucleation of new grains could occur either on the surface of the melt pool or within the melt pool itself [64].

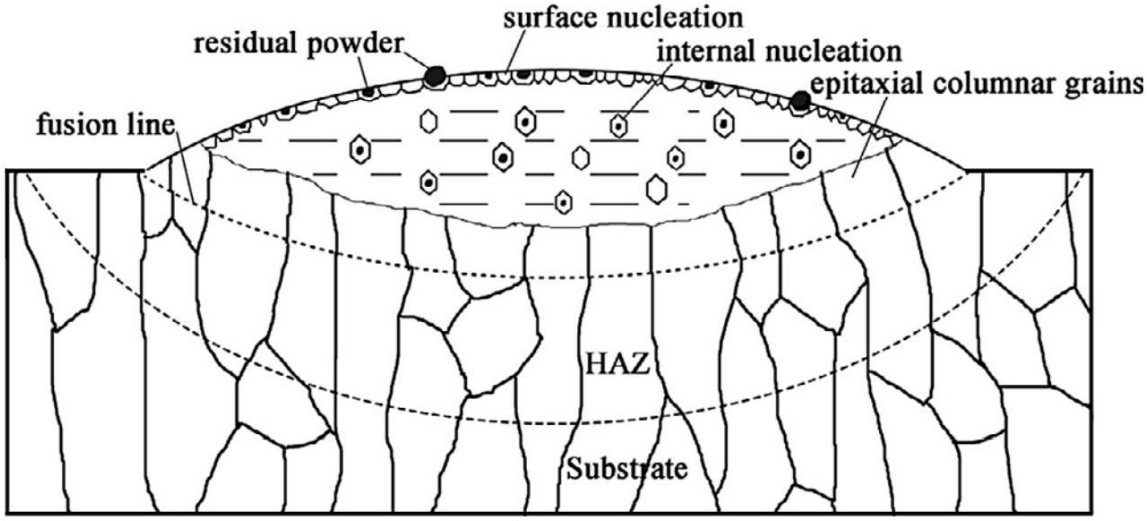

Figure 2.7 Schematic illustration of possible solidification mechanisms within a local melt pool [64].

2.3.2 Grain growth behavior

After heterogeneous nucleation, the solidification growth forms by the addition of atoms from the molten melt pool to the crystal grain at the solid-liquid interface. The basic solidification growth modes are planar, cellular, dendritic and equiaxed dendritic as shown in Figure 2.8. These different solidification growths are due to the different super cooling/undercooling that the melt pool experience as presented in Figure 2.8.

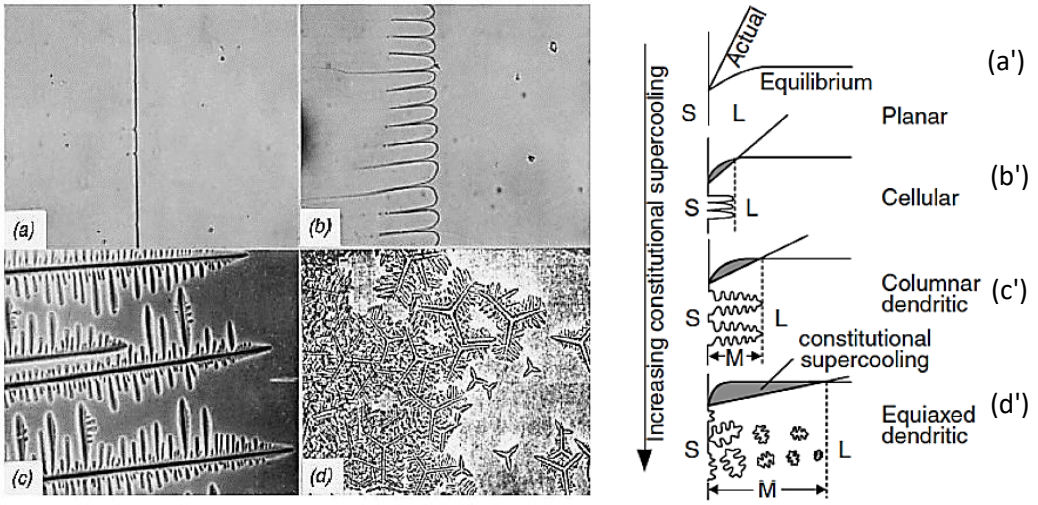

Figure 2.8 Micrographs & degrees of supercooling and growth modes; (a and a') planar solidification; (b and b') cellular solidification; (c and c') dendritic solidification and (d and d') equiaxed dendritic solidification respectively [65].

Planar solidification grows in the direction of the thermal gradient and is observed to have a lack of substructure. Cellular solidification morphology is observed as a breakdown of planar growth into individual cells that are uniformly spaced apart. With greater super cooling, columnar dendritic growth occurs and is characterized similarly to cellular growth with the introduction of substructures like arms. The columnar dendritic grows along specific crystal direction known as easy growth directions in which the diffusion of atoms from the liquid front to the solid is the fastest. Lastly, equiaxed dendritic growth occurs under the greatest supercooling condition allowing spontaneous nucleation to occur in the melt pool as shown in Figure 2.8 (d). Both columnar dendritic

and equiaxed dendritic are commonly seen in the microstructure of AM Ti-6Al-4V titanium alloy.

2.3.3 Melt pool solidification behavior

Some variables have been found to influence the melt pool solidification behavior in welding and AM processes. They are crystallography, thermal gradient, and cooling rate (C) [60, 61, 66-69]. These will be discussed in the following sub-sections:

2.3.3.1 Crystallography

Crystallography of a material affects the solidification rate, through specific easy growth direction where crystal growth along a specific direction is faster as compared to other directions. For BCC crystal structure the easy growth direction is <100> and for HCP the easy growth direction is <1010> [70]. The growth direction also follows the maximum temperature gradient. Thus when the grain's crystal orientation is favorably orientated in the direction of the thermal gradient, it could competitively outgrow other less favorably orientated crystal grain orientation based on the classical competitive grain growth theory [71].

2.3.3.2 Thermal gradient and cooling rate

Another variable that affects the microstructure of the solidified melt pool is the cooling rate (C) which is the product of the solidification rate (R) and the thermal gradient (G). Figure 2.9 shows how cooling rate affects the scale of microstructure on the solidification map, where a higher cooling rate results in smaller microstructural features. The highest cooling rate is at the top right quadrant, while the lowest cooling rate is at the bottom left quadrant in Figure 2.9. This is because cooling rate is the result of the multiplication of the solidification rate, R and the thermal gradient, G.

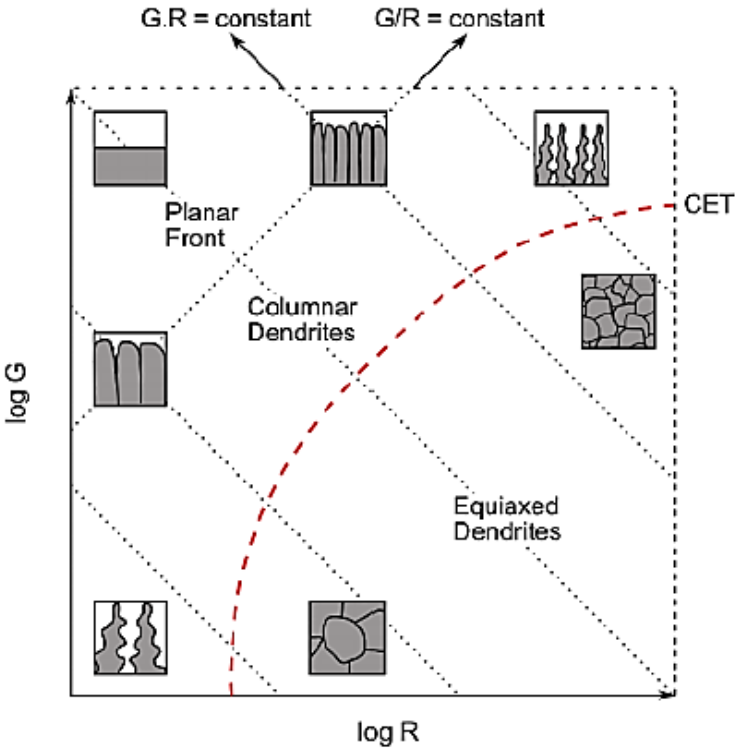

Figure 2.9 Solidification map of melt pool microstructure as a function of solidification rate and temperature gradient [61, 62].

A study has also mentioned that grain nucleation is also affected by such variables in Equation 2.1 [72]:

$$\frac{G^n}{R} = a\left\{\sqrt[3]{\frac{-4\pi N_0}{3\ln[1-\phi]}}.\frac{1}{n+1}\right\}^n \qquad \text{Eqn 2.1}$$

where G is the thermal gradient, a & n are material constant, R is the solidification rate, N_0 is the nuclei density, Ø is the volume fraction of equiaxed grain. When Ø >0.49 fully equiaxed growth occurs and when Ø <0.0066 then fully columnar occurs [72]. For SEBM AM process the typical cooling rate ranges from 10^3 to 10^6 K/s depending on the parameters used [61]. Accurate measurements of the cooling rates involved in the AM process is still not certain due to the difficulties in obtaining such measurements during the process. Additionally, the shape of the moving melt pool also changes with travel speed, from an ellipse to a tear drop shape affecting the solidification rate/growth rate.

2.3.4 Solid state phase transformation and microstructure in α+β titanium

The solid-state transformation occurs when titanium is cooled from a high temperature to below the β-transus temperature. The β to α solid state phase transformation phase that occurs significantly influences the final microstructure of α+β titanium. Depending on the cooling rates the process can either be a diffusion controlled transformation or a martensitic diffusionless transformation [63]. Figure 2.10 shows the α+β microstructure after undergoing various heat treatment annealing process [73]. The study reported that when the Ti–6Al–4V samples were heat treated in the β-phase region, the resultant microstructure had a plate-like α and inter-granular β as shown in Figure 2.10 (a-c). Slow cooling will produce grain boundary/colony alpha and the lamellar features shown. The light regions are alpha and the dark regions are beta in this lamellar microstructure. In contrast, Ti-6Al-4V samples that were heat treated in the α+β duplex phase region had an equiaxed α phase in a transformed β matrix instead as shown in Figure 2.10 (d-f).

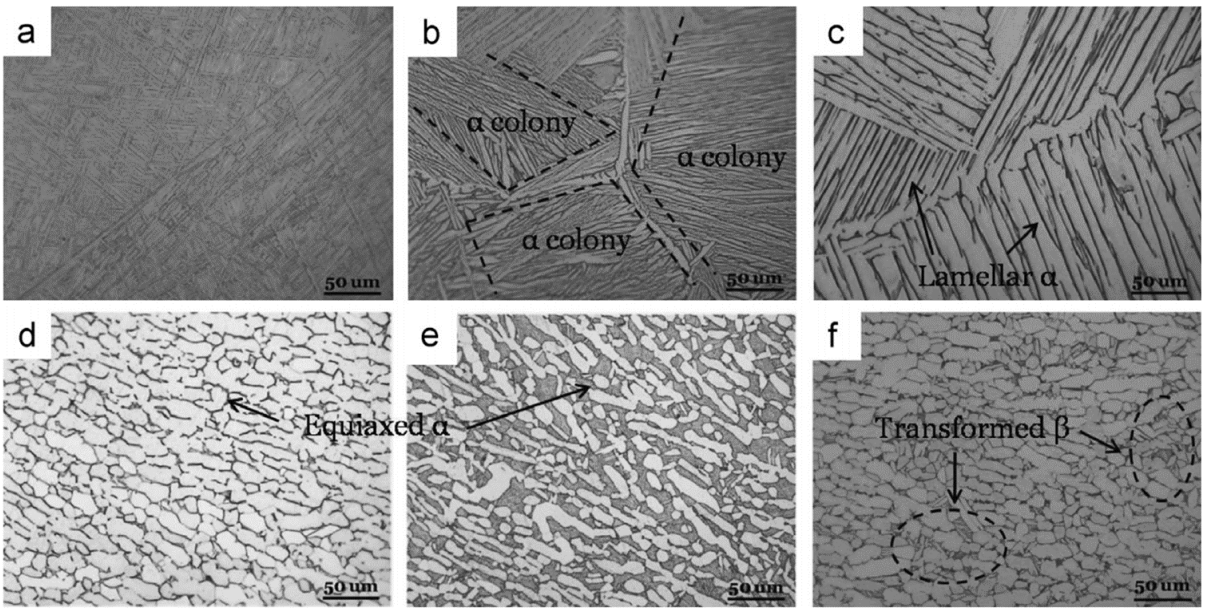

Figure 2.10 Micrographs of a range of α/β titanium alloy microstructure after transformation of the β phase by different heat treatments [73].

Figure 2.11 shows in greater detail the schematics of the formation of α phase from the prior β grain. Burgers studied the crystallographic orientation relationship that occurs during the phase transformation from β to α phase and is thus referred to as the Burgers orientation relation [74] as seen in Figure 2.12. The Burger relationship can be expressed as:

$$\{110\}\ \beta_{bcc} \,||\, \{0002\}\ \alpha_{hcp}$$

$$\langle 111\rangle\ \beta_{bcc} \,||\, \langle 11\bar{2}0\rangle\ \alpha_{hcp}$$

It has been shown that the Burgers orientation relationship provides the lowest total interface energy between the β and α phase due to a minimum crystal lattice spacing misfit [74].

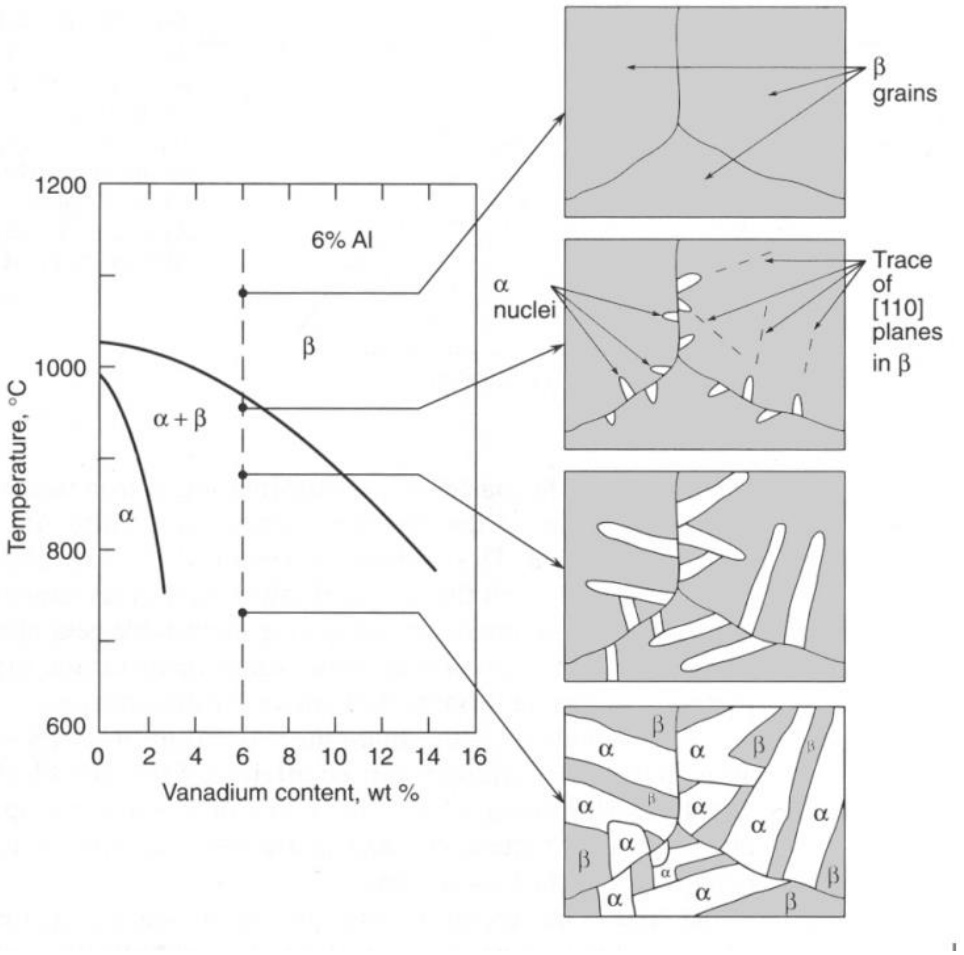

Figure 2.11 Phase diagram for the Ti-6Al-4V alloy with accompanying schematics of the formation of α phase from the prior β grains [75] following the Burgers orientation relationship between α and β phase [39].

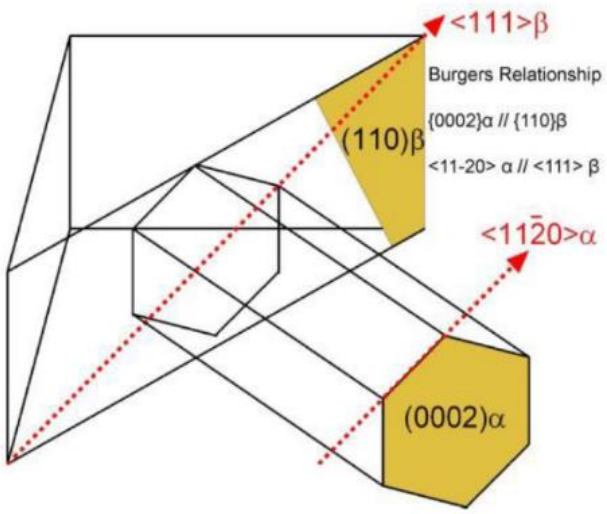

Figure 2.12 Schematic of the Burgers orientation relationship between α and β phase [39].

2.4 Metal additive manufacturing (AM)

AM is a layer-by-layer fabrication process capable of producing near-net-shape parts. This process was first invented in 1988 by Chuck Hulls. AM has been referred to as rapid prototyping (RP), rapid manufacturing (RM), freeform fabrication (FFF) layer additive manufacture (LAM) through the years [76]. Recently, metallic AM has gained considerable interest due to its capability of producing functionally superior parts. AM of complex industrial parts, e.g. fuel nozzles, turbine blades, turbocharger wheels, pump impellers, etc., has been carried out around the world recently [77, 78]. Due to the inherent advantages compared to conventional forming technologies, such as investment casting, AM is being explored for the manufacturing of such complex parts. The powder bed fusion SEBM technology will be the subject of this work.

2.4.1 Metal AM systems

2.4.2 Classification of AM technologies

The American Society for Testing and Materials (ASTM) group "ASTM F42" classified AM technologies into seven process categories in total [79]. The categories pertaining to metal AM are the following directed energy deposition (DED), powder-bed fusion (PBF), and sheet lamination (SL). Despite not being listed in one of the seven process categories, cold spray welding is also a type of metal AM technology. Figure 2.13 shows the representative metal AM methods under each category.

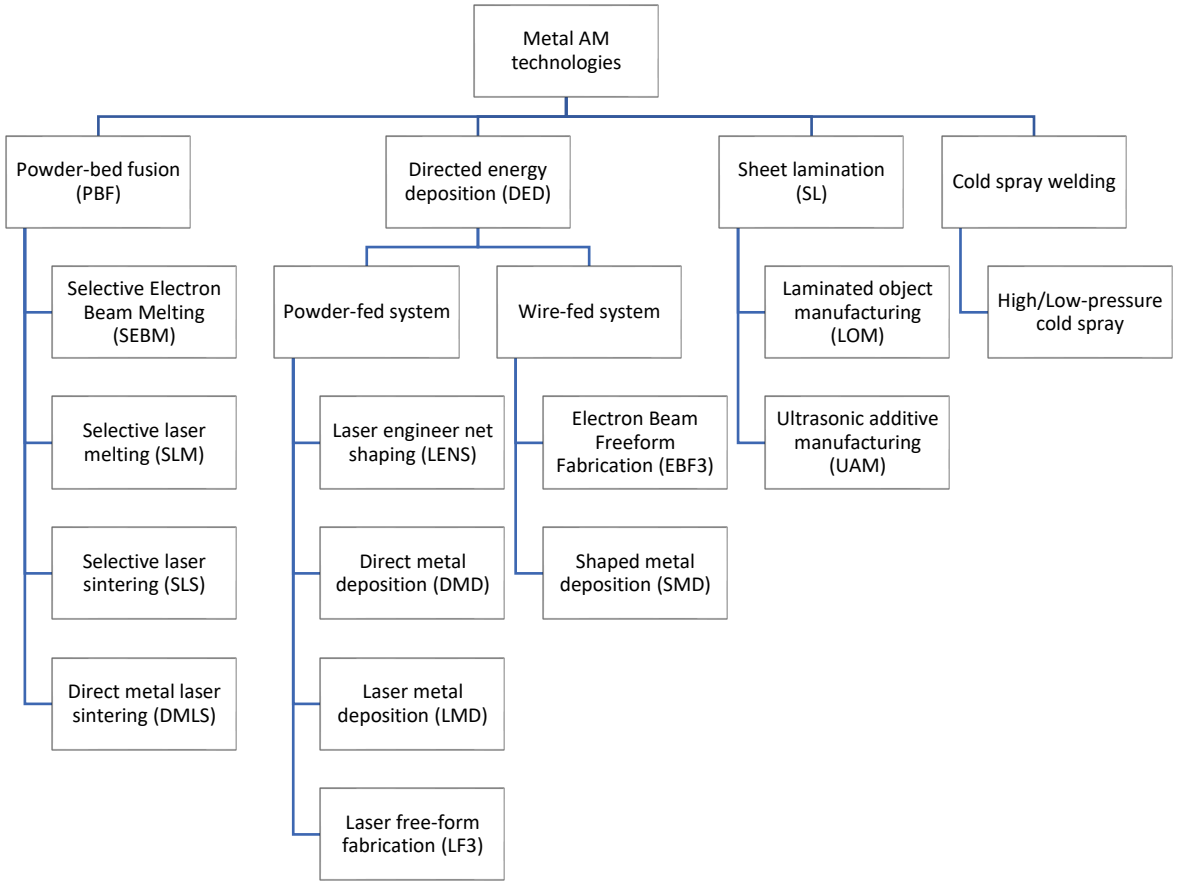

Figure 2.13 Summary of Metal AM systems for metallic tools and components.

Powder-bed fusion (PBF)

PBF processes typically involve selective sintering or melting of powder materials using either a laser or an electron beam based on a powder-bed [80]. The laser beam imparts energy to the metallic powder via the absorption of radiation, while the electron beam works via the kinetic collisions between electrons and powder [81]. At the beginning of the process, a fresh layer of metallic powder was spread evenly using a rake or roller mechanism. The high-energy laser/electron beam then selectively melted the deposited layer of powder. After a layer was selectively melted, the build table was lowered and the cycle repeated till the part was fully fabricated.

A generic schematic of a PBF system is shown in Figure 2.14. There are some laser-based AM techniques such as Laser Cusing, Direct Metal Laser Sintering, Selective Laser Sintering and Selective Laser Melting, though they are all essentially share a similar working principle [8]. The term "SLM" will be used to refer to all laser-based AM techniques under the PBF process for clarity in the following section. Unlike the SLM technologies, Arcam AB (Mölndal, Sweden) is currently the only commercial manufacturer of electron beam-based PBF systems, i.e. SEBM.

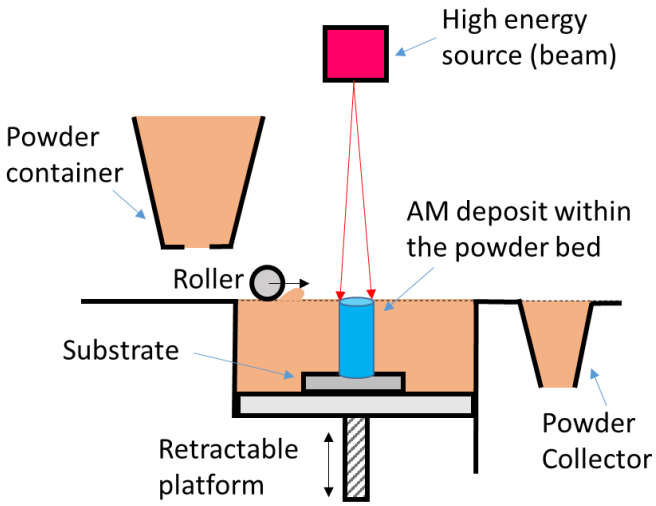

Figure 2.14 Generic illustration of a PBF AM system [82].

Electron beam heating have been used to sinter metallic powders materials since 1959 by Candidus, Hablanian, and Steinherz [83]. SEBM is a recent AM technique using an electron beam to selectively melt a metallic powder bed directed by a computer aided design (CAD) model developed by Arcam AB in 2002. A schematic of an SEBM machine is shown in Figure 2.15. The electron beam is generated within the electron beam gun via a tungsten filament located in the upper column. The tungsten filament is heated to 2200-2700K with a high voltage ~60kV being applied between the filament and the anode. The electron beam is controlled and focus by three magnetic coils, which are housed in the lower column. The first one is the astigmatism lens is used to correct astigmatism and to generate a circular electron beam.

The second one is the focus lens which focuses the electron beam into the desired diameter (~0.15 µm) spot. Lastly, the third one is the deflection lens which deflects the electron beam across the powder bed during the printing process.

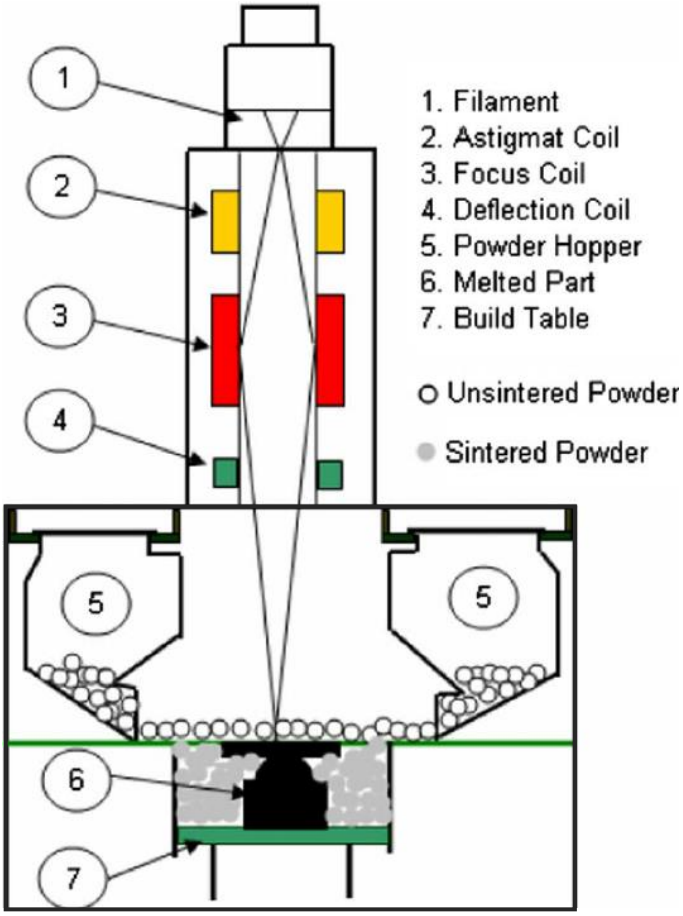

Figure 2.15 Schematic of Arcam A2XX SEBM machine [84].

The focused impingement of electrons onto a solid material will result in some reflection due to elastic and inelastic collision though a majority of the electrons will penetrate the solid [76]. The transformation of kinetic energy from the electron to the solid material generates heat and the production of x-rays, resulting in sufficient energy for the processing of this method. Equation 2.2 shows the penetration range of the electron (R_p) is dependent on the electron acceleration voltage (V) and the density of the target material (ρ) [85].

$$R_p = \frac{2.2\ x\ 10^{-11}.V^2}{\rho} \qquad \text{Eqn 2.2}$$

The electrons that penetrate the solid material then dispense into various paths as seen in Figure 2.16. The use of electrons can also lead to powder charging due to the accumulation of electrons and cause the "smoke" phenomenon. The EBM system works in a helium (positive ion) + vacuum environment with a two stage process to avoid the charging of electrons and use to regulate the pressure in the build chamber [63]. The typical pressure of the helium filled gas environment is 10^{-1} Pa in the build chamber and 10^{-3} Pa in the column chamber. Firstly, the electron beam is defocused to scan the area rapidly to preheat the powder bed so as to sinter the powder particle lightly together [63]. Next, the power density of the electron beam is increased significantly, and rapid melting of the powder particle occurs [63].

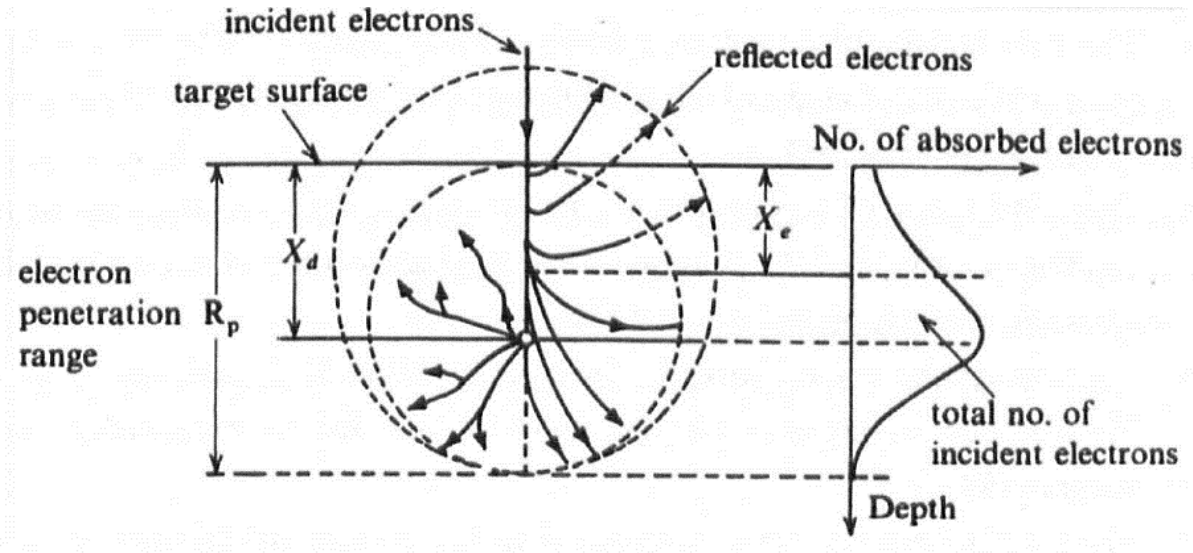

Figure 2.16 Schematic of the electron penetration range in a solid medium [86].

Inside the build chamber houses two hoppers and a heat shield. The hopper is used to hold the powder material with a size distribution of 45-100 µm that is gravity fed to the raking system. The heat shield is made of several polished stainless-steel metal sheets that help maintain the high built temperature during the building process. Below the hopper is the build table where the raking system is used to deposit each layer of powder with a thickness range of 50 to 200 µm. The computer controlled electron beam then selectively scans the contours and then the hatch area at speeds reaching 10 m/s and ~0.5 m/s respectively. The built table is then lowered with a screw mechanism to the desired layer thickness. The new layer is deposited, and the process is repeated until the part is fully fabricated. When a part is fully fabricated, the part can cool inside the built chamber till the temperature is below 100^{o}C. Helium is let into the built chamber to assist in the cooling duration. The part is later removed from the powder bed, and the surrounding sintered powder is removed using the powder recovery system.

SEBM is capable of producing functional parts with high mechanical properties more rapidly and more energy-efficiently as compared to laser based metallic AM technologies, such as selective laser melting (SLM) [1, 2]. In addition to the advantages such as the rapid manufacturing process and high energy efficiency, electron beam melted parts are also reported to have less residual stresses as compared to laser based processes [1, 2]. Post-processing heat treatment may not be necessary for the SEBM built functional parts.

Directed Energy Deposition (DED)

DED processes cover the following systems such as Laser Engineer Net Shaping (LENS), Direct Metal Deposition (DMD), Laser Metal Deposition (LMD) and Shaped Metal Deposition (SMD). The DED process can be further subcategorized according to their material feedstock mode (i.e. powder-fed systems and wire-fed systems) as shown in Figure 2.17.

Generic illustrations of the DED powder-fed system and wire-fed system are shown in Figure 2.17. DED process is a category of AM techniques that use a focused beam or an electric arc to fuse metallic powder or wire materials feedstock by layer-wise melting [17, 87]. Metal parts fabricated by DED processes exhibited high cooling rate solidified microstructures [2]. The layer of material being deposited can vary between 0.1 to a few millimeters in thickness [17]. Powder-fed AM systems have shown unique advantages in the repair of worn or damaged metal components as they are not restricted to a powder bed [88].

Of particular interest is that DED processes are capable of producing functionally graded (heterogeneous) parts due to its flexibility to change materials' compositions at each layer, by simply adjusting feeding materials and process parameters [2, 89]. Additionally, wire-fed systems have the highest deposition rates due to the feedstock of wire materials.

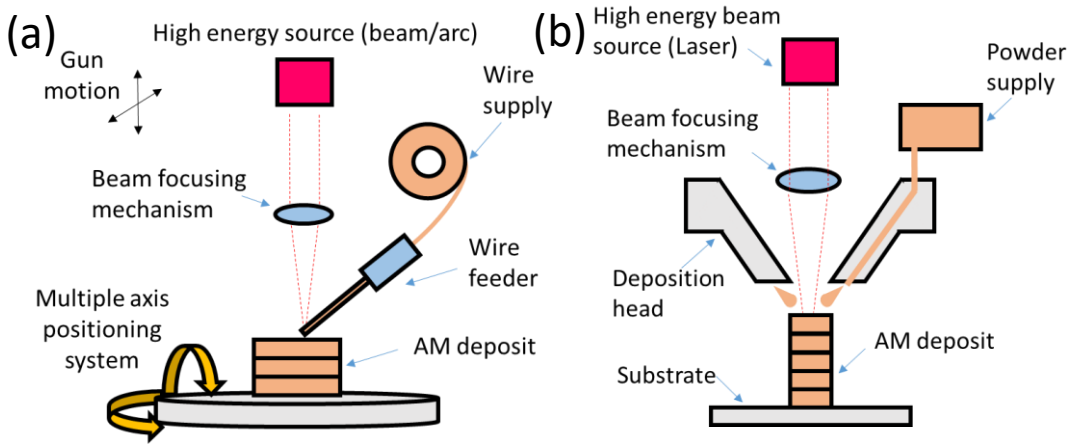

Figure 2.17 Generic illustrations of a DED AM systems (a) powder-blown system, and (b) wire-fed system [20].

Sheet Lamination (SL)

Sheet lamination processes include Ultrasonic additive manufacturing (UAM) and Laminated object manufacturing (LOM). Sheet lamination processes typically bond thin sheets of metallic foils by brazing, diffusion bonding, laser welding, resistance welding, or ultrasonic seam welding. A promising SL process is UAM, which uses ultrasonic vibrations to bond metal tapes into near net shape components [90]. Generic schematics of two UAM systems are shown in Figure 2.18.

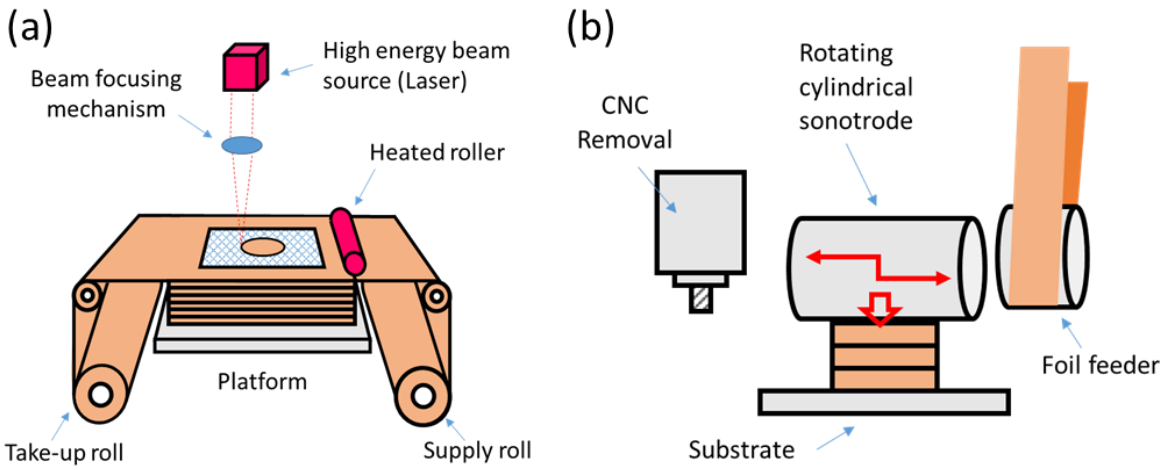

Figure 2.18 Generic illustrations of SL AM systems (a) Laminated object manufacturing (LOM) [2] and (b) Ultrasonic additive manufacturing (UAM) [91].

An advantage of SL process is in its capability of processing different metal materials. The process does require additional post machining to remove unbound metals and to produce features such as channels and holes to achieve the desired geometry. Due to the joining of metal sheets, anisotropy in mechanical properties was prevalent in SL parts [17]. This is mainly due to the weaker bonding formed across the foil interfaces as compared with the intergranular bonding within each foil tape [2].

It was found that each metal AM system may have their specific applications based on their advantages. PBF systems are typically employed to produce complex geometries requiring high resolution and rigorous build accuracy. While DED systems are commonly applied to repair and refurbishment of metal parts and large-scale manufacturing. Lastly, sheet lamination systems have the capability of joining dissimilar metals to produce components with some specific properties.

2.4.3 Influence of processing variables on anisotropy and heterogeneity

A summary of the operating conditions and specifications of typical PBF, DED and SL systems is shown in Table 2.3. AM processing variables such as deposition rate, beam size, process temperature, deposition rates, deposition mode or scanning strategy, materials would result in differences in the microstructure of the as fabricated part. The following subsections will discuss such processing variables with regards to their influence towards anisotropy and heterogeneity of microstructures and properties for metal AM parts.

Table 2.3 Various operating conditions and specifications of PBF, DED and SL systems.

System	Build Volume (mm)	Energy Source	Preheat Temperature (^{0}C)	Beam Dia. (µm)	Deposition Rate/cc h^{-1}	Layer Thickness (µm)	Ref.
Powder-bed System							
Electron beam based							
Arcam (A2)	Ø300×200	3.5 kW Electron Beam	700	~455	~60	100	[17, 26, 92]
Laser beam based							
SLM (SLM250)	250×250×250	400 W Nd: YAG laser	up to 200	~80	~20	10-50	[17, 93]
Powder-fed systems							
Optomec	900×1500×900	1 - 4 kW IPG fiber laser	-	~250	~230	250	[1, 17]
Wire-fed systems							
Sciaky (EBAM 300)	7620×2743×3353	>40 kW @ 60 kV welder	-	~380	~2000	3000	[1, 17]
Sheet lamination systems							
VHP UAM	1500x1500x600	9 kW @ 20 kHz	-	-	-	150	[94, 95]

2.4.3.1 Deposition rate

Some AM processes such as powder-fed DED are capable of producing material heterogeneity through in-situ variation in the deposition rate [64]. Figure 2.19 shows the result of a study that investigated the effect of deposition rates on the area fraction of equiaxed or columnar grains in the microstructure of DED titanium parts [64]. Though the reduction in deposition rate and beam size are often required to achieve better geometrical accuracy in such processes [2].

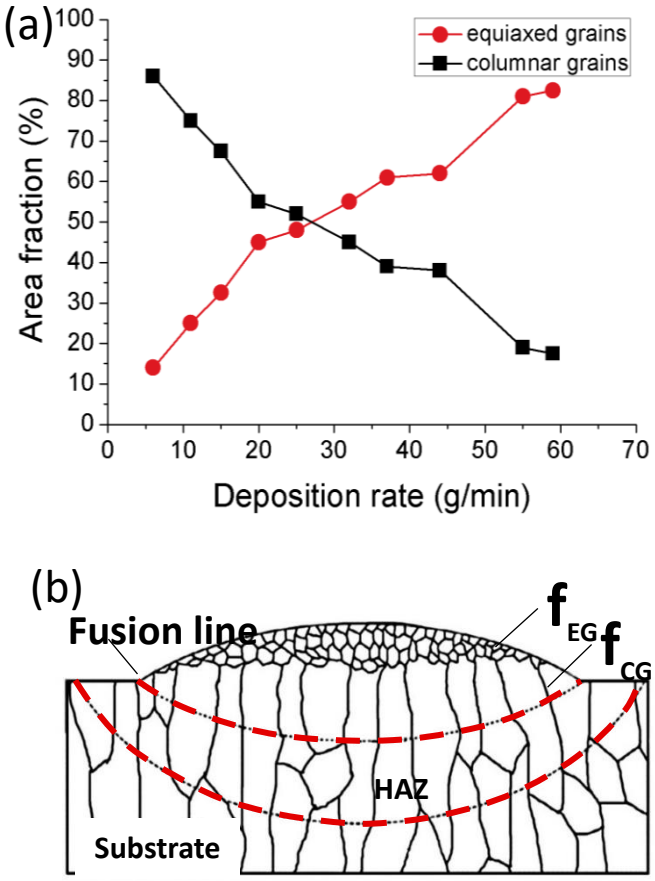

Figure 2.19 Effect of deposition rate on the microstructure of DED process; (a) A plot of the deposition rate against the area fraction of the equiaxed and columnar grains within a melt pool for the powder-fed DED process. (b) A schematic illustrating the measurements of area fractions of equiaxed and columnar grains f_{EG} and f_{CG} [64].

2.4.3.2 Beam size and power

Beam size and power may influence particle ejection during the layer-wise melting process. There are three basic particle ejection modes in beam melting processes: (1) the convective transport of liquid or plasma metal out of the molten pool commonly called spatter ejection or sometimes referred to “fireworks” during the melting process, (2) kinetic recoil of powder in DED and (3) electrostatic repulsion of powder particles in SEBM [17]. The former has been known to result in welding defects and is an underlying mechanism for the formation of process-induced porosity [17, 96]. Such defects can, in turn, affect the anisotropy and heterogeneity of the metal AM part.

2.4.3.3 Build environment

The AM build environment is an important processing variable. It was found that the absorption of atmospheric gasses during the building process might negatively impact the mechanical properties of the materials [97]. Thus, inert gas or vacuum atmosphere were often used during the metal AM processes [8]. However, operating in high vacuum environment will lead to an increased melt vaporization and outgassing of impurities [17, 98], which could cause heterogeneity in chemical composition. Also, it was reported that the flow rate and the pathway of inert gas had an effect on the porosity in SLM-built Ti-6Al-4V [99] because impurities generated from the melting process were re-deposited onto the scanned area.

2.4.3.4 Processing temperature

Processing temperature varies among the different metal AM systems. Some metal AM systems like LENS and UAM typically work at low process temperatures, while others such as EBM could require a processing temperature as high as ~1000 ^{o}C for some high-temperature materials [100]. The low substrate temperature in metal AM systems can reduce the

heterogeneity in microstructure due to differences in part size [101]. However, low substrate temperature could induce a higher magnitude of residual stress distributed unevenly in metal AM parts [102], which has been reported to affect the bulk mechanical behavior negatively [17].

2.4.3.5 Deposition mode and scan strategy

Deposition mode is the way in which material is delivered onto the melt surface in the metal AM system. The angle at which the material is fed in DED processes has been shown to be significant to minimize the defects during melting [103]. In the case of PBF processes, the beam scanning strategy is the important factor for controlling build defects [104]. The scan strategies that are commonly used in PBF systems include bi-directional, snaking and checker box [105-107]. Scan strategies have been reported to influence the crystal texture of the grains due to differences in the overall direction of the thermal gradient [108]. Crystallographic texture mainly contributes to anisotropy in the material [66, 109]. Other than crystallographic texture, scan strategy has also been attributed to be able to control the formation of either equiaxed or columnar grains, by altering the scan strategy across layers [110, 111]. Figure 2.20 shows a crystallographic orientation map with that the letter's "DOE" being of a different crystal orientation as compared to the surrounding grains. The material used in the study in Inconel 718. As such it can be seen that deposition mode and scan strategy could play an important role in controlling the anisotropy and heterogeneity in metal AM parts.

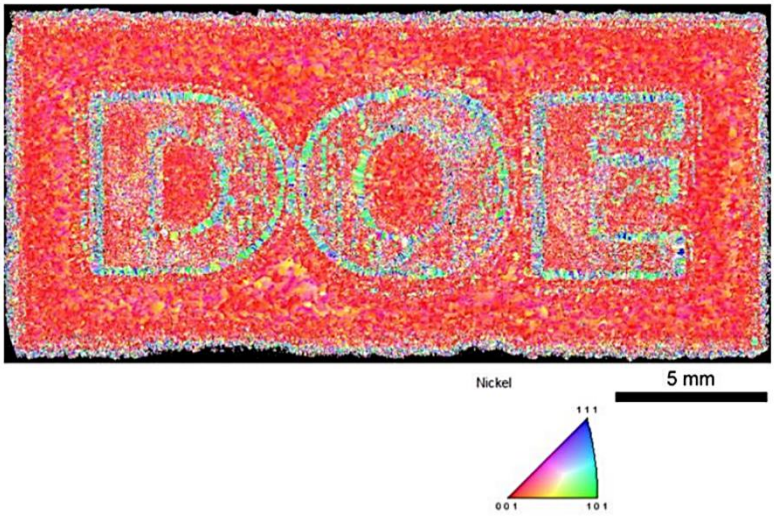

Figure 2.20 Crystallographic orientation map shows site-specific control of the crystallographic orientation of grain in Inconel 718 via optimization in scan strategy [111].

2.4.3.6 Materials

Most of metal AM technologies such as PBF, DED, and SL, adopt raw material in the forms of powder, wire, and sheet. The quality of powder (e.g. morphology and size distribution) used in PBF systems can determine the uniformity of material spreading across the powder bed [112, 113]. Such physical properties can also affect the density of metal AM parts [114]. The difference in the powder's quality is due to the different powder production methods [17]. Some powder production methods such as gas atomization can induce gas porosity into the final AM part. Post heat treatment processes (e.g. hot isostatic pressing) was needed to eliminate such pores [98]. The technology for the production of wire feedstock for the DED process is more mature as compared to the production of powder feedstock [17]. However, there still exist some defects relating to wire-type feedstock. Defects such as cracks or scratches on the wire surfaces can directly lead to porosity in the final AM part [17].

2.4.4 Applications and challenges of metal AM in Marine & Offshore industries

The potential of AM for the industries has been recognized and that is to reduce production/repair time of components at a lower cost. Though there are still little reports on the use of metal AM in the marine and offshore industry. Application of AM in the Marine and Offshore industry have mainly been reported to be used on naval ships. One possible application is in the gas turbine engine used in naval ships. The reason for the lack of current applications in the marine and offshore industry might be that the build volume of metal AM is still confined to a small volume. This section will discuss applications relating to the marine and offshore industry that are possible to be additively manufactured with today's current technologies.

2.4.5 Titanium alloys in marine and offshore industries

Titanium alloy with its high specific strength, good creep resistant up to 550^0C, and excellent corrosion resistant has been recognize as a very good choice for the marine application in 1950 [115]. Figure 2.21 shows the excellent corrosion properties of titanium as compared to various marine alloys [116].

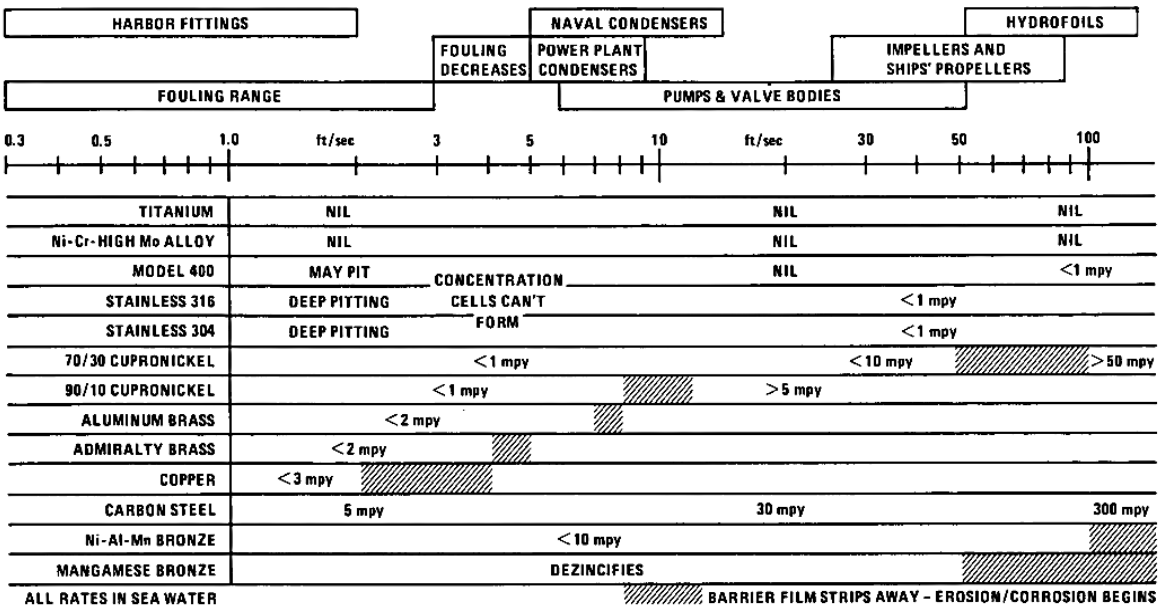

Figure 2.21 Corrosion resistance of titanium against other marine alloys [116]. The imperial unit for corrosion rates is "mpy" = mils per year. 1 mpy is equivalent one thousandth of an inch.

A majority of structurally material used in the offshore platforms are steel which requires some form of active sacrificial anodes and/or cathode protection against corrosion. Drawback of titanium as a material for marine and offshore applications is the high cost of production and repair using conventional methods. Titanium has to be manufactured in an inert atmosphere due to its high affinity with oxygen to form brittle carbide precipitates [117]. However, with the introduction of AM, it is now cheaper to manufacture titanium parts as compared to before. Other concerns with titanium are the stress corrosion and low toughness of some of its alloys and the lack of antifouling characteristics against bio-organisms [118].

2.4.5.1 Heat Exchangers

It has been reported that heat exchangers on offshore platforms in the North Sea uses titanium alloy (Ti Code-12 which contains 0.3 wt. % molybdenum and 0.8 wt. % nickel) for increased reliability resulting in cost saving over the life cycle of their operating life and their heat transfer characteristic are comparable to other popular materials (e.g. cupronickel) [115].

Thus heat exchangers with titanium tubing with rolled integral fins are a favorable choice over cheaper copper-based tubing based heat exchangers in the cooling of seawater and crude oil applications [115, 119]. Figure. 2.22 (a and b) shows two types of titanium-based heat exchangers, tubular and plate type. Tubular heat exchangers are used to cool the crude oil directly with flowing sea water via a series of tubes. Plate-type heat exchangers uses metal plates to transfer heat between two fluids instead [115]. AM has enabled new designs of heat exchanges to be explored as shown in Figure 2.22 (c and d). Research regarding the effect of geometry on the heat dissipation capabilities of heat exchanger has thus been revisited academically.

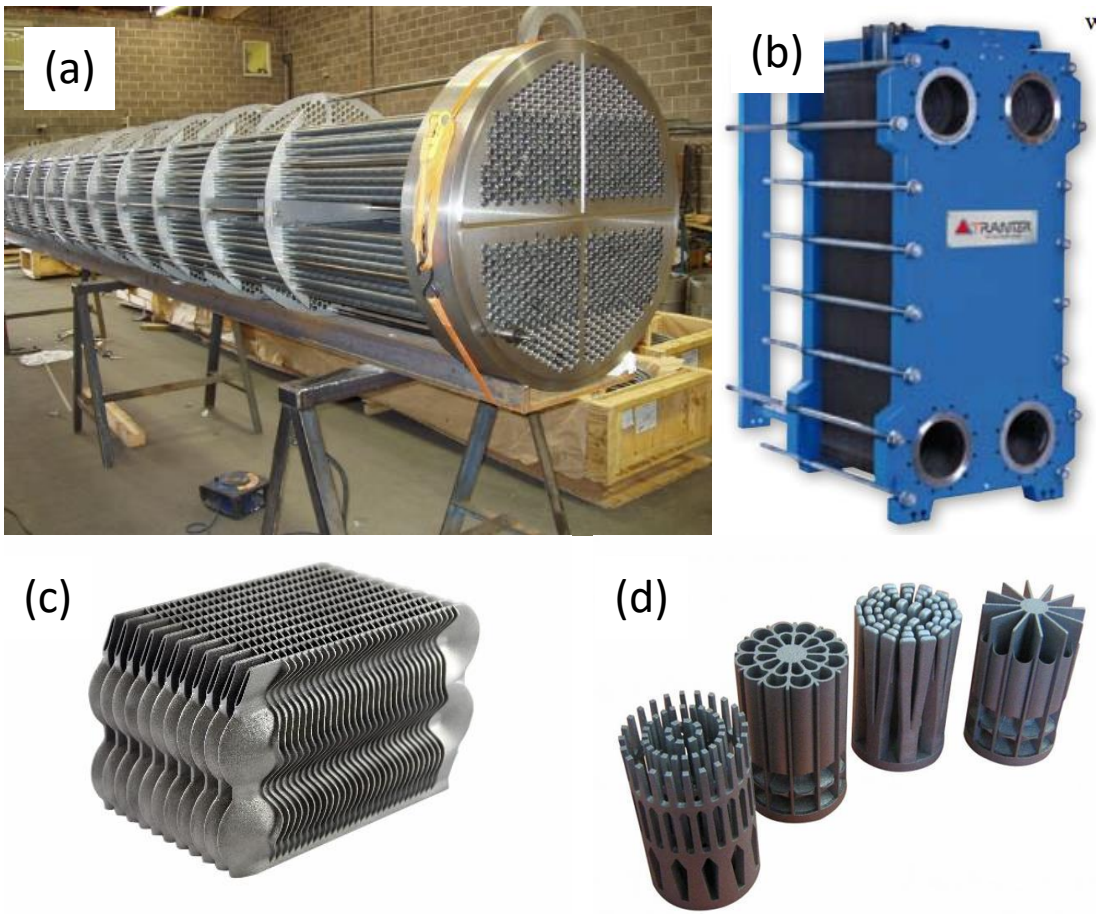

Figure 2.22 Images of various types of heat exchangers: (a) Titanium based tubular type heat exchanger with titanium tubing [120], (b) Titanium based plate-type heat exchanger [119] and (c and d) Examples of AM heat exchangers.

2.4.5.2 Valves and Plumbing Fixtures

Given titanium's excellent pitting and crevice corrosion resistance, it can be used in plumbing fixtures and valve applications. Ball valves utilized in the marine industry have been reported to be switching from Monel (70 Ni/30 Cu) to cast titanium Ti-6Al-4V [118, 121]. Advantages of the use of titanium in such application mainly stem from the longer operating life and the lesser maintenance requirement. Such fixtures are also used in aircraft hydraulic systems and are likely to be also used in the submarines [122]. Figure 2.23 shows various types of valves and plumbing fixtures.

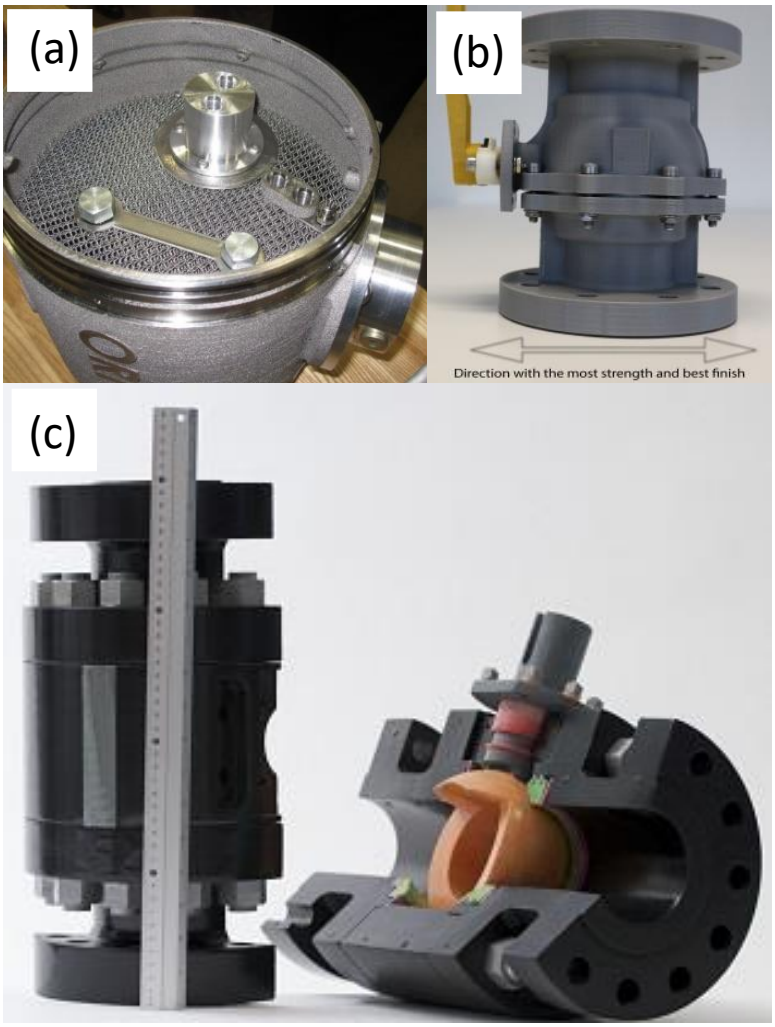

Figure 2.23 Images of several AM valves and prototypes: (a) An additive manufactured hydraulic manifold use in submersible robots by Oak Ridge National Laboratory (b) A ball valve additively printed in ABS polymer [123] and (c) Prototype of a ball valve that was made by AM.

2.4.5.3 Pumps, Impellers & Propellers

Titanium pumps used in crude oil recovery systems have shown to have less corrosion and abrasive wear by brine as compared to stainless steel pumps [115]. Such high-pressure pumps have been reported to be operating for more than seven years [124]. Investment cast Ti-6Al-4V have been reported to be used in pump's casing and impellers handling brine, while Ti-0.15 wt.% Pd alloy are used in sour crude systems, due to its corrosion resistance against sulphuric acid. Table 2.4 and Figure 2.24 shows various applications that titanium alloys can be used.

Table 2.4 Titanium alloy application in marine and offshore industry [116].

		Reason for selection				
Equipment	**Material**	**Strength-to-weight Ratio**	**Corrosion Resistance**	**Fatigue Resistance**	**SCC Resistance**	**Cavitation Resistance**
Propeller	Cast Ti-6Al-4V	X	X	X		X
Television re-entry systems	Ti-621/0.8 Mo	X	X		X	
Couplings	Ti-6Al-4V	X	X	X		
Buoyancy	Ti-6Al-4V	X	X			
	Ti-621/0.8 Mo	X	X		X	
Submersibles	Ti-621/0.8 Mo	X	X	X	X	

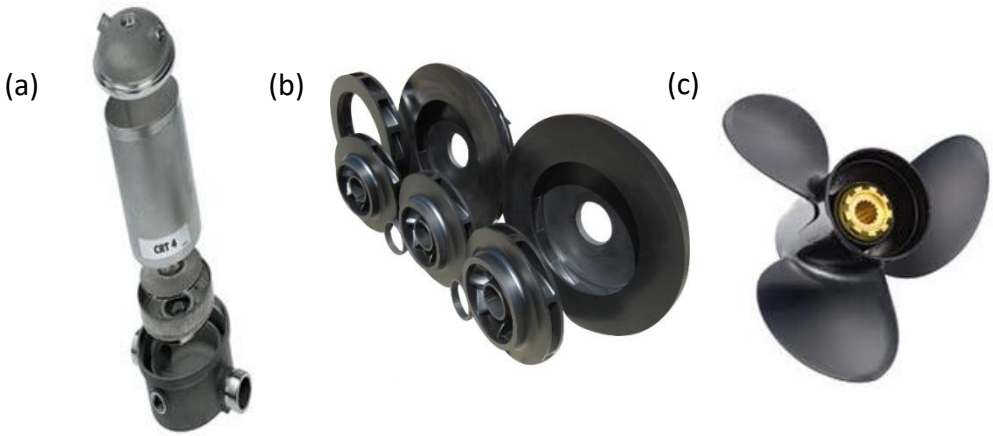

Figure 2.24 Examples for possible applications that can be AM (e.g. pump, impeller and propeller); (a) Shows a pump used for sea water applications, (b) shows the impeller component in a pump [125], (c) shows a propeller [126].

2.4.6 Summary

Metal AM has been available for the last 25 years, there have been many metal AM technologies that have been developed during that time. This section has reviewed the major category of Metal AM technologies that are currently available. In this thesis, the Metal AM technology in focus is the SEBM technology. This section also reviewed potential applications of additive manufactured titanium alloy in the marine and offshore applications. Due to the limitation of the build volume of current technologies, the possible application of AM in the marine and offshore industry is limited to smaller components such as ball valves, propeller, hydraulic manifolds, and impellers. With AM the cost of fabricating such applications in low volume is likely to be more cost effective as compared to conventional methods due to the lack of tooling cost.

2.5 Anisotropy and heterogeneity of microstructure and mechanical properties in metal additive manufacturing

2.5.1 Anisotropy in metal AM

Metal AM systems allow the fabrication of near-net-shaped parts with excellent tensile properties [9]. Some researchers reported anisotropic mechanical properties in metal AM parts, while other researchers reported the contrary [127-132]. The discrepancy in the studies may be due to the complex microstructure that exists in metal AM parts [133, 134]. This section thus aims to discuss the relationship between microstructure and mechanical properties on anisotropy.

2.5.2 Anisotropy in microstructure

2.5.2.1 Grain morphology

A common microstructure feature observed in metal AM parts was the epitaxial columnar grain morphology [26, 135-137]. Figure 2.25 shows an example of the epitaxial columnar grain morphology in SLM Co-alloy via a SEM micrograph and its corresponding crystal orientation map [138]. Such columnar grains that are aligned parallel to the build direction have been mainly attributed to causing anisotropy of mechanical properties in metal AM parts [10]. In the build direction, there the accumulation of slip dislocations along the prior β grain boundaries is greater as compared to the orientation perpendicular to the build direction due to the longer length of the prior β grain boundaries [139]. As such more plastic deformation before failure is reported in the vertically orientated samples [9]. Epitaxial columnar grain growth is because of the re-melting of previous layers during the material deposition process. It induced sufficient thermal gradient within the melt pool, which would prevent nucleation ahead of the solidification front [111].

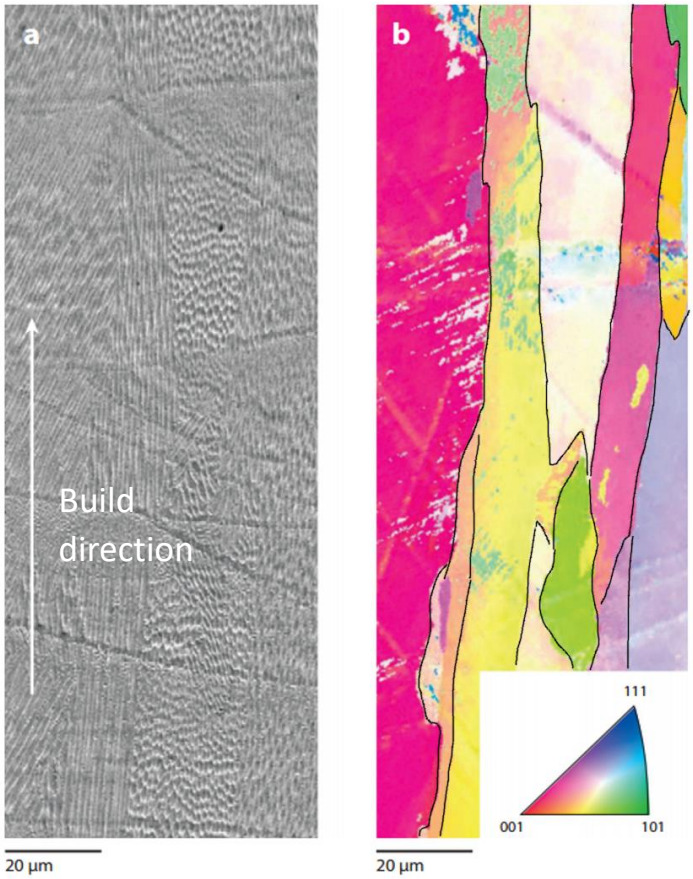

Figure 2.25 Columnar grain morphology in AM Co-base alloy; (a) SEM micrograph of the cross section of a Co-base alloy produced using the SLM process. (b) The corresponding crystal orientation map of the micrograph [138].

2.5.2.2 Crystallographic texture

Given the steep thermal gradient along the build direction, the SEBM-built Ti-6Al-4V exhibited a preferential <001> crystallographic texture for the reconstructed prior β grains [92]. Figure 2.26 shows that the $<001>_{\beta}$ texture of the reconstructed prior β grains of EBM-built Ti-6Al-4V improved with build height due to the grains with a <001> orientation having the greatest growth advantage [92]. Strong crystallographic texture has been known to result in anisotropy in mechanical properties [140]. However, due to the phase transformation from β to α phase following the Burgers orientation relationship, the resultant crystallographic orientation of the predominantly α phase showed an almost isotropic distribution [26, 133]. It is thus likely that the resultant crystallographic texture

in the case of SEBM-built Ti-6Al-4V may not be a significant contributor to anisotropy. Another study on laser-based PBF tantalum likewise suggested that the elongated grain morphology along the build direction had a larger influence on the anisotropy as compared to the crystallographic texture [109].

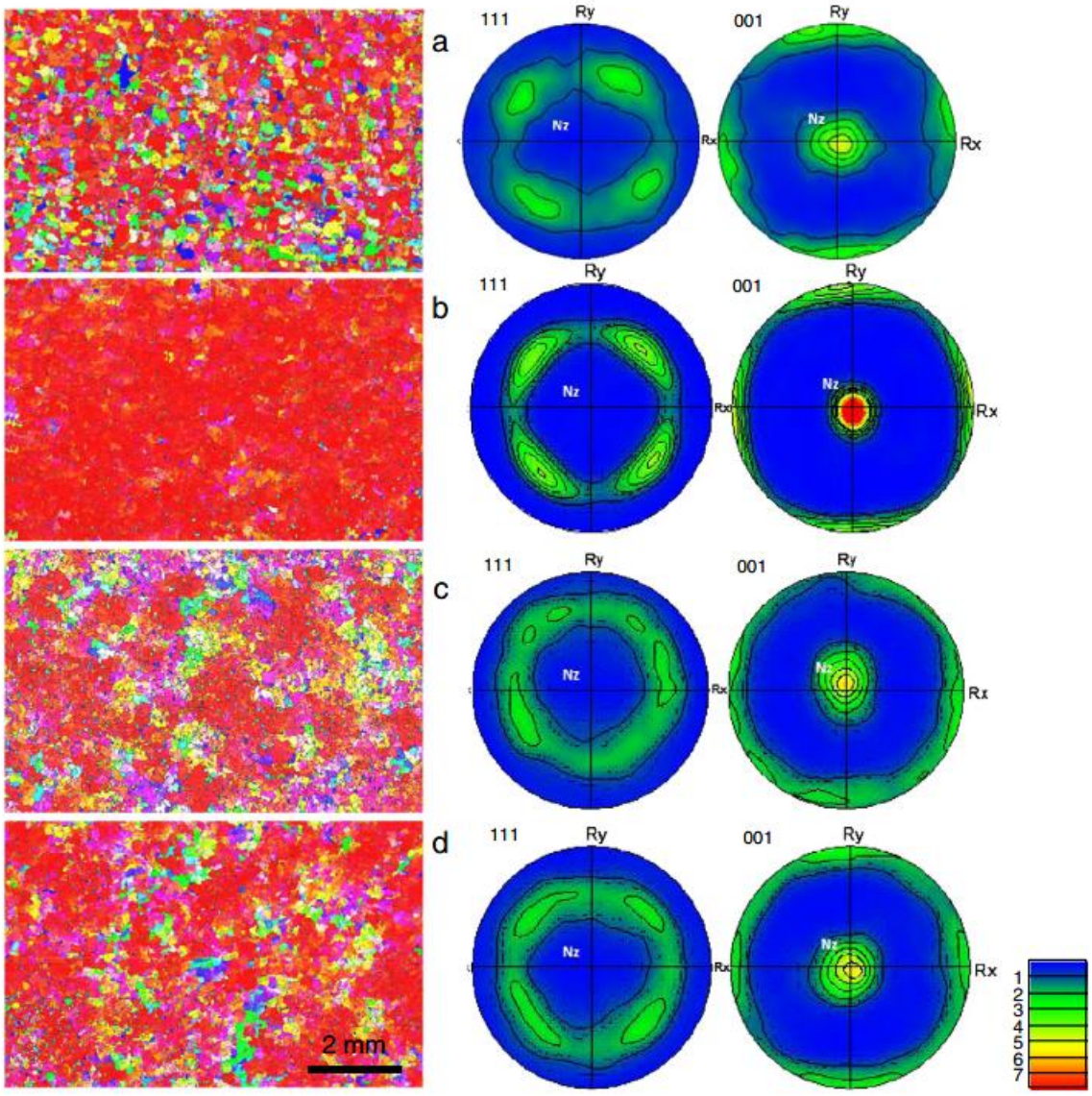

Figure 2.26 Reconstructed β-phase IPF maps and their corresponding texture pole figures at different build heights of; (a) 0.5 mm, (b) 5 mm, (c) 25 mm, (d) 35 mm near the build top surface of SEBM-built Ti-6Al-4V [39].

2.5.2.3 Lack-of-fusion defects

Lack-of-fusion defects can be formed possibly due to unoptimized process parameters [141]. Such processing defects can range from ~50-500 µm in size [142]. The directionality of such defects has an effect on the anisotropy in mechanical properties [18]. This is attributed to the tensile stress being normal to the plane of the defect, thus inducing crack propagation along the tip of the defect leading to material failure. As such, it is important to identify such processing-induced defects during the AM process. Many researchers are actively conducting research in the area of in-situ process monitoring, to identify such material discontinuities during the manufacturing process [142]. Figure 2.27 shows micro computerized tomography (CT) scans of the spatial distribution of defect in as-built SEBM Ti-6Al-4V alloy [143]. Post heat treatment process like HIP may eliminate a majority such lack-of-fusion defects from metal AM parts [9].

In summary, columnar grain morphology, crystallographic texture, and lack-of-fusion defects are the three factors contributing to the anisotropy in the microstructure of metal AM part. With on-going research to improve the quality of metal AM parts, it can be foreseen that such lack-of-fusion defects will be significantly reduced [9]. Therefore, the columnar grain and the strong crystallographic texture mainly contribute to anisotropy in metal AM parts.

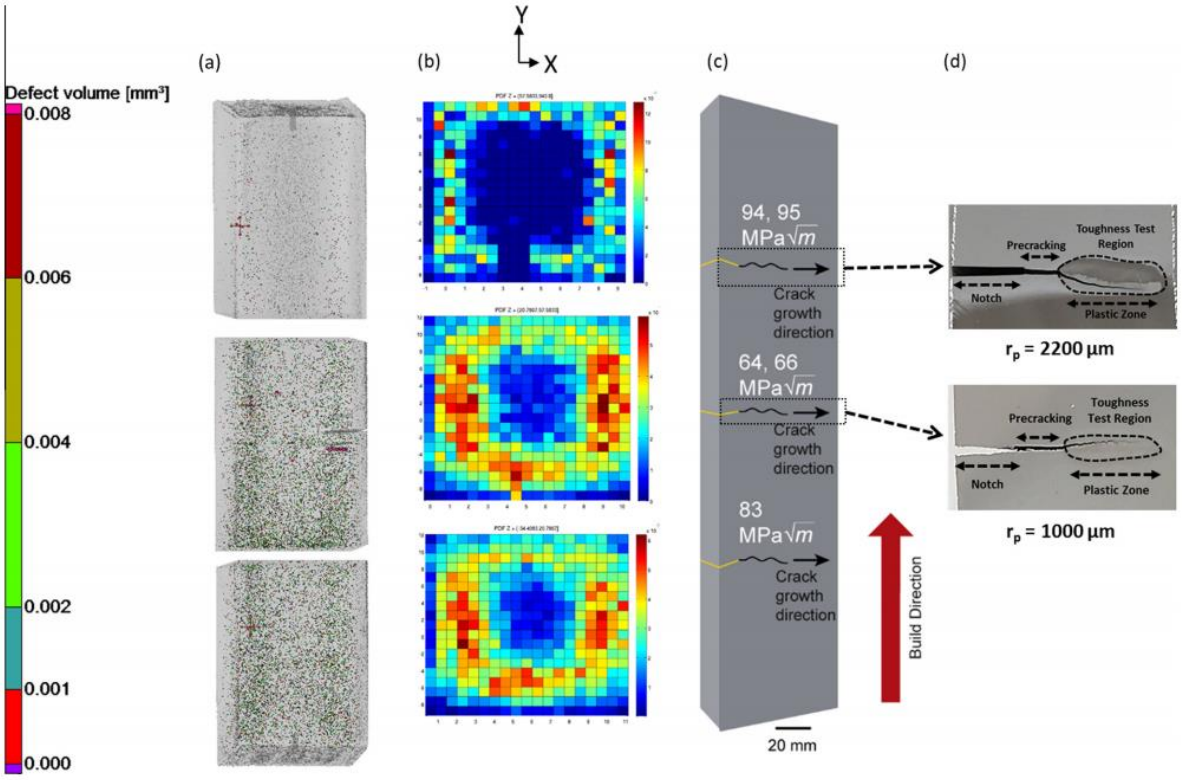

Figure 2.27 (a) µCT scans showing defects spatial distribution in SEBM Ti-6Al-4V (b) defect histogram for the SEBM Ti-6Al-4V at the bottom, middle and top region (c) fraction toughness variation at the bottom, middle and top region respectively [143].

2.5.3 Anisotropy in mechanical properties

The published literature regarding the anisotropic mechanical properties (e.g. tensile, compressive, fracture and fatigue) from metal AM parts will be discussed in the following sections. The majority of the available results was based on AM titanium alloys. Other metals or alloys (e.g. cobalt chrome (CoCr), Inconel superalloys, stainless steels and aluminum alloys, etc.) will also be discussed in this thesis. In addition, the thesis will examine whether the anisotropic mechanical properties of metal AM parts could meet the minimum requirements for practical applications. As anisotropy is an orientation-dependent property, the orientation designation standard will be presented to provide clarity.

2.5.3.1 Orientation designation standard

The International Organization for Standardisation (ISO) and ASTM have formed a joint committee, called F42 in 2009, to work on developing standards for AM [144]. This thesis will adopt the ISO and ASTM standard regarding the orientation designations for mechanical testing to provide consistency in comparison [145]. Figure 2.28 (a) shows the orientation designation for mechanical testing based on the ISO and ASTM standard. In this terminology, rectangular test coupon requires three alphabets (X, Y, and Z) to provide a complete orientation designation. The X-axis is designated to be parallel to the front of the machine while the Z-axis is in the vertical direction. The Y-axis is perpendicular to both the X and Z-axis, with a positive direction following a right-hand rule coordinate system. The first alphabet in the designation corresponds to the axis parallel to the longest overall dimension and the second and third alphabets correspond to the axis parallel to the second and third longest overall dimensions.

Additionally, Figure 2.28 (b) shows the possible ISO designations for determining the orientation dependence of mechanical properties for AM samples based on a study [146]. The first letter in this nomenclature represents the directions normal to the crack plane, and the second letter represents the predicted direction of the crack propagation. The last letter represents the plane in which the crack begins (e.g. start (s), end (e), middle (m) and both (b)). These orientation designation standards thus provide a starting point for a comparison of the published literature in the current work.

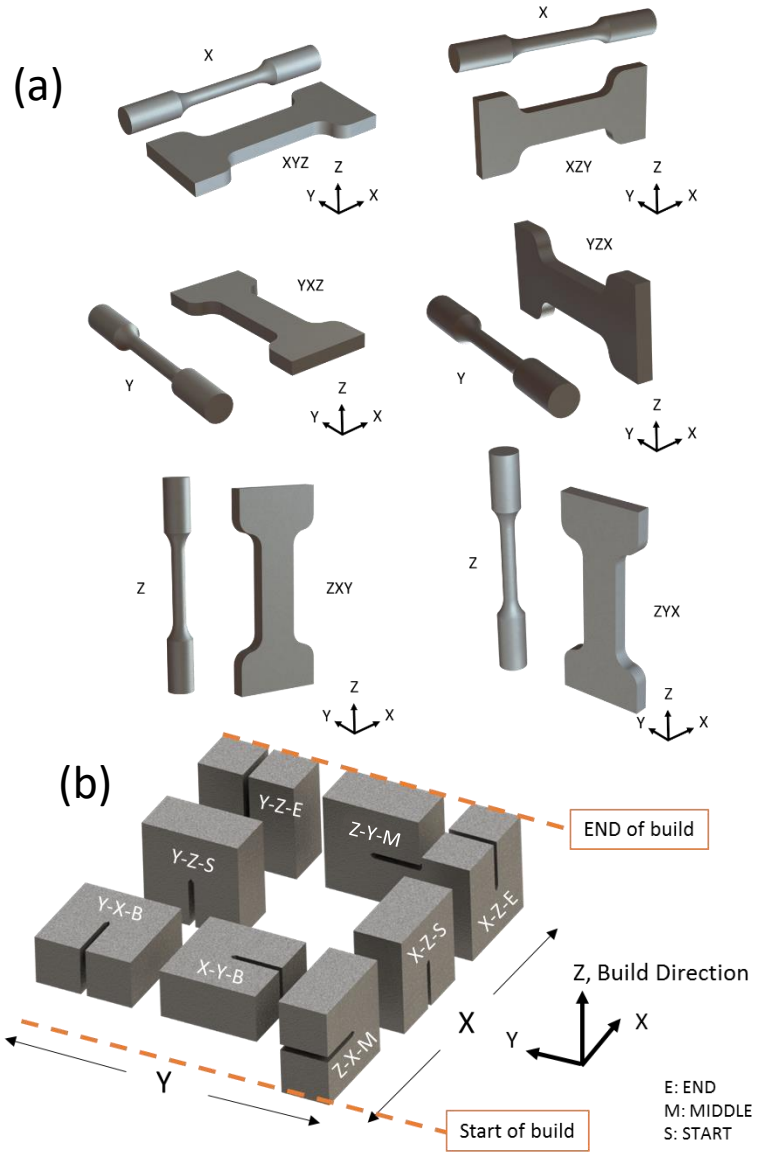

Figure 2.28 Orientation designations for mechanical testing of AM materials; (a) tensile test [9] (b) determining the orientation dependence of mechanical properties [146].

2.5.3.2 Tensile properties

Many studies have shown that the tensile properties of AM Ti-6Al-4V are comparable to their cast and wrought material equivalents [9, 20, 147]. However, less emphasis has been placed on investigating the anisotropic mechanical properties of metal AM parts using various technologies. More importantly, it is still not well understood if the lower limit of anisotropic mechanical properties in metal AM parts could meet the minimum requirements of their cast and wrought equivalents. Table 2.5 summarizes the anisotropic tensile properties of various metal AM parts. As a number of the research papers did not comprehensively report the build orientation of their samples, some of the orientation indicated in the table does not follow the notation system described in section 2.5.3.1 earlier.

Anisotropy will be defined as $\frac{\sigma_x - \sigma_z}{\sigma_x} \times 100\%$ [148], where σ_x and σ_z denotes the mechanical properties (e.g. yield strength, elongation, fracture toughness and fatigue threshold) in the x and z directions, respectively. It is worth noting that the trend of anisotropy is opposing for tensile strength and ductility [149]. In the majority of the studies on SEBM-built and DED-built Ti-6Al-4V, no significant anisotropy in yield strength was observed. However, in the case of SLM-built Ti-6Al-4V, there existed higher anisotropy in the yield strength between the different build orientations. Anisotropy in tensile properties was also observed in SL aluminium alloy [11, 14]. Despite anisotropy being exhibited by the SLM-built Ti-6Al-4V, a majority of the reported yield strength either matched or surpassed the minimum values for their cast and wrought equivalents.

However, the majority of ductility results observed in SLM-built and DED-built Ti-6Al-4V was below the minimum value of 8-10 % elongation for wrought material. The low ductility of SLM-built and DED-built Ti-6Al-4V is mainly attributed to the brittle martensitic phase formed during the SLM and DED processes [10, 150]. Ductility of metal AM parts can be improved through post heat treatment processes [148, 151]. In some studies, anisotropy in

ductility remains between the different orientations, suggesting that the anisotropic property is most likely due to the columnar grains [131, 149, 152].

Table 2.5 Summary of tensile properties of various metal AM parts.

Material	Condition	Process	Tensile Axis Orientation	Anisotropy in yield strength (%)	Anisotropy in elongation (%)	Yield Strength (MPa)	Ultimate Tensile Strength (MPa)	Elongation (%)	Ref.
Powder-bed fusion Electron beam based									
Ti-6Al-4V	As-built	Arcam	Horizontal (XY)	-1.0	-14.0	870.0 ± 8.1	971.0 ± 3.1	12.1 ± 0.8	[153]
			Vertical (Z)			879.0 ± 12.0	953.0 ± 8.8	13.8 ± 0.9	
Ti-6Al-4V	As-built	Arcam A1	Horizontal (XY &YX)	-3.7	-33.3	783.0 ± 15.0	833.0 ± 22.0	2.7 ± 0.4	[132]
			Vertical (ZXY)			812.0 ± 12.0	851.0 ± 19.0	3.6 ± 0.9	
Ti-6Al-4V	Machined	Arcam S400	Horizontal(X/Y)	27.3	-98.0	1195.0 ± 19.0	1269.0 ± 9	5.0 ± 0.5	[32]
			Vertical (Z)			869.0 ± 7.2	928.0 ± 9.8	9.9 ± 1.7	
Ti-6Al-4V	As-built	Arcam S2	Horizontal (XY)	-0.1	26.2	982.9 ± 5.7	982.9 ± 5.7	12.2 ± 0.8	[130]
			Vertical (Z)			984.1 ± 8.5	1032.9 ± 12.9	9.0 ± 2.9	
Ti-6Al-4V	As-built	Arcam A2	Horizontal (XYZ)	23.6	-	825	907	-	[139]
			Vertical (ZXY)			630	792	-	
Ti-6Al-4V	HIP	Arcam	Horizontal (XYZ)	-0.2	5.1	866 ± 6.4	959 ± 8.2	13.6 ± 0.6	[153]
			Vertical (Z)			868 ± 2.9	942 ± 2.6	12.9 ± 0.8	
Ti-6Al-4V ELI	As-built	Arcam	Horizontal (XYZ)	0.0	-4.1	803	896	17	[154]
			Vertical (Z)			803	896	17.7	
Ti-6Al-4V ELI	As-built	Arcam	Horizontal (XYZ)	1.8	-9.5	817 ± 4.3	918 ± 1.0	12.6 ± 0.8	[153]
			Vertical (Z)			802 ± 7.9	904 ± 6.9	13.8 ± 0.9	
Ti-6Al-4V ELI	HIP	Arcam	Horizontal (XYZ)	0.9	-8.8	814 ± 2.4	916 ± 2.5	13.6 ± 1.2	[153]
			Vertical (Z)			807 ± 8.4	902 ± 8.7	14.8 ± 0.5	
CoCrMo	As-built	Arcam	Horizontal (XYZ)	-9.6	84.0	717	1110	5	[155]
			Vertical (Z)			786	869	0.8	
CoCrMo	HIP & HT	Arcam	Horizontal (XYZ)	0.2	0.0	586	1145	30	[155]
			Vertical (Z)			585	1151	30	

Table 2.5 Summary of tensile properties of various metal AM parts (continue).

Material	Condi-tion	Process	Tensile Axis Orientation	Anisotro-py in yield strength (%)	Anisotropy in elongation (%)	Yield Strength (MPa)	Ultimate Tensile Strength (MPa)	Elongation (%)	Ref.
		Powder-bed fusion Laser beam based							
Ti-6Al-4V	As-built	SLM	Horizontal (XYZ)	-2.9	0.0	1093 ± 64	1279±13	6±0.7	[131]
			Vertical (ZXY)			1125 ± 22	1216±8	6±0.4	
Ti-6Al-4V	As-built	Renishaw AM250	Horizontal (XYZ)	10.0	-17.1	1075 ± 25	1199 ± 49	7.6±0.5	[149]
			Horizontal (XZY)	1.1	24.6	978 ± 5	1143 ± 6	11.8 ± 0.5	
			Vertical (ZXY)			967 ± 10	1117±3	8.9±0.4	
Ti-6Al-4V	Machined	EOS M270 SLM	Horizontal (X/Y)	4.4	2.2	1195 ± 19	1269±9	5±0.5	[32]
			Vertical (Z)			1143 ± 30	1219±20	4.89±0.6	
Ti-6Al-4V	Machined	SLM	Horizontal (XY)	15.4	77.6	1137 ± 20	1206±8	7.6±2	[151]
			Vertical (Z)			962 ± 7	1166±25	1.7±0.3	
Ti-6Al-4V	As-built	Concept Laser M2 Cusing SLM	Horizontal (XY)	1.9	-54.5	1070 ± 50	1250±50	5.5±1	[150]
			Vertical (Z)			1050 ± 40	1180±30	8.5±1.5	
Ti-6Al-4V	SR	SLM	Horizontal (XYZ)	1.1	-14.3	1145 ± 17	1187 ± 10	7 ± 2.7	[131]
			Vertical (ZXY)			1132 ± 13	1156 ± 13	8 ± 0.4	
Ti-6Al-4V	SR	Renishaw AM250	Horizontal (XYZ)	3.8	-37.1	974 ± 7	1065 ± 21	7.0 ± 0.5	[149]
			Horizontal (XZY)	2.2	22.6	958 ± 6	1057 ± 8	12.4 ± 0.7	
			Vertical (ZXY)			937 ± 9	1052 ± 11	9.6 ± 0.9	
Ti-6Al-4V	HT	SLM	Horizontal (XYZ)	0.9	-100.0	973 ± 8	996 ± 10	3 ± 0.4	[131]
			Vertical (ZXY)			964 ± 7	998 ± 14	6 ± 2	

Material	Condi-tion	Process	Tensile Axis Orientation	Anisotro-py in yield strength (%)	Anisotropy in elongation (%)	Yield Strength (MPa)	Ultimate Tensile Strength (MPa)	Elongation (%)	Ref.
Ti-6Al-4V	HT	SLM	Horizontal (XY)	2.0	11.8	944 ± 8	1036 ± 30	8.5 ± 1	[151]
			Vertical (Z)			925 ± 14	1040 ± 4	7.5 ± 2	
IN718	-	SLM	Horizontal (X/Y)	9.7	-7.9	816 ± 24	1085 ± 11	19.1 ± 0.7	[156]
			Vertical (Z)			737 ± 4	1010 ± 10	20.6 ± 2.1	
IN718	HT	SLM	Horizontal (X/Y)	2.9	-9.4	1222 ± 26	1417 ± 4	15.9 ± 1.0	[156]
			Vertical (Z)			1186 ± 23	1387 ± 12	17.4 ± 0.4	
Al-Si-10Mg	As built	SLM	Horizontal(XY)	0.1	-11.0	169 ± 1	272.8 ± 2.9	8.2 ± 0.3	[157]
			Vertical(Z)			168.8 ± 1.3	267	9.1 ± 0.5	
Al-Si-10Mg	As-built	Concept Laser M2	Horizontal (X/Y)	4.0	16.7	250	330	1.2	[158]
			Vertical (Z)			240	320	1	
Al-Si-10Mg	-	Concept Laser M1	Horizontal(XY)	-	37.5	-	391 ± 6	5.55 ± 0.4	[159]
			Vertical(Z)			-	398 ± 8	3.47 ± 0.6	
CoCrMo	As-built	Dimetal-100	Horizontal(XY)	7.1	25.0	738 ± 9.9	1050 ± 12.2	5.2 ± 0.3	[160]
			Vertical(Z)			685.3 ± 10.5	970 ± 9.8	3.9 ±0.2	
		DED systems							
		Powder-fed deposition							
Ti-6Al-4V	Machined	Trumpf DLD system	Horizontal (X/Y)	0.0	58.3	950 ± 2	1025 ± 10	12 ± 1	[161]
			Vertical (Z)			950 ± 2	1025 ± 2	5 ± 1	
Ti-6Al-4V	As-built	Tritons Laser Free-Form Fabrication (LF3)	Horizontal (XYZ)	41.5	73.4	892 ± 10	911 ± 10	6.4 ± 0.6	[148]
			Vertical (ZXY)			522	797 ± 27	1.7 ± 0.3	

Material	Condi-tion	Process	Tensile Axis Orientation	Anisotro-py in yield strength (%)	Anisotropy in elongation (%)	Yield Strength (MPa)	Ultimate Tensile Strength (MPa)	Elongation (%)	Ref.
Ti-6Al-4V	Machined	Tritons Laser Free-Form Fabrication (LF3)	Horizontal (XYZ)	2.6	29.6	984 ± 25	1069 ± 19	5.4 ± 1	[148]
			Vertical (ZXY)			958 ± 14	1026 ± 17	3.8 ± 0.9	
Ti-6Al-4V	Machined	DED	Horizontal (YZX)	0.2	-28.4	960 ± 26	1063 ± 20	10.9 ± 1.4	[10]
			Vertical			958 ± 19	1064 ± 26	14 ± 1	
Ti-6Al-4V	ASTM F1472	Cast material				>758	>860	>8	[162]
Ti-6Al-4V	ASTM F1108	Wrought material				>860	>930	>10	[163]
CoCrMo	ASTM F75	Cast material				450	655	8	[164]
CoCrMo	ASTM F1537	Wrought material				517	897	20	[165]
Al-Si-10Mg		A360 Die Cast				160	325	3	[166]
IN718	AMS 5382	Cast material				758	802	5	[167]
IN718	AMS 5662	Wrought material				1034	1241	10	[167]

2.5.3.3 Fracture toughness

Fracture toughness is a property describing the ability of a material containing a crack to resist fracture [168, 169]. Table 2.6 compiles the reported fracture toughness values of some metal AM parts from a variety of studies. The samples are defined by the author as vertical and horizontal based on the orientation of the longest edge of the sample to the build platform. If the longest edge of the sample is parallel to the build platform, the sample is termed as horizontal and if the longest edge is perpendicular to the build platform, the sample is termed as vertical. In both SLM-built and SEBM-built Ti-6Al-4V, anisotropy in fracture toughness

was reported [143] [170]. An important reason for the orientation dependent fracture toughness in SEBM-built Ti-6Al-4V is the interaction of the crack propagation path with the microstructure of the material. As such the direction of the crack plane and the orientation of the columnar grains in SEBM-built Ti-6Al-4V will affect the fracture toughness of the material. Crack propagation through the prior β grains would result in a higher fracture toughness as compared to when the crack is propagating along the columnar grain boundary [143]. It is noted that the fracture toughness of SEBM-built Ti-6Al-4V, was comparable to the value of 44 - 66 MPa $m^{0.5}$ and 88 - 110 MPa $m^{0.5}$ for Ti-6Al-4V with equiaxed and transformed α morphology [171]. The lower toughness values observed in SLM-built Ti-6Al-4V is due to the fine acicular α' martensitic microstructure that is brittle as compared to the α/β duplex microstructure observed in the SEBM-built Ti-6Al-4V [170].

Additionally, residual stresses within the metal AM parts can lead to anisotropy in fracture toughness [131]. Such residual stresses can be reduced by post heat treatment processes such as HIP or stress relief treatment. A study based on SLM Ti-6Al-4V observed an increase in fracture toughness and the lost in anisotropy after HIP and stress relief heat treatments for SLM-built Ti-6Al-4V [131]. A study on SEBM-built Ti-6Al-4V however reported a decrease in fracture toughness after heat treatment processes, which was due to the coarsening of the microstructure [143]. Thus, understanding of the as-built microstructures for the different metal AM systems is important in determining the post heat treatment schemes in order to achieve superior fracture toughness.

Table 2.6 Summary of fracture toughness of various metal AM parts.

Material	Condition	Process	Orientation	Anisotropy in fracture toughness (%)	Fracture toughness (MPa √m)	Ref.
		Powder-bed fusion				
		Electron beam based				
Ti-6Al-4V	As-built	Arcam A1	Horizontal (Y-X-B, X-Y-B)	7.3	110±7.4	[132]
			Vertical (Z-X-M, Z-Y-M)		102±8.9	
Ti-6Al-4V	As-built	Arcam A2	Horizontal (X-Z-E, X-Y-B, Y-X-B)	18.8	67-80	[146]
			Vertical (Z-X-M)		65	
		Laser Beam based				
Ti-6Al-4V	As-built	SLM	Horizontal (X-Y-B)	17.9	28±2	[131]
			Vertical (X-Z-E, Z-X-M)		16-23	
Ti-6Al-4V	As-built	MTT 250	Horizontal (Y-X-B)	3.1	66.9 ± 2.6	[170]
			Vertical (Z-X-M, Z-Y-M)		41.8-64.8 ± 16.9	
Ti-6Al-4V	SR	SLM	Horizontal (X-Y-B)	-10.7	28±2	[131]
			Vertical (X-Z-E, Z-X-M)		30-31±2	
Ti-6Al-4V	HT	SLM	Horizontal (X-Y-B)	-19.5	41±2	[131]
			Vertical (X-Z-E, Z-X-M)		49±2	

2.5.3.4 Compressive properties

Compressive testing was also commonly used to evaluate the mechanical properties of metal AM parts [28]. A study on SLM-built tantalum alloy reported that compressive yield strength was higher in the vertical direction as compared to that in the horizontal direction. This is attributed to the different crystallographic textures [109]. The compression yield strength of SLM tantalum alloy were found to be better than those fabricated by either electron beam furnace or powder metallurgy despite the anisotropic tensile strength [109]. Anisotropy in mechanical properties can be designed into a part through structural design [19]. A study on SEBM builds (Ti-6Al-4V) showed that different lattice designs exhibited varying degrees of

anisotropy [97]. Anisotropy in compressive strength was shown to be dependent on the unit size of the lattice structure [172].

2.5.3.5 Fatigue properties

The evaluation of fatigue properties is critical to understand how metal AM parts fail under cyclic loading. Table 2.7 provides a summary of the published data regarding fatigue properties of metal AM parts. It can be observed that higher fatigue strengths were exhibited in the horizontal orientation as compared to the vertical orientation in PBF systems. In general, SLM fabricated parts exhibited a higher Paris slope as compared to the counterparts EBM, indicating a higher fatigue crack growth rate [9]. The cycles to failure of the as-fabricated metal AM parts are significantly lower as compared to their wrought equivalent, due to the rough build surface and the presence of internal defects acting as crack initiation sites [9]. However, the fatigue strength of metal AM parts can be improved through post heat treatment and surface machining as shown in Figure 2.29 [9, 173]. In addition to surface roughness and internal defects, fatigue crack propagation was also found to be dependent on the crystallographic orientation of the grain containing the crack tip, the number of grain boundaries surrounding it and the direction of internal residual stress [149, 170].

Table 2.7 Summary of fatigue properties of PBF metal AM Ti-6Al-4V parts and ASTM wrought Ti-6Al-4V.

Material	Condition	Process	Test Orientation	Load Ratio (R)	Anisotropy in fatigue overload (%)	Fatigue overload (MPa √m)	Cycles (m/cycle)	Paris Slope	Anisotropy in fatigue threshold (%)	Threshold (MPa √m)	Ref.
		Electron beam based									
Ti-6Al-4V	As-built	Arcam A2	Horizontal (X-Z,X-Y)	0.1,0.3, 0.7	28.1	63-96		1.4-3.1	33.3	3.5-5.7	[146]
			Vertical (Z-X)	0.3		69		2.6		3.8	
Ti-6Al-4V	As-built	MTT 250	Horizontal (X-Y)		32.7	33.3	1.2×10^{7}	2.61	7.9	6.3	[170]
			Vertical (X-Z,Y-Z)			22.4-36.0	1.7×10^{7}-2.1×10^{7}	2.37-2.45		5.8-5.9	
		Laser beam based									
Ti-6Al-4V	As-built	SLM	Horizontal (X-Y-B)				5.79×10^{12}	3.37			[131]
	As-built	SLM	Vertical (X-Z-E,Z-X-M)				2.08×10^{12} - 7.51×10^{12}	4.17-4.41			
Ti-6Al-4V	SR	SLM	Horizontal (X-Y-B)				9.93×10^{15}	5.84			[131]
	SR	SLM	Vertical (X-Z-E,Z-X-M)				1.16×10^{11} - 8.85×10^{12}	3.24-3.35			
Ti-6Al-4V	HT	SLM	Horizontal (X-Y-B)				2.04×10^{12}	3.83			[131]
	HT	SLM	Vertical (X-Z-E,Z-X-M)				1.71×10^{11}-2.58×10^{11}	3.11-3.35			
Ti-6Al-4V		Wrought								2.3-4.2	[174] [175]

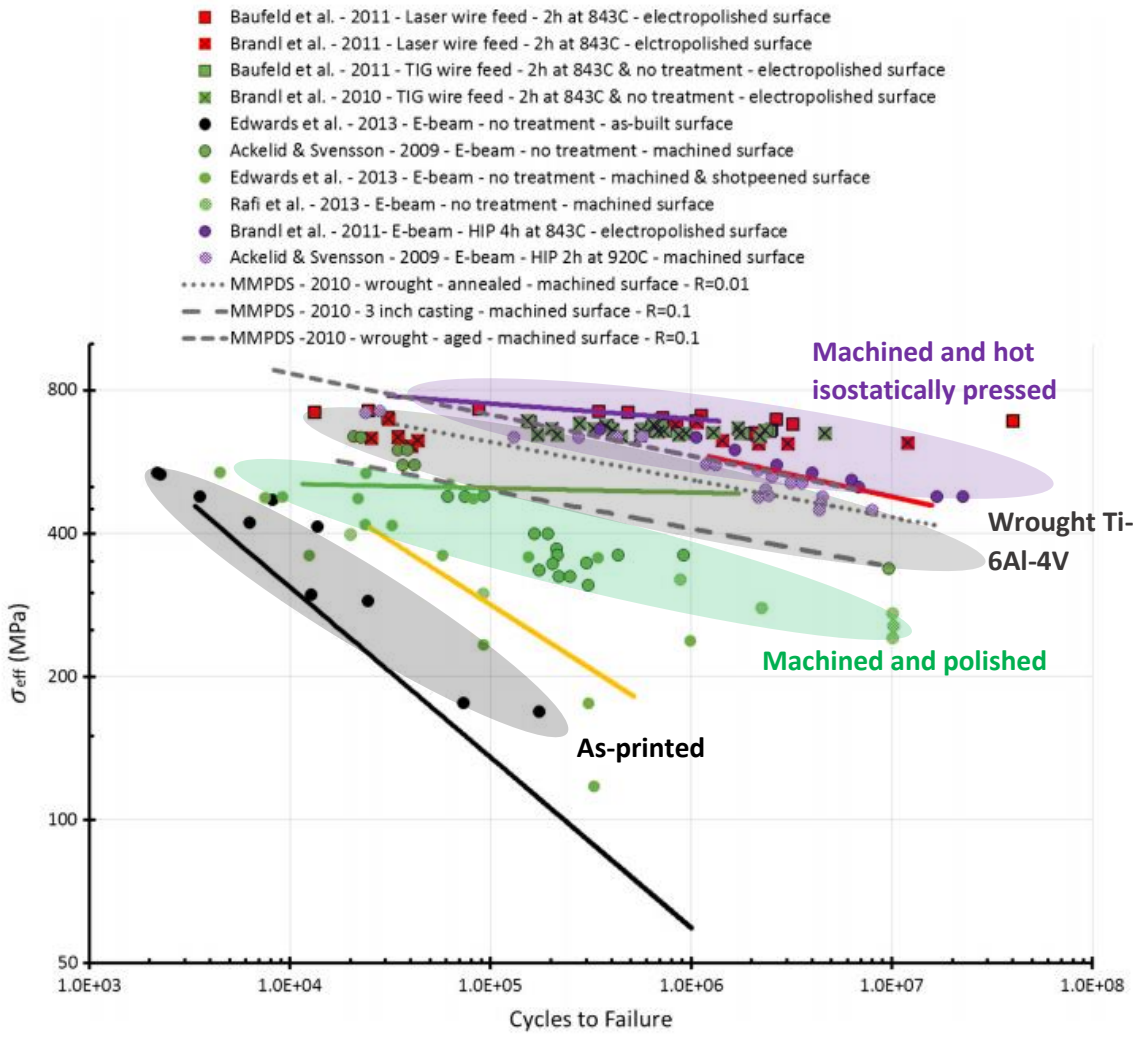

Figure 2.29 Fatigue test result shows the effect of various post-processing treatments on the fatigue properties of AM Ti-6Al-4V [173].

To sum up**,** it can be concluded that anisotropy in mechanical properties was indeed exhibited in metal AM parts. Nevertheless, some parts fabricated from certain metal AM systems could exhibit less anisotropy. This is due to the differences in processing variables that lead to a more homogenous microstructure and residual stress distribution. Moreover, it is important to note that post-processing such as surface machining and heat treatment can effectively improve the fatigue properties of metal AM parts to be comparable and even superior to their cast and wrought equivalents.

2.5.4 Heterogeneity in metal AM

Given that one of the main advantages of AM is its ability to directly manufacture complex geometries, understanding the heterogeneity that exists in metal AM parts is equally important as the anisotropy [17]. A comprehensive set of materials database would allow designers better utilize metal AM technologies for more demanding end-use applications [176]. Microstructural heterogeneity of metal AM parts can arise from differences in morphology, size, orientation, and chemical composition of phases and grains. Such differences resulted from the varying thermal conditions (e.g. thermal gradient and cooling rate) that were included in different metal AM processes [21].

2.5.5 Heterogeneity in microstructure

2.5.5.1 Phase constitution

The difference in phase constitution is an important source of microstructural heterogeneity in metal AM parts. For example, in the case of α+β titanium alloys (Ti-6Al-4V), three phases were often reported, i.e. α phase, β phase and α’ martensitic phase [26]. A study on SLM-built Ti-6Al-4V has also shown microstructural variation along the build direction [31]. It was suggested that the microstructural variations were caused by a cyclic thermal history from successive depositions. Moreover, the top region only exhibited α’martensitic

phase that indicated the as-deposited condition without phase decomposition [31]. Likewise, for the CoCr alloys processed with EBM, the elevated build temperature caused the metastable γ-face centered cubic (fcc) phase transform to the stable ε-hexagonal closed packed (hcp) phase during the build process [177, 178], resulting in microstructural heterogeneity along the build direction as shown in Figure 2.30 [177]. Figure 2.30 (a, c and e) shows the phase compositions within the EBM-built CoCr sample while Figure 2.30 (b,d and f) shows the crystallographic orientations within the EBM-built CoCr sample. Base on Figure 2.30 (a, c and e) it can be observed that the initial phase composition was made up of γ-fcc phase that is indicated in red. However, after some duration of exposure to the elevated build temperature grain recrystallisation occurs. The new grains were made up of the ε-hcp phase which are indicated as green in the figure. The 0001 crystal orientation of the original grains were also lost.

A study based on DED-built IN718 superalloy has also attributed the formation of precipitates to cause heterogeneity in hardness [13]. Microstructural heterogeneity was thought to be due to solidification segregation, with the presence of niobium along the grain boundary promoting the heterogeneous nucleation and growth of γ'' phase [13]. Thus, it can be seen that the different phase constitution at different locations for varying geometry may induce heterogeneity in metal AM parts.

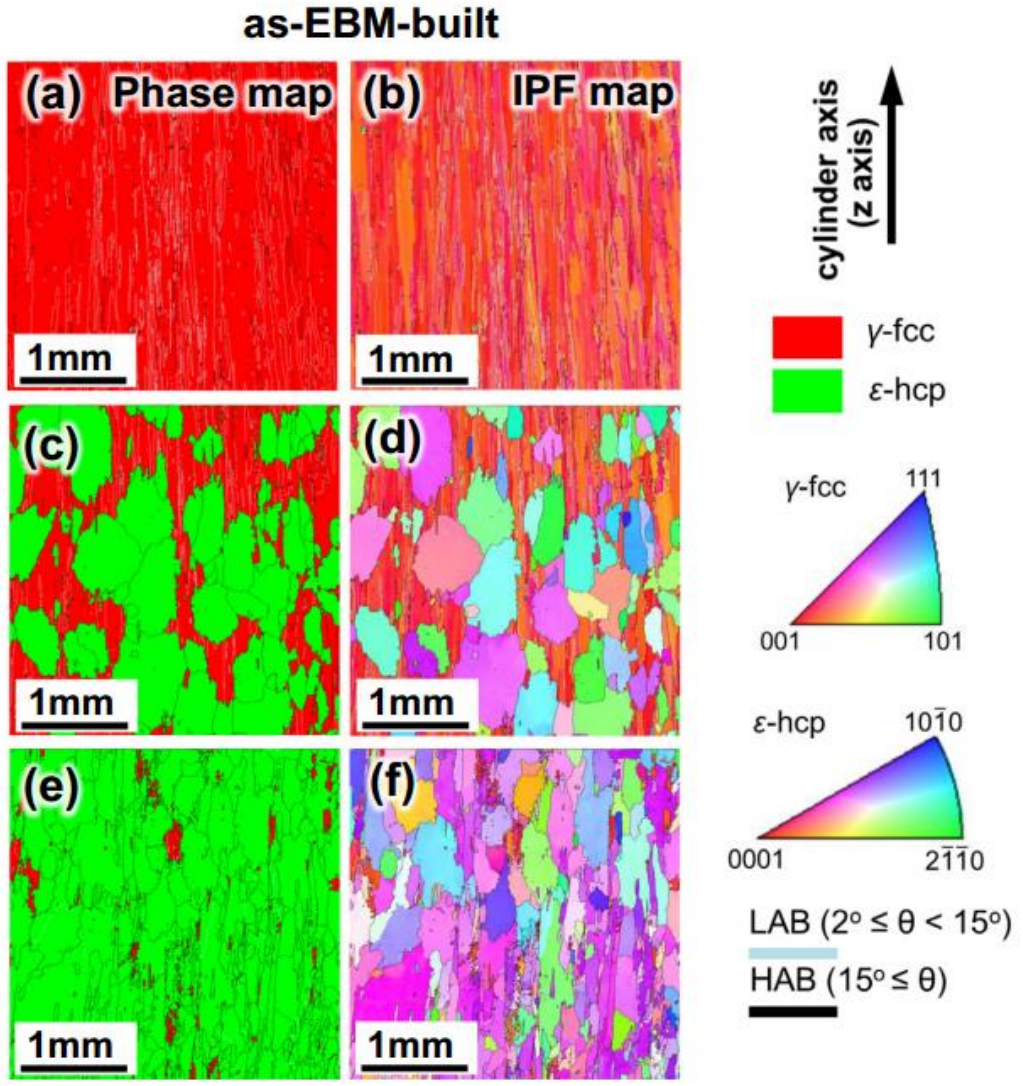

Figure 2.30 EBSD phase maps of SEBM-built CoCr showing variation in phase composition and grain morphology; (a, c, e) and IPF crystallographic orientation map (b, d, f) on the longitudinal cross-section of EBM-built CoCr showing variation in phase composition and grain morphology [178].

2.5.5.2 Layer banding and microstructure coarsening

Layer bandings is a popular observed phenomenon in metal AM materials [21, 179, 180]. Prior research has shown that in titanium alloys, layer banding was a result of segregation of vanadium and aluminum. However, a study by Kelly & Kampe revealed no systematic elemental variation in DED-built Ti-6Al-4V [179], and concluded that such layer bands is due to the cyclic thermal history that the part experienced after multiple layers' deposition [21,

180]. A study on wire-fed DED-built Ti-6Al-4V developed a schematic diagram showing the formation of the layer bands as illustrated in Figure 2.31 [179]. Differences in the microstructure feature (e.g. mean width of α laths) could be clearly observed between the top and the bottom of a layer band [179]. Despite the unique microstructural morphology, it is still unclear how such heterogeneity affects the mechanical property of metal AM parts.

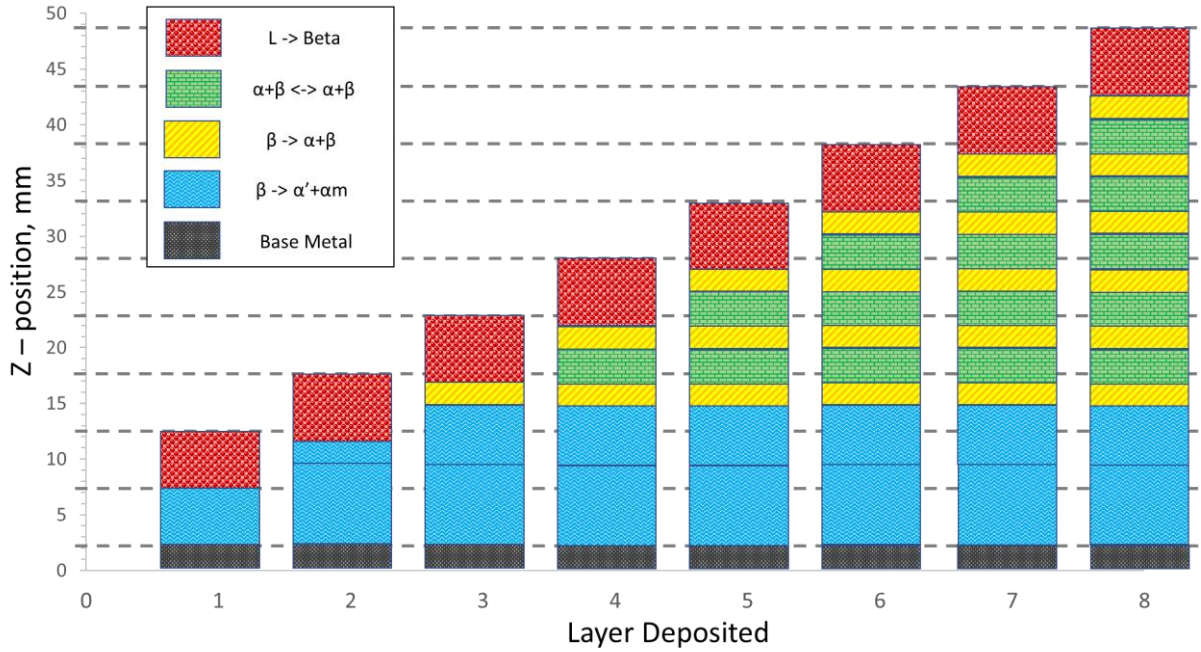

Figure 2.31 Microstructural evolution map of the layer by layer deposition via the DED process (reproduced from [21, 179]).

2.5.5.3 Grain morphology

The grain morphology within metal AM parts has been shown to depend on the process parameters and materials [111, 181, 182]. Studies on SEBM-built IN718 has shown that site-specific control of the grain morphology by varying the processing parameters (e.g. line offset, speed function) was possible with metal AM [111, 182]. Heterogeneity in grain morphology was also observed in SEBM-built CoCr parts, due to recrystallization caused by the high build temperature [178].

2.5.5.4 Microstructural feature

Several studies have shown that the microstructure of AM Ti-6Al-4V tended to become is finer at the top region as compared to the bottom [29, 183, 184]. The microstructural scale is known to decrease with increasing cooling rate [185]. At the very top region of the metal AM parts, the fine microstructure is likely due to the high cooling rate induced by heat loss of convection and radiation and the lack of remelting and thermal cycling that prior layers experienced [179]. A study has also shown that it is possible to induce refinement of microstructure through the use of in-situ printed heat sinks in SEBM of Ti-6Al-4V [186].

2.5.5.5 Processing deficiency

AM processing defects have been reported to contribute to anisotropy in mechanical properties of metal AM parts such as fracture toughness and tensile strength [9, 151]. Additionally, there have also been studies reported that such defects were not homogenously distributed within the build as shown in Figure 2.32 (a) [9, 28]. Powder bed fusion processes like the EBM often utilise gas-atomised metallic powder as the raw material for processing due to their high sphericity. Such gas-atomised powder often contains trapped gas porosity within them due to the method of fabrication. A study has also shown that trapped gas porosity defect decreased with decreasing speed function parameter of EBM, possibly by allowing more time for the trapped gas to escape from the slowly moved melt pool [187].

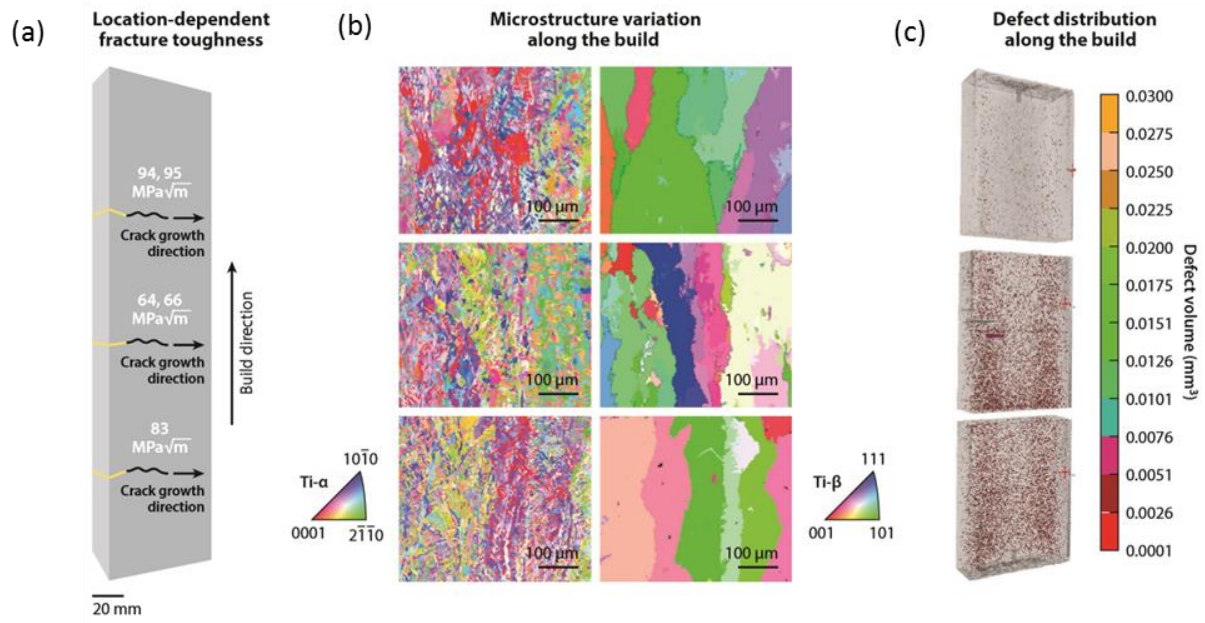

Figure 2.32 Heterogeneous microstructure in SEBM-built Ti-6Al-4V: (a) Illustration of location dependent fracture toughness in SEBM-built Ti-6Al-4V. (b) Variation in microstructure and (c) defect distribution along the SEBM-built Ti-6Al-4V [9].

A study on a SL process reported that defect distribution within the aluminum alloy sample was not homogenous [14]. A point to note from the study was that region where cracks originate, did not correspond to the location of voids. Instead, it attributed the mechanism of the formation of the cracks to the strain localization caused by the high strain rate deformation induced from the rotating sonotrode that was used to fuse the metal sheets together [14].

2.5.5.6 Heterogeneous recrystallization

Post heat treatment is a common method to homogenize the microstructure of the as-deposited metal AM part [151, 188]. A study has reported that partial recrystallization in heat treated SLM-built IN718 resulted in a heterogeneous grain structure [189]. It was suggested that heterogeneous residual stresses within the metal AM parts may account for such partial recrystallization [17]. It is also reported by another study that residual thermal stresses are a driving force for recrystallization in SLM-fabricated iron parts [190]. Another study by Brandl and Gretemeier reported that they were unable to induce recrystallization in DED-built Ti-6Al-4V after post heat treatment [191]. They were however able to obtained homogeneous coarse grains (~500 - 3000 µm in size) instead. A study based on SLM-fabricated iron parts reported that a columnar to fin equiaxed grain transformation occur after vacuum annealing treatment [190].

As such post-processing procedures for metal AM parts may have to take into account of both the materials and manufacturing techniques. A study reported that while the possibility of recrystallization may be dependent on the amount of residual stresses/stored energy in the as-fabricated material, material specific properties such as the fast diffusivity of atoms in titanium alloys may reduce the effect of defects which contributes to the stored energy within a material [192]. This may lead to grain growth in titanium material instead of recrystallization as seen in the study by Brandl and Gretemeier.

Lastly, recent study by Yang et al. also reported that there exist coarse recrystallized grains surrounding partially melted inclusions and/or along the interpass boundaries in LENS-built 316L SS. In such interpass boundaries, the study also reported the present of porosity/gross interpass defects. Such defects may provide sufficient stored energy for recrystallization of the microstructure to occur. Studies regarding the heterogeneous recrystallization is also an ongoing research and there exists not many literature is available at

the point of writing. Additionally, it is worth while to note that residual stresses in the parts were not considered as literature [193, 194] indicate that there was minimal residual stress found in SEBM-built parts due to the high operating temperature (e.g. 600 ^{O}C) which acts as a stress relieving process over the long duration of a typical build (e.g. >12 hours) and the subsequent slow cooling (e.g. ~7 hours).

2.5.6 Heterogeneity in mechanical properties

2.5.6.1 Tensile properties

Table 2.8 lists the differences in tensile strength along the build direction of the AM Ti-6Al-4V by various studies [10, 11]. Higher tensile properties were reported in the lower half of the block samples as compared to the upper half, which was attributed to oxygen strengthening and finer microstructure [10, 11]. The study by Carrol at al. reported that there was an increased of 0.0124 wt. % oxygen in the upper half of the build part. Oxygen is an interstitial element in titanium alloy that strengthens and stabilised the α phase. The tensile strength of Ti-6Al-4V parts typically increases with increasing oxygen content and finer microstructure [161, 195]. The study by Carrol et al. also concluded that the in addition to dependence on oxygen, the location dependence of the tensile properties is also due to the variance in thermal history as a function of build height. There existed finer microstructure at the bottom due to the water cooled base plate as compared to coarser microstructure away from the base plate. The correlation between the microstructure size with the yield and tensile strength in Ti-6Al-4V has also been known by prior literature [196].

The difference in size of the α+β microstructure was also the conclusion from Wang et al. with regards to the difference in tensile properties in their big-sized Ti-6Al-4V sample fabricated using the SEBM process. It is also worth while to note that there existed not many

studies that focused on such location dependent mechanical properties of AM parts, possibly due to the costly nature of destructive testing experiments.

Table 2.8 Summary of tensile properties of various metal AM parts (sample size, n = 4-5)

Material	Condition	Process	Position	Yield Strength (MPa)	Ultimate Tensile Strength (MPa)	Elongation (%)	Ref.
Ti-6Al-4V	Machined	DED Ti-6Al-4V	Upper half	945 ± 13	1041 ± 12	14.5 ± 1.2	[10]
			Lower half	970 ± 17	1087 ± 8	13.6 ± 0.5	
Ti-6Al-4V	Machined	EBM Ti-6Al-4V	Upper half	~850	~910	19.5	[11]
			Lower half	~920	~990	17	

2.5.6.2 Hardness

Hardness testing is an effective method to characterize the localized mechanical strength of metal AM parts. Table 2.9 summarised the hardness properties of various AM metal alloys. A study had been carried out to investigate the effect of cross-sectional area on hardness values [134]. The study reported that the effect of part size on the microhardness was insignificant [134]. The study reported that the cause may have been due to the insufficient thermal isolation between the different samples. Other studies reported otherwise, such studies showed that with increasing cross-sectional area, the microhardness was decreased due to microstructural coarsening [92, 197]. Studies have also been conducted on the effect of built height on the hardness [45, 134]. However, such studies showed conflicting results. For example, a study by Hrabe et al. reported no significant differences in Vickers microhardness values up to 25 mm from the substrate.

Table 2.9 Summary of hardness properties of various metal AM parts.

Material	Process	Microhardness (Hv)	Distance Measured from the substrate (mm)	Ref.
Ti-6Al-4V	Arcam S400	~360 - 460	~68	[29]
Ti-6Al-4V	Arcam S2	347 - 352	22	[134]
Ti-6Al-4V	Arcam A2X	343 - 362	40	[45]

Wang et al. systematically examined the microhardness within an impeller component [45]. The study reported that microhardness value increased with increasing build height. It must be noted that the part in Wang et al. work had a decreasing cross-sectional area with increasing build height. The difference in cross-sectional area may contribute to that result.

Many studies have thus concluded that heterogeneity in hardness values was dependent on the thermal input experience by the specific layer. A larger cross-sectional area would lead to a higher thermal input as compared to a smaller cross-sectional area, resulting in different final microstructures. Future improvement on varying the process parameters with regards to the cross-sectional area could help alleviate such heterogeneity in hardness.

2.5.6.3 Fracture toughness

Location dependence in fracture toughness has been observed in SEBM-built Ti-6Al-4V due to the heterogeneity in the microstructure and defect distribution [9]. A related study also performed HIP process to investigate its effect on the heterogeneity in fracture toughness [143]. However, the measured fracture toughness was found to be lesser due to coarsening of the microstructure after the HIP process and the heterogeneity observed was not eliminated.

In summary, it can be deduced that anisotropy and heterogeneity in the mechanical properties of metal AM parts are due to the anisotropic and heterogeneous microstructure and material properties. Despite the anisotropy and heterogeneity in the mechanical properties, it can be

concluded that the mechanical properties of post-processed metal AM parts are equivalent or better as compared to their cast equivalent. Further improvement regarding the optimization of heat treatment process parameters is highly demanded to produce end-use parts with fine microstructure in order to approach the static and dynamic mechanical properties of their wrought equivalent.

2.5.7 Modelling on anisotropy and heterogeneity in metal AM parts

Numerical modeling of the thermal conditions of AM processes allows a better understanding of the anisotropic and heterogeneous microstructure which determines the final mechanical properties. An early study has developed a thermo-kinetic model of multilayer laser-based powder deposition, coupled FE heat transfer calculations, phase transformation data, and microstructure-property relationships, showing the increase in Vickers hardness with increasing build height and with minimizing substrate size [198]. Numerical modeling has also been used to simulate beam power-velocity (P-V) process maps as shown in Figure 2.33. The P-V process map in Figure 2.33 (a and b) was plotted based on the electron beam wire feed AM process and the L/d refers to the length to depth ratio of the melt pool.

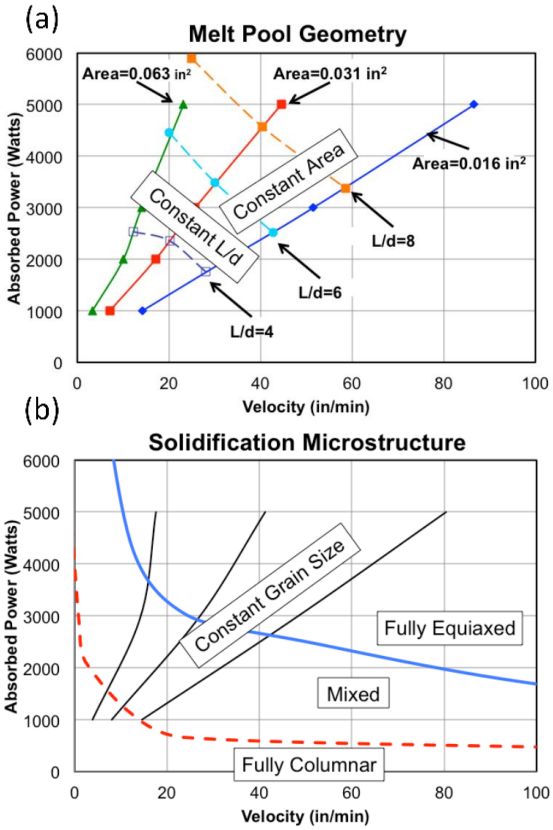

Figure 2.33 Simulated process maps for microstructural control; (a,b) Simulated Beam Power–Velocity process map for microstructure and melt pool dimension control of a single bead deposit of electron beam wire-fed AM Ti-6Al-4V [199]

Other studies have also developed heat transfer and microstructural evolution equations for SEBM Ti-6Al-4V showing that the heat transfer arising from the selective melting was sufficient to induce microstructure evolution through several layers below. Figure 2.34 Shows the evolution of volume fraction of α phase due to the variations in the temperature field within the metal AM part [200]. The β phase is indicated as blue and the α phase is indicated as orange. It provided support to experimental works regarding the phase constitution and microstructural coarsening [179, 200].

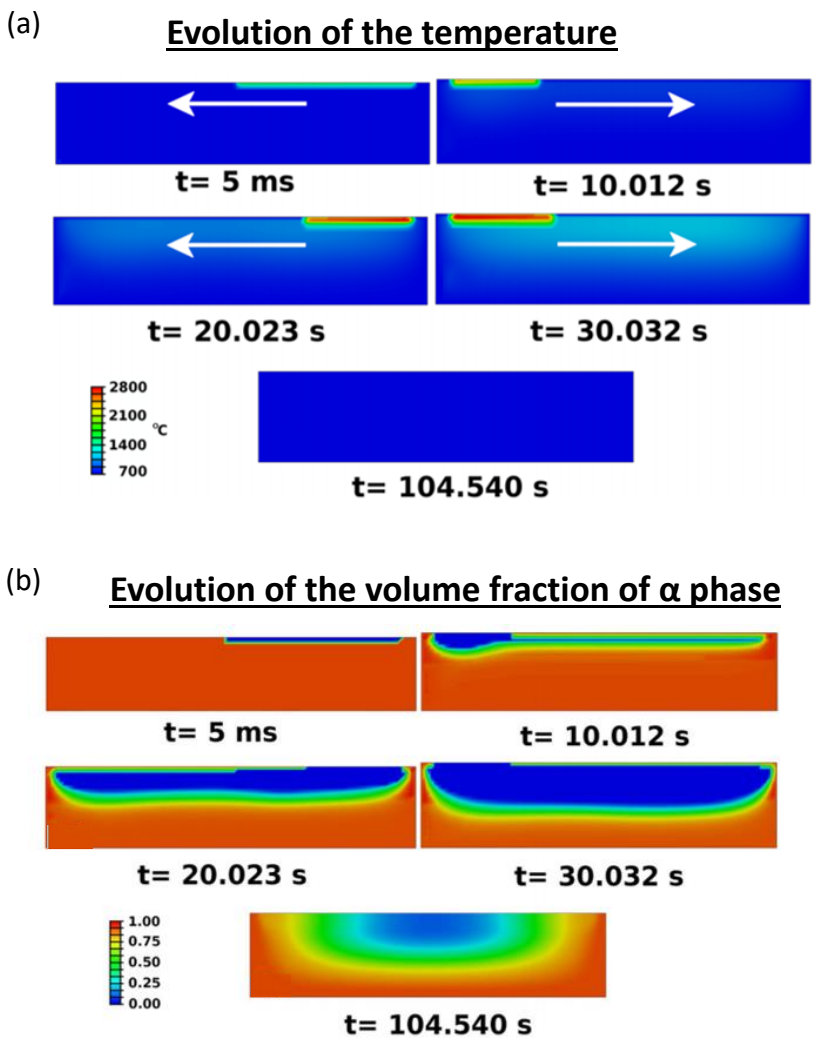

Figure 2.34 Simulation of a moving energy source and the evolution of the α phase in Ti-6Al-4V; Evolution of the (a) temperature field and (b) volume fraction of α phase after deposition of 4 layers of powder [200]. The β phase is indicated as blue and α phase is indicated as orange.

A recent study has also developed a model that was capable of calculating fraction, morphology and size of phases, with a measured or modeled thermal history in AM Ti-6Al-4V [201]. With the more research focusing on modeling metal AM processes, a better understanding of the interrelationship between process-microstructure-mechanical properties can be achieved.

2.5.8 Summary

Metal AM in a competitive manufacturing process to conventional manufacturing process such as machining and casting with regards to the fabrication of components with complex geometries out of hard to process materials (e.g. titanium alloys). Metal AM processes could be broadly categorized into powder-bed fusion (PBF), directed energy deposition (DED) and sheet lamination (SL). During the layer-by-layer fabrication, the metallic part was subjected to processing variables such as deposition rate, beam power, build environment and processing temperature which have an influence towards its final microstructure and mechanical properties. In general, despite the reported anisotropy and heterogeneity in literature, the quasi-static mechanical properties (e.g. tensile strength and hardness) of metal AM parts often could meet the minimum requirements in comparison with cast and wrought equivalents. However, post processing of metal AM parts must be implemented to obtain comparable dynamic mechanical properties (e.g. fatigue properties) as conventionally produced parts. Such post processing techniques are currently a costly means to control the anisotropic and heterogeneous microstructure within metal AM parts.

It can be deduced via the published datum summarized in this chapter, that the causes of the anisotropic and heterogeneous microstructure and mechanical properties of metal AM parts were due to several influencing factors. The influencing factors for the anisotropy and heterogeneity in the microstructures include: (1) grain morphology; (2) crystallographic texture; (3) lack-of-fusion defects; (4) phase transformation; (5) heterogeneous recrystallization; (6) layer banding and (7) microstructural coarsening. These factors were systematically discussed in terms of the SEBM processing parameters within the metal AM process. Given the current state-of-the-art in metal AM, it is difficult to vary the processing variables in-situ with respect to a part's geometry and size so as to control its microstructure.

However, with continued development in this technology, it is likely that better control over the processing variables during the fabrication process can be achieved.

Additionally, literature have also shown that microstructural modification of AM metallic materials can be achieved via the use of a roller mechanism that applied a load after each deposited layer or through the use of in-situ printed heat sink [180, 186]. Traditionally, adjusting the build orientation and specifying a minimum cross-sectional thickness were ways to reduce the effects of the anisotropy and heterogeneity in material properties. Moreover, it was widely shown in Table 2.5 that horizontally orientated AM parts typically had a higher tensile mechanical strength (UTS and elongation%) as compared to vertically orientated ones. As such if the build part is horizontally orientated along the load direction and the fine geometrical features are scaled up to increase mechanical strength, the anisotropy and heterogeneity might be effectively minimized or even eliminated.

2.6 Detailed research scope and roadmap

The detailed literature review has shown that the increase in research interest with regards to metal AM technologies in the last 5 years has led to the significant advancement of the technology. Metal AM technologies such as SLM and SEBM are now capable of fabricating fully functional metallic parts directly. Among the two technologies, SEBM shows greater promise as a metal AM technology that can deliver parts with superior as-built properties.

To characterise the microstructure and mechanical properties of AM Ti-6Al-4V, below is the research scope:

1. The identification of the phase constitution in the microstructure of the as-built SEBM Ti-6Al-4V alloy via phase characterisation techniques. This is to understand the phase evolution in SEBM Ti-6Al-4V alloy and its relationship to the thermal phenomena experienced during the SEBM process.

2. The study of the effects of build geometry (thickness, shape and height) on the microstructures and mechanical properties of the as-built SEBM Ti-6Al-4V alloy. This help to understand the heterogeneous microstructure and mechanical properties of as-built SEBM Ti-6Al-4V alloy. This will be studied via experimental and computational approaches.
3. The study of the grain selection and competition mechanism that governs the columnar grain growth in the as-built SEBM Ti-6Al-4V alloy. This help to further the understanding of the anisotropic microstructure that exists in SEBM-built Ti-6Al-4V. This will be studied via experimental and computational approaches.

The objectives and scope mentioned above is developed into a research road map as shown in Figure 2.35. The road map outlines the steps taken to achieve the objective of this Ph.D. study, which is to develop an in-depth understanding on the microstructure and mechanical properties of as-built SEBM Ti-6Al-4V. Firstly, a literature review of metal AM and Ti-6Al-4V have to be done to identify the research direction for the study. Based on the literature review, the author proposed to look at the microstructure and mechanical properties of as-built SEBM Ti-6Al-4V from the perspective of its inconsistency. As such the author first planned to understand the phase transformation that happens in the material during the SEBM process. Next the author planned to understand the microstructure transformation and macrostructure growth during the SEBM process. It is deemed that the scope of the study would provide sufficient depth to achieve a good understanding of the microstructure and mechanical properties of as-built SEBM Ti-6Al-4V from the perspective of its inconsistency.

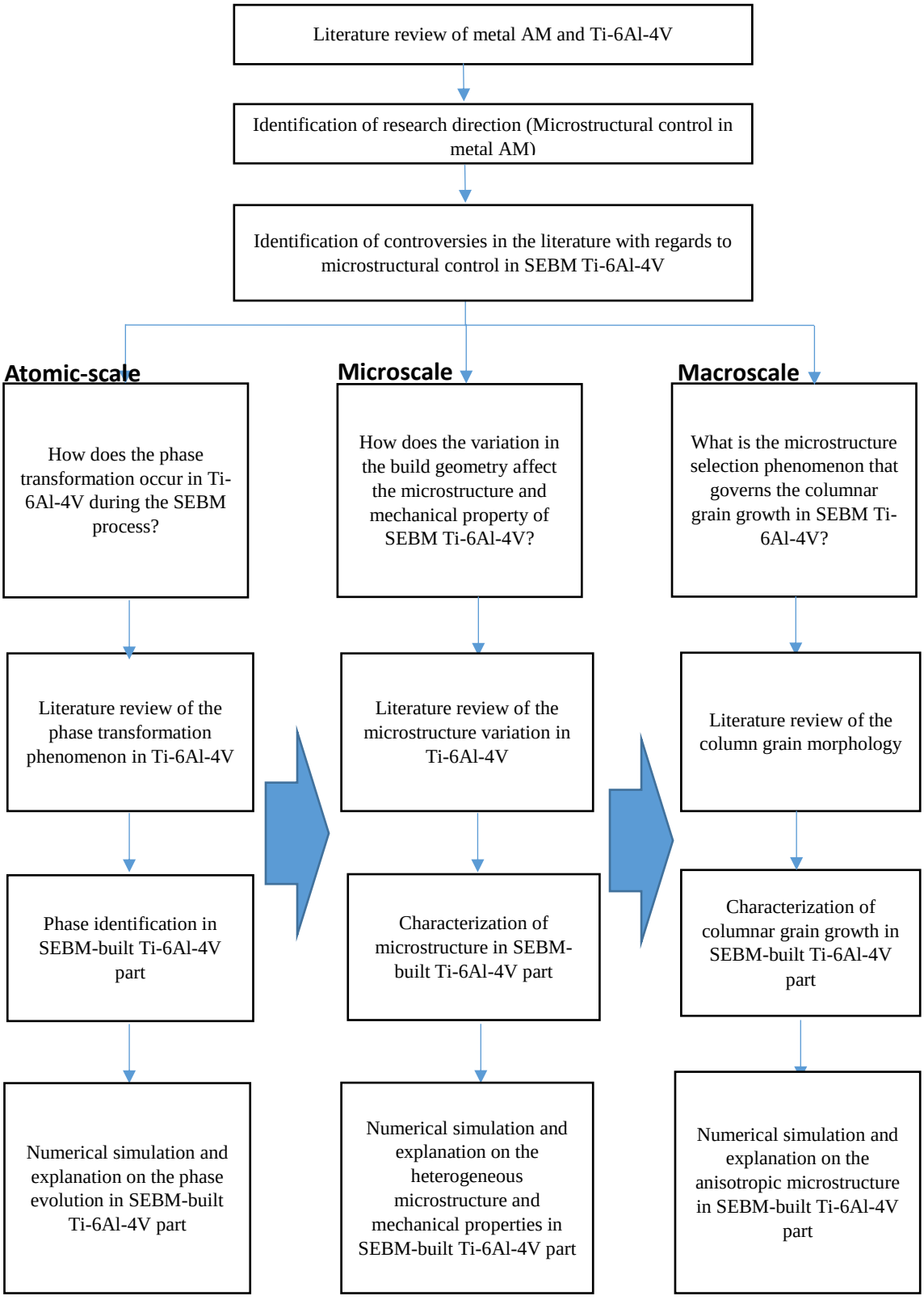

Figure 2.35 Research Road Map

Chapter 3: Materials and Experimental Procedures

Based on the research road map planned, a series of experiments were planned to satisfy the objectives of the thesis to understand the microstructure and the mechanical properties of EBM-built Ti-6Al-4V alloy. This chapter thus describes the materials, experimental procedures and characterization techniques in this study. It also describes the machine setup and the experimental parameters used in the SEBM AM system. Various characterization techniques used to analyse the sample are described and explained. The numerical simulation methodology is also described briefly.

3.1 Ti-6Al-4V powder

Ti-6Al-4V ELI (Grade 23) powder (Batch No. 877) supplied by Arcam AB was used for fabricating the samples. The powder size distribution ranges from 45 to 106 μm. The larger particles size ensures safer handling of the powder. The nominal chemical compositions of the material is shown in Table 3.1. Recycling of non-melted and/or sintered powder was achieved via the powder recovery system (PRS) and a vibrating sieve (mesh size ≤ 150 μm). All powder involved in the fabrication of SEBM builds (both in the build tank and on the powder table) was first passed through the PRS in which Ti-6Al-4V powder was used as a blasting medium, to break up sintered blocks of powder collected from the previous build under a pressure of approximately 6 bar. Powder recovered from the PRS was sifted by using the vibrating sieve before being mixed with any powder remaining in the two powder hoppers or new powder. Figure 3.1 shows the spherical geometry of the powder used after several jobs. This indicates that the recycled powder still maintains its spherical form after the PRS despite being partially sintered during the process.

Table 3.1 Chemical compositions of Ti-6Al-4V powder from supplier (wt.%).

Elements	**Arcam Ti6Al4V ELI**		**ASTM F136 Ti6Al4V ELI**	
	Wt.%	At.%	Wt.%	At.%
Aluminium, Al	6.0	10.2	5.5 - 6.5	10.1
Vanadium, V	4.0	3.6	3.5 - 4.5	3.6
Carbon, C	0.03	0.1	<0.08	<0.3
Iron, Fe	0.1	0.28	<0.25	<0.2
Oxygen, O	0.1	0.03	<0.13	<0.36
Nitrogen, N	0.01	0.03	<0.05	<0.16
Hydrogen, H	0.003	0.14	<0.012	<0.54
Titanium, Ti	Balance	Balance	Balance	Balance

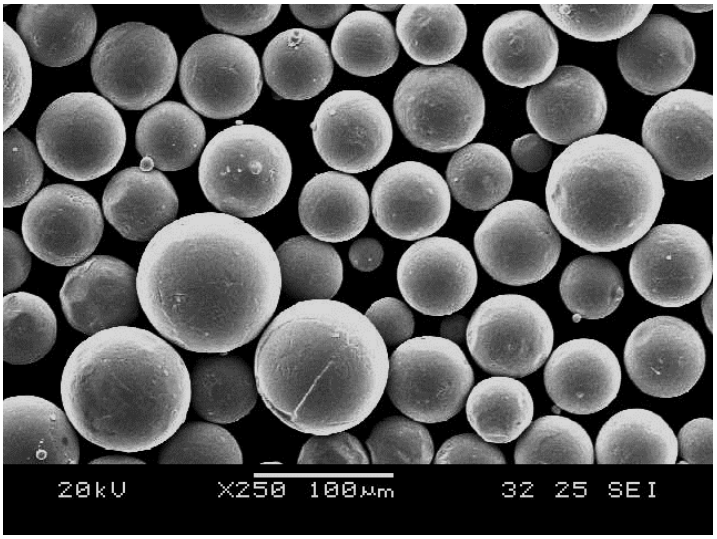

Figure 3.1 SEM Image of Ti-6Al-4V ELI (Grade 23) powder purchased from Arcam AB.

3.2 Electron beam melting (EBM) processing parameters

All the parts and samples produced for evaluation were built using an Arcam A2XX (Arcam AB, Sweden) SEBM machine. The Arcam A2XX is the largest SEBM machine available currently (Arcam AB). It offers a build envelope of Ø 420 × 380 mm^3. It consists of two main cabinets, i.e. the electrical control cabinet and the vacuum chamber cabinet. Figure

3.2 illustrates a simple schematic view of the SEBM system. The electron beam is generated within an electron gun via a tungsten filament. The filament is heated to above 2000 ^{o}C by the filament current, which allows the electrons escape freely from it (Arcam AB). The emitted electrons are accelerated in an electrical field, obtained by applying a high voltage of ~60 kV between the filament and the anode, and then focused by means of an electromagnetic coil (focusing coil). The focused electron beam is selectively scanned over the powder bed with a layer-by-layer process directed by an SEBM Control 3.2 software.

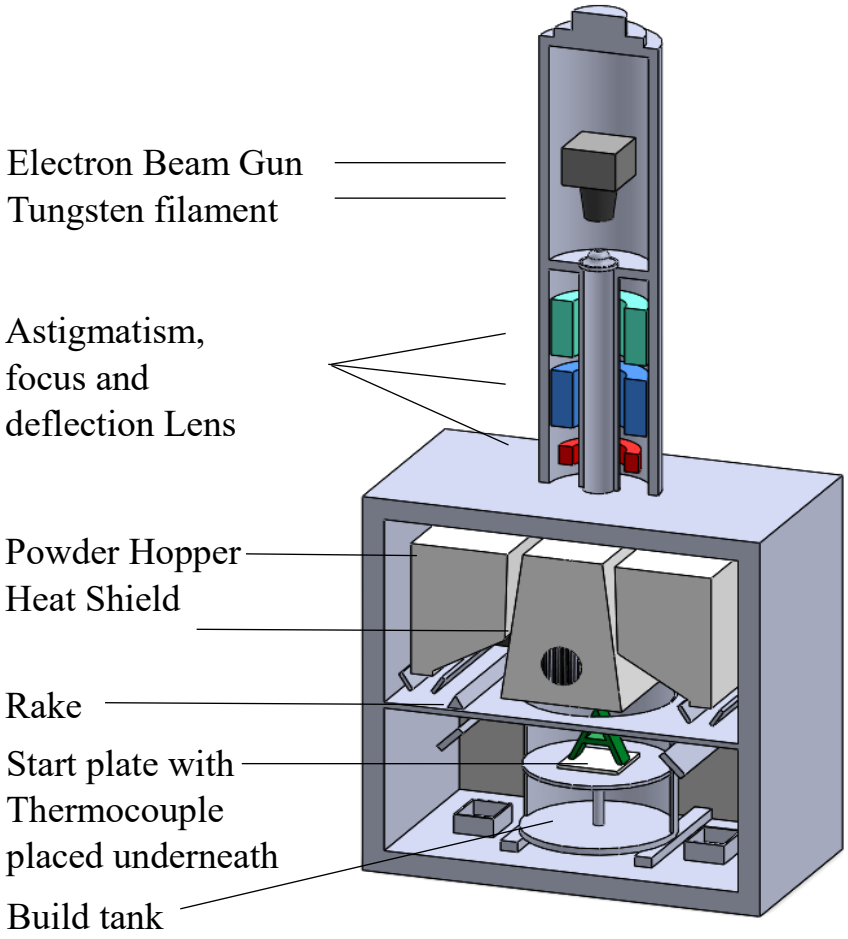

Figure 3.2 (a) Schematic image of the A2XX SEBM machine

There are three softwares used for creating and running builds on the EBM machine, namely, Magics, Build Assembler and EBM control as shown in Figure 3.3. The detailed workflow for generating a build via these three softwares will be discussed in this section. Moreover, three build themes were involved in this work, i.e. Ti6Al4V-PreHeat-50um, Ti6Al4V-Wafer-50um and Ti6Al4V-melt-50um. These process settings were identified by Arcam AB to achieve optimal building results.

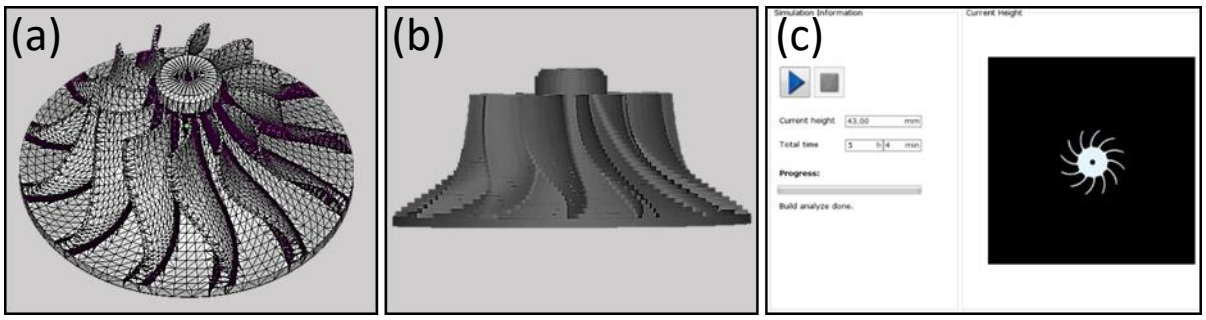

Figure 3.3 Workflow of file preparation for a typical SEBM print job; (a) STL file exported from Magics software. (b) ABF file showing the sliced structures after SEBM Build Assembler software. (c) Simulation results by SEBM Build Control 3.2 software.

Contour melting and in-fill hatching melting are included in the melt theme. Contour melting consists of two steps: outer contouring and the subsequent inner contouring. In particular, outer contouring should be more important because it may determine the properties of thin parts. Here, a beam melting current of 4 and 10 mA, a focus offset of 0.29 and 0.25 mA, and a beam speed of 340 and 800 mm/s were used for outer and inner contouring, respectively. In addition, a current of 15 mA, a focus offset of 3 mA and a beam speed of 4530 mm/s were used for hatching. A 10 mm-thick stainless steel start plate could begin heating by the electron beam when a pressure of ~5×10^{-4} mBar (0.05 Pa) within the build chamber is achieved. Once a bottom temperature of 730 ^{o}C is reached, parts are built directly onto the preheated start plate

by selectively melting layers of 50 μm under a controlled vacuum in the temperature range of 600-750 ^{o}C. The entire building process was kept under vacuum at ~2e^{-3} mBar, controlled by using high-purity helium as regulating gas in order to prevent powder charging. The build temperature was reported as what was observed via the data collected from the build jobs. It is noteworthy to note that the differences in the build preheat temperature could produce different thermal profiles and thereby lead to different results.

3.3 Electrical discharge machining (EDM)

As-built specimens were cut into smaller samples to get to the required size with an EDM CNC wire cutting machine (TROOP economical model, TP-25). The EDM was used due to its ability to cut geometries such as tensile coupon from a block of titanium alloy with little damage to the sample. The EDM has a wire diameter of 0.2 mm and a cutting precision of ±10 microns.

3.4 Sample preparation

Samples for the metallographic and mechanical strength analysis were fabricated on the Arcam A2XX EBM machine based on the methodology described in the section 3.2. The following section describes the samples used in this study. In total there are three different sets of samples, namely the individual thickness-dependent samples (Figure. 3.4), joint thickness dependent samples (Figure. 3.5) and lastly the built height and geometry dependent samples (Figure 3.6 and 3.7 respectively).

Figure 3.4 shows four block samples with varying thicknesses of 1 mm, 5 mm, 10 mm and 20 mm that were fabricated. They were termed 1mm, 5mm, 10mm, and 20mm samples, respectively. The length and height of the samples are 100 mm and 30 mm respectively.

The samples were fabricated to investigate the microstructure and mechanical properties with varying built thicknesses. Additionally, industrial components often consist of geometries of varying thickness as well. The spacing between each sample was 5 mm to minimise the effect of thermal field from the other sample.

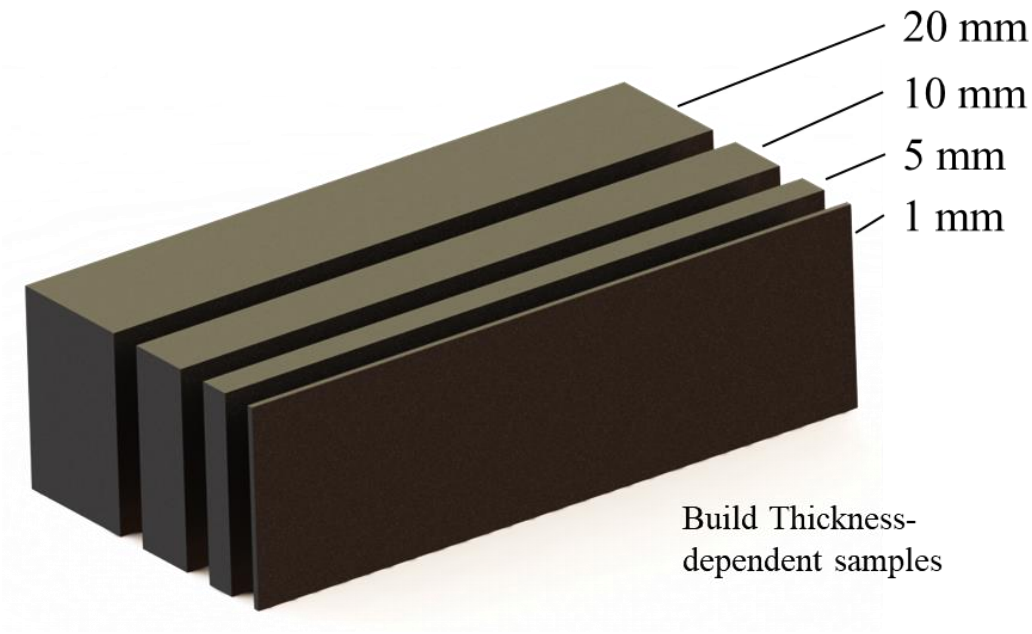

Figure 3.4 Schematic of the SEBM-built samples with varying thicknesses of 1, 5, 10 and 20 mm. Spacing between samples are 5 mm apart to reduce thermal interaction between samples.

Figure 3.5 shows the straight-finned part and the curved-finned part samples. The built height of these two parts is ~30 mm. Each part has fin structure with thickness of 1 mm, 5 mm, 10 mm and 20 mm respectively. Figure 3.5 (b) shows a schematic of the built layout and the measurement points that are taken at the same height. The measurement points are located along the fin structure with position 1 (S1) at the intersection between the bulk (i.e. main body) and the fin structure, and position 4 (S4) being the furthest away from the bulk section. The measurement points were chosen to investigate the microstructure and mechanical properties at various location of the different fin structure geometry. The fin structure was also designed

to investigate whether a curved finned geometry would have a different effect as compared to the straight plate geometry in Figure 3.4.

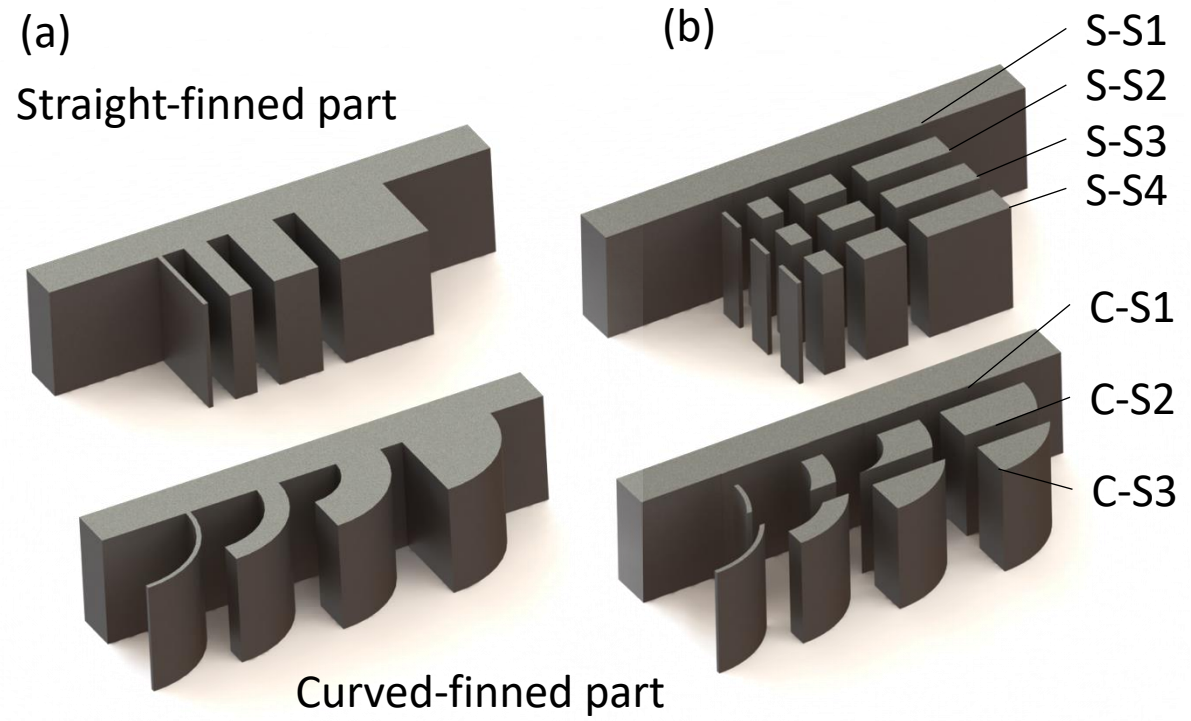

Figure 3.5 Schematic of the samples used to investigate the effect of build geometry; (a) Schematic of the straight-finned and curved-finned part with varying fin thicknesses of 1mm, 5mm, 10mm, 20 mm (b) Schematic showing the various location in which the microstructure observation and Vickers microhardness measurements were conducted. The spacing between the straight-finned part is 5 mm while in the curved-finned part the minimum spacing between each fin feature is 5 mm.

Figure 3.6 shows two horizontal blocks (100 mm × 10 mm × 30 mm) that were fabricated. Four tensile test pieces were wire-cut one-by-one from a horizontal block. They are designated as 10 mm-1, 10 mm-2, 10 mm-3 and 10 mm-4 from bottom to top (as illustrated in Figure 3.6). The samples were fabricated to investigate the microstructure and mechanical properties with build height. The dimensions of the block was designed so that tensile samples that follows the ASTM E8 standard can be fabricated from them.

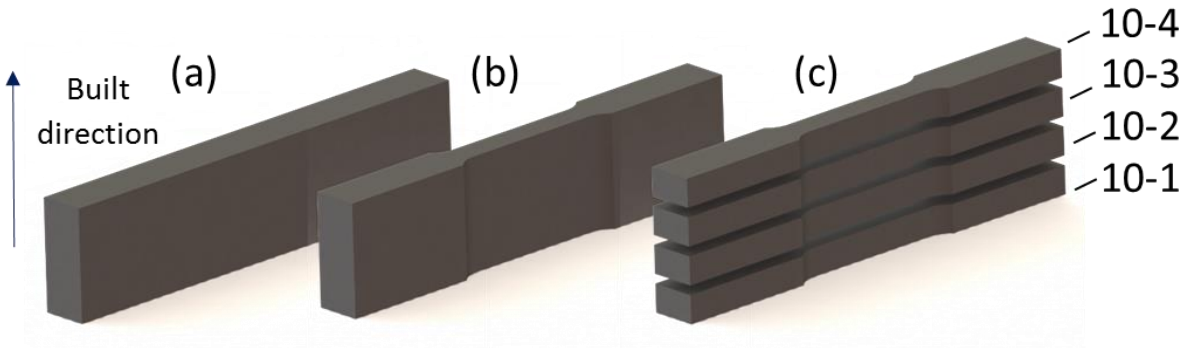

Figure 3.6 Schematic of the samples used to investigate the effect of build height. (a) Schematic illustration of the horizontal Ti-6Al-4V ELI block (100 mm x 10 mm x 30 mm) built by SEBM. (b) Machinery of the block into standard tensile test pieces. (c) Layout of the four tensile test pieces. The build direction is indicated by an arrow.

Lastly, Figure 3.7 shows the build-geometry dependent samples (I-shaped, A-shaped, and V-shaped) with a height of 100 mm that were fabricated to investigate the columnar grain growth phenomenon in the Ti-6Al-4V alloy. The different geometries were also designed to investigate whether a changing cross-sectional area can influence the as-built columnar grain microstructure or microstructural features (e.g. β-interspace). The A-shaped sample has a decreasing cross-sectional area with the build height while the V-shaped sample has an increasing cross-sectional area with the built height. The I-shaped sample has a constant cross-sectional area with build height.

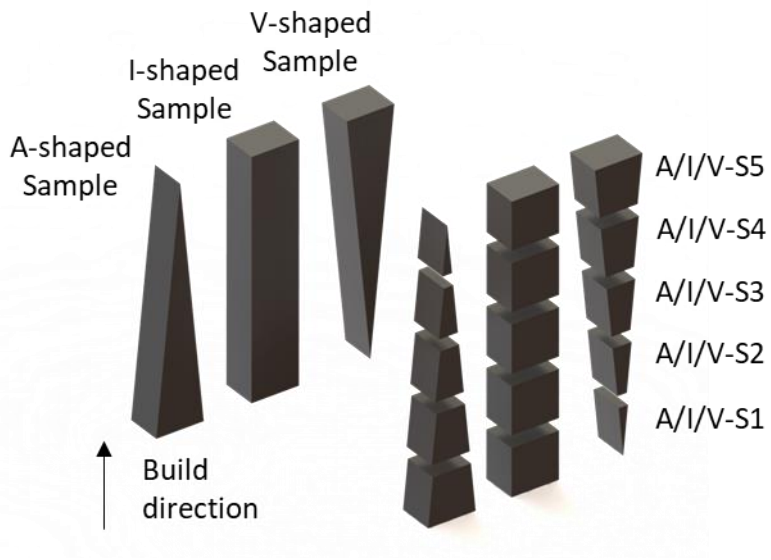

Figure 3.7 Schematic of the samples used to investigate the columnar grain growth and how it was wire cut into the individual samples. The block sample has a width of 20 mm, thickness of 10 mm and 100 mm of height. The wedge samples have one of its end tapered to an edge. The samples were cut into five positions designated S1, S2, S3, S4 and S5. The samples are indicated with the letter A, I and V in front for easy identification between the different geometries. Thin slice was obtained from the various positions for XRD analysis. The samples had a spacing of 5 mm between them to reduce the thermal interaction between samples.

3.5 Metallographic Analysis

Metallographic analysis of the samples was observed via various techniques. They are the optical microscopy (OM; ZEISS Axioskop 2 MAT), scanning electron microscopy (SEM; JEOL JMS-6700F), X-ray diffraction (XRD; PANalytical Empyrean) , transmission electron microscopy (TEM; JEOL-2010) and Atom Probe Tomography (Atom probe LEAP 3000X HR) were used to examine the microstructure of as-built Ti-6Al-4V. Data analysis was performed using IVAS 3.6.2 software.

3.5.1 Stereo and light optical microscopy (LOM)

Olympus SZX7 stereo microscope (Magnification Range: 10x - 50x) and ZEISS Axioskop 2 MAT optical microscope (Magnification Range: 50x - 500x) were used to provide microstructure characterization of the specimen and to measure properties such as porosity size distribution of samples. Each sample section was first hot mounted and then polished using Struers Tegramin-25 with the following process, 3 minutes Si-C 320# paper, 10 minutes largo with Dia Pro 9 and lastly MD Chem with OP-S for 4 minutes as recommended by the manufacturer. After which the section was etched with Kroll's Reagent (1 - 3% HF, 2 - 6% HNO_3, and 91 - 97% H_2O) for 5-10 secs. OM and quantitative image analysis was carried out by using Image J software.

Grain width and grain growth angle measurements

There are a few microstructural features that were investigated in this thesis. They are the prior β grain size and β rod interspace, which were sorted in a descending order in terms of their length scale. The α/β colony size is difficult to quantify, as its microstructure is composed of irregular mixture of colony and basket-weave structures due to the extremely high cooling rate. As such the microstructural features that was investigated were the β grain size and β rod interspace. Quantitative measurement of the α-phase grain boundary was not done in this study.

Columnar grain width measurements were carried out by using Image J software. The columnar grain width was measured individually from micrograph images with a magnification of 200x. At least 60 columnar grain width measurements were performed for each sample and the averages are presented in the results. Columnar grain widths of greater than 100 μm were excluded from the data as they caused large deviations in the results. It was also difficult to accurately distinguish the columnar grain boundaries at lower magnifications if larger columnar grains were to be measured. The grain growth angle was also measured by measuring

the angle that the grain makes with respect to the build direction. An illustration showing how the measurements were taken is shown in Figure 3.8.

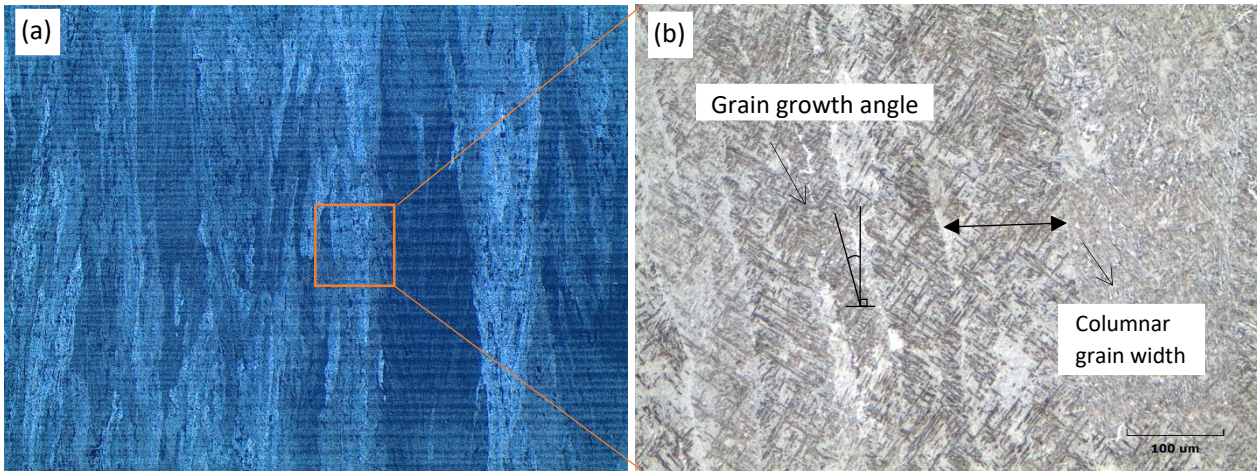

Figure 3.8 Illustration showing how the columnar grain width and grain growth angle measurements were taken. (a) Stereomicrograph of the SEBM Ti-6Al-4V microstructure. (b) OM of the SEBM Ti-6Al-4V microstructure.

3.5.2 Scanning Electron Microscopy (SEM)

Scanning Electron Microscopy (JEOL JMS-6700F) was used to provide a more precise study of the microstructure of the specimen and to measure properties such as the columnar grain width, rough approximation of the different phase and each individual β-interspace more precisely as compared to optical microscopy (Magnification Range: 1000x - 5000x). Specimens were prepared with a similar process as specimens for OM observation. However, an additional step in the gold/platinum sputtering of specimens for the duration of ~40 s, was carried out to provide better electrical conduction of specimens so that the specimen does not experience charging in the scanning electron microscope process. An accelerating voltage of 20 kV with a working distance of 15 - 22 mm was used. The system was equipped with a EDX unit which allowed the detection of elements within the scanned image when necessary.

3.5.2.1 β-interspace measurements

The β-interspace was measured manually by measuring the linear distance between two β-rods as shown in Figure 3.9. Freeware image analysis software, Image J, was used to measure the distance between the β-rods. The micrographs used for measurements have a magnification of either 5000x or 10000x so that measuring error can be minimized.

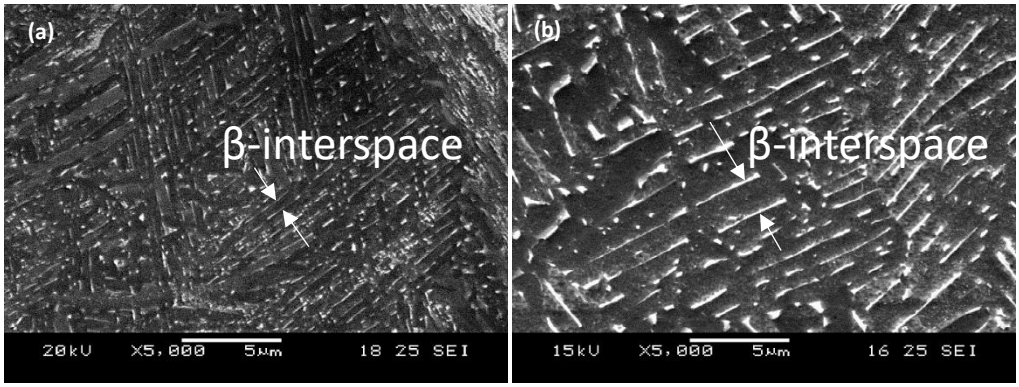

Figure 3.9 SEM micrographs of SEBM Ti-6Al-4V's α/β duplex microstructure for (a) 1mm thick specimen and (b) 10 mm thick specimen with labels indicating how the β-interspace is being defined

3.5.3 Transmission Electron Microscopy (TEM)

Transmission Electron Microscopy (JEOL-2010) provides further information of the microstructure of the specimen and the crystal structure of the specimen by the use of the diffraction patterns to correlate with the TEM images. For our experiments, a double tilt specimen holder was used to allow for a better imaging of the specimen. (Magnification Range: 8000x - 50000x). The JEOL-2010 also has Energy-dispersive X-ray spectroscopy capability. This was used to identify the at.% of elements found in the specimen. Specimens were prepared firstly by EDM wire cutting into a thin strip with a thickness of less than 3 mm and then ground manually to around 150 μm using silicon carbide paper. To avoid heat-induced artifacts, the grinding process was conducted under a constant stream of water. Further grinding down till the thin strip are 50 μms and then the small circular test specimens were punched out and ball

milled till the specimen was within 10 µm. The test specimens then undergo ion milling till small holes were seen in the test specimens. To avoid stress-induced artifacts, a low current (~10 - 14 mA) was used for the ion milling process.

3.5.4 X-Ray diffraction (XRD)

Diffraction of X-rays is a versatile method to study the crystal structure of materials. The diffraction of X-rays was used to assess the composition of the different phases and crystallographic orientation and texture in the titanium samples. This is possible due to each crystal phase having its own unique set of diffracted intensities. X-ray diffraction (XRD) analysis was done using a Cu Kα source over the 2Θ range of 30º to 90º with a step size of 0.013°). The measurements were done using the PANalytical Empyrean system with an applied voltage and current 40 kV, 40 mA, respectively. The raw data were then processed using the HighScore software and Mtex's plugins for Matlab to generate the peak figures and pole figures, respectively.

3.5.4.1 Phase Crystal Analysis

XRD peaks were used to examine the phase constitution within the SEBM-built samples. The raw data for the phase analysis were obtained by performing a phase analysis scanned. The raw data were then corrected for background noise and smoothed to further reduce the noise within the data.

3.5.4.2 Texture Analysis

Pole figures have been used to present the texture of the room temperature α phase within the titanium samples. The raw data of the texture analysis that was produced from performing a texture scanned was processed using the Mtex (version: 4.4 beta) plugin for Matlab.

The following codes were used to obtain the processed pole figures.

plot(pf)

odf = calcODF(pf,'silent')

plotPDF(odf,pf.h)

plotIPDF(odf,[xvector,yvector,zvector],'antipodal')

3.5.5 Atom Probe Tomography

APT specimens were prepared by focused ion beam (FIB) on a FEI Helios dual-beam via the lift-out technique, and the micro-tips were prepared using the annular milling method to obtain an end radius of ~50 nm. The APT specimens were taken from the block samples at Figure 3.6. APT specimens were analyzed at 40 K and a gauge pressure <2e^{-11} Torr. Pulses of green laser light (532 nm wavelength) were applied at a 200 kHz repetition rate with an energy of 0.9 nJ pulse^{-1}, yielding an evaporation rate of 0.30%. The APT data were analysed using IVAS® 3.6.6 software and the compositional information was obtained by employing the proximity histogram (proxigram) methodology. Errors bars were plotted in each compositional profile. The error bars were calculated using $Error\% = \pm\sqrt{C * (100 - C)/N}$, where C is the composition value in at.% and N is the number of atoms in the distance step over which these values were being averaged.

3.6 Mechanical Testing

3.6.1 Tensile Testing

Tensile tests were carried out using the Instron Static Tester Series 5569 tensile tester. The specimens have a rectangular cross section, with a gauge dimension of 25 mm × 6 mm × 6 mm according to the ATM E8 sub-sized standard. Specimens were fabricated from block samples using an EDM machine. A strain rate of 3.33e^{-4} s^{-1} was used during the test. An extensometer has been applied for the elongation measurements. The load cell used was rated to 50 kN.

3.6.2 Vickers Microhardness indentation

Vicker's microhardness tests were carried out on the samples using a Future Tech FM-300e micro hardness tester. A load of 1 kg and a 15s dwell time were adopted. Hardness test is a suitable mechanical test for our experiment since it allows us to quantify the mechanical properties for samples with different microstructure easily.

3.6.3 Porosity measurement

The density of the titanium alloy samples has been determined by means of the Archimedes principle and image analysis. The density of the samples was calculated using Equation 3.2. The density measurements have been performed using a weight balance. The density of the titanium alloy sample can also be approximated via image analysis using the Image J software. A threshold procedure is used to differentiate the pores from the background prior to performing the measurement of the area fraction of the pore in the image. The area fraction of the pores is then taken as the approximate porosity within the titanium sample. An illustration showing the thresholding procedure used is shown in Figure 3.10.

$$\frac{density\ of\ sample}{density\ of\ fluid} = \frac{apparent\ weight\ in\ air}{apparent\ weight\ in\ air - apparent\ immersed\ weight} \quad \text{Eqn. 3.2}$$

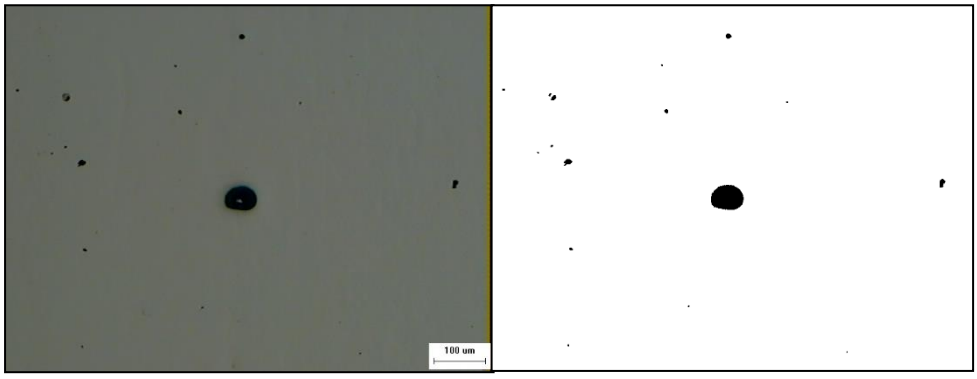

Figure 3.10 An example showing the thresholding procedure used to distinguish the pores from the background using the Image J software. The area fraction of the black region (pores) can then be measured by the software.

3.7 Numerical modelling of SEBM process

3.7.1 Macro-scale modelling of moving energy source

For the first model, a two-dimensional mesh with a dimension of 2.5 mm × 500 μm was built with quadrilateral elements with an element size of 25 μm × 25 μm. The electron beam was modelled as a moving Gaussian heat source, where the peculiar absorption profile of an electron beam was considered. Beam absorption depth was set to be 28 mm [202], beam voltage 60 kV, beam current 10 mA, and spot size 200 μm, according to the working parameters of Arcam EBM machine [203]. Heat loss was considered from the top surface in terms of radiation, where the emissivity of Ti-6Al-4V was set at 0.35 [204]. No heat convection was included because the process occurs in vacuum. The other boundaries of the mesh were kept at a fixed temperature of 650 ^{o}C. The temperature was also set to be 650 ^{o}C to reproduce the average temperature in actual SEBM building. The change in different phases (powder, melt, solid) during melting and solidification was considered following the approach developed earlier [205], where the thermal properties were dependent on the phase and they were taken from Ref. [206]. During the simulation, temperature distributions in the model were generated and temperature-time curves at selected locations were recorded. Figure 3.11 (a) and (b) shows typical temperature profiles as the beam travelled from right to left. It is worth noting that Multispot contours were employed in the A2XX EBM machine. Due to the small mesh dimensions used for the first model, the so-called “dummy sweep” with a speed of 140 m/s was used for small contour lengths that would be suitable for the model.

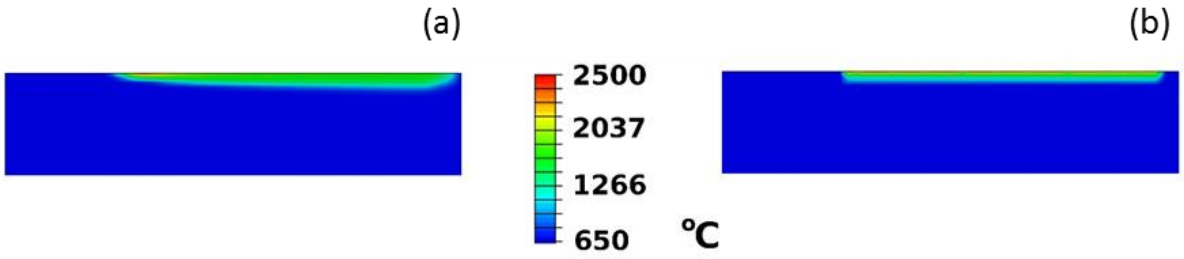

Figure 3.11 (a) and (b) Temperature distribution obtained from the in-fill hatch melting and contour melting scan parameters, respectively.

For the second model, calculations were designed in three-dimensions by reproducing the real dimensions of samples and embedding them into powder material, as shown in Figure. 3.12. Here, since the samples were simulated in real scale, the precise modelling of the beam becomes computationally intractable because it would require too many mesh elements. Therefore, it is necessary to model the SEBM process in an equivalent way. As the scanning speed of electron beam is ~ 4.5 m/s, the in-fill hatching takes seconds to complete the scan of one layer. Therefore, scanning along the direction perpendicular to in-fill hatching can be assumed to be instantaneous compared to that along the hatching direction. Using a scanning speed of 4.5 m/s, the effective beam speed along the hatching direction was estimated as 14 mm/s, 7 mm/s and 3.5 mm/s for the 5mm, 10 mm, and 20 mm samples, respectively. This estimate was computed considering that the build time for each sample is directly proportional to its cross-section area and that the total build time was ~50 seconds per layer. In this way, scan times of 7.1, 14.3, and 28.6 seconds were obtained for the 5 mm, 10 mm, and 20 mm samples respectively, while it was only 1.5 ms for the 1mm sample because of its fast scanning speed.

The effective beam heat profile is shown in Figure 3.12 (c) and (d) for the 20 mm sample during scanning and cooling, respectively, where the beam size was taken of the order of the melt pool (2 mm) and the intensity was tuned such that the surface temperature was

~2400 °C [204]. Special attention was devoted to the simulation of the 1 mm sample (Figure 3.12 a and b), because it consisted of pure contour melt scan. For this case, the beam speed was set to 140 m/s and beam scan was simulated in two passes, in accordance with the real SEBM build, with an effective beam size of 4 mm, which is comparable to the length of the melt pool. In each of the four cases, a cooling step was modelled after the scan, where the cooling time was set to reproduce the actual time that the beam spends to scan the other samples.

For example, the cooling time of the 20 mm sample was equal to (7.1 + 14.3) seconds, i.e., the time that the beam took to scan the 5 mm and 10 mm samples, where the scan time for the 1mm sample was neglected because it is very short compared to the scan time of the other samples. In each simulation, the bulk material was embedded into a sufficient volume of powder material (Figure 3.12 e and f), where the powder was set with its relevant values for thermal conductivity and specific heat, and the cooling temperature was set at the mesh boundaries.

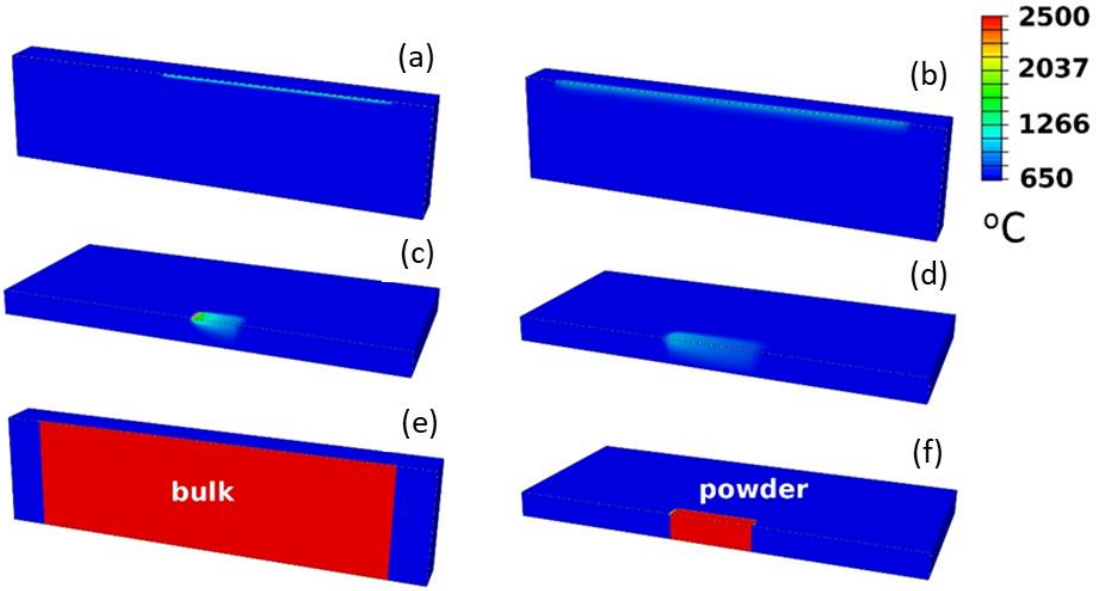

Figure 3.12 Temperature distribution for the full-scale 1mm ((a) and (b)) and 20mm ((c) and (d)) samples with an effective beam heat source. (a) and (c) show the temperature during scanning, while (b) and (d) show the temperature during the cooling process. The samples are embedded into powder material, where the two phases are shown explicitly in (e) and (f) for the 1mm and the 20mm samples, respectively.

3.7.2 Macro-scale modelling of heat flux in varying 2D-planar geometries

FEM simulation was performed to study the thermal history of the two types of parts. The simulation enables the study of the thermal flux within the two parts with relevant thermal boundaries associated with the SEBM process. The thermal simulation was conducted using SolidWorks Simulation. The boundary conditions were 1700 ºC for the hatch region for the two parts and 700 ºC for the surrounding powder bed region. The simulation did not consider the scan strategy of the moving heat source. A uniform and consistent temperature was given on the hatch region and the powder bed region respectively. Only the heat flux result was used in this simulation. The boundary condition of 1700ºC and 700ºC was selected to match the approximate melting temperature of Ti-6Al-4V and the approximate powder bed temperature based on the thermocouple reading.

3.7.3 Study on the columnar grain growth

Multi-scale numerical modeling, representative of melting/solidification phenomena occurring during a SEBM process was carried out in this study. The macro-scale model was developed using a finite element analysis software COMSOL while the mesoscale modeling of the grain growth phenomena during melt pool solidification was carried out using a cellular automata finite difference (CAFD) based open-source code - μMatIC [207].

3.7.4 Macro-scale modelling of melting/solidification

The macro-scale numerical model was built for electron beam scanning of Ti-6Al-4V, due to the vast amount of experimental data available for model validation. The domain for the simulation was developed with symmetry boundary condition for a single scan and was divided into three subdomains - the deposited metal, the sintered metal powder and the stainless-steel start plate as shown in Figure 3.13

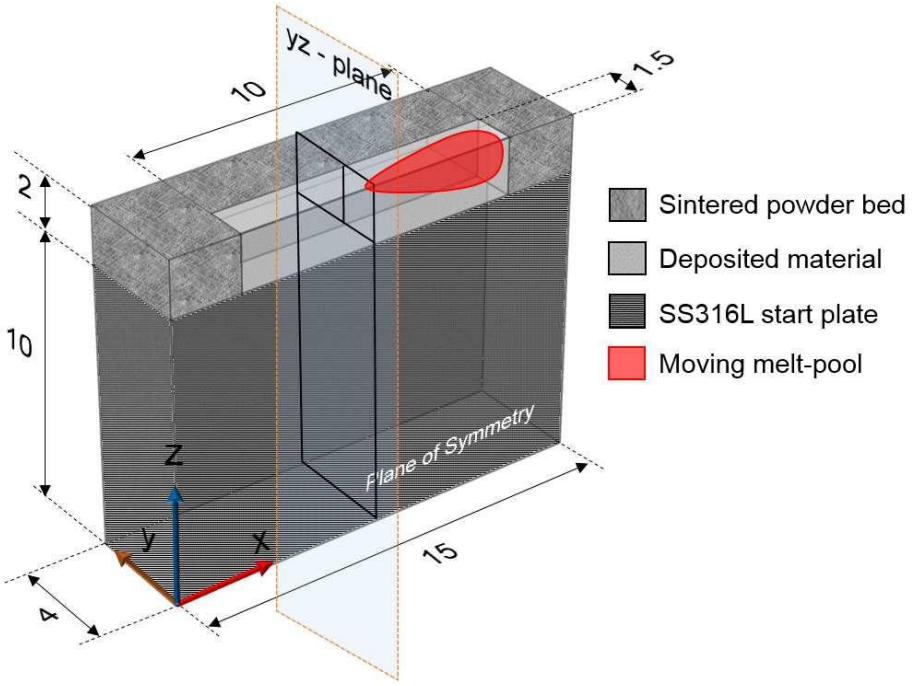

Figure 3.13 3D numerical model showing the melt-pool schematic (All dimensions in mm).

Heat transfer equations associated with solid/liquid phase change [208] have been solved for the deposited metal domain with the incorporation of a moving heat influx in positive x-direction with gaussian distribution of σ = 127.4 μm. The sintered metal powder domain comprised of the material properties calculated by [209] for sintered Ti-6Al-4V alloy but taken as a value independent of temperature. No phase change was considered for this domain given its close distance from the center of the simulated beam. The stainless-steel domain represents the start plate used in SEBM experiments to simulate the heat sink effect provided by the start plate during real-time experiments.

This study was extended further in two dimensions in a yz-plane associated with x = 5 mm of the deposited material with the heat source moving perpendicular to the yz-plane as shown in Figure 3.13. The material properties and the process parameters defined for the 2D simulations were the same as for the 3D simulations, with the exception of the presence of adaptive meshing in 2D, in order to establish the validity of the modelling process.

This 2D approximation of the SEBM process relies on the observations from 3D simulations that the thermal gradient within the melt-pool in the x-direction is < $1/10^{th}$ of the gradients in y- and z-directions during solidification. This implies that the magnitude of the resultant thermal gradient in the melt pool is inclined to the z-axis at an angle less than 4 degrees towards x-axis; the solidification of the melt pool, hence, is mainly in the yz-plane.

The simplification proves beneficial in terms of lower computational resources required to carry out the simulations. The time taken for 2D simulations in man hours was 90 times less than that for 3D simulations. Due to this reason, this study in two dimensions was extended to incorporate the effect of deposited material shape on the resulting thermal history in the melt-pool with build height. The 2D heat transfer simulations were extended for SEBM simulation of A-, I-, and V-shapes for large domain sizes comparable to that of the experiments with the deposited metal build height variation of 2 - 100 mm.

In the case of the 3D modelling, heat transfer physics related to phase change during melting/solidification was considered. Hence, only energy equation was solved for the 3D domain. Since the SEBM process took place in a vacuum chamber, heat transfer due to forced convection, as in the case of SLM, was absent. The boundary conditions for the model only consist of radiative boundary condition on the top surface and insulation on every other boundary. Table 3.2 gives a detailed description of the material properties of Ti-6Al-4V utilized for the macro and mesoscale modeling process. Table 3.3 provides the SEBM process parameters utilized for model development and validation for Ti-6Al-4V.

Table 3.2 Material properties of Ti-6Al-4V utilized for the macro and mesoscale modelling process

Material Property	Value
T_l	1947 K [201]
T_m	1888 K [201]
k_{liq}	37 W/m.K [202]
k_{sol}	28.27 W/m.K [202]
k_{sint}	2.4 W/m.K [200]
Cp_{sol}	848 J/kg.K [203]
Cp_{liq}	921 J/kg.K [203]
ρ_{liq}	4200 kg/m^3 [200]
ρ_{sol}	4100 kg/m^3 [200]
ρ_{sint}	2500 kg/m^3 (50% porosity [200])
α	0.9[200, 204]
ε	0.8

Table 3.3 SEBM process parameters utilized for model development and validation for Ti-6Al-4V

Parameter	Value
P	900 W
I	15 mA
V_s	3220 mm/s
ro	254.8 μm
d_s	100 μm
h_l	50 μm

3.7.5 Meso-scale modelling of grain growth during solidification

In order to visualize the competitive grain-growth phenomena occurring during solidification process inside one melt-pool, a cellular automata finite difference (CAFD) model [210, 211] was developed for a two-dimensional rectangular domain using an open-source code μMatIC. Fixed nucleation of fifty grains with random orientations ranging from -20 degrees to 20 degrees with build direction was carried out at random positions at the bottom of a domain measuring 300 μm in width and 105 μm in height. The thermal gradient and cooling rate data obtained from the macro-scale FE model were coupled with this CAFD model to visualize the

microstructure development during melt-pool solidification. The current study has focused on the model development for a binary alloy approximation for Ti-6Al-4V with linear partition coefficient. A modification was carried out in the open-source code's library files to incorporate time-dependent variation of thermal gradient to the third degree. However, incorporation of the variation of the thermal gradient with respect to position within the melt pool with the evolution of the solid/liquid interface is necessary as observed from the macro-scale simulation results and will be carried out in future work.

This chapter presents the experimental methods employed to produce and characterize the SEBM Ti-6Al-4V samples. The next three chapters discussed the results obtained from the use of these methods and their implications with respect to the anisotropy and heterogeneity within the SEBM-built titanium samples.

Chapter 4: Phase transformation in SEBM-built Ti-6Al-4V parts

4.1 Introduction

In order to understand the heterogeneous macro scale mechanical properties in SEBM-built Ti-6Al-4V, it is important to first understand the nano/microscale phenomenon (e.g. phase transformation) that takes place within the material during the manufacturing process. This chapter focuses on the phase transformation and identification of SEBM-built Ti-6Al-4V. Prior literature has shown that there exists α, β and α' phases in titanium AM components. However, there is less focus on investigating the microstructure and phase transformation that occurs with different build geometry (e.g. thickness, shape, and height). An understanding of the microstructure and phase transformation would deepen the understanding of microstructural heterogeneity in titanium AM components.

More precisely, the knowledge and prediction of the exact amount of the different phases in the final SEBM-built part still encounter many open questions, including whether martensite will form or not during the SEBM process [30]. For example, recent investigations have clearly shown the formation of martensite in SLM-built Ti-6Al-4V samples [31] due to the higher cooling rates experienced in the SLM process as compared to SEBM. As the amount of martensite has a direct impact on the mechanical properties, including strength and fatigue resistance [32], the study on microstructural evolution involved in EBM process is imperative.

The result and discussion sections of this chapter consist of three parts: (1) phase identification in the thickness dependent samples, (2) investigating the martensitic phase transformation process and (3) characterization of the α/β interface. The author will then discuss the results in relation to the anisotropic and heterogeneity in SEBM-built Ti-6Al-4V.

4.2 Results

To understand the phases that exist within the SEBM-built Ti-6Al-4V and the transformation process, block parts were fabricated with thickness of 1, 5, 10 and 20 mm as shown in Figure 3.4. The parts were then sectioned into several samples to for the various characterisations that will be discussed later in this section. Details of the sample preparation were described in Chapter 3. To study the phase constitution in the thickness-dependent samples, OM, SEM, TEM, XRD and APT analysis were carried out on the samples.

4.2.1 Microstructural characterisation

Figure 4.1 shows typical α/β duplex microstructures of SEBM-built Ti-6Al-4V observed under OM and SEM. The micrographs were taken from the block sample (10 mm thickness) as shown in Figure 3.6. Figure 4.1 (a) shows the wavy columnar prior β grains that delineated by the grain boundary (G.B) α. The wavy grain boundaries formed because in-fill hatch melting direction rotated 90^0 after each layer during the EBM process, which aims to minimize residual stress. It is noted that a significant number of black lines can be clearly seen inside the prior β grains as in Figure 4.1 (a). After a detailed observation using OM and SEM, they were found to be the singular α bulges with a β/α/β sandwich structure (as shown in Figure 4.1 (b) and (c). The width of these columnar β grains ranges mainly from 10 μm to 100 μm. Figure 4.1 (d) shows a typical a/b duplex microstructure. As α phase was etched out by Kroll's reagent, it exhibits dark contrast while β is bright when observed under the SEM. In general, there are two types of transformed α/β structures existing inside the prior β grain, i.e. lamellar colony (Figure 4.1 (e)) and basket-weave (also called Widmanstätten pattern in Figure 4.1 (f)) morphologies. It is of interest to note that β phase was found to be rod-like under observation. The volume fraction of retained β phase was calculated as only 5% under image analysis via SEM. As its volume fraction is quite low in the volume, β phase formed as discrete flat rods

that are embedded in the continuous α phase. To be more precise, the microstructure should be colonies with a cellular morphology instead of the lamellar structure in Figure 4.1 (e). The thickness of the rod-like β phase was approximately 50 nm as measured on the SEM images.

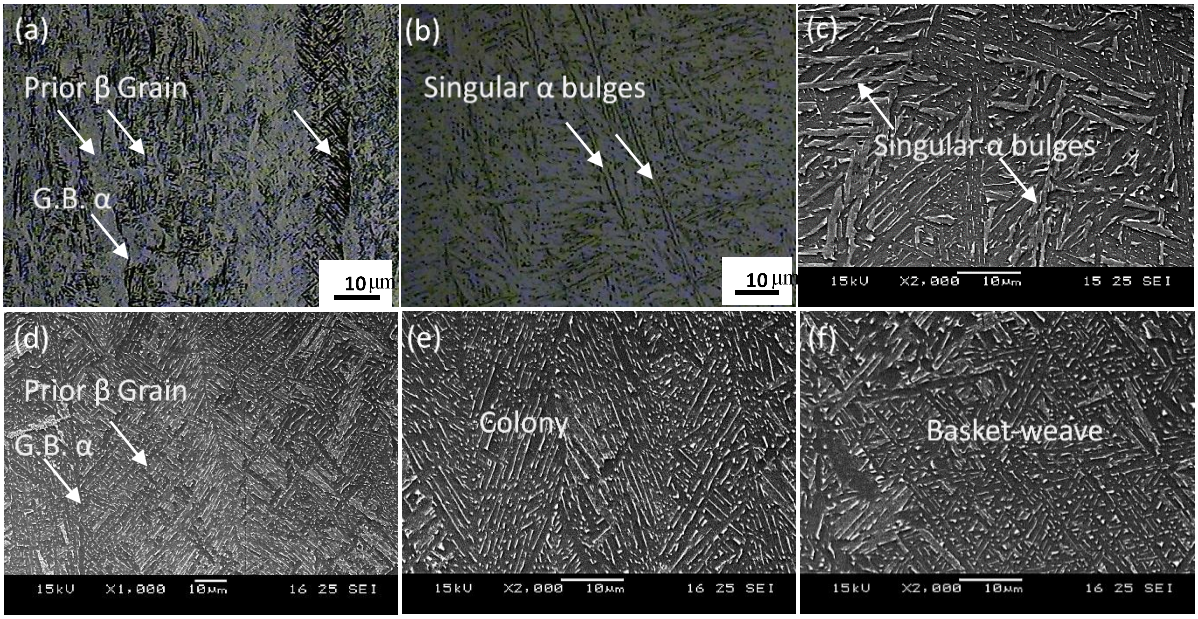

Figure 4.1 OM and SEM images showing the microstructure in SEBM-built Ti-6Al-4V: (a) wavy columnar prior β grains and (b) singular α bulges, (c) singular α bulges in (d) columnar prior β grains, (e) colony α+β microstructure and (f) basket-weave α+β microstructure.

4.2.2 Twinned microstructure and α/β interface

Figure 4.2 shows a mixed microstructure of alternate α/β with acicular α' martensite observed under SEM for the 1 mm thick sample. The heavily twinned α' is seen in Figure 4.2 (c). The image was taken from the top half of the 1 mm thick sample. Figure 4.2 (b) shows the microstructure inside the 5mm sample that is typical of SEBM-built Ti-6Al-4V. The image was taken from the bulk section of the 5 mm thick sample. Additionally, many micro twins exist inside the α phase (as shown in Figure 4.2 (d)) for both 1 mm and 5 mm thick sample. The micro twins were not likely produce by the TEM sample preparation.

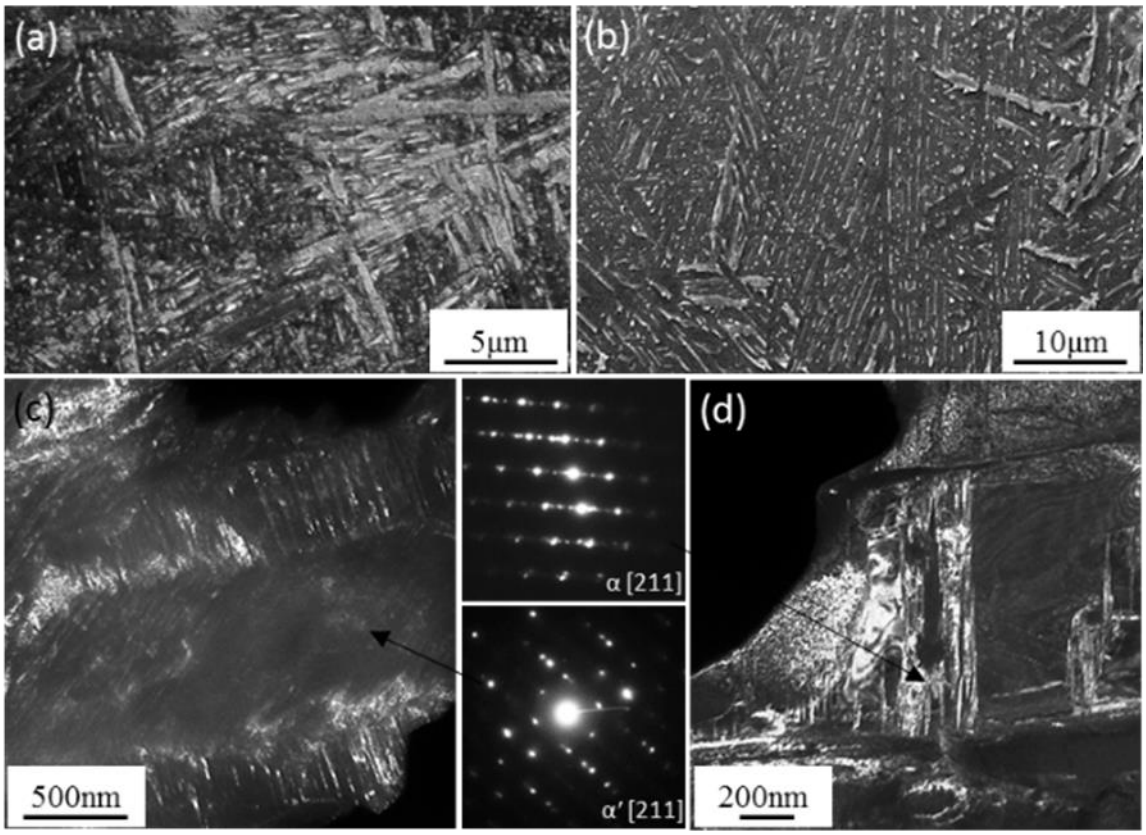

Figure 4.2 SEM and TEM images showing the twinned microstructure in SEBM-built Ti-6Al-4V. SEM images are showing (a) a mixed microstructure of alternate α/β and α' martensite in 1mm sample and (b) full microstructure of alternate α/β in 5mm sample. Dark-field TEM images are showing (c) α' martensite microstructure with numerous micro twins and (d) alternate α/β microstructure with some micro twins.

Figure 4.3 shows a more detailed micrograph of the micro-twins existing inside the α phase of the 10 mm samples. It is noted that an interface layer between α and β phases evident in Figure 4.3 (c). Moreover, the interface layer was found to be prevalent in all our SEBM-built Ti-6Al-4V samples. This interface layer appears to be quite similar with the α/β interface phase observed in the previous studies [212-214].

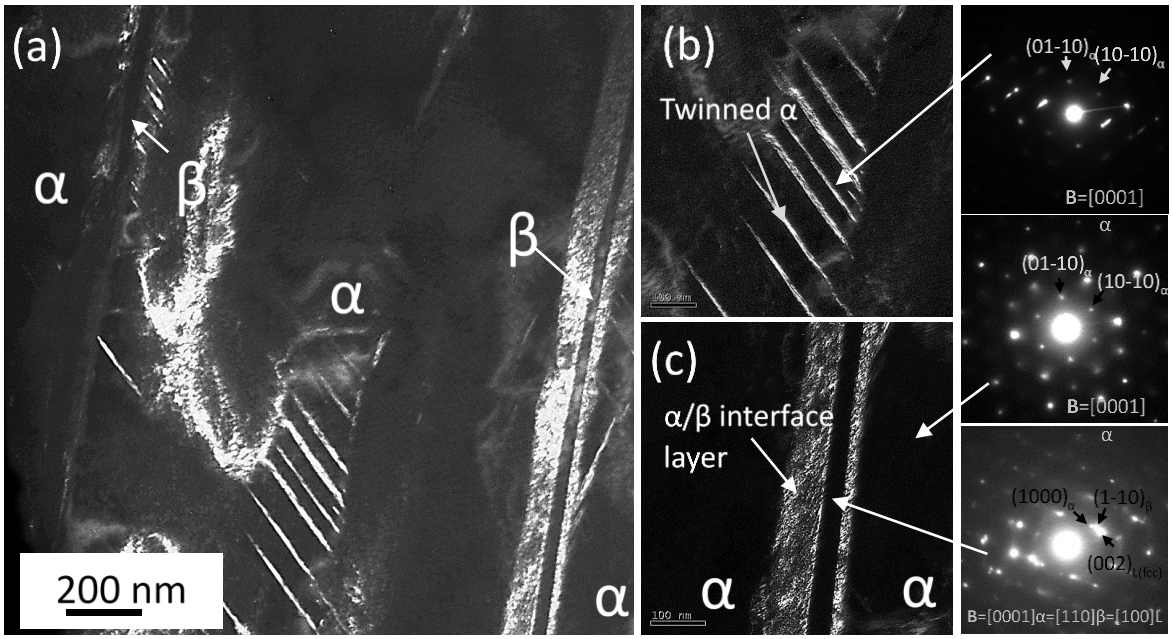

Figure 4.3 TEM images showing the twinned α phase and the suspected α/β interphase; (a) TEM dark field image showing α and β phases in 10 mm sample. (b) and (c) Enlarged DF images showing micro-twins in α phase and a α/β interface layer, respectively. Inserts indicate the SAED patterns with zone axis [0001]α and [001]β.

4.2.3 Martensitic phase identification

Figure 4.4 shows the XRD patterns for the SEBM-built Ti-6Al-4V samples with thicknesses of 1 mm and 10 mm. All the detected XRD peaks are presented in Table 4.1. It can be observed that the peak counts for the 10 mm sample are weaker as compared to the 1 mm sample.

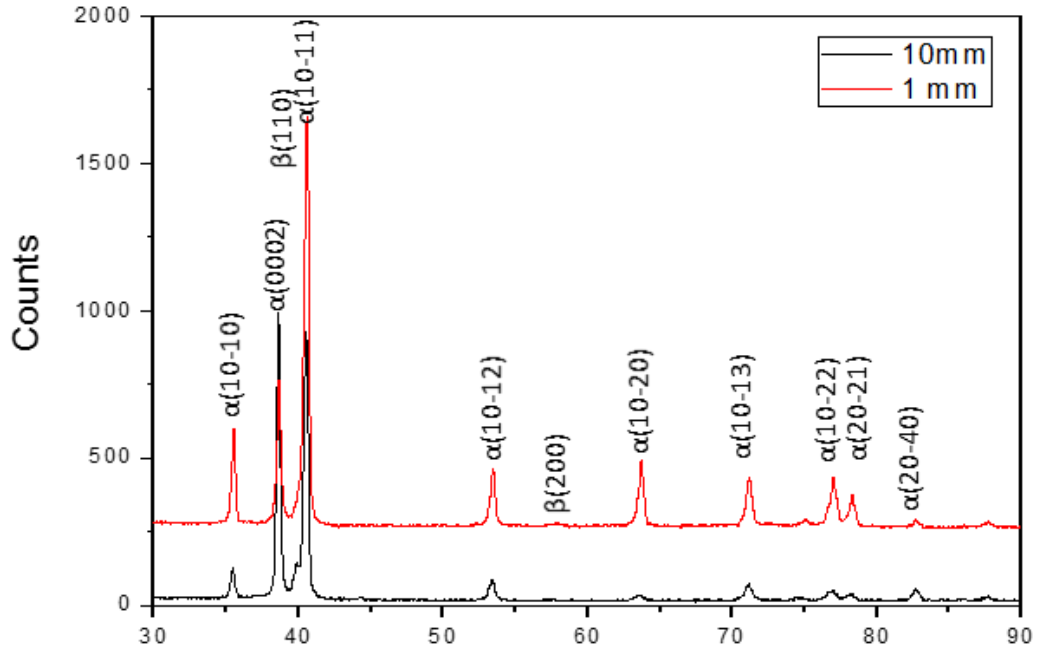

Figure 4.4 XRD pattern for the SEBM-built Ti-6Al-4V samples with thickness of 1 mm and 10 mm.

Table 4.1 XRD data for SEBM-built Ti-6Al-4V

Peak No.	1mm Sample		10 mm Sample			
	2θ (°)	**d-spacing (nm)**	**2θ (°)**	**d-spacing (nm)**	**hkl-α**	**hkl-β**
1	35.58	2.5235	35.41	2.5353	100	
2	38.63	2.3306	38.58	2.3338	002	
3			39.83	2.2632		110
4	40.62	2.2211	40.60	2.2220	101	
5	53.46	1.7141	53.41	1.7156	102	
6	57.96	1.5913	57.55	1.6015		200
7	63.69	1.4612	63.57	1.4637	110	
8	71.23	1.3239	71.11	1.3258	103	
9	76.93	1.2394	76.86	1.2404	112	
10	78.33	1.2207	78.27	1.2215	201	
11	82.59	1.1682	82.65	1.1676	004	

Figure 4.5 (e), (f), (g) and (h) shows the XRD patterns for the 1, 5, 10 and 20 mm thickness-dependent samples. It can be seen from Figure 4.5 that the XRD peak positions are basically consistent for all four samples. Upon closer analysis, there exists a peak shift in the 1mm sample in comparison with the other sample (Figure 4.5 (i)), this suggests that there is some form of lattice strain in the α phase crystals. Based on a study by Zeng et al. [215] it was shown that stress-induced martensite in a Ti-Mo-based alloy caused a similar phenomenon in the XRD pattern. In that study, the stress-induced martensite Ti-Mo alloy was obtained via quenching. Additionally, the enlarged XRD profiles in Figure 4.5 insets ii reveals that peak width tends to increase with the increase of build thickness for the samples. The presence of β peaks are also identified in the thicker 20 mm sample as compared to the 1 mm sample.

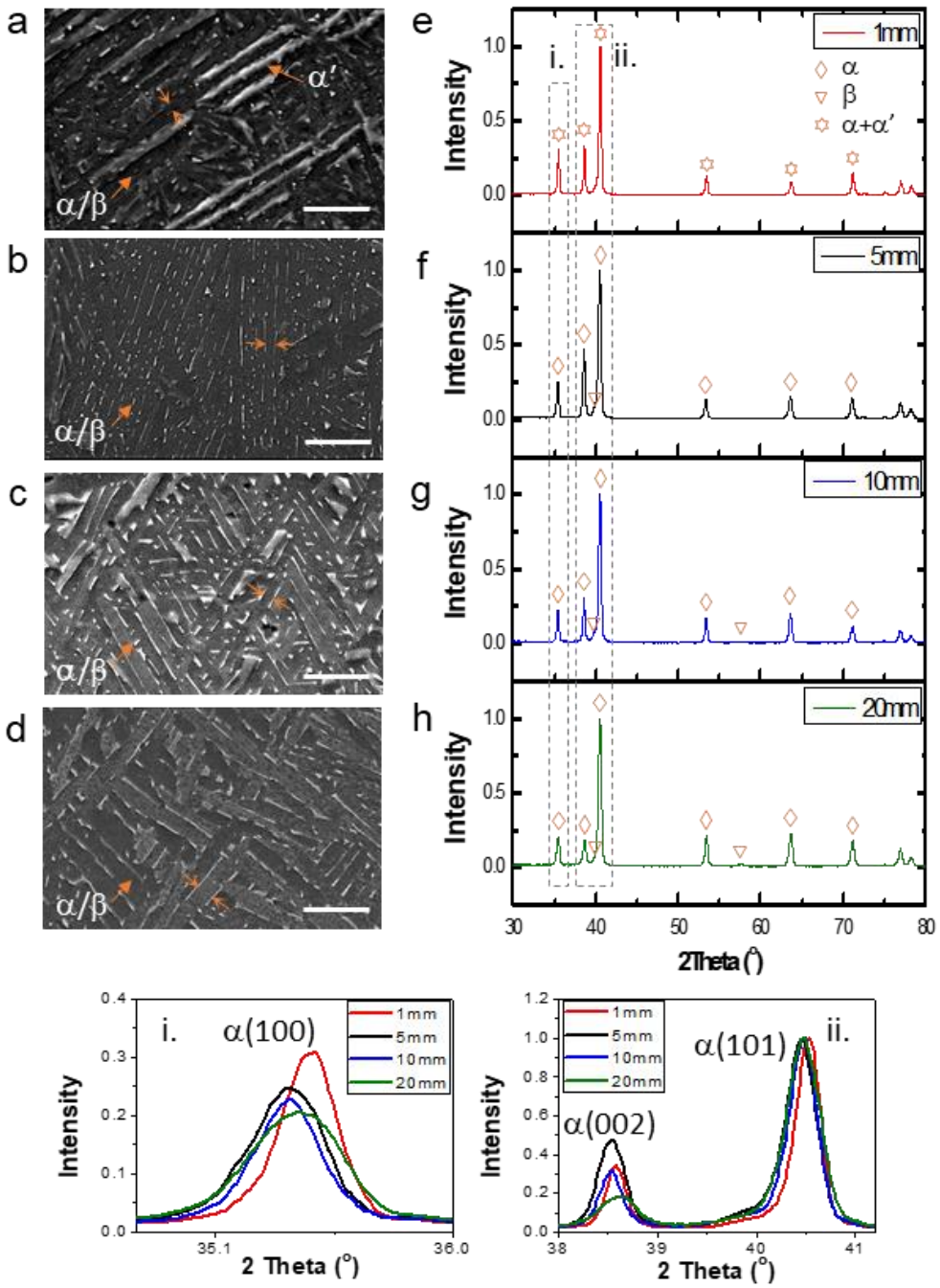

Figure 4.5 Differences in microstructure and phase in samples with varying build thickness; (a–d) SEM images showing microstructure of 1 mm, 5 mm, 10 mm and 20 mm samples, respectively. Scale bar = 5 μm. (e–h) XRD profiles of 1 mm, 5 mm, 10 mm and 20 mm samples, respectively. Insets (i) and (ii) are enlarged profiles showing α(100), α(002) and α(101) peaks.

4.2.4 Elemental distribution of Ti, Al and V

XRD analysis can show the phase constitution information regarding the bulk area of the sample. However, for a more precise and accurate analysis of the microstructure, APT was used. APT analysis of the 1 mm, 10 mm and 20 mm samples was done to reveal more information with regards to the microstructural transformation process.

Figure 4.6 (a) displays the elemental distribution of Ti, Al and V in a Ø30 × 90 nm [216] cylinder that was extracted from an APT reconstructed volume of the 1 mm sample. There are two distinct regions, i.e. dense atom columns and sparse atom matrix. Such a difference in atomic density indicates a difference in phase [217]. In order to better distinguish these two regions, isodensity surfaces of Ti + Al + V = 22 at. nm^{-1} were generated. Isodensity surface means that the atomic percentage of the various element is consistent in the unit volume. The value of 22 at. nm^{-1} was selected empirically based on the reconstructed image obtain via the APT software. Cylindrical region of interest (ROI) that passes perpendicularly through the dense and sparse atom regions is shown in Figure 4.6 (b) was created. The one-dimensional concentration profiles in Figure 4.6 (c) clearly reveal the different compositions in these two regions. It was found that the sparse atom region has very close compositions with the initial Ti-6Al-4V ELI. The high-temperature body-centered cubic (bcc) β phase will be decomposed via diffusional, diffusionless or mixed modes upon cooling [218]. Martensitic transformation is the most important type of military transformations, which do not require diffusion for the change in crystal structure to occur. Therefore, the sparse atom matrix should be the martensite that retained the same compositions of high-temperature β phase. With the aid of SAED technique, it was confirm that the atom matrix was α′ martensite.

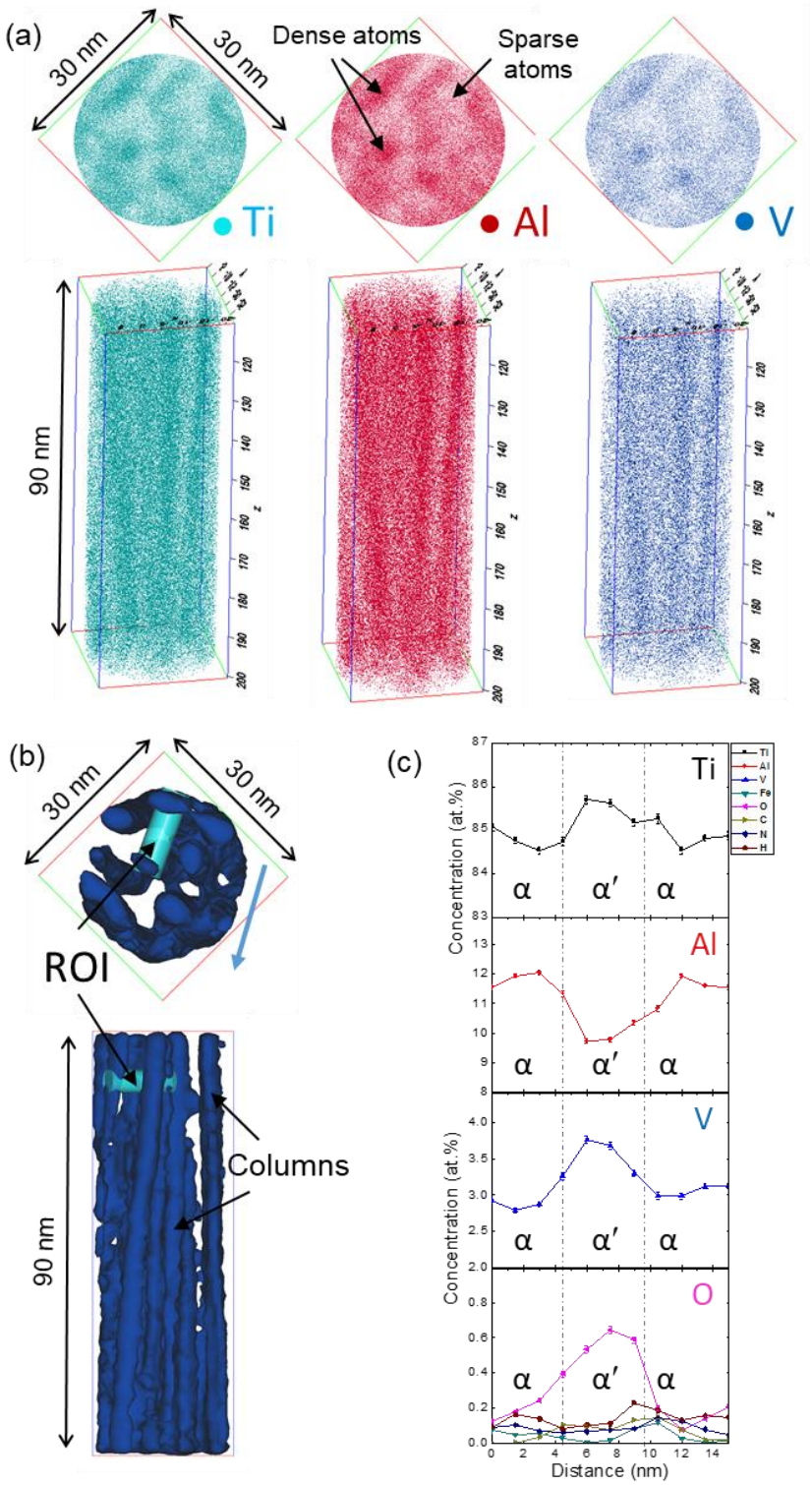

Figure 4.6 Partial decomposition of α′ martensite in the thin SEBM-printed Ti-6Al-4V sample. (a) Element distribution of Ti, Al and V from views of transverse and longitudinal directions respectively in a reconstructed volume of 1 mm sample. (b) A cylindrical ROI cross over columns that delineated with iso-density surfaces of Ti + Al + V = 20 at. nm^{-1}. The columns with a higher atomic density were indicated by arrows. (c) 1D concentration profiles of all alloying elements in the ROI along the arrow direction indicated in (b). The APT samples were likely taken from the upper half of the 1 mm sample.

Additionally, elemental distribution of Ti, Al and V in APT reconstructed volumes of 10 mm and 20 mm samples are shown in Figure 4.7 (a) and (b). Two phases are present as shown by the difference in composition. Al is α phase stabilizer while V is β phase stabilizer [24]. In addition, the microstructure of EBM-printed Ti-6Al-4V consists of fine β rods embedded into continuous α phase. Therefore, α and β phases are easily distinguished. Figure 4.7 (c) and (d) present the two proxigrams that were generated on the base of 13 at.% and 16 at.% V iso-concentration surfaces (iso-surfaces) in the APT reconstructed volumes of 10 mm and 20 mm samples, respectively. Both proxigrams reveal that Ti, Al and O preferentially partition to α phase while V, Fe and H more likely to diffuse into the β phase. Moreover, no evident partitioning trend was observed for C and N. Table 4.2 reveals that Al and V are the most heavily partitioned alloying elements. Moreover, the partitioning ratios were markedly increased in 20 mm sample when compared to 10 mm sample. Iso-concentration surfaces mean that the atomic percentage of the particular element is consistent across the surface. The value of 13 at.% and 16 at.% V were selected empirically based on the reconstructed image obtain via the APT software.

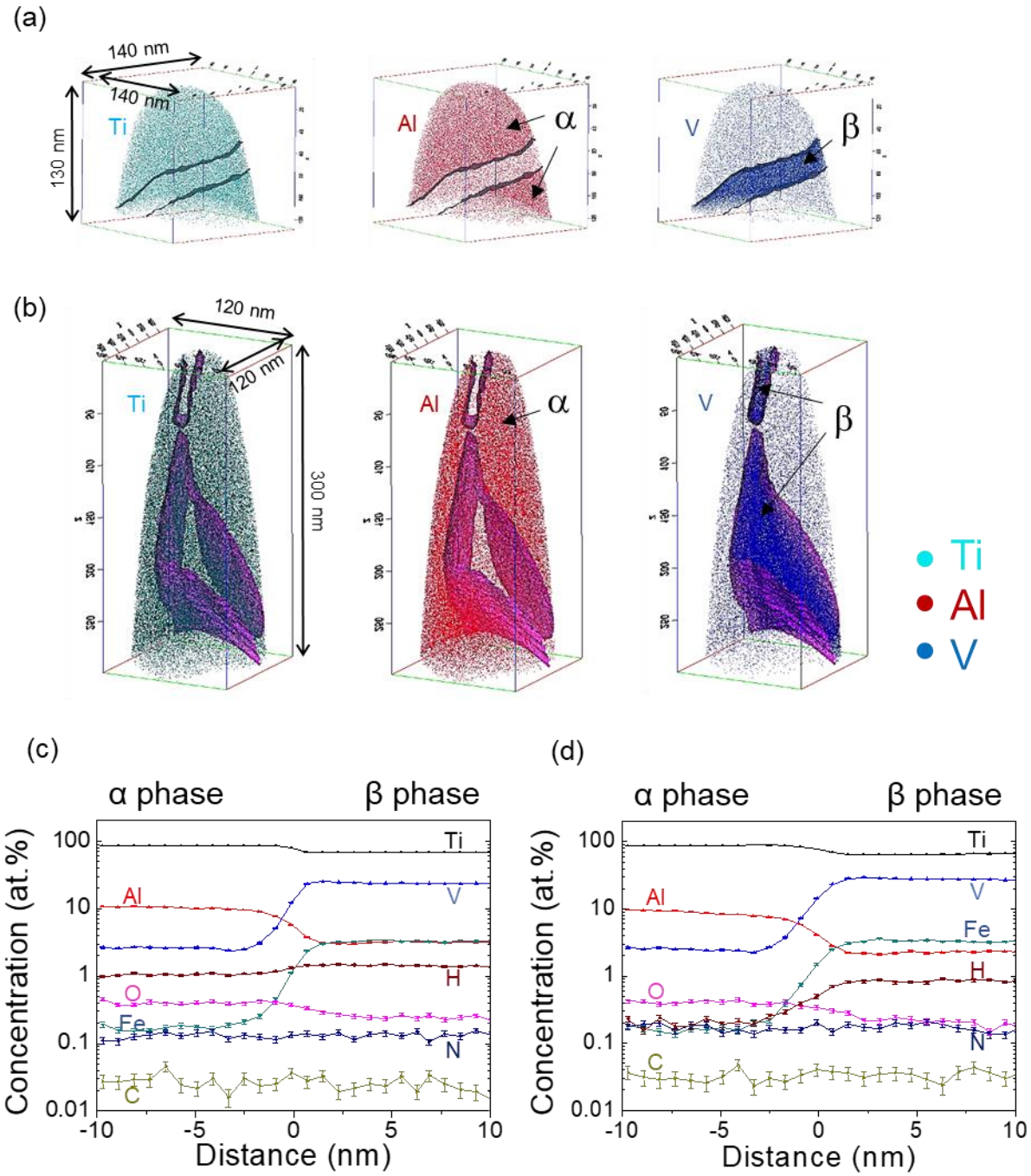

Figure 4.7 Full decomposition of α′ martensite in the thick SEBM-printed Ti-Al-4V samples. (a,b) Elemental mappings of Ti, Al and V in 10 mm and 20 mm samples, respectively. 13 at.% and 16 at.% V iso-concentration surfaces (iso-surfaces) were adopted in the APT reconstructed volumes of 10 mm and 20 mm samples, respectively. (c,d) Proxigrams showing elemental partitioning behavior across α/β interfaces in (a,b), respectively. Partitioning behavior of each element and quantitative compositions of α and β phases are easily obtained from the proxigrams.

Table 4.2 Compositions (in at. %) of α and β phases in 10 mm and 20 mm samples obtained from APT data as well as the partitioning ration of each element.

	Sample	Ti	σ (Ti)	Al	σ (Al)	V	σ (V)	Fe	σ (Fe)	O	σ (O)	C	σ (C)	N	σ (N)	H	σ (H)
α	10 mm	85.15	0.13	10.49	0.12	2.65	0.06	0.16	0.02	0.41	0.02	0.03	0.01	0.12	0.01	0.99	0.04
	20 mm	87.02	0.14	9.41	0.12	2.57	0.07	0.16	0.02	0.42	0.03	0.03	0.01	0.18	0.02	0.2	0.02
β	10 mm	68.22	0.18	3.13	0.07	23.68	0.16	3.28	0.07	0.24	0.02	0.03	0.01	0.13	0.01	1.29	0.04
	20 mm	65.66	0.21	2.32	0.07	27.43	0.2	3.34	0.08	0.2	0.02	0.03	0.01	0.16	0.02	0.86	0.04
k or k'	10 mm	1.2		3.4		8.9		20.5		1.7		1		1.1		1.3	
	20 mm	1.3		4.1		10.7		20.9		2.1		1		1.1		4.3	

*The partitioning ratio k (for α-partitioning elements) or k′ (for β-partitioning elements) were defined as or $k = C_\alpha/C_\beta$ or $k' = C_\beta/C_\alpha$, respectively. The larger than unity for k or k′, the severer partitioning for the corresponding element.

As the microstructures of 10 mm and 20 mm samples comprised only of α and β phases, it obeys the following relationship: $C_0 = C_\alpha \cdot V_f(\alpha) + C_\beta \cdot V_f(\beta)$, where C_0 is the overall composition of Ti-6Al-4V ELI; C_α and C_β are the compositions of α and β phases; $V_f(\alpha)$ and $V_f(\beta)$ are the volume fractions of α and β phases, respectively. Then $V_f(\beta)$ can be derived from the following equation:

$$V_f(\beta) = (C_0 - C_\alpha)/(C_\beta - C_\alpha) \qquad \text{Eqn. 4.1}$$

The $(C_0\text{-}C_\alpha)$–$(C_\beta\text{-}C_\alpha)$ graphs were plotted, and the slope of the fit line is approximately equal to the volume fraction of β phase. Hence, the β volume fraction in 10 mm and 20 mm samples were 3.5 ± 0.5% and 4.6 ± 0.8% from Figure 4.8 (a) and (b). Figure 4.8 (c) and (d) shows the vanadium and aluminium concentration profile at the interface of the α and β phase. The relative Gibbsian interfacial excess (Γ_i^{rel}) of both vanadium and aluminium is indicated in the figure by the hatched region. It can be observed that in the case of vanadium that it has the tendency to segregate at the vicinity of the α/β interface due to the positive relative Gibbsian interfacial excess value. In the case of aluminium it can be observed that it has a tendency to deplete at the vicinity of the α/β interface due to the negative relative Gibbsian interfacial

excess value. The relative Gibbsian interfacial excess (Γ_i^{rel}), which is defined by the excess number of solute atoms per unit area for an arbitrary interface.

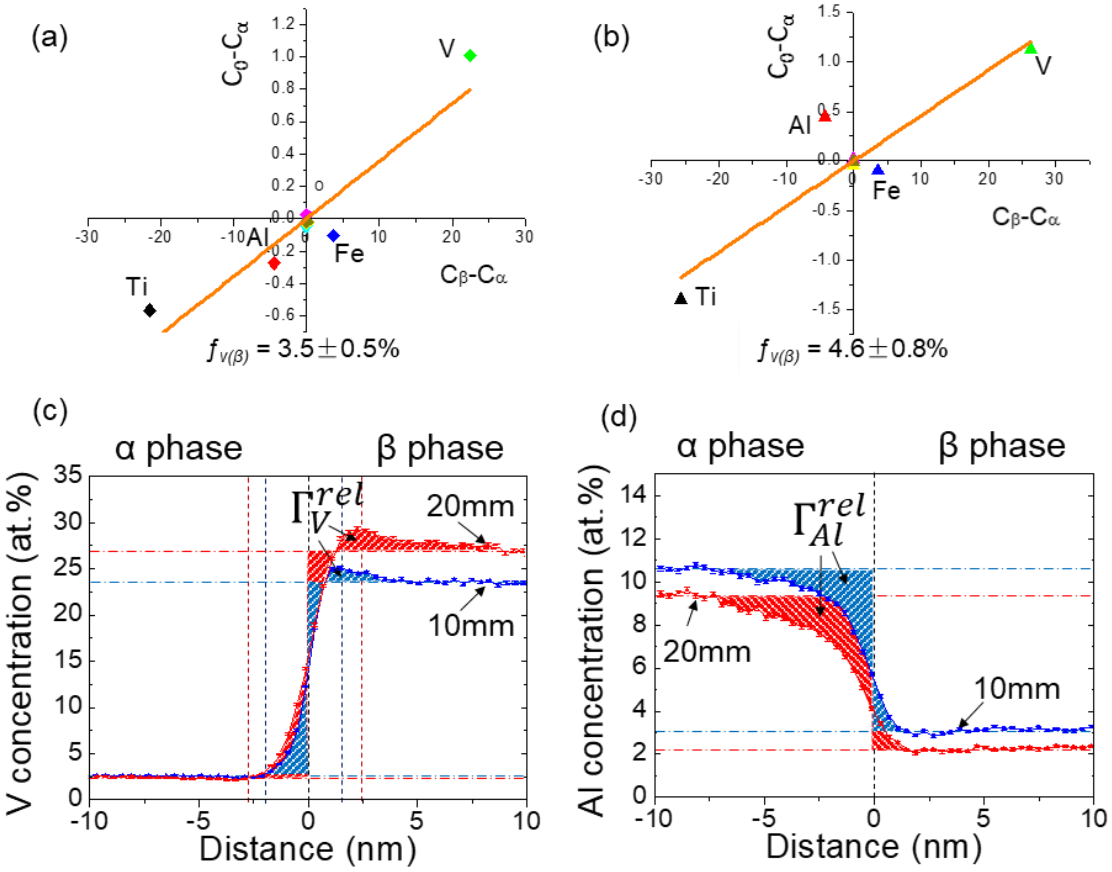

Figure 4.8 β phase volume fraction change and α/β interface characteristics. (a, b) (C_0-C_α)-(C_β-C_α) plots for 10 mm and 20 mm samples, respectively. (c) Vanadium concentration profiles showing kinetic vanadium segregation (hatched region) at interface front of β phase in 10 mm and 20 mm samples. (d) Aluminum concentration profiles showing kinetic aluminum depletion (hatched region) at interface front of α phase in 10 mm and 20 mm samples. α/β interface was found to be widened in 20 mm sample due to vanadium segregation and aluminium depletion. Γ_i^{rel} is the relative Gibbsian interfacial excess.

4.3 Discussion

4.3.1 Microstructure and phase transformation path

Ti-6Al-4V is a classical α/β dual phase titanium alloy, and an important engineering material with broad applications [24]. Also, it is the most developed material for SEBM processing till today. The microstructure of as-built Ti-6Al-4V by SEBM consisted of columnar prior β grains delineated by wavy grain boundary α and transformed α/β structures with both colony and basket-wave morphology as well as numerous α platelets/bulges within the prior β grains. While the fabrication and characterisation of SEBM-printed Ti-6Al-4V were extensively conducted within the past 5 years [26, 27, 29, 181], there is still a lack of direct evidence to verify its phase transformation sequence involved in SEBM. Of particular interest is the study of martensitic transformation because of its significance to engineer SEBM-built Ti-6Al-4V's microstructure. Moreover, α/β interface was found to play a primary role in strengthening SEBM-built Ti-6Al-4V by acting as barriers to dislocation motion.

Figure 4.9 (c) schematically illustrates the α′ martensitic formation and decomposition during EBM process.

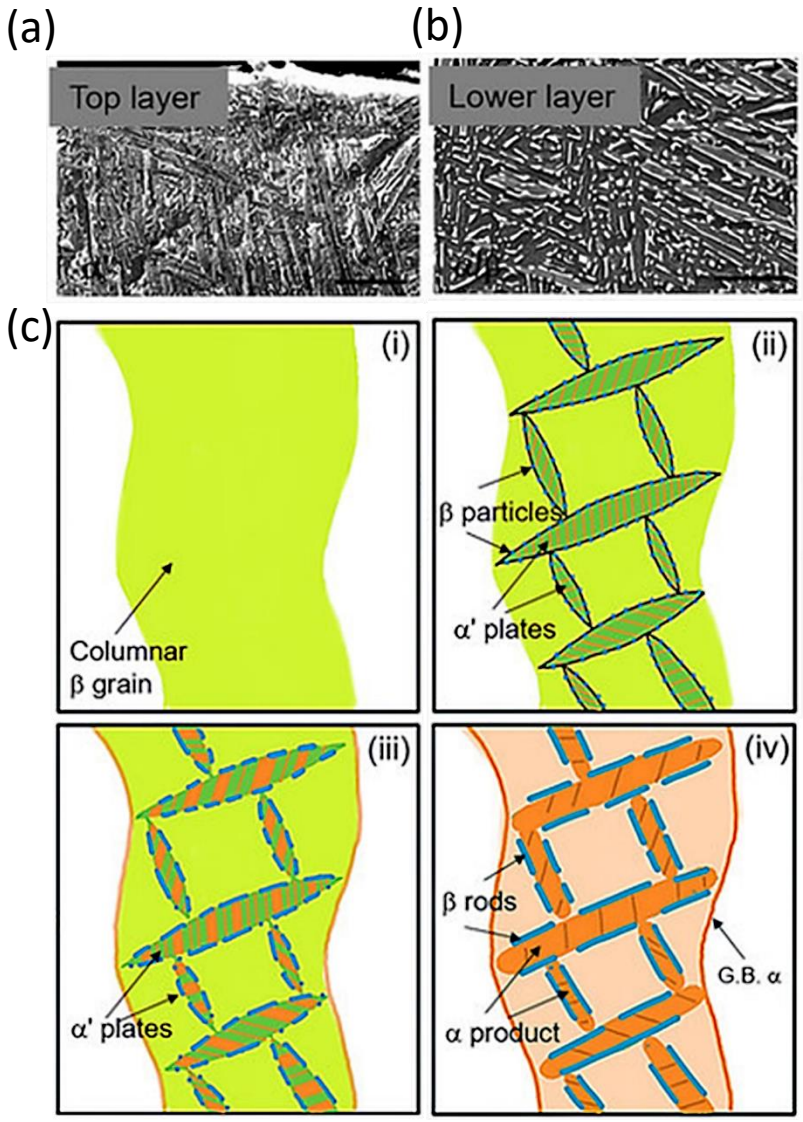

Figure 4.9 General microstructural evolution of SEBM-printed Ti-6Al-4V. (a and b) SEM images showing martensitic microstructure at the very top area and fully decomposed α/β microstructure at the lower area of 10 mm sample. (c) Schematic illustration of microstructural evolution (prior β and α′ are in cyan, α in orange and β in blue), i.e. martensitic formation and decomposition, involved in SEBM-built Ti-6Al-4V. The top layer is approximately 250 μm based on OM image. The top layer is identified based on the different contrast observed under OM.

Firstly, wavy columnar β grains might transiently form and then transformed into heavily faulted and/or twined α′ plates as well as some retained β phase (i → ii). During the decomposition of α′ into α, vanadium is constantly being rejected from the forming α phase and diffuse along accommodation twin boundaries and/or stacking faults toward the boundaries

between adjacent α′ martensite plates. The intergrowth of α within α ′plates could be taken into account as planar defects driven growth [219]. Discrete β particles will first form along α′ martensite plate boundaries and then continuously grow at the expense of vanadium (ii → iii). Accordingly, these grown discrete β particles may be connected and β rods would eventually form at the fully decomposed α plate boundaries (iii → iv). To differentiate with the primary α that formed during rapid cooling, the α phase appeared after decomposition should be named secondary α. Thus, the complete phase transformation path that is involved in SEBM processing of Ti-6Al-4V should be as follows: $S_{(powder)} \rightarrow L_{(melt)} \rightarrow \beta_{prior} \rightarrow \alpha' + \alpha_{primary} + \beta_{retained} \rightarrow \alpha_{secondary} + \beta$. This possible phase transformation path is derived from extensive microstructural observation and quantitative chemical and structural investigation on Ti-6Al-4V[181, 203, 220-222]. The phase transformation correlates well with the SEBM thermal cycling and Ti-Al-V phase diagram as well.

Additionally, the β volume fraction in 10 mm and 20 mm samples can be determined to be $3.5 \pm 0.5\%$ and $4.6 \pm 0.8\%$ from Figure 4.8. The enhanced β volume fraction with the increase in printing thickness is thought to be related with the larger thermal mass of thick sample. A large thermal mass enables SEBM builds to stay at a high temperature for some time, which has been verified by FEM simulations [221]. The SEBM build temperature of approximately 650 - 700 °C induces the main microstructural evolution to take place at $\alpha + \beta$ two phase field based on the Ti-6Al-x%V pseudo phase diagram. Therefore, a rising temperature would result in an increased volume fraction of β phase. It is worth noting that the β stabilizer of Fe that potentially diffused from the stainless-steel start plate could also significantly increase the volume fraction of β phase particularly for the base of an SEBM-built Ti-6Al-4V part. However, its influence is avoided in this work as the specimens for the APT detection were extracted at a printing height of ~20 mm away from the base. As β-Ti (bcc) is considerably softer than α-Ti (hcp) [223], the increase in β volume fraction would give rise to

material strength deterioration from a macroscopic view. It is worthwhile to point out that the effects of the lost aluminium due to vaporisation on the β phase was not considered in this study. Though since aluminium is an α-stabilizer it is hypothesise that the lost of aluminium will result in a greater percentage of the β phase.

Lastly, numerical simulation was used to investigate the decomposition of martensite. Temperature was extracted at three positions, namely, the top, the middle, and the bottom of the SEBM builds. The results are compiled in Figure 4.10. Starting from the "top" position (Figure. 4.10 (a)), the temperature profiles clearly show that the temperature inside the 20 mm, 10 mm, 5 mm and 1 mm samples decreases progressively in this order. This effect is due to two reasons. Firstly, the higher thermal capacity of a thicker sample allows it to retain more heat as compared to the thinner sample, because it has a larger mass. Moreover, thicker sample also have less time to cool down between successive scans, because the time required to scan thicker sample is longer. This trend is also visible by comparing the temperature in the middle of the samples (Figure 4.10 (b)), where again the thicker sample has a higher average temperatures than the thinner sample. However, a different temperature behavior is found at the lower part of the samples (Figure 4.10 (c)). This is due to the competitive effect of the different cooling time for each sample. In particular, the 20mm sample has the shortest time to cool down. Since the lower part of the sample is the farthest from the heat source, the heat simply did not have sufficient time to reach the bottom before the cooling time is over. Overall, Figure 4.10 shows that the average temperature is higher for thicker sample. This means that the kinetics of martensite decomposition into α and β is expected to be higher for thicker sample. On the other hand, the 1mm sample shows a relatively low temperature, indicating fast dissipation of heat into the powder. Therefore, the kinetics of martensitic decomposition is expected to be slow. This is the reason why some amounts of martensite are still retained inside the 1mm sample.

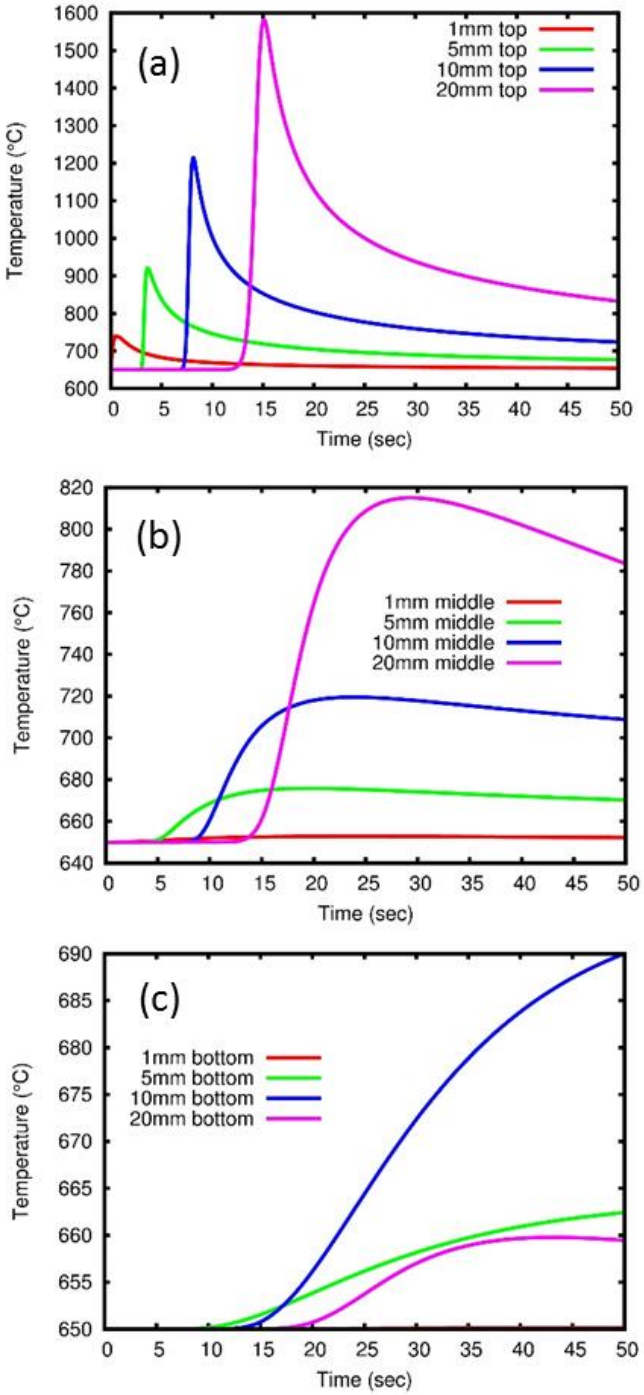

Figure 4.10 Temperature evolution curves with respect to time for different positions (a) top, (b) middle, and (c) bottom of the samples, respectively.

4.3.2 α/β interface evolution

SEBM-built Ti-6Al-4V could have superior tensile properties as compared to as-cast form largely owing to its fine Widmanstätten α/β microstructure. The Hall-Petch relation [224] can help to understand why the hardness or strength of SEBM-built Ti-6Al-4V samples will be decreased with increasing printing thickness; indeed the finer microstructure will lead to a higher strength. The higher strength obtained from the finer β spacing is due to more α/β interfaces in the microstructure contains. It was observed that dislocations were always first emitted from α/β interfaces in Ti-6Al-4V and plastic deformation started with dislocations emitted from there [225]. Moreover, α/β interface is believed to play the primary role in strengthening SEBM-built Ti-6Al-4V [181]. It thus becomes very necessary to study the characteristics of α/β interface in order to explain the printing thickness dependent properties from a microscopic viewpoint.

In order to quantitatively study the α/β interface, APT was used to analyze the specimen cut from the SEBM-built Ti–6Al–4V block samples. According to the mass-to-charge spectrum illustrated in Figure 4.11, the form of the interstitial elements, e.g. O, Fe, N, C, H etc. that exist in the initial pre-alloyed powder could be directly known. O mainly exists as TiO and it also combine with Al and H to form AlO and H_2O. Otherwise, the H_2O detected in Figure 4.11 might also be from the absorbed moisture. Fe and C will not react with other elements. N can exist either as element or compound of TiN and Ti_2N. H exists in the form of TiH and VH but it may mainly come from the analysis chamber of APT.

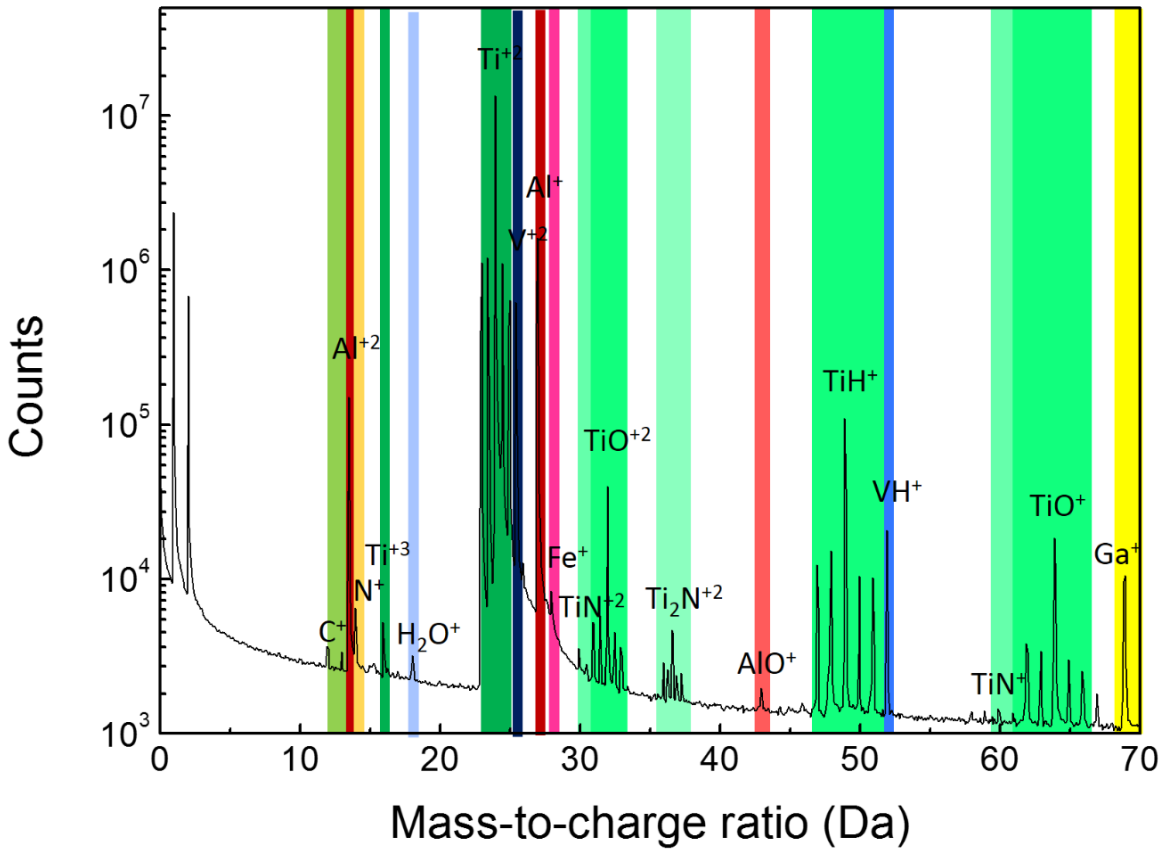

Figure 4.11 Mass-to-charge spectrum of an APT reconstruction volume showing the ions or complex ions detected in the sample of SEBM-built Ti-6Al-4V.

Figure 4.12 (a) shows a micro-tip specimen prepared by using FIB for APT analysis. The APT reconstruction volume shown in Figure 4.12 (b) was obtained from the apex of this micro-tip. For clarity, only three major elements, i.e. Ti, Al and V, were illustrated. As known, Al can stabilize α phase while V is a β stabilizer [226]. Moreover, it has been stated above that the microstructure of SEBM-built Ti–6Al–4V consists of fine β rods embedded into continuous α phase. Therefore, α and β phases could be indicated respectively in Figure 4.12 (b). Al and V are two major alloying elements in Ti–6Al–4V; meanwhile they exhibit obvious partitioning behavior as shown in Figure 4.12 (d) and (e), i.e. Al preferentially partitions to α phase while more V diffuses into the β phase. In addition to Al and V, Fe also exhibit an obvious partitioning to β phase. Based on the 16 at. % V iso-surfaces in Figure 4.12 (f), a proxigram was obtained in order to better reveal elemental partitioning behavior.

The values of 16 at.% V was chosen because it approximately lay midpoint of the V elemental concentrations between the α and β phases in the proxigram shown in Figure 4.8 c. Moreover, C and N almost homogeneously disperse into α and β phases. The α/β interface could be determined to be 1.8 ± 0.2 nm in terms of the Ti concentration profile. Of particular note is that obvious concentration gradients of V and Fe exist at both sides of the interface, which enables the interface width to extend 3.2 nm. Table 4.2 lists the accurate chemical compositions of α and β phases as well as the partitioning ratios of each element.

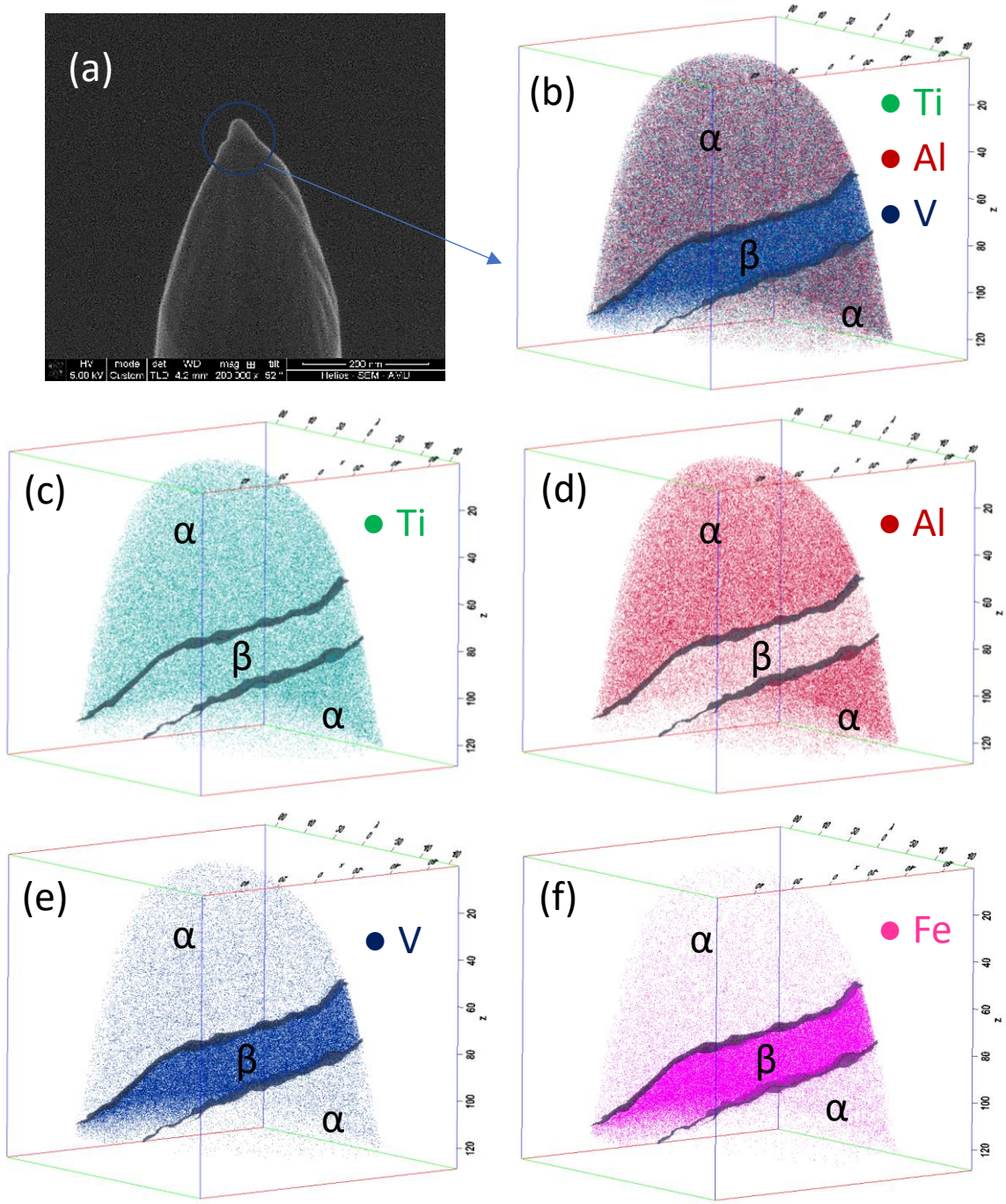

Figure 4.12 Identification of the partitioning of elements between the α and β phase via APT reconstruction volume. (a) SEM image showing a micro-tip specimen prepared by FIB for APT analysis. (b) An APT reconstruction volume showing α and β phases. 16 at. % V iso-concentration surfaces (isosurfaces) was adopted to delineate the α/β interface. (c), (d), (e) and (f) show the elemental distribution of Ti, Al, V and Fe in the APT reconstruction, respectively.

The partitioning ratio k (for α-partitioning elements) or k' (for β-partitioning elements) are defined as $k = C_\alpha/C_\beta$ or $k' = C_\beta/C_\alpha$; respectively. The larger than unity for k or k', the severer partitioning for the corresponding element. As seen in Figure 4.13 (b), a pair of parallel interfaces could be indicated by the 16 at.% V iso-surfaces. It is known that these two planes should be the flat sides of β rod, i.e. the coherent $\alpha_{(0001)}/\beta_{(110)}$ interface. Moreover, the accurate determination of α and β compositions in this work is thought to greatly facilitate the simulation on a α ↔ β phase transformation in additive manufacturing of Ti–6Al–4V by SEBM. To precisely measure the thickness of β phase, a region of interest (ROI) that vertically goes across the two parallel iso-surfaces was created. The thickness of β phase was determined to be ~25 nm according to the depth concentration profiles in Figure 4.13 (c).

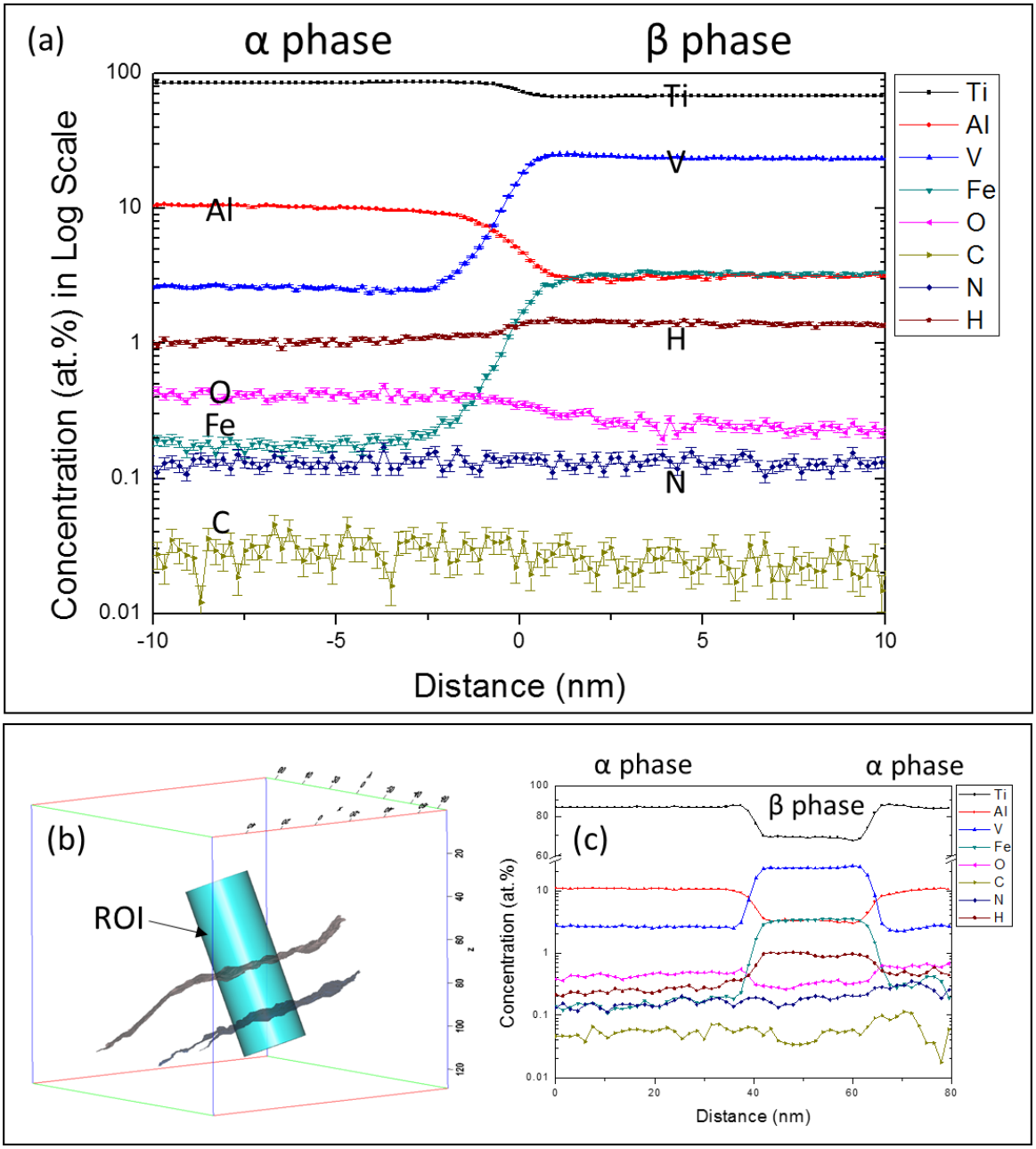

Figure 4.13 Identification of the element concentration across the α/β interface; (a) A proxigram showing the concentration profiles of alloying elements across the α/β interface delineating with a 16 at. % V iso-surface in the APT reconstruction in Figure. 4-11. (b) A region of interest perpendicularly passes through two 16 at. % V iso-surfaces in the APT reconstruction volume. (c) 1D concentration profile along the Z axis of ROI in (b).

4.4 Conclusions

The results demonstrates that α′ martensite was formed first in SEBM of Ti-6Al-4V regardless of printing geometries. Unlike other powder-based metal 3D printing methods, the martensitic phase is then decomposed into α/β microstructure depending on the subsequent thermal cycling history due to the elevated build temperature. This study have shown the formation and decomposition of α′-Ti martensite from quantitative structural and chemical information.

In terms of the general phase transformation path suggested in this study, it is possible to further modify the microstructure and optimize its comprehensive mechanical properties for SEBM-built Ti-6Al-4V parts by varying the printing temperature. It is possible to reduce the average beam current of SEBM process to achieve a lower printing temperature, for example, and thus obtains a mixed microstructure of (α′ + α/β) that is strong and tough.

In addition, quantitative microstructural characterization helps us understand the deteriorating strength with the increase in in-fill hatching thickness from a macroscopic view, namely, due to the increasing β spacing and β volume fraction. Moreover, quantitative examination of the elemental partitioning and segregation behavior at the α/β interface was conducted. The increasing α/β lattice mismatch and α/β interface width are believed to account for the strength degradation from the microscopic view.

Chapter 5: Heterogeneous microstructure and mechanical properties of SEBM-built Ti-6Al-4V parts

5.1 Introduction

After an understanding of the phase transformation process within SEBM-built Ti-6Al-4V was established in the previous chapter. An understanding of how it would affect parts with various thickness, 2D-planar geometry and build height was sought. This chapter thus focuses on the effects of build thickness on the microstructure and mechanical properties of SEBM-built Ti-6Al-4V. Prior literature has shown that there exists heterogeneity in the microstructure due to the different build thickness. This is due to the thermal cycling involving rapid solidification, high cooling in solid state and long-term annealing at a build temperature of 600 - 650 ^{0}C is involved layer by layer during the entire SEBM process. Thus, an out-of-equilibrium, very fine, and build geometry-dependent microstructure will be obtained in the as-built materials. It is thus easy to imagine that heterogeneous microstructure as well as the resulting heterogeneous properties would be formed in SEBM-built Ti-6Al-4V parts.

However, there is lesser focus on the microstructure and phase transformation that occurs with varying build thicknesses or geometries. An understanding of the microstructure transformation could deepen the understanding of microstructural heterogeneity in titanium AM components. Complex industrial parts like the impeller often consist of features with varying thickness. Thus, an investigation to observe the microstructure of SEBM-fabricated Ti-6Al-4V ELI with varying thicknesses was undertaken.

The result section of this chapter consists of three parts: (1) investigating the effect of build thickness on the microstructure and mechanical properties of SEBM-built Ti-6Al-4V, (2) investigating the effect of 2D-planar geometry on the microstructure and mechanical properties of SEBM-built Ti-6Al-4V and lastly (3) investigating the effect of build height on the microstructure and mechanical properties of SEBM-built Ti-6Al-4V.

5.2 Results

5.2.1 Effects of build thickness on the microstructure and mechanical properties of SEBM-built Ti-6Al-4V parts

After observing the microstructure of the SEBM-built Ti-6Al-4V parts in the preceding chapter, the study moved on to investigate and compare the microstructural differences between the various thickness dependent samples namely 1 mm, 5 mm, 10 mm, and 20 mm. Figure 5.1 (a), (b) and (c) show the wavy columnar prior β grains that are delineated by grain boundary α phase in the 1, 5 and 10 mm samples. The thickness of α platelet widens with increasing sample thickness as shown in Figure 5.2 (d), (e) and (f). Figure 5.2 shows the representative SEM image of the α/β microstructure in the thickness dependent samples. There is an obvious increase in β-interspace with increasing thickness in the four experimental samples.

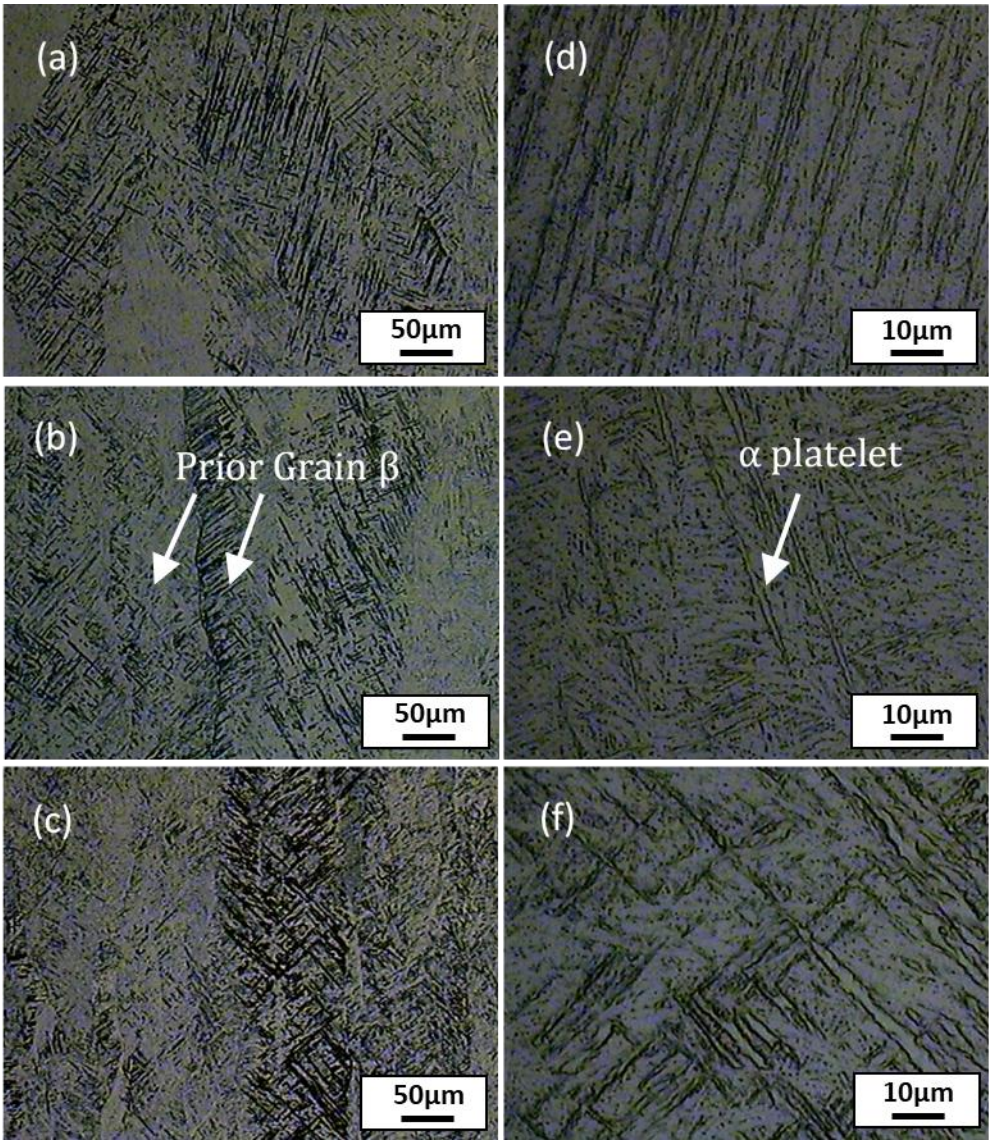

Figure 5.1 Optical micrograph images of the microstructure of SEBM Ti-6Al-4V of varying build thickness: (a) 1mm sample at 100x magnification (d) 1mm sample at 500x magnification (b) 5 mm sample at 100x magnification (e) 5 mm sample at 500x magnification (c) 10 mm sample at 100x magnification (f) 10 mm sample at 500x magnification. Scale bars for the micrographs taken at 100x and 500x magnifications were added in Figure 5.1 (c) and (d) respectively.

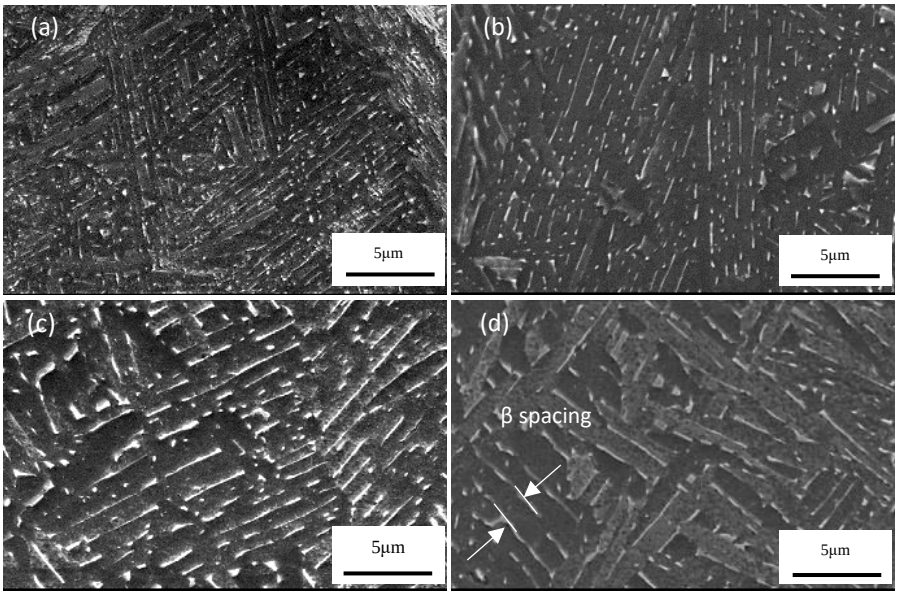

Figure 5.2 (a–d) Scanning electron microscopy (SEM) images showing microstructure of 1 mm, 5 mm, 10 mm and 20 mm samples, respectively. Scale bar = 5 μm. The martensitic microstructure can only be observed in 1 mm sample. β phase (in white) exhibits a morphology of discrete rod that embedded into continuous α phase (in dark). The distance between two facing arrows denotes β phase spacing. Obviously, microstructure becomes coarser with an increase in building thickness.

Table 5.1 lists the β interspace as well as the corresponding Vickers microhardness of the four samples. The microhardness decreases with increasing β phase spacing. This can be explained by the classical Hall-Petch relation [224, 227], i.e. the finer of the microstructure, the higher is the yield strength of the material. It is hypothesized that the α/β interface strengthening might play the primary role in determining the strength of SEBM-built Ti-6Al-4V which has a multiscale microstructure with cellular colony and basket-weave morphology [181]. Of particular note is that the duplex microstructure, i.e. the soft rod-like β phase homogeneously embedded in the continuous hard α phase, could provide good ductility to the SEBM-built titanium part.

Table 5.1 The β phase interspacing and Vickers hardness of the four experimental samples.

Sample	β-interspace (μm)	Vickers Hardness (HV)
1mm	0.283 ± 0.068	362.2 ± 6.0
5mm	0.463 ± 0.097	332.5 ± 4.6
10mm	0.610 ± 0.105	322.2 ± 5.4
20mm	0.813 ± 0.185	320.0 ± 4.9

A study by Lu et al. [228] also showed that there is a linear relationship among Vicker's hardness (HV), yield strength (σ_y) and ultimate tensile strength (σ_u) for Ti-6Al-4V, which is given by:

$$\sigma_y = 3.013H_V - 127.012 \quad \text{Eqn. 5.1}$$

$$\sigma_u = 3.586H_V - 237.900 \quad \text{Eqn. 5.2}$$

The estimated yield strength (879 MPa) and ultimate tensile strength (959 MPa) of the sample are comparable with wrought Ti-6Al-4V.

5.2.2 Effect of 2D-planar geometry on the microstructure and mechanical properties

After the initial investigation on the individual thickness-dependent samples, the microstructure and mechanical property of samples that were connected were studied. This led to the subsequent investigation that features a common block connecting the different fin thicknesses as shown in Figure 3.5. Additionally, two different fin structures were fabricated namely the straight-finned and the curve-finned structures. They were used to investigate the effect of 2D-planar geometry on microstructure and mechanical properties. The schematic of the samples is discussed in greater detail in Chapter 3.

Figures 5.3 and 5.4 show a typical α/β duplex microstructure in the straight-finned structures and the curved-finned structures respectively, where the dark region is the α phase that was etched out by the Kroll's reagent while the rod-like β phase is the bright region [27].

There are two types of transformed α/β structure inside the prior-β grain, namely the colony and the basket-weave morphology. It is observed that the continuity of the microstructure morphology is also more evident in the straight-finned structure as compared to the curve-finned structure from Figure 5.3 and 5.4. Additionally, it can be observed that the β-interspace in the 1 mm thick curve-finned structure are coarser as compared to the 1 mm thick straight-finned structure. The presence of α-bulges in the curve-finned structure is also lesser. This observation is supported by Vicker's hardness measurements plotted in Figure 5.7 which indicates that the curve-finned structure is approximately 10 Hv softer as compared to the straight finned structure.

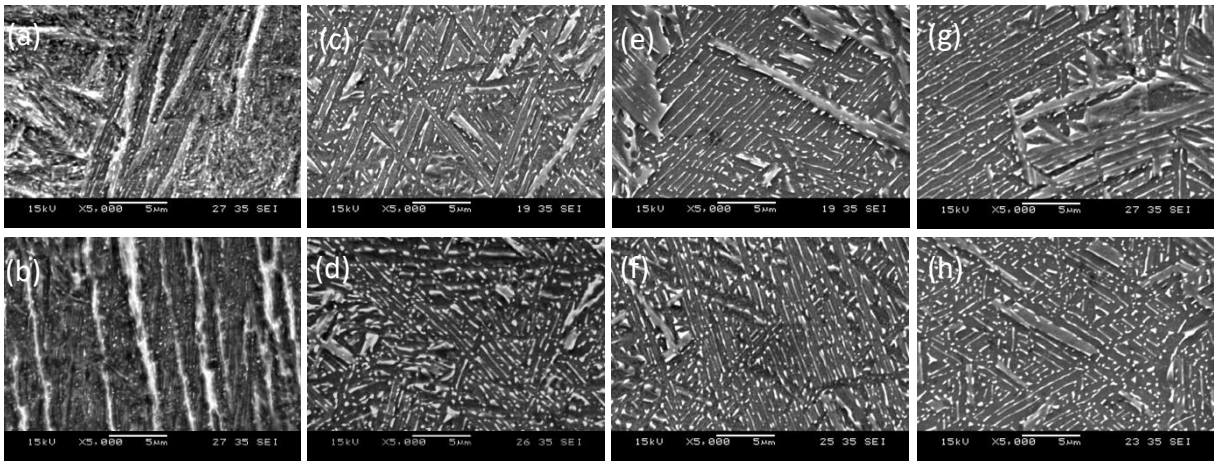

Figure 5.3 SEM images of the microstructure in the straight-finned part for position 2 and 4: (a) and (b) 1mm, (c) and (d) for 5mm, (e) and (f) for 10mm, (g) and (h) for 20mm straight-finned structures, respectably.

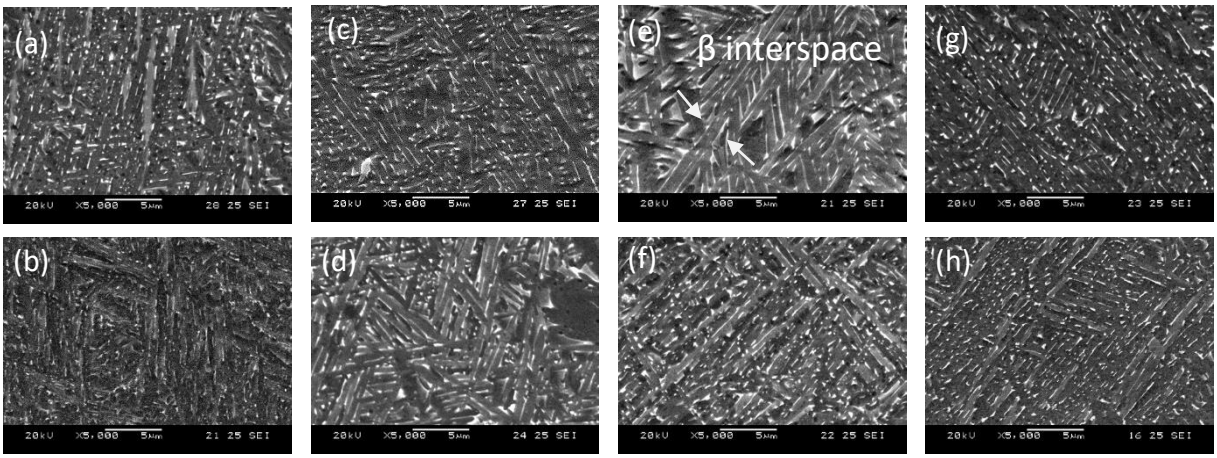

Figure 5.4 SEM images of the microstructure in the curved-finned part for position 3 and 4: (a) and (b) for 1mm, (c) and (d) for 5mm, (e) and (f) for 10mm, (g) and (h) for 20mm curve-finned structures.

Figures 5.5, 5.6 and 5.7 plot the β interspace, prior β columnar grain width and the Vickers microhardness of the various samples respectively. The microhardness values obtained from both finned structures for the four thicknesses, ranging from 1 to 20 mm decreases from 350 HV to 330 HV as shown in Figure 5.7. There is also an increase in β interspace and prior β columnar grain width of 0.2 to 0.7 μm and 35 to 50 μm, respectively as shown in Figure 5.5 and 5.6. The good correlation between microhardness values and β interspace is in good agreement when compared with the previous study on the individual thickness-dependent samples. It is worthwhile to note that when compared to the individual thickness dependent samples, the samples in this study exhibit a finer β interspace. This suggests that the connecting block acts as a heat sink and increases the cooling rate experienced by the sample.

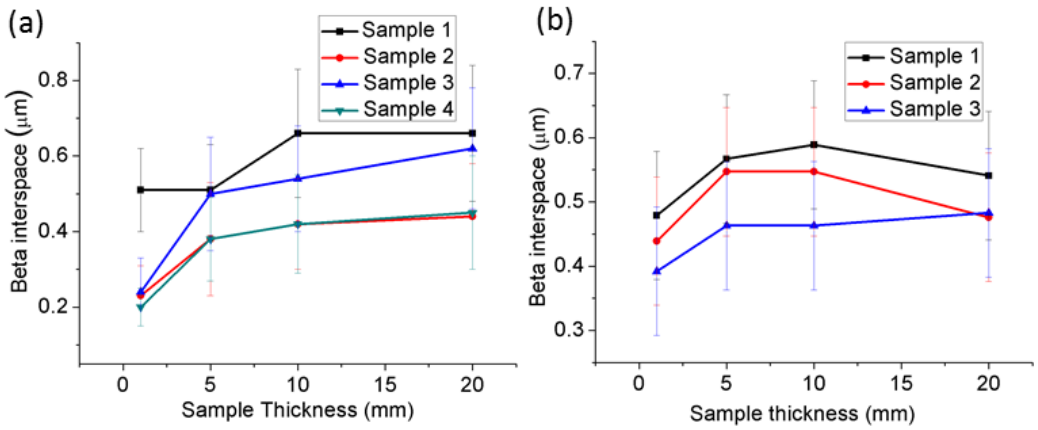

Figure 5.5 Plots of the average β interspace (μm): (a) straight-finned structure and (b) curved-finned structure.

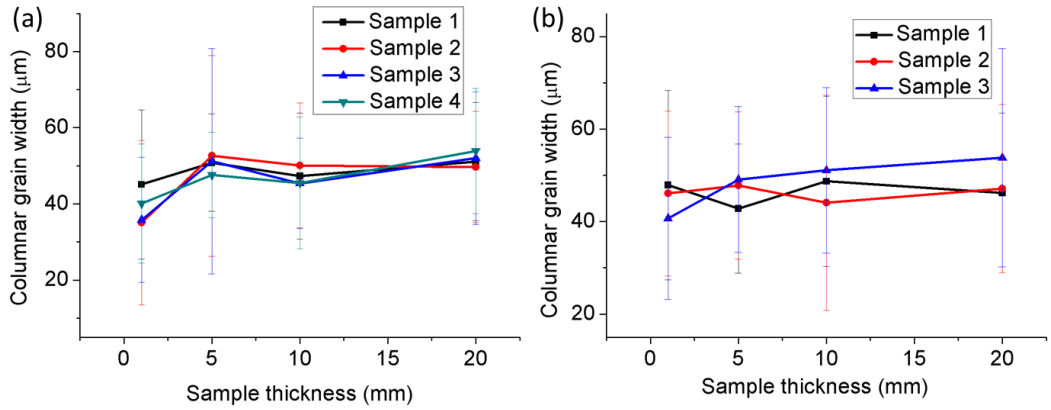

Figure 5.6 Plots of the average prior β columnar grain width (μm) of the (a) straight-finned structure and the (b) curved-finned structure.

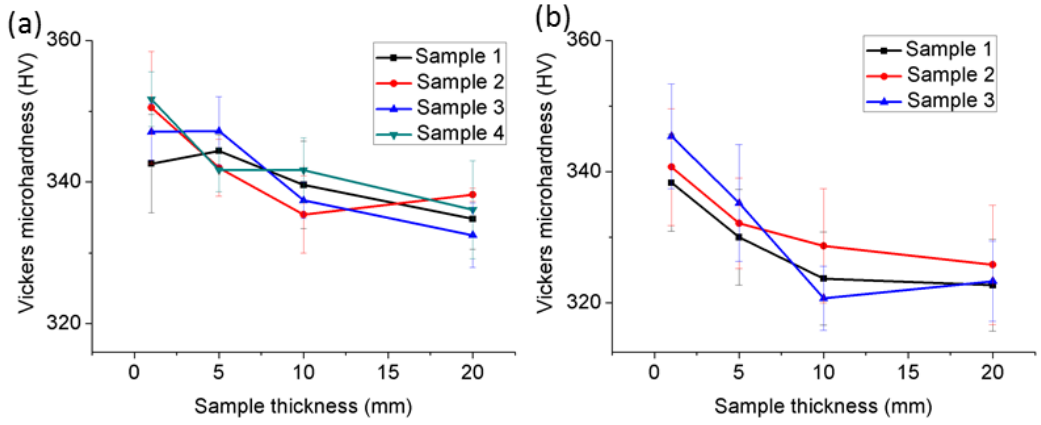

Figure 5.7 Plots of the average Vickers microhardness (HV) of the (a) straight-finned structure and the (b) curved-finned structure.

5.2.3 Effect of build height on the microstructure and mechanical properties

In order to quantitatively investigate the effect of build height on the microstructure and microhardness, samples were analyzed via SEM and tested via Vicker's microhardness methods. Figure 5.8 (a), (c), (e) and (g) show the α/β duplex microstructures of 10 mm-4, 10 mm-3, 10 mm-2 and 10 mm-1 samples at the X–Z plane, respectively. For uniformity, all microstructures were taken from the mid-line area of each tensile test piece. The size distribution histograms in Figure 5.8 (b), (d), (f) and (h) show that β interspace continuously increases with the build height. The average β interspace of 10 mm-1, 10 mm-2, 10 mm-3 and 10 mm-4 are 0.58 ± 0.11 µm, 0.66 ± 0.16 µm, 0.74 ± 0.14 µm and 0.77 ± 0.20 µm, respectively.

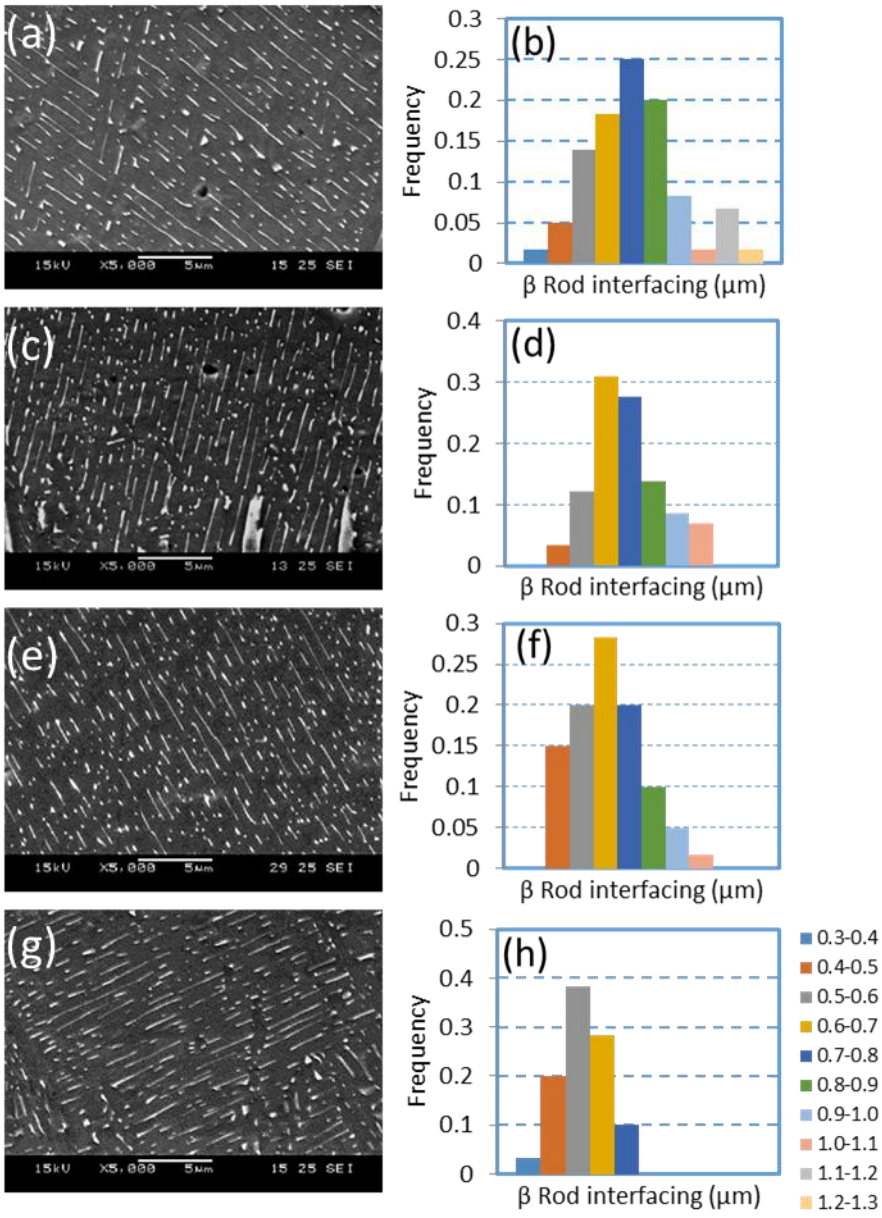

Figure 5.8 SEM images showing the α/β duplex microstructure as well as the corresponding β rod interspacing distribution histograms of (a) and (b) for 10mm-4, (c) and (d) for 10mm-3, (e) and (f) for 10mm-2, (g) and (h) for 10mm-1 samples.

Figure 5.9 shows that the prior β grain width gradually increases with build height, i.e. an average width of 42.77 ± 14.52 μm, 46.85 ± 13.46 μm, 54.77 ± 20.15 μm and 56.82 ± 13.73 μm in 10 mm-1, 10 mm-2, 10 mm-3 and 10 mm-4 samples, respectively. Both of β interspace and β grain width increase as the build layer increases. As a result, cooling rate is higher at the build bottom, and it would constantly decrease with rising build height. It is clear that graded

microstructure occurs along the build direction for SEBM-built Ti–6Al–4V. In general, the mechanical properties of engineering materials depend on their microstructure. Therefore, graded mechanical properties will be produced as a result of a graded microstructure.

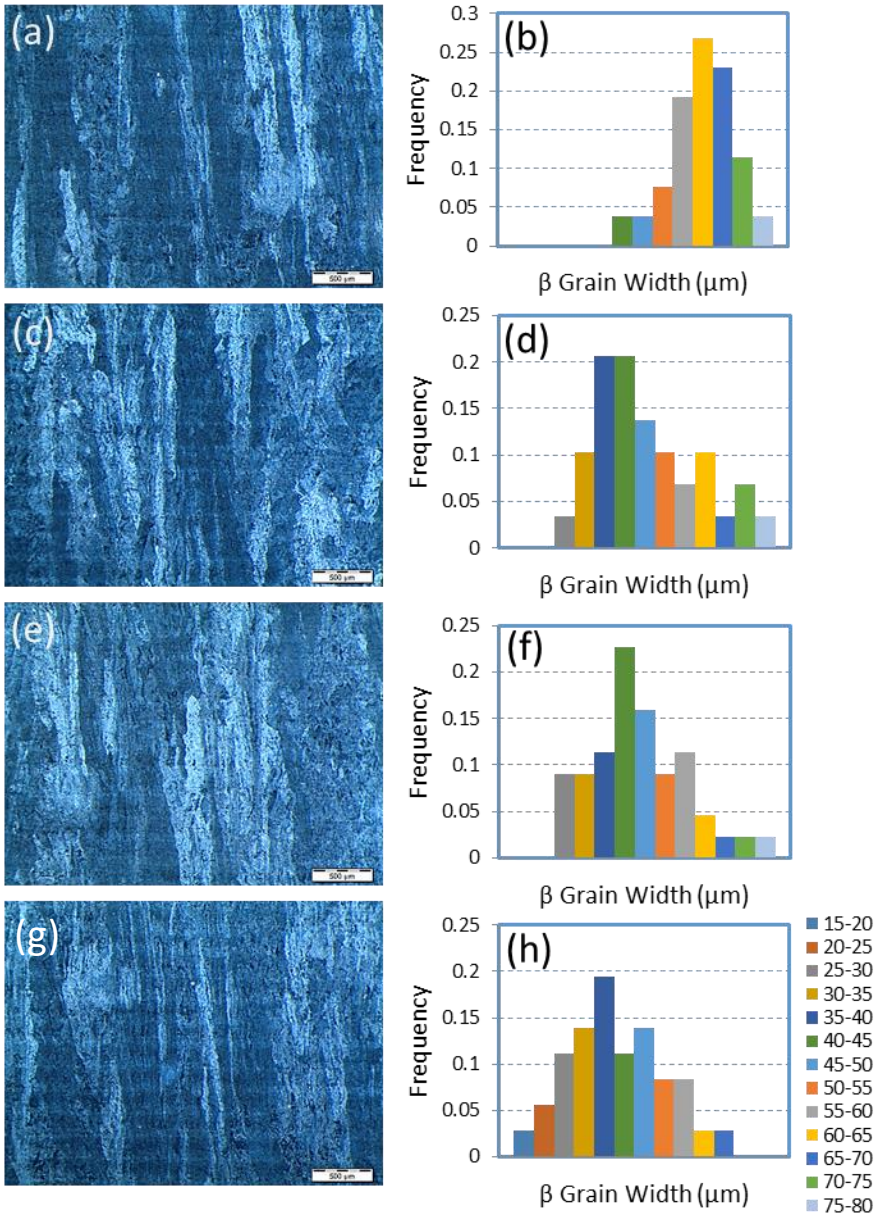

Figure 5.9 OM images showing the columnar prior β grains as well as their corresponding width distribution histograms of (a) and (b) for 10mm-4, (c) and (d) for 10mm-3, (e) and (f) for 10mm-2, (g) and (h) for 10mm-1 samples.

In order to verify the graded mechanical properties of SEBM-built Ti–6Al–4V, microhardness and tensile tests were carried out on the 10 mm-1, 10 mm-2, 10 mm-3 and 10 mm-4 samples. The Vickers microhardness of these four samples are 327 ± 5 HV, 324 ± 5 HV, 322 ± 7 HV and 319 ± 5 HV, respectively. The results show that the microhardness continuously decreases with increase in build height. Furthermore, the tensile strength decreases with increasing build height as shown in Table 5.2, i.e. all the yield strength, the ultimate tensile strength and elongation decrease. It is also confirmed that a graded microstructure as well as resulting graded mechanical properties take place along the build direction for SEBM-built Ti–6Al–4V. Figure 5.10 (a) shows that the microstructure and mechanical properties obeys the Hall-Petch's relationship. Figure 5.10 (b) shows that there is an increase in strain hardening exponent with an increase in build height.

Table 5.2 Tensile properties of four SEBM-built Ti-6Al-4V samples with different build heights.

Specimen	Yield Strength (0.2% offset) (MPa)	Ultimate Tensile Stress (MPa)	Elongation (%)
10mm-4 (Top)	823.3	934.0	12.5
10mm-3	828.2	938.7	13.5
10mm-2	845.3	949.4	14.0
10mm-1 (Bottom)	857.6	964.2	15.5

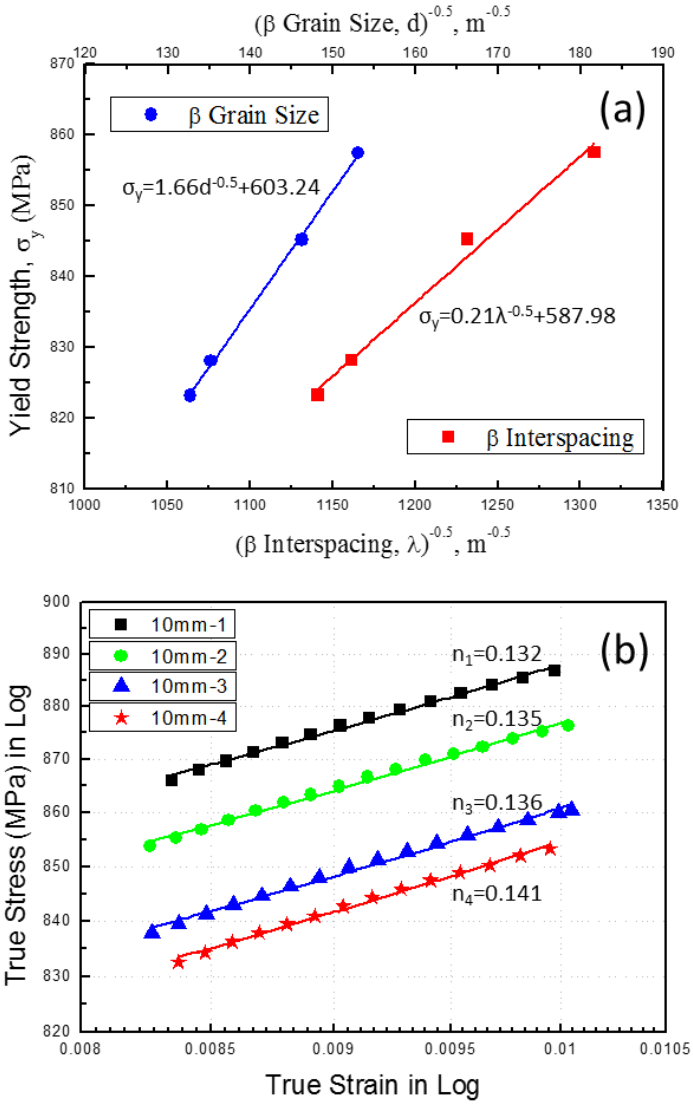

Figure 5.10 Plots of the yield strength against the β interspace and True stress against True strain at varying build height; (a) Variation of average yield strength σ_y with inverse of square root of average prior β grain size (d) and average β rod interspacing (λ). (b) True stress-true strain curves for the plastic response of the four SEBM-built samples, plotted on logarithmic axes. The measured power-law strain hardening exponents and strength coefficients are indicated for each sample.

Additionally, a region containing near-equiaxed prior β grains with a height of 250 μm (5 layers) is clearly observed at the bottom (Figure 5.11). An equiaxed-to-columnar transition for the prior β grains occurs due to the variation of solidification conditions (e.g. thermal gradient and solidification rate) in melt pool. The SEM observation of microstructure shows that β phase would become increasingly

discontinuous with build height in the initial tens of layers. It indicates that different volume fractions of β phase are retained, which depends on the temperature within the two-phase region as illustrated in the vertical section of the Ti-6Al-xV phase diagram [229]. The lower the terminate temperature of the rapid cooling process, the lesser the amount of β phase retained. In practice, the bottom part, i.e. the observed equiaxed-to-columnar transition region that directly built on the start plate, will be removed once a build is completed. Nevertheless, this equiaxed-to-columnar transition phenomenon could give a major clue for precise control of SEBM-built microstructure.

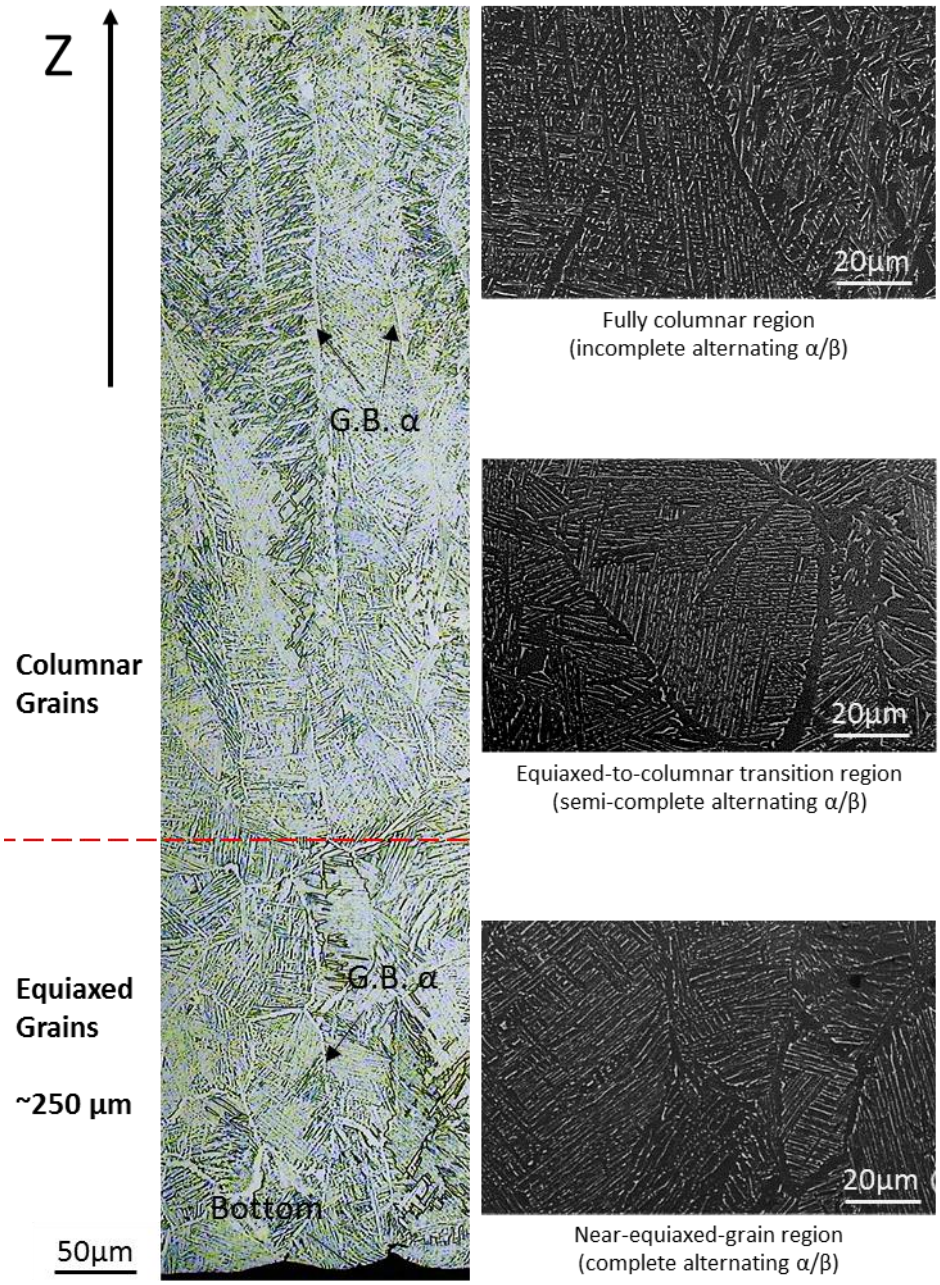

Figure 5.11 OM micrograph showing the Equiaxed-to-columnar transition of prior β grains at the initial tens of layers. SEM micrographs showing the alternating α/β evolution with the build height.

5.3 Discussion

5.3.1 Thickness dependent microstructure and mechanical properties

The adoption of metal AM to fabricate functional end use parts is becoming a reality. Such industrial parts used in the aerospace or biomedical applications often consist of features with varying thickness. Most initial efforts focused on optimizing the process parameters to obtain near-fully dense parts; lesser focus was put on understanding the anisotropy and heterogeneity of microstructure and mechanical properties of SEBM-built metallic parts. As such, the investigation of the thickness dependence of microstructure and mechanical properties of SEBM-built metallic parts is significant in promoting greater understanding of the heterogeneity in the microstructure and mechanical property in SEBM-built Ti-6Al-4V. The quantitative characterization of the 2 sets of thickness-dependent samples (individual and connected) is also novel.

SEBM is a selective melting process where each molten pool may experiences a different cooling rate and annealing duration depending on its spatial location and the part geometry. The three main paths that heat are lost in the SEBM process are: (i) radially through the surrounding sintered powder, (ii) vertically downwards through the built plate via conduction and (iii) vertically upwards from the top layer via radiation towards the ambient. Thus, the thin structures in the sample will likely experience a higher cooling rate due to a higher surface area to volume ratio allowing heat lost to the surrounding powder and to previously deposited layers. A FEM simulation model of the thermal history in the various thickness-dependent samples shown in Figure 4.10 indicates that the temperature profiles inside the thicker sample have higher average temperature as compared to thinner sample. Thus, the different temperature profiles could explain the difference in β interspace seen in the 1 mm, 5 mm, 10 mm and 20 mm thick straight-finned structures.

The microstructure becomes finer with reducing build thickness, i.e. both prior β grain width and β rod interspacing decreases. A mixed microstructure of alternate α/β with acicular α' martensite is observed inside the 1mm sample, while only fully decomposed alternate α/β microstructure is observed inside the 5 mm, 10 mm and 20 mm samples. In addition, numerous micro-twins occurred inside both the α and α' phases. The Vickers microhardness increase with decreasing β-interspace. This can be explained by the classical Hall-Petch relation [224, 227], i.e. the finer of the microstructure, the higher the yield strength of the material. It is found that the α/β interface strengthening plays the primary role in determining the strength of SEBM-built Ti-6Al-4V that possesses a multiscale microstructure with cellular colony and basket-weave morphology [181]. Of particular note is that the highest microhardness obtained in the 1 mm sample is not only due to its finest β phase spacing but also the retained α' martensite. As an extremely high cooling rate is involved in the SEBM process, very fine β spacings are observed in this work. As a result, SEBM-built Ti-6Al-4V will exhibit a high strength with ultrafine microstructure. Moreover, the duplex microstructure, *i.e.* the soft rod-like β phase homogeneously embedded in the continuous hard α phase, could provide good ductility. As we know, α' martensite is very hard, which gives high strength but low ductility. It was previously accepted that martensite could be avoided in SEBM-built Ti-6Al-4V via an elevated build temperature. However, it has also been pointed out that the Ti-6Al-4V microstructure containing a mixture of α and α' will have superior mechanical properties [230]. If the control over microstructure can be achieved for SEBM-built Ti-6Al-4V, *e.g.* obtaining a mixed microstructure of α/β and α', this could further improve its mechanical properties.

Lastly, the effect of build thickness not only influence the microstructure morphology and mechanical properties, but it also influences the phase constitution in the material as well. XRD and APT analysis show that the β-phase content increases with build thickness as well. Though the influence of the increased β-phase content has not been quantitatively investigated

it is likely that it will improve the ductility of AM Ti-6Al-4V. Additionally, the XRD profiles previously shown in Figure 4.5 inset ii shows that the $(0002)_{\alpha}$ peak width tends to tends increase with the increase in build thickness. This suggests that the mean crystal size gets smaller with increasing build thickness.

In summary, it can be said that the microstructure of SEBM-built Ti-6Al-4V is metastable and that there is a microstructure evolution phenomenon that occurs during the fabrication process that has significant influence on the microstructure morphology and mechanical properties.

5.3.2 2D-planar geometry on the heterogeneous microstructure and mechanical properties

Apart from understanding that the effects of build thickness on the heterogeneous microstructure and mechanical properties are due to the different thermal mass that each sample had, the author also wanted to understand the synthetical influence of build geometry and in-fill hatching strategy on the two types of fin structures.

It was observed that the curve-finned structure has a coarser, less complete and irregular α/β morphology microstructure than the straight-finned structure. A possible reason for the coarser microstructure may be due to its greater cross-sectional area as compared to the straight-finned structures. Thus, the thermal input is greater. This difference in the cross-sectional area affects the hatch length used in each of the finned structure. It can be observed from Figure 5.12 that a longer hatch length is performed in the curve-finned sample as compared to the straight-finned sample. It is known that in the SEBM process the longer the hatch length, the higher the beam current applied to ensure sufficient thermal input to the hatch. This increase in thermal input within the curve structure results in an increase in annealing temperature and time, which in turn leads to a coarser microstructure [231] as compared to the straight finned structure.

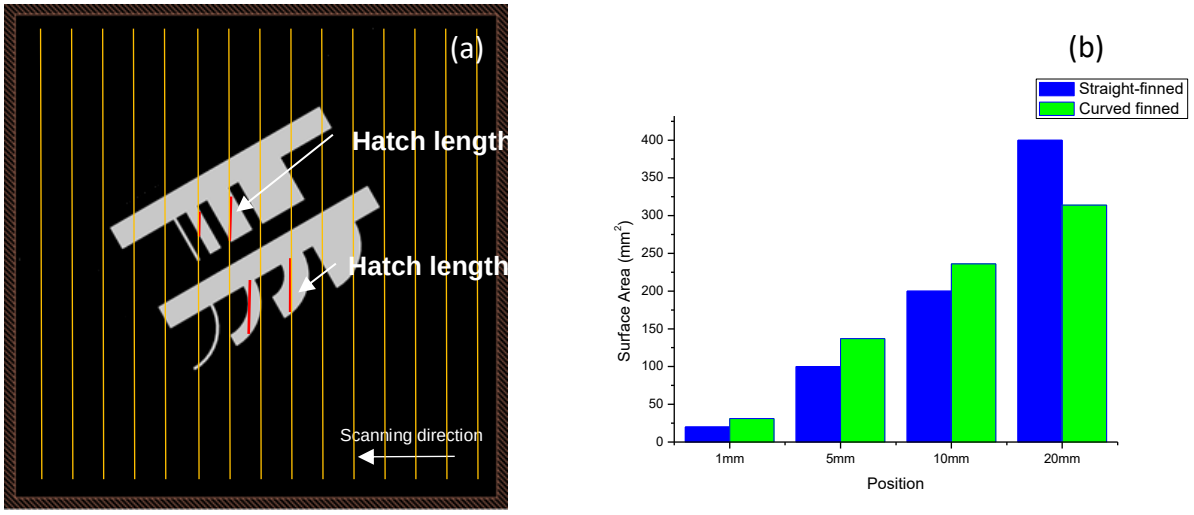

Figure 5.12 Difference in hatch length and hatched surface area between the straight-finned and curved-finned part; (a). Schematic of the different scan line length between the straight-finned structure and the curved-finned structure (b) Surface Area of the fin structure region (mm^2)

Additionally, the curve-finned structure sample is observed to have a less complete and irregular α/β morphology microstructure as compared to the straight-finned structure. It indicates the difference in the volume fraction of the β phase retained in the curved finned structure as compared to the straight finned structure. The higher the terminate temperature of the rapid cooling process, the greater the amount of retained β phase and a complete α/β morphology microstructure is likely to be observed [181]. Thus, a reason for the lower terminate temperature by the curve-finned structure is likely due to the greater surface area (at the side) of the fin structure being exposed to the partially sintered powder bed. The heat flow of the straight-finned structure is also more consistent and direct towards the neighbouring fins thus a higher terminate temperature can be assumed as can be seen in Figure 5.13. FEM simulation was performed to study the thermal history of the two type of parts. The simulation enables a study on the thermal flux within the two parts with relevant thermal boundaries associated with the SEBM process. The thermal simulation as shown in Figure 5.13 shows both the heat flux and the heat flow direction within the two parts and correlates well with the

experimental findings. The heat flux and heat flow of the curve-finned part are larger and more inconsistent as compared to the straight-finned part which could lead to a lower terminate temperature and more irregular α/β morphology.

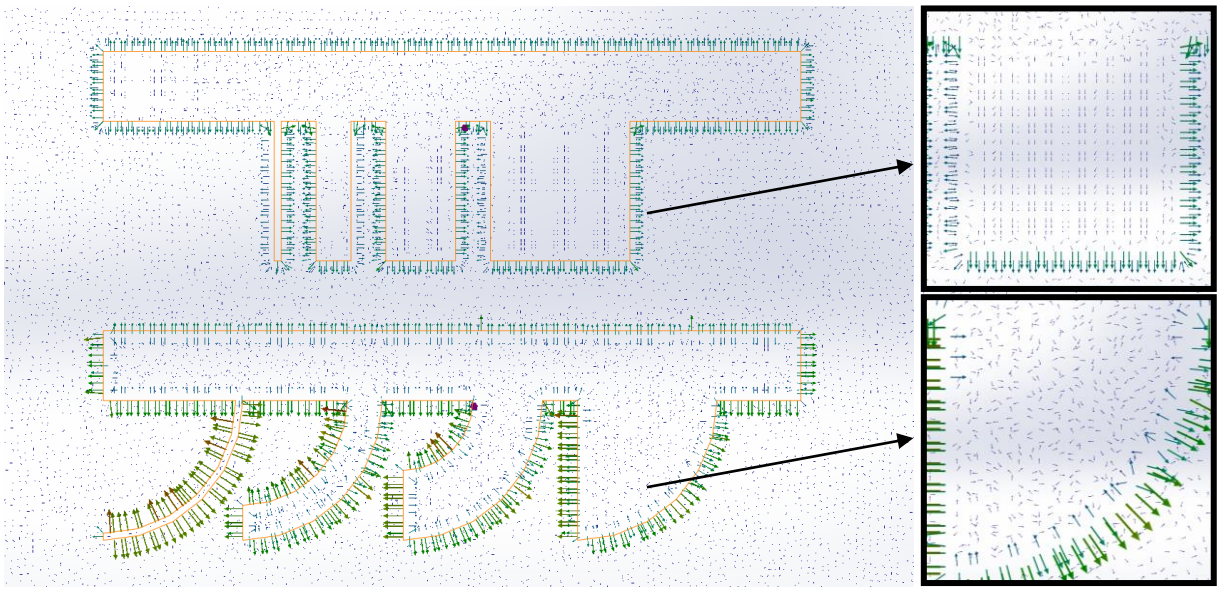

Figure 5.13 Schematic of the heat loss direction from the straight-finned and curve-finned part. (The scale of the arrow represents the heat flux, and the direction of the arrow represents the heat flow.)

In summary, the effects of sample build geometry and in-fill hatching strategy on the as-built microstructure are the presence of martensitic phase in the 1 mm straight-finned structure as compared to the partially decompose martensitic phase observed in 1 mm curve-finned structure. Vickers micro-hardness and β interspace results between the two finned structures are also different. The differences in the completeness of the α/β morphology are also observed.

5.3.3 Graded microstructure and mechanical properties

The study on the effect of build height on the microstructure and mechanical properties shows that β interspace increases with the build height and a corresponding decrease in tensile properties. The following section will to discuss the phenomenon behind the results.

The thermal process of SEBM is very complex as electron beam is the only heat source that is involved in a complicated relationship between maintaining a constant build temperature and melting. In any SEBM setup there are two major heat losses: the heat radiation from the top surface and the heat conduction through the sintered powder from the surrounding surface of the part and start plate. Since only a low pressure of 2.0×10^3 mbar is maintained during melting via introducing high pure He into the high vacuum build chamber, the heat loss due to convection could be neglected. Infrared (IR) imaging technique has been increasingly employed for in-situ surface temperature measurements and build flaws detection [232]. Unfortunately, it is challenging to monitor the temperature distribution inside SEBM-built parts. Temperature was only measured by a thermocouple mounted at the bottom of start plate and it was not used in any feedback due to practical reasons. The measured temperature was plotted versus time in Figure 5.14 for the entire SEBM build process of horizontal Ti–6Al–4V blocks. The temperature during melting process can be divided into three stages: (1) a sharp decrease, (2) a slow increase and (3) an appropriate constant.

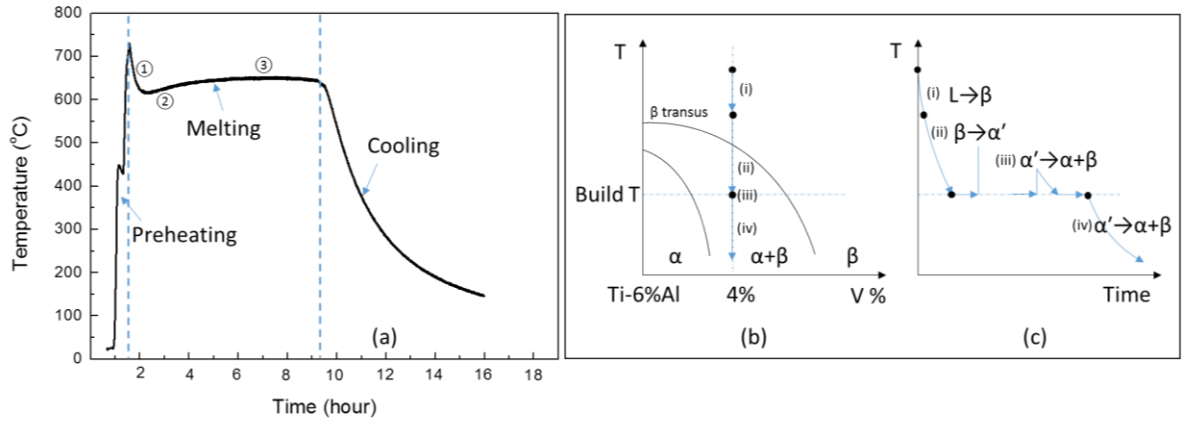

Figure 5.14 Plots of the temperature measured during the SEBM process and the phase transformation sequence of SEBM-built Ti-6Al-4V; (a) Plot of the temperature (measured by a thermocouple beneath start plate) against the time taken during the entire SEBM build process. (b) Schematic phase diagram of Ti-6Al-4V and (c) simplified thermal process showing the four main phase transformation processes involved in SEBM-built Ti-Al-4V.

The heat transfer (q) by thermal conduction and radiation is given by [233]:

$$q = -kA\frac{\partial T_1}{\partial x}t + \sigma eA\partial T_2^4$$

Eqn 5.3

where k is the thermal conductivity of materials (k = 14.1 W m^{-1} K^{-1} for Ti–6Al–4V at 650 °C [24]), A is the cross-section area (A = 1.0×10^{-3} m^2), δT_1 is the temperature difference between top surface and bottom part, δx is the build height, t is the build time, σ is the Stefan–Boltzmann constant, e is the emissivity (unity for a black body), and δT_2 is the temperature difference between top surface and ambient. Therefore, the heat transfer rate δq/δt, which directly reflects the cooling rate, could be derived as:

$$\frac{\partial q}{\partial t} = -kA\frac{\partial T_1}{\partial x}$$

Eqn 5.4

Here, it is assume that the temperature of the melt pool (top surface) is constant as the heat provides by an electron beam to melt powder bed is supposed to be fixed for each built layer with the same cross geometry. Moreover, the melting as well as the subsequent heat radiation from the melt pool to the ambient are completed immediately due to the fast scan velocity of the electron beam and high vacuum. Provided that the heat loss through radiation from the melt pool to the ambient is invariable for each layer, the heat loss due to radiation could be assumed to be independent of time and build height. For stage (1) in Figure 5.14 a, corresponding to the very bottom part (1 - 2 mm in height), both δT_1 and δx increase, hence the variation of cooling rate was not known. For stage (2), δT_1 decreases and δx increases, as a result that the cooling rate decreases. For stage (3) δT_1 remains constant while δx continuously increases, consequently the cooling rate will continue falling down.

On the other hand, a slow cooling rate will definitely result in a coarse microstructure. Thus, it explains the microstructural variation mentioned earlier, i.e. the prior β grain width and the β rod interspace gradually increase with the build height. A schematic of the columnar grain growth is shown in Figure 5.15.

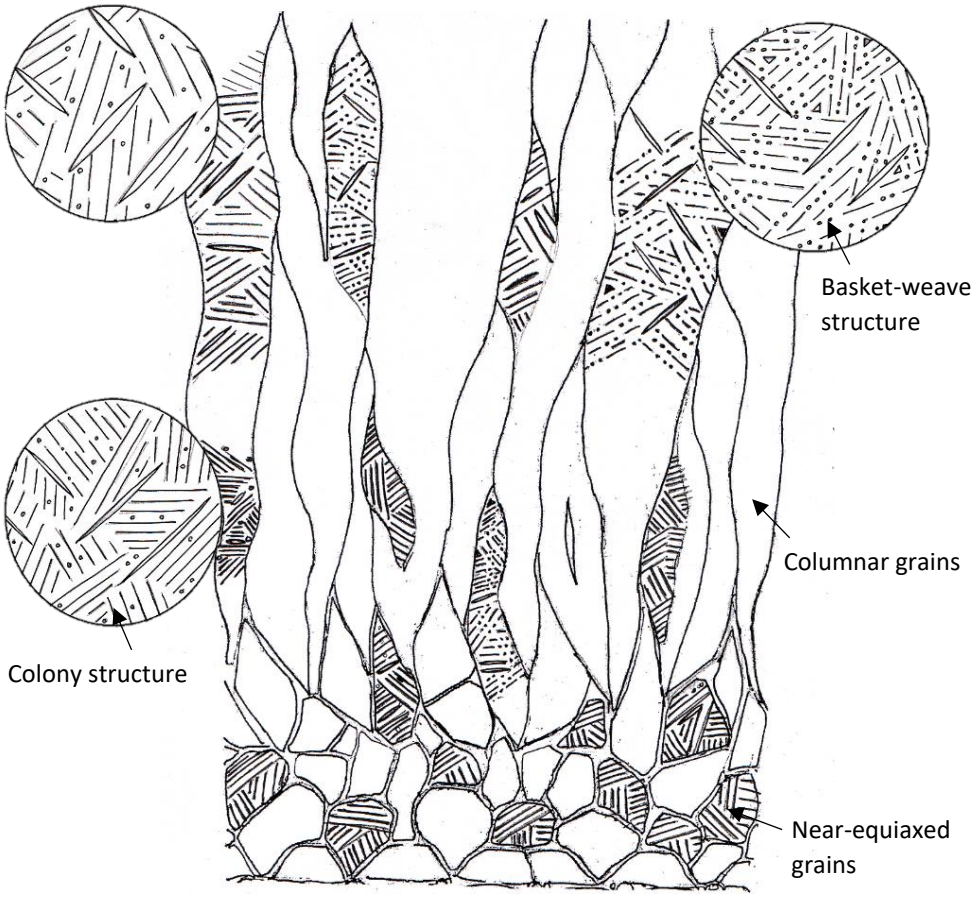

Figure 5.15 Schematic microstructure of SEBM-built Ti-6Al-4V on X-Z plane

5.4 Conclusions

In summary, this chapter presents and discusses the results regarding the effects of various build geometries (e.g. thickness, shape, and height) on the microstructure and mechanical properties of SEBM-built Ti-6Al-4V parts.

Firstly, Ti-6Al-4V parts with different thicknesses were built using SEBM in order to investigate its build thickness-dependent microstructure. A mixed microstructure of alternate α/β with acicular α' martensite is observed inside the 1mm sample, while only fully decomposed alternate α/β microstructure is observed inside the 5 mm, 10 mm and 20 mm samples. In addition, numerous micro-twins occurred in both α and α' phases. It is found that β phase spacing increases with the build thickness. Meanwhile the microhardness decreases accordingly.

FEM simulations to investigate martensitic formation and decomposition also show that thicker sample has an higher average temperature compared to thinner sample, thus suggesting a faster kinetic for martensite decomposition for thicker sample. This in turn, depends on the combined effect of longer scan time, higher thermal mass, and shorter cooling time for the thicker sample as compared to the thinner sample.

Secondly, a microstructural characterization study on the synthetical influence of build geometry and in-fill hatching strategy on SEBM was carried out. Based on the experimental results, it can be concluded that the selective melted geometry and in-fill hatching strategy have significant effect on the microstructure of as-SEBM-built Ti-6Al-4V parts. The effect can be observed from the amount of martensitic phase between the curve and block parts and the microstructure, morphology and mechanical property variation among the different structures with different thicknesses. FEM simulation was also performed to study the thermal history of two types of parts. The thermal simulation as shown in Figure. 5.13 showed that the heat flux and heat flow of the curve-finned part are larger and more inconsistent as compared to the

straight-finned part which could lead to a lower terminate temperature and more irregular α/β morphology respectively. The thermal simulation correlates well with the experimental findings.

Lastly, the microstructure and mechanical properties of as-built Ti-6Al-4V ELI by SEBM were systematically investigated with varying build height. Based on these experiments, the following conclusions can be drawn:

1. Graded Ti–6Al–4V microstructure including varying prior β grains and β phase interspace is seen, i.e. near-equiaxed prior β grains as well as equiaxed-to-columnar transition region at the initial several build layers and the subsequent columnar prior β grains with increasing grain width and β rod interspacing. The coarser columnar microstructure mainly arises from the decreasing cooling rate. In addition, an increasingly pronounced strain hardening effect is observed with increasing build height as the previously built layer is subjected to a longer annealing as compared to the subsequent layer.

2. Graded mechanical properties of Ti-6Al-4V with degraded microhardness and tensile properties are observed from bottom to top, i.e. decreasing microhardness, yield strength and ultimate tensile strength and elongation as the build height increases. A good agreement with the Hall– Petch relation indicates that the graded property takes place mainly due to the graded microstructure. In addition, the α/β interface strengthening is found to play the primary role in determining the strength of SEBM-built Ti-6Al-4V that possesses a multiscale microstructure with cellular colony and basket-weave morphology. Nevertheless, β grain refinement strengthening seems to be more effective as the prior β grain boundaries could absorb a higher amount of dislocations in comparison with α/β interfaces.

Chapter 6: Anisotropic columnar grain growth in SEBM-built Ti-6Al-4V parts

6.1 Introduction

The understanding of the phase transformation and the microstructure of the as-built SEBM Ti-6Al-4V provides a good perspective of the heterogeneity that exists in the material. Additionally, anisotropy has been reported to exist in metal AM materials as well. As such it is of interest to study the columnar grains which are often reported to be the cause of anisotropy in metal AM materials. The dominant microstructure morphology in metal AM is the columnar grain. In order to optimize the mechanical properties of as-SEBM-built metals and alloys, the study of the commonly observed columnar grains in SEBM process is important as it has a direct influence on the macroscale mechanical properties as well. Additionally, the investigation of the columnar grain growth behaviour can also give new insights into the grain selection phenomena that is significant to the ultimate microstructure.

The classical model for competitive grain growth was first proposed by Walton and Chalmers [71]. The theory states that a dendrite well-oriented with the temperature gradient direction will overgrow a less favorably oriented dendrite. Though experimental studies based on directional solidification experiments have challenged the classical model for competitive grain growth [234-236]. Simulation-based studies using phase-field (PF) models have revealed that misoriented grains might be eliminated much slower than expected based on the classical model or even eliminate better-oriented grains [237, 238]. A prior study based on SEBM-built Ti-6Al-4V has shown that there exists grain competition between the grains formed due to the bulk and contour scanning parameters that follows the classical model [92]. Though thermal history experienced by a sample of a taller build height (e.g. 100 mm) is suspected to be different from that of a shorter build height (e.g. ~20mm) used in the prior study due to the different paths where heat is lost. Recent simulation-based research has also simulated the grain

structure evolution during powder-bed fusion AM and showed that the simulated grains grow followed by the classical rule of grain selection [239]. It is, therefore, important to investigate the effects of build height on the microstructure and mechanical properties of SEBM-built Ti-6Al-4V.

This chapter presents the study on the columnar grain growth during the SEBM of Ti-6Al-4V. The author will then discuss the build height dependent microstructure and mechanical property followed by the grain selection phenomenon that occurs in SEBM-built Ti-6Al-4V based on the results presented.

6.2 Results

Based on the previous study that was done on samples with a height of 30 mm, it is observed that there exist graded microstructure and mechanical properties within the SEBM-built Ti-6Al-4V parts caused by the thermal history experience. It is the author's hypothesis that varying the build geometry and build height might influence the thermal history experience and as such produce a more uniform microstructure throughout the build height. As such 100 mm tall samples with different geometries, namely, I-shaped, A-shaped and V-shaped were vertically fabricated using the EBM A2XX system. More details on the samples can be viewed in section 3.4.

6.2.1 Columnar grain width

The average values of the columnar grain width measured from the I-shaped, A-shaped and V-shaped samples are shown in Figure 6.1. It is noteworthy to point out that the measured values consist of a mixture of columnar grain and sub-columnar grain widths. The mean value of the columnar grain widths measured were in the range of 45 - 50 µm for the three samples.

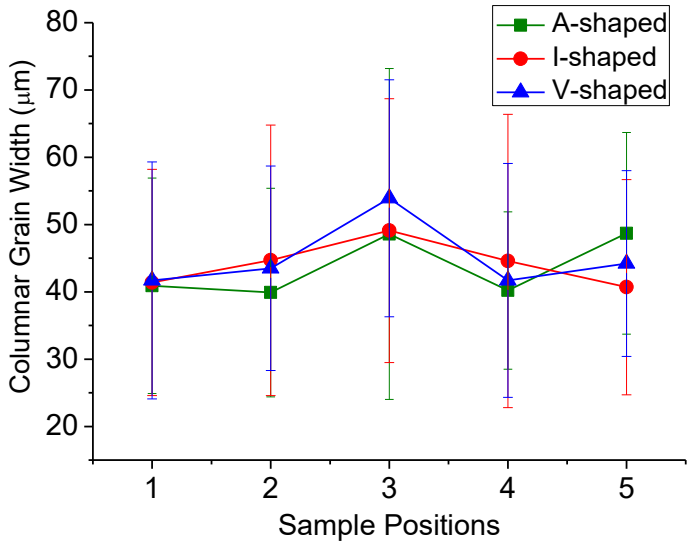

Figure 6.1 Plots of the columnar grain width within the various sample position

The results show that the columnar grain widths are generally coarsest at position 3 for all three samples. A rationale for the coarse columnar grains at middle sections may be due to the turning point in the cooling rate experienced during layerwise deposition process. There are three main paths where heat is lost during the SEBM process. Firstly, vertically downwards through the build start plate via heat conduction. Secondly, radially through the surrounding sintered powder and lastly vertically upwards via thermal radiation. Initially, at positions 1 and 2 (lower section), the influence of the stainless steel build start plate resulted in a higher cooling rate. This is due to the stainless steel having 3 times of the thermal conductivity than that of the titanium alloy. However, at position 3 (middle section) the heat is no longer dissipating effectively through previously deposited layers due to the increasing distance from the start plate. With increasing distance away from the start plate, the majority of the columnar grain widths in position 4 and 5 (upper section) are finer as compared to position 3. This suggests that a higher rate of cooling was experienced in this position. This may be due to the radial heat dissipation via the cooler surrounding sintered powder bed. It is worthwhile to note that for the A and V-shaped samples the β interspace is coarsest in position 3 before becoming gradually

finer. In addition, the β interspace within the columnar grains is, in general, coarser at position 1 (bottom section) as compared to position 5 (top section) as shown in Table 6.1. The coarsening of the β interspace at position 1 is likely due to the longer exposure to the build temperature of 600 - 650 ºC. Figure 6.2 shows representative micrographs of the bulk section of the samples taken at different build heights.

Table 6.1 Summary of columnar grain width and β interspace of the different samples.

	Columnar grain width (µm)			**β interspace (µm)**		
Position	**I-shaped**	**A-shaped**	**V-shaped**	**I-shaped**	**A-shaped**	**V-shaped**
S5	41.4 ± 16.8	48.7 ± 15.0	41.7 ± 17.6	0.381 ± 0.1	0.301 ± 0.1	0.358 ± 0.1
S4	44.7 ± 20.1	40.2 ± 11.7	43.5 ± 15.2	0.436 ± 0.1	0.426 ± 0.1	0.419 ± 0.1
S3	49.1 ± 19.6	48.6 ± 24.6	53.9 ± 17.6	0.438 ± 0.2	0.491 ± 0.1	0.503 ± 0.1
S2	44.6 ± 21.8	39.9 ± 15.5	41.7 ± 17.4	0.481 ± 0.1	0.469 ± 0.1	0.471 ± 0.1
S1	40.7 ± 16.0	40.9 ± 16.0	44.2 ± 13.8	0.509 ± 0.1	0.448 ± 0.1	0.411 ± 0.1

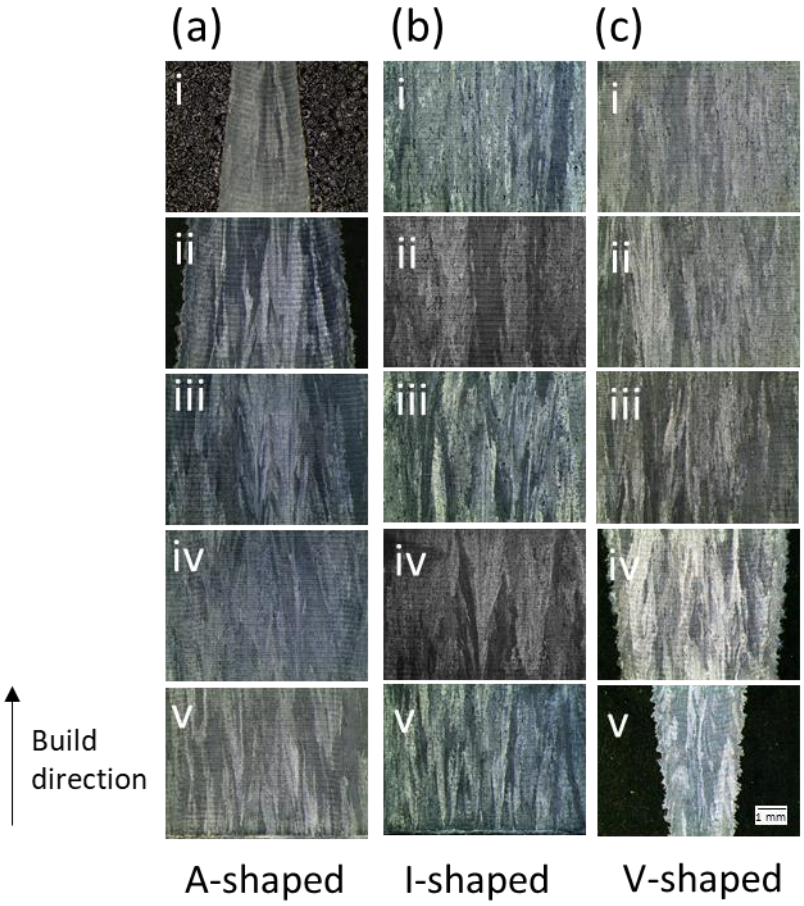

Figure 6.2 Representative micrographs of the bulk section taken at different build heights with a magnification of 10x. The scale bar for the figures are shown in figure (c v).

6.2.2 Grain growth angle

An indicator to identify the competition among the columnar grains could be the grain growth angle. The grain growth angle is defined as the angle deviation between the grain growth direction with the build direction as shown in Figure 3.8. With the competition between columnar grains, it can be expected that the grain growth angle would decrease with the build height since the better orientated grains would impede the growth of lesser well-orientated grains.

A plot of the grain growth angle against the build direction for the various samples is shown in Figure 6.3 (a-c). The average grain growth angle for the I-shaped, A-shaped, and V-shaped samples are 5.5 º, 6.25 º and 5.5 º, respectively. From the finite element (FE)

simulations, it can be observed that the thermal gradient is largest along the build direction. Thus, it can be assumed that the prior-β columnar grains will grow in the direction of the thermal gradient. Prior EBSD studies have also reported that the prior β columnar grains have a strong $(001)_{\beta}$ crystal orientation [92, 240]. Despite the direction of the thermal gradient to be along the z-axis, the slight deviation in angle is likely due to the moving melt pool during the selective melting process.

The average grain growth angle of the I-shaped and A-shaped sample does not show any significant trend with the increase in the build height as shown in Figure 6.3 (a) and (b). However, in the V-shaped sample, there is a decrease in average grain growth angle with an increase in build height. The higher grain growth angle in the V-shaped sample in position 1 and 2 is likely due to grain nucleation from the contour region as reported in earlier studies [92]. The heterogeneous nucleation of columnar grains as observed in the earlier studies were found to grow competitively with the better orientated columnar grains within the bulk section [92]. With the increase in build height, the better orientated columnar grains out-grew the columnar grains that nucleate from the contour section. This could explains why the measured grain growth angle reduces with increasing build height in the V-shaped sample as shown in Figure 6.3 (c).

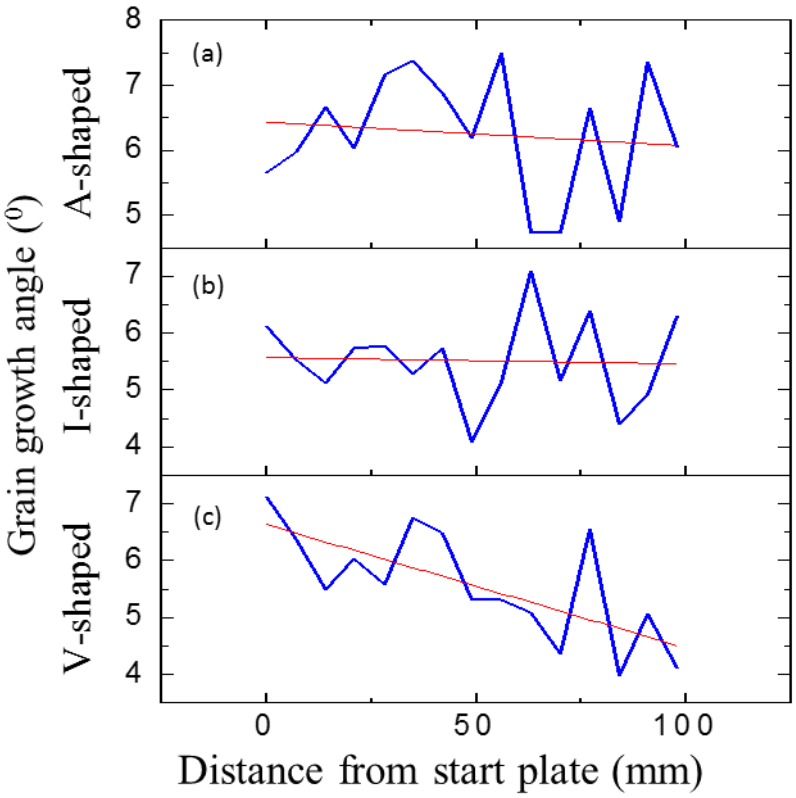

Figure 6.3 (a-c) Grain growth angle along the built height across the three geometry

6.2.3 Phase analysis

X-ray diffraction (XRD) analysis was conducted on the samples to investigate the crystallographic orientations of phases. Slices of the material were cut approximately 5 mm in thickness from each position for crystallographic texture analysis to analyse the texture evolution with build height. The sample size of positions 5 and 1 from the A-shaped and V-shaped respectively were too small to be analysed as such data for the two positions were not obtained.

Three peaks designating $(10\bar{1}0)$, (0002) and $(10\bar{1}1)$ crystal planes are selectively highlighted in Figure 6.4, due to their strong peak intensity with respect to the other crystal planes. These planes are coincidentally are the prismatic, basal and pyramidal planes respectively within the HCP crystal structure of α-Ti phase.

It can be observed that the $(0002)_\alpha$ peak varies obviously with the various positions. In the A- and V-shaped samples, it can be observed that the $(0002)_\alpha$ peak is weak in sample position with a smaller cross-sectional area (i.e. position 4 and 2 in A- and V-shaped samples, respectively) as compared to those with a larger cross-sectional area (i.e. position 1 and 5 in A- and V-shaped samples, respectively). The strength of the $(0002)_\alpha$ peak correlates well with the increase in sample cross sectional area. Moreover, it can be observed that the I-shaped samples has stronger $(0002)_\alpha$ peak intensities as compared to the A-shaped and V-shaped samples.

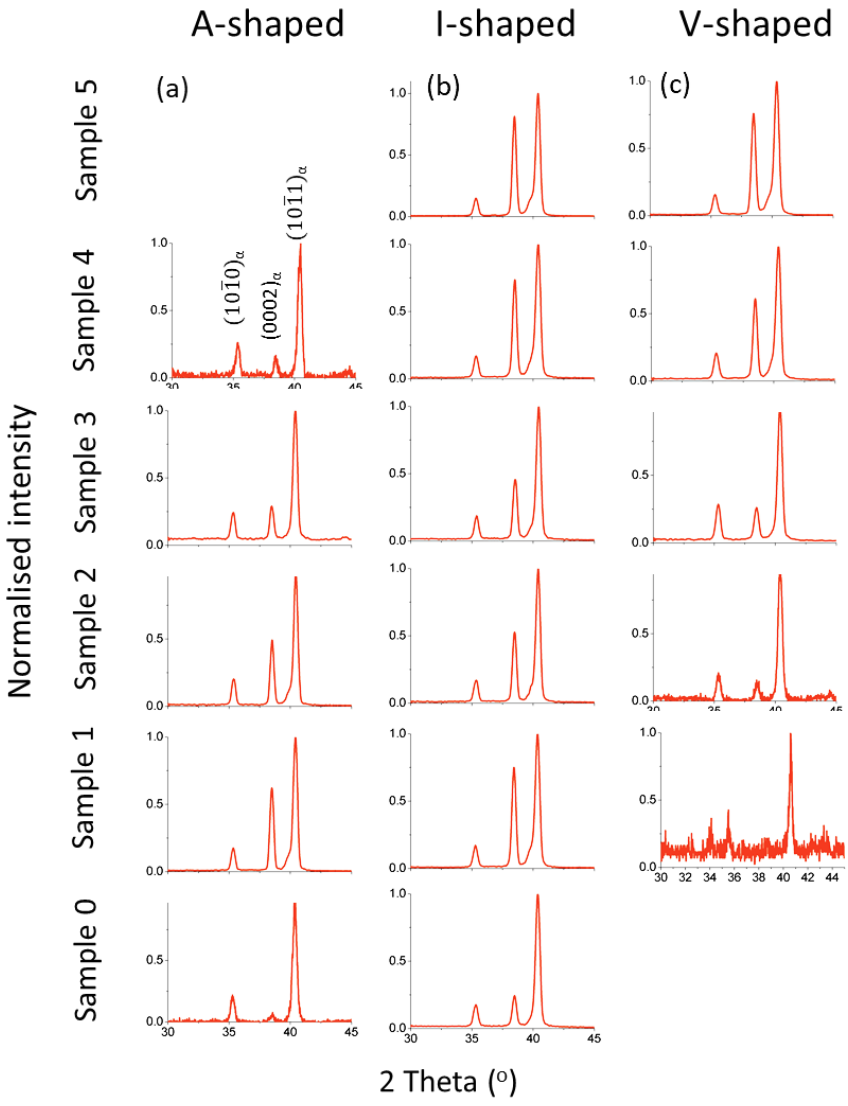

Figure 6.4 Peak count intensity differences among the three SEBM-built Ti-6Al-4V geometries with varying built heights. (a) X-ray diffraction (XRD) profiles of A-shaped, I-shaped and V-shaped geometries with varying build heights.

6.2.4 Crystallographic texture analysis

Crystallographic texture analysis was conducted on the block sample to obtain the texture strength of the three crystallographic planes (i.e. $(10\bar{1}0)$, (0002) and $(10\bar{1}1)$) to investigate the relationship between texture strength and build height.

It can be observed from the $(0002)_{\alpha}$ pole figures shown in Figures 6.5 and 6.6 that the strength of the texture was increased with build height. Corresponding micrographs also show that initially at Position 0, the competition between the columnar grains is the most evident. From the Burger's relationship in titanium alloy, it was understood that the $(0002)_{\alpha}$ plane was transformed from the $(101)_{\beta}$ plane. The schematic of the Burger's relationship of $\alpha \leftrightarrow \beta$ phase transformation is illustrated in Figure 6.5 (c).

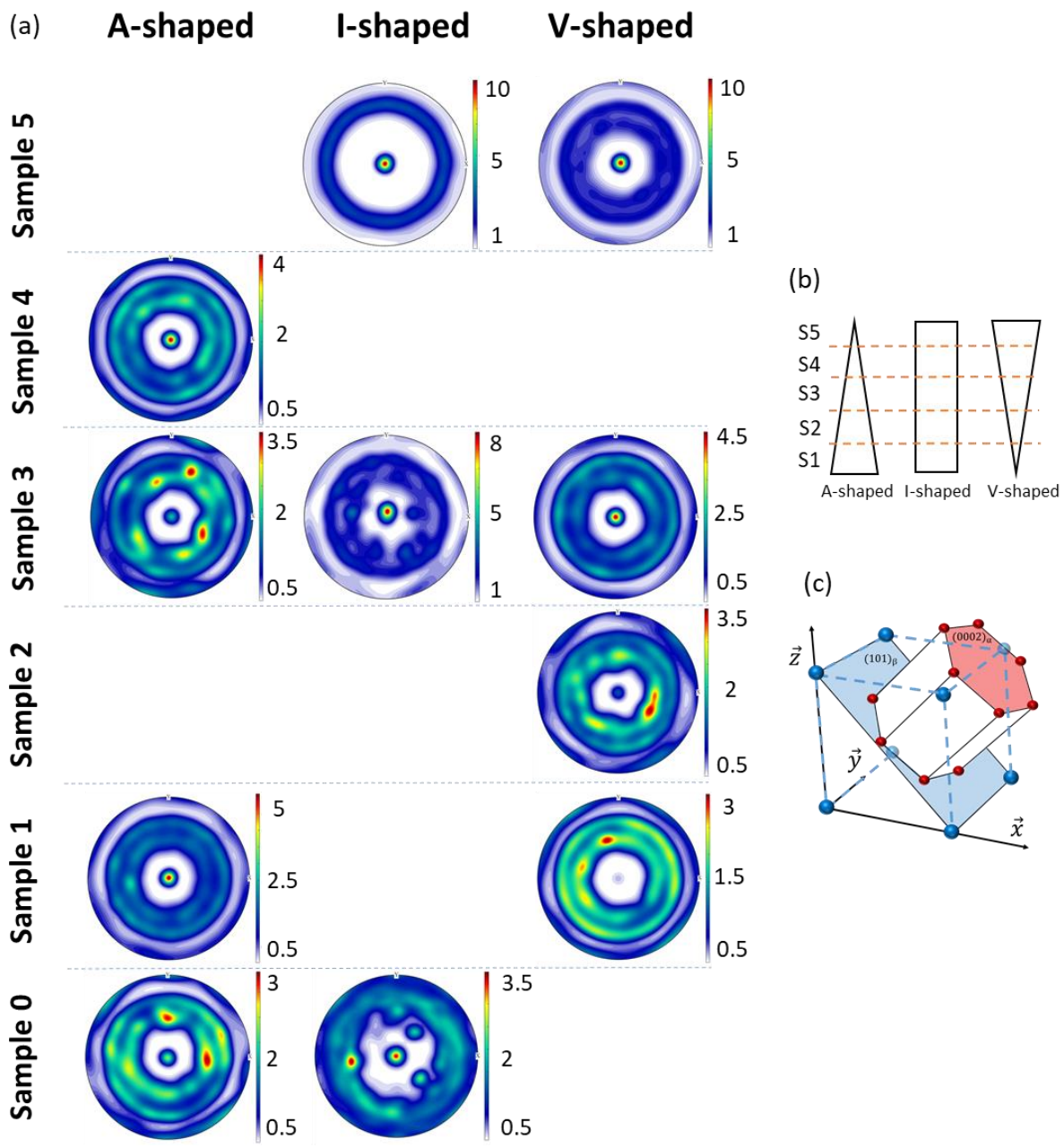

Figure 6.5 (a) XRD pole figures of A-shaped, I-shaped and V-shaped geometries with varying build height. (b) Schematic of the varying sample positions. (c) Schematic of the Burger's relationship between the $(101)_\beta$ to $(0002)_\alpha$ crystal orientation for titanium alloy.

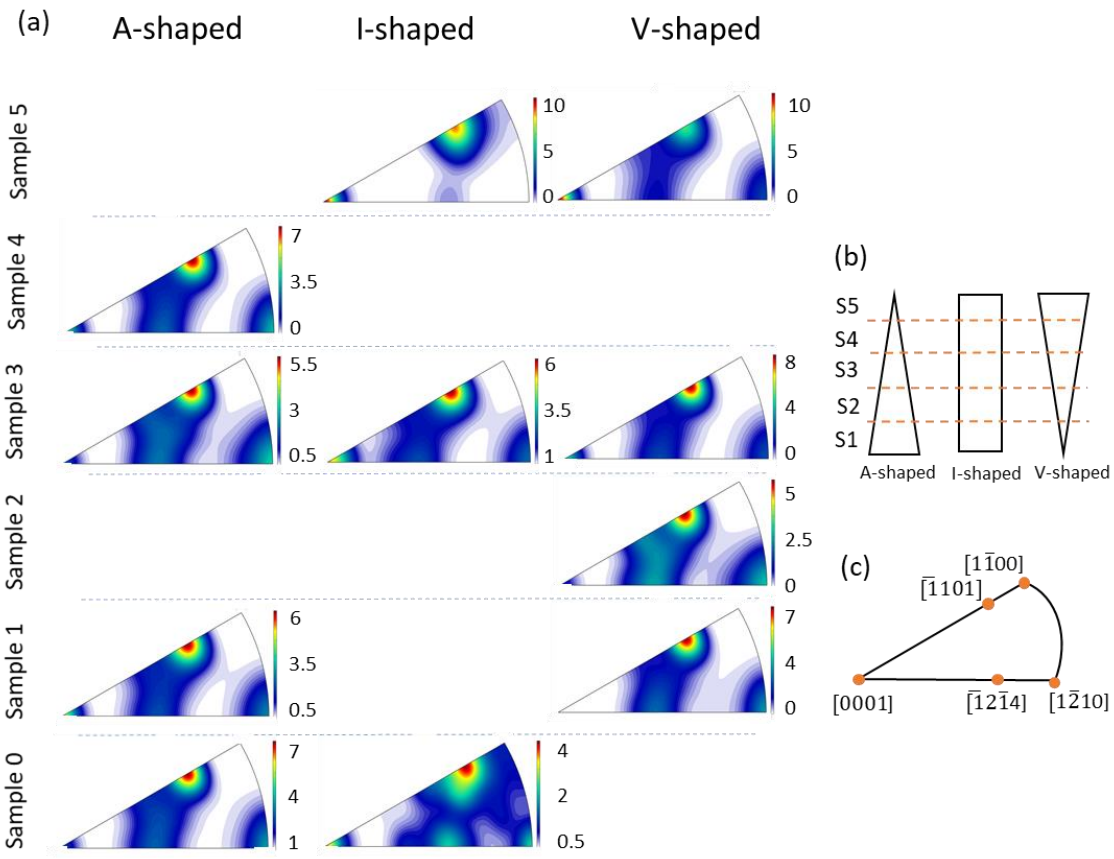

Figure 6.6 (a) XRD <001> inverse pole figures of A-shaped, I-shaped and V-shaped geometries with varying build heights. (b) Schematic of the varying sample positions. (c) Schematic of the stereographic triangle with the observed pole orientations labeled.

6.2.5 Layer banding phenomenon

Given the SEBM's layer-by-layer build process, distinct periodical layer bandings are also observed within the as-built Ti-6Al-4V samples through OM as shown in Figure 6.7. These layer bands are also observed to curve upwards within one millimeter from the contour. The top-most region of the sample is a representation of the microstructure evolution prior to prolong exposure to the high elevated build temperature.

Figure 6.7 shows that there are distinct microstructures around the layer banding at the top most region. The periodic layer band consists of a fine duplex α+β microstructure (white region) and coarse duplex α+β microstructure (dark region). In the region above the layer band, the β phase shows up on the SEM micrograph as fine dots.

Figure 6.8 illustrates the possible transformation of the microstructure with the addition of each layer. Figure 6.8 i shows a 3D model of the part and the respective heat affected zones caused by the melt pool. Figure 6.8 iii, iv and v shows the step by step addition of the heat affected zone as the electron beam is melting along the longitudinal and traverse directions. Based on the numerical modelling done and experimental validation it is concluded that the geometry influences the heat affected zone depth caused by the melt pool. This difference led to the periodic layer bandings observed. In the case of a square sample, the periodic layer bandings was observed to be of 50 μm spacing and the dark region is limited to a line under OM.

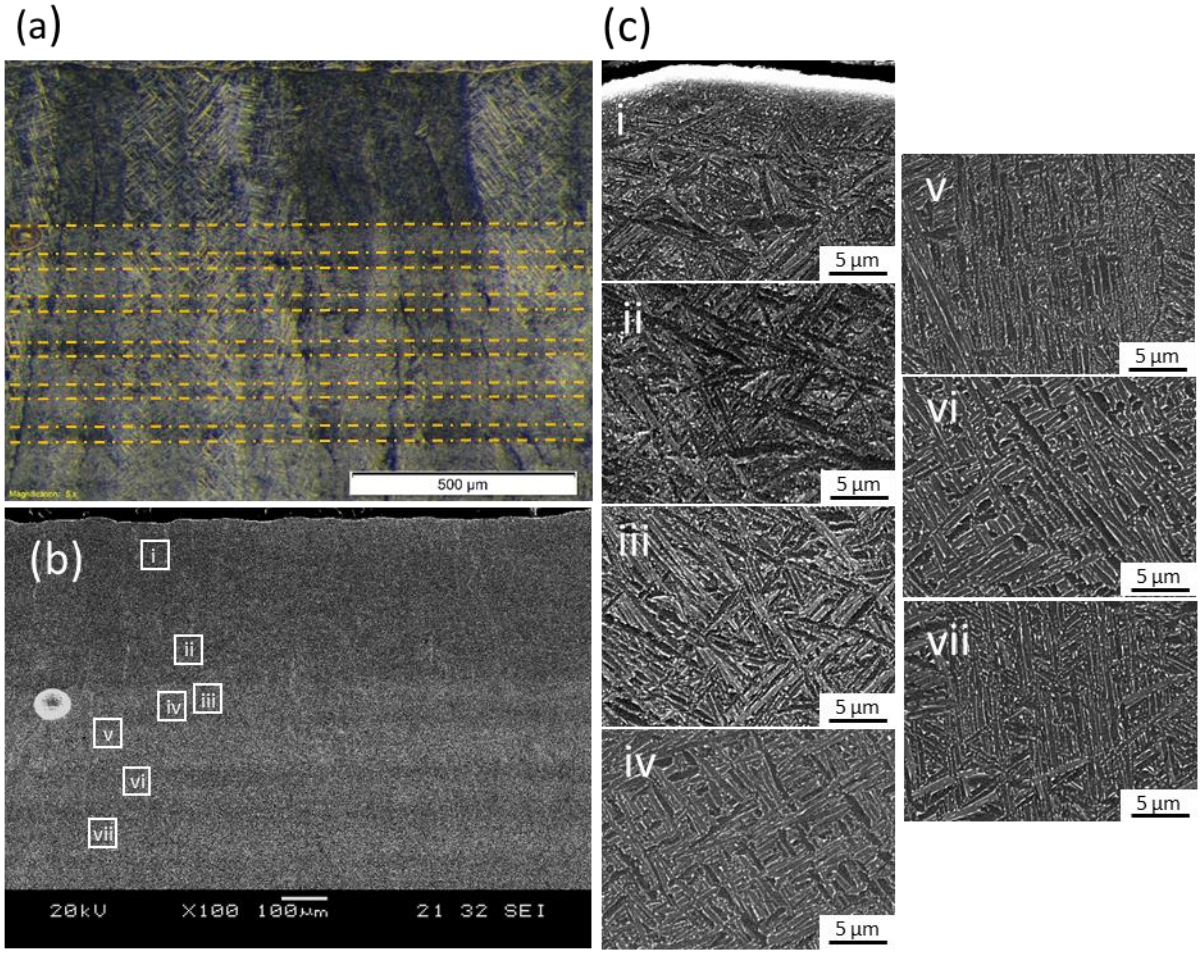

Figure 6.7 Micrographs of the microstructure showing the difference across the layer bands; (a) OM image of the microstructure showing the locations of interest. (b) SEM micrograph of the same region. (c) i - vi SEM images taken from various location at 5000x magnification, respectively.

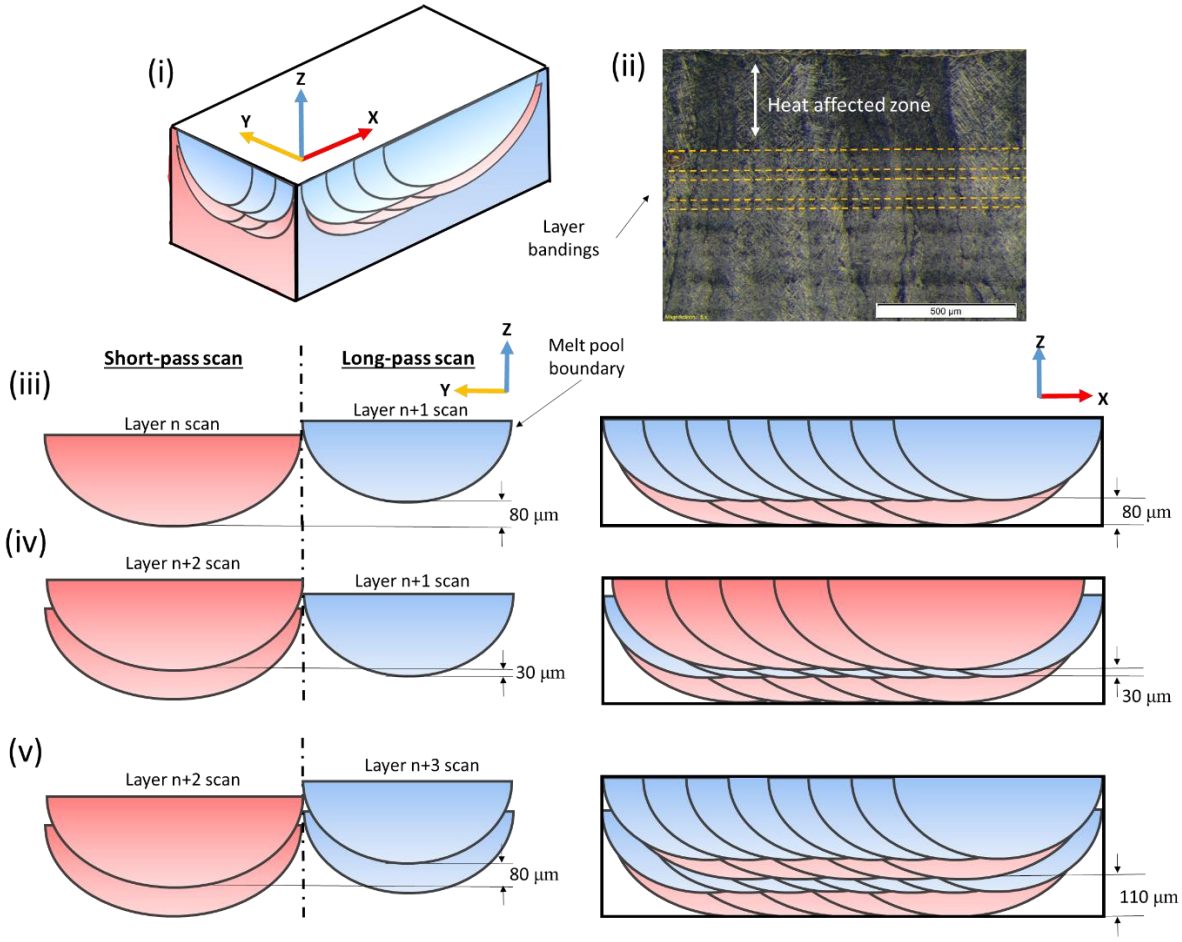

Figure 6.8 Schematic of the formation mechanism of the non-uniform periodical layer banding.

Additionally, such layer banding has been observed through OM to study the columnar grain growth within the bulk region. The different contrast of the regions is due to the different degree of etching. Differences in crystal orientation of the grain has been known to result in such contrast differences during the etching process. In Figure 6.9, it can be observed that the layer bandings are approximately 100 µm spaced apart to one another. The columnar grains have been observed to be interrupted by such layer bandings as observed from the difference in the dark regions.

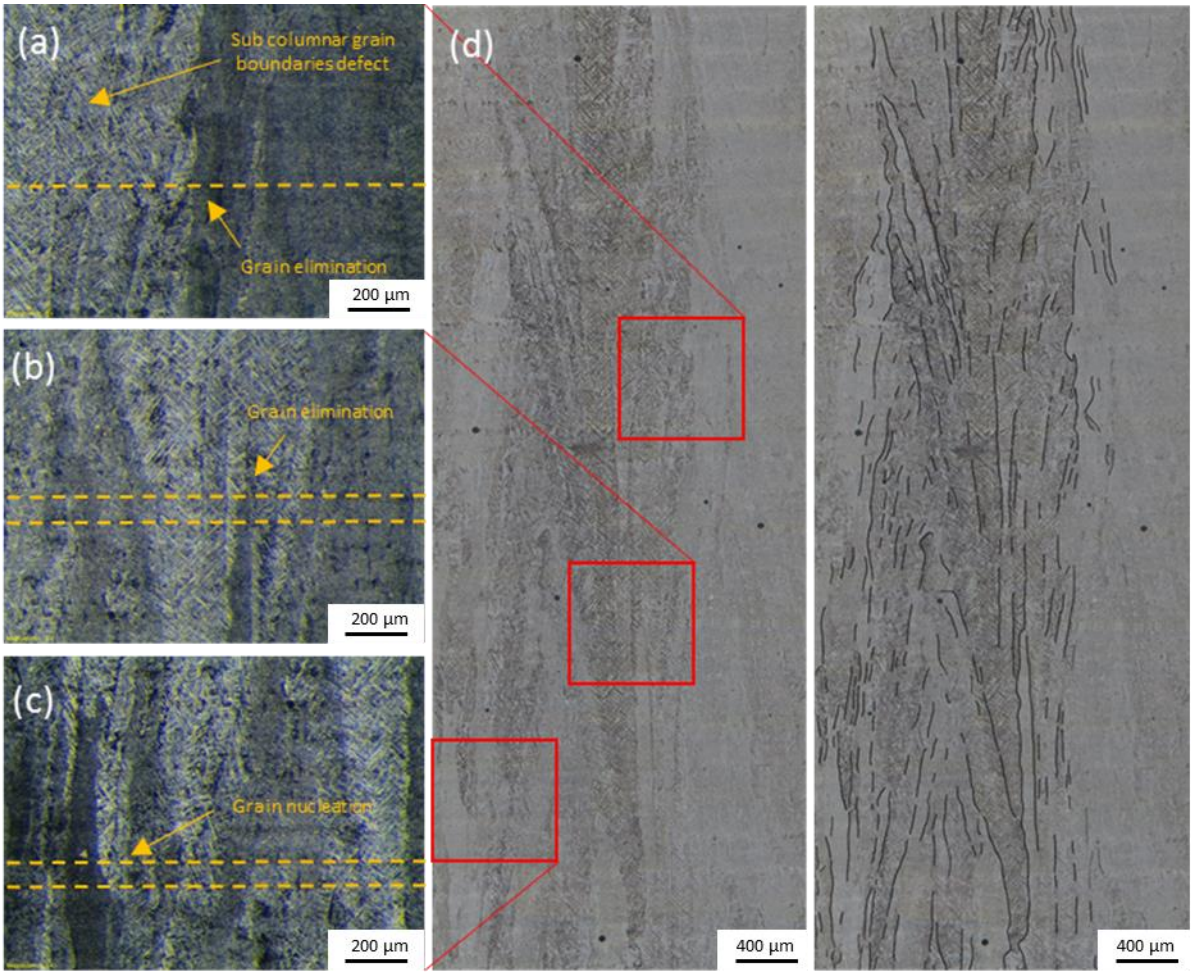

Figure 6.9 OM images showing the grain nucleation and elimination phenomenon in SEBM of Ti-6Al-4V; (a), (b), (c) OM images shows evidence of grain nucleation and termination with each deposited layer (c) which enables the growth of sub-columnar grains with similar crystallographic orientation. (d) OM image of the columnar grain morphology in SEBM-built Ti-6Al-4V and (e) with highlighted grain boundaries.

6.3 Discussion

6.3.1 Competitive grain growth in SEBM-built Ti-6Al-4V

The study of grain growth behavior has been a topic of interest to material scientists for a long time. This study is important because grain morphology and size have a direct influence on the mechanical properties of the material. A classical model for grain growth is the competitive grain growth mechanism.

A prior study [92] studied on the crystallographic texture evolution with build height has shown that the reconstructed <001>-orientated β grains on the average have the greatest growth advantage with each subsequent layer through the increased in $(001)_{\beta}$ texture intensity obtained via EBSD analysis. However, the machine used to fabricate their samples was an early version of the EBM machine (Arcam S-12), and the samples were only 30 mm in height. Based on other researches, it is known that the different generation of machine and the difference in build height are likely to result in differences in the microstructure [11, 45, 143]. This is largely due to the rapid development of the technology and the different paths of heat dissipation. As such, this study is important to investigate further whether this phenomenon exists in the SEBM process for larger parts.

Based on the experimental results in this chapter and from a prior study, it may be concluded that the classical model for competitive grain growth applies in the case for SEBM-built Ti-6Al-4V parts. Numerical simulations of the thermal gradient as shown in Figure 6.10 indicate that the dominant thermal gradient is along the build direction (Z-axis). Based on the simulation the thermal gradient for the various geometries at the start of solidification ($T_{liquidus}$= ~1700^0C) is 8.5×10^6 K/m, 8.1×10^6 K/m and 8.9×10^6 K/m for the A-, I- and V-shaped samples, respectively. The cooling rate was also simulated to be 233000 K/s, 237000 K/s and 228000 K/s for the A-, I- and V-shaped samples, respectively.

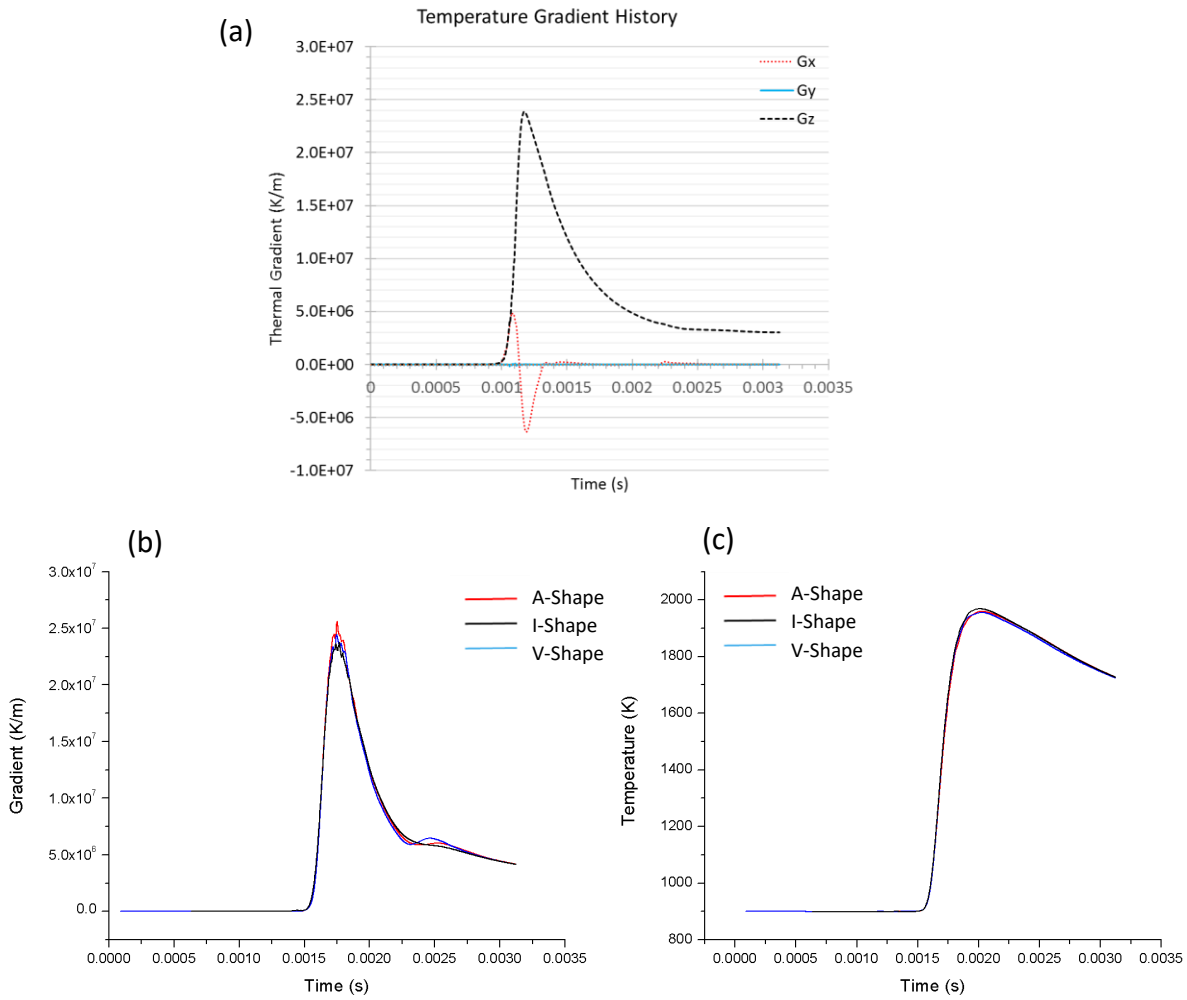

Figure 6.10 Simulated thermal gradient and the cooling rate curve for different sample shapes.

Experimental evidence has shown that the grains that grow parallel to the build direction outgrew neighboring grains that are less well-orientated as in Figure 6.9 (d). The direction in which the grain grows indicates the growth of the grains during the rapid solidification process (~1990 - 1880K) and it is unaffected by subsequent exposure to the elevated temperature. As such it provides a glimpse of the grain selection mechanism during the rapid solidification process.

Firstly, the grain growth angle measured from the three geometries was either decreased with increasing build height or remained at the same. Furthermore, Figure 6.9 (d) shows that

the columnar/sub-columnar grains with a high grain growth angle were stopped by the neighboring grains. Additionally, based on Walton and Chalmer's model, it might be expected that the columnar grain width should continue to increase with increasing build height. However, this is not observed in the samples. This suggests that the competitive grain growth phenomenon is not the dominant factor that governs the width of the columnar grain. A possible factor is due to the variable cooling rates. Cooling rate is known to affect the grain size [67] Factors that may affect the cooling rate are the geometry of the melted region as investigated previously and the geometry of the moving melt pool. The simulations conducted have shown obvious differences in the cooling rate experienced by the various geometries.

Secondly, texture analysis conducted via the XRD technique also showed that the strength of the $<0002>_{\alpha}$ texture was enhanced with build height for the I- and V-shaped geometries. The presence of the $<0002>_{\alpha}$ texture is commonly observed in sheet rolled titanium at room temperature. Early research on cold rolled commercially pure (CP) titanium regarding the transition of texture due to phase transformations has shown that at room temperature the dominant crystallographic texture of the annealed CP titanium has the $<0002>_{\alpha}$ texture while at high temperature (950 ^{o}C) the rolled CP titanium has the $<001>_{\beta}$ texture [241]. This suggests that there might be a relationship between the two orientations. However, there have not been any direct evidence to support it. The absent of the $<110>_{\beta}$ texture in the rolled CP titanium at high temperature which is expected according to Burger's relation is also not well explained.

With regards to SEBM-built Ti-6Al-4V, publications often report that variant selection does not exist due to the weak α-phase texture in the as-built material [26, 92]. As such a theoretical reconstructed β phase is often presented to have a strong $<001>_{\beta}$ texture due to the <001> crystal orientation being the preferred direction of growth in cubic metals [26, 92, 240]. However, a recent publication on SEBM-built Ti-6Al-4V has also shown that the reconstructed β grains from EBSD images do not show a clear $(001)_{\beta}$ unlike those shown in prior studies. It

is also observed that in SEBM-built Ti-6Al-4V the $<0002>_{\alpha}$ texture close to the build direction was preferentially selected and variants that were perpendicular to the build direction disappeared after the hot isostatic pressing (HIP) process [143]. This suggests that <0002> α-phase texture in the bulk material may be preferentially formed in the samples that were experienced elevated temperatures which enables annealing effect.

In the case of the I-shaped sample, it can be observed that the preferential growth of the $<0002>_{\alpha}$ is not only influenced by the cross-sectional geometry but also across the build height. This suggests that another factor is influencing the preferential texture transformation. Given the lack of capability to perform in-situ XRD, it would be difficult to prove whether the strengthening of the $(0002)_{\alpha}$ with build height is related to the $<001>_{\beta}$ orientation that is preferred by the prior-β grains.

Numerical simulations have thus been conducted to better understand the competitive grain growth phenomenon. Based on Figures 6.11 and Table 6.2, it can be observed that the classical definition of the competitive grain growth is not being obeyed at all times. The findings from the simulations thus point to possible cases where non-classical competitive grain growth can occur. It is important to note that the author has not managed to find such cases yet though microscopy techniques. As such, it is the opinion of the author that the grain selection phenomenon in the SEBM process most likely follows the classical definition of competitive grain growth mechanism.

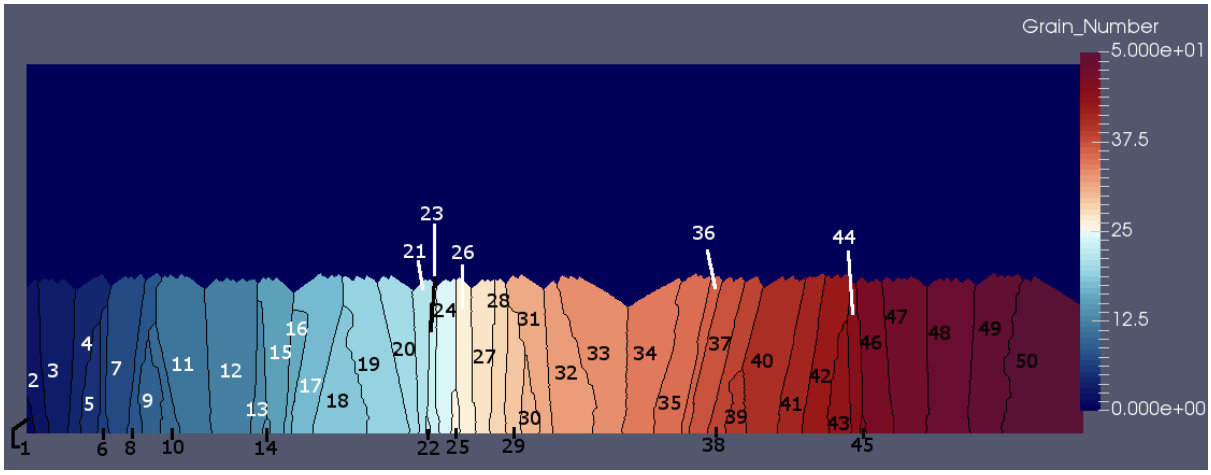

Figure 6.11 2D simulation of the grain growth after time = 0.00031s

Table 6.2 Simulated grains with their respective grain orientations.

Grain	**1**	**2**	**3**	**4**	**5**	**6**	**7**	**8**	**9**	**10**
Orientation (°)	4.5	11.3	-13.1	-12.2	1.9	2.7	-16.6	16.3	-9.4	2.3
Grain	**11**	**12**	**13**	**14**	**15**	**16**	**17**	**18**	**19**	**20**
Orientation (°)	2.7	6.7	9.8	-18.3	-2.1	4.8	7.2	4.0	18.8	-2.7
Grain	**21**	**22**	**23**	**24**	**25**	**26**	**27**	**28**	**29**	**30**
Orientation (°)	-11.9	-1.8	-13.8	16.1	-0.6	9.3	-0.4	15.9	0.8	-18.6
Grain	**31**	**32**	**33**	**34**	**35**	**36**	**37**	**38**	**39**	**40**
Orientation (°)	10.8	14.7	-2.5	0.6	-0.3	-1.8	-10.5	-6.9	2.6	-5.0
Grain	**41**	**42**	**43**	**44**	**45**	**46**	**47**	**48**	**49**	**50**
Orientation (°)	-0.6	1.6	-10.3	-10.2	-14.2	1.6	16.6	-10.5	-15.6	-8.9

6.3.2 Layer banding formation mechanism

The formation of the layered microstructure within metallic additive manufactured alloys was commonly reported [21, 242]. The common characteristic between the reported layered microstructure is that the repeating pattern has approximately the same thickness as each build layer thickness and also that the top layer that precedes the layer banding is often free from layer bandings. The layer bands have been reported to be formed by the eutectoid reaction when a single solid phase transitions into two other solid phases [242].

Though based on Figure 6.7, it can be observed that the thickness of the layered microstructure formed in the sample is not uniformly spaced. It is proposed that this is due to slight differences in depth of the heat affected zone due to the rectangular geometry of the sample. Numerical simulations were done to investigate the effect of build geometry on the melt pool. The results in Figure 6.12 (a) and (b) show that there are indeed differences in the melt pool that may have contributed to the uniform periodical layer bandings.

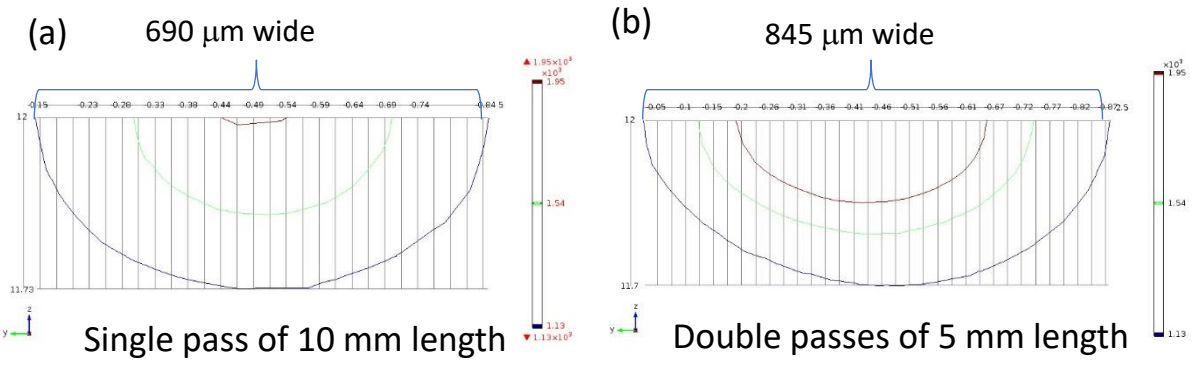

Figure 6.12 Numerical simulation of the melt pool; (a) shows the heat affected zone (HAZ) of the longitudinal (10 mm) scan had a melt pool width of 690 µm and a depth of 270 µm while (b) shows the HAZ of the transverse (5 mm) scan had a melt pool width of 845 µm and a depth of 300 µm.

6.3.3 Formation of sub-columnar grains

It is found that the difference in the melt pool geometry is likely to lead to a disruption to the columnar grain growth which may result in the formation of defects. For example, the formation of sub-columnar grain boundaries within a larger columnar grain. The sub-columnar grain being of a slightly differed crystal orientation is proposed to grow with a slight deviation from the build orientation, resulting in the morphology shown in Figure 6.9 (d). It can also be observed that the grain that grows along the build direction outgrows the grain that is less well-orientated. This further support that the classical competitive growth is obeyed. The formation of the sub-columnar grains is currently not yet well understood though it suggests that differences in the melt pool geometry can be utilized to promote finer columnar grains within the SEBM-built Ti-6Al-4V.

6.4 Conclusions

The experimental results have shed more understanding on the grain growth behavior of SEBM-built titanium alloy. Based on these experimental observations, it can be concluded that the classical model of competitive grain growth applicable to the SEBM-built Ti-6Al-4V alloy.

Grain growth misorientation angle along the build direction in the A- and V-shaped samples was decreased with increasing build height. This indicates a grain selection process occured during the rapid solidification process of the SEBM-built Ti-6Al-4V alloy. The grain growth misorientation angle was ranged from 4 ^{o} to 7 ^{o} with regard to the build direction. XRD results showed that the $(0002)_{\alpha}$ peak varies with sample position and cross-sectional area. There is a possible connection between the $<0002>_{\alpha}$ and the $<001>_{\beta}$ crystallographic orientation based on the Burger's relation implying that a strong <001> crystollographic texture was acompanied with a strong $(0002)_{\alpha}$ peak. Pole figure analysis also showed a stronger crystollographic texture with increasing build height. This is consistent with the classical model of competitive grain growth phenomenon. Less well-orientated grains were systematically eliminated with increasing build height by better-orientated grains. Additionally, layer bandings were observed to cause the formation of sub-columnar grain boundaries defects within the columnar grains. The sub-columnar grains that not grown along the preferred orientation were eventually eliminated by better-orientated columnar grains.

Chapter 7: Conclusions

The investigations on anisotropy and heterogeneity of SEBM-built Ti-6Al-4V alloy carried out in this thesis are best summarized into two sections. Firstly, the study of the microstructure and the mechanical properties of the build thickness-dependent samples, discussed in Chapters 4 and 5, provides insights into the microstructural evolution phenomenon that occurs during the melting and rapid solidification process layer by layer and its effect on the mechanical properties. It is about the issue of heterogeneity. Secondly, the study of the microstructure and the mechanical properties of the build height-dependent samples, discussed in Chapters 5 and 6, provides insights into the grain selection phenomenon that occur during the layerwise material deposition process and its effect on the mechanical properties. It is about the issue of anisotropy. The conclusions from these chapters are summarized as below:

7.1 Study on phase identification and transformation (Chapter 4)

- The work demonstrates that α′ martensite is first formed in SEBM processing of Ti-6Al-4V regardless of build geometries. FEM simulations also find that the temperature profiles and cooling rates are favorable for the formation of martensite. This provides the possibility to further improve the mechanical properties of EBM-built Ti-6Al-4V alloy via a mixed microstructure of α/β and α'.
- The formation and decomposition of α′-Ti martensite were also investigated structurally and chemically, with a view to enrich the knowledge on martensite in titanium alloys. Numerous micro-twins also occurred inside both α and α' phases.
- Quantitative microstructural characterization found that β phase interspace and β volume fraction constantly increases with the build thickness, meanwhile the Vickers microhardness was decreased accordingly. Simulations of the temperature profiles

inside the samples showed that thicker samples underwent a higher average temperature compared to thinner samples.

- The hcp α phase and bcc β phase were identified by XRD and TEM. The lattice constants are a = 0.293 nm and c = 0.467 nm for α phase and a = 0.320 nm for β phase, respectively. The β phase formed as discrete flat rods embedded in continuous α phase and its volume fraction was determined to be ~3 - 4%. Quantitative examination of the elemental partitioning and segregation behavior at the α/β interface was also conducted.

7.2 Study on effects of build geometry on the microstructure and mechanical properties of SEBM-built Ti-6Al-4V (Chapter 5)

- A mixed microstructure of alternate α/β with acicular α' martensite is observed inside the 1mm sample, while only fully decomposed alternate α/β microstructure is observed in the 5 mm, 10 mm and 20 mm samples. The selective melted geometry and in-fill hatching strategy have significant effects on the microstructure and mechanical properties of as-SEBM-built Ti-6Al-4V parts.
- In the 25 mm high sample, graded Ti-6Al-4V microstructure including varying prior β grains and β phase interspace was seen, i.e. near-equiaxed prior β grains as well as the equiaxed-to-columnar transition region at the initial several build layers and the subsequent columnar prior β grains with increasing grain width and β rod interspace. The coarser columnar microstructure mainly arises from the decreasing cooling rate. In addition, an increasingly pronounced strain hardening effect was observed with the rising build height as the previously built layers were subject to a longer annealing compared to the subsequent layers.
- Selective melted geometry and in-fill hatching strategy have significant effects on the microstructure of as-SEBM-built Ti-6Al-4V parts. The effects can be observed from the amount of martensitic phase between the curve and block parts and the

microstructure, morphology and mechanical property variation among the different structures with different thicknesses.

- Graded mechanical properties of Ti-6Al-4V with degraded microhardness and tensile properties were also observed from bottom to top of the 25 mm high sample, i.e. increasing microhardness, yield strength and ultimate tensile strength and elongation as the build height rises. A good agreement with the Hall-Petch relation indicates that the graded property takes place mainly due to the graded microstructure.
- Despite that the α/β interface strengthening was thought to play the primary role in determining the strength of SEBM-built Ti-6Al-4V that possesses a multiscale microstructure with cellular colony and basket-weave morphology. The β grain refinement strengthening seems to be more effective as the prior β grain boundaries could absorb a higher amount of dislocations in comparison with α/β interfaces.

7.3 Study on columnar grain growth in SEBM-built Ti-6Al-4V parts (Chapter 6)

- Overall, in the SEBM process, the coarse columnar grains obey the classical competitive growth mode throughout the various build heights of the samples fabricated. It is worthwhile to note that FEM simulations suggest that non-classical competitive grain growth is a possibility. This finding suggests the possibility to fabricate near single crystal materials from the SEBM process, due to the favorably orientated grain being dominant throughout the build height.
- There exists a low grain growth angle that ranged from 4 to 7 ^{o} from the build direction. The grain growth angle in the various samples alsowas decreased with increasing build height to varying extent.
- XRD results show that the $(002)_{\alpha}$ peak varies with sample position and cross-sectional area. There is a possible link between the $<0002>_{\alpha}$ and the $<001>_{\beta}$ crystallographic

orientation based on prior research, indicating the observation of the following two orientations in rolling operations. Pole figure analysis also shows a stronger crystallographic texture with increasing build height for the I- and V-shaped samples. FEM simulations indicate that the thermal gradient along build direction for the A-shaped sample to be the weakest and could be a reason for the lesser texture strength.

- Layer bandings are observed to cause the formation of sub-columnar grain boundaries defects within the columnar grains. The sub-columnar grains were observed to grow with a slight grain growth angle before being eliminated by better-orientated grains.

Chapter 8: Suggestions for future work

The SEBM process is a valuable metal AM manufacturing process. This study has provided a better understanding of the microstructure evolution of SEBM-built titanium alloy via experimental and numerical simulation results. This chapter discusses the potential research for further investigation and they are discussed below:

1. In this current study, the microstructure and mechanical properties have been investigated primarily on a single part. However, SEBM is capable of nesting several parts in the vertical direction. Nesting of parts is unique to SEBM technology and can improve production throughput. It is thus important to investigate the microstructure and mechanical properties of such nested parts.
2. Developing new materials for the SEBM process is equally important to validate the existing knowledge and to discover new phenomena that are inherent to the metal AM process. A possible research would be the development of single crystals or near single crystal materials, given the high thermal gradient along the build direction.
3. Based on Chapter 6, numerical simulations has shown that the thermal conditions in the SEBM process provide favorable conditions for non-classical competitive columnar grain growth. Further studies on the competitive grain growth mechanism in SEBM will provide a deeper understanding of the phenomenon.
4. Numerical simulation of the microstructure evolution in metal AM process has proven to be useful in validating many of the experimental observations. Development of an application for metallurgist/material scientists to simulate such phenomena effectively would be useful and important for the development of metal AM. Additionally,

sensitivity analysis of the variables and their effects on the thermal profiles in SEBM process can be investigated.

5. Lastly, the effects of other build pre-heat temperature on the microstructure observations made in this study can be further investigated. This would provide a deeper understanding of the heterogeneity microstructure in the EBM-built Ti-6Al-4V. Other mechanical tests such as fatigue and fracture analysis would also provide a more comprehensive view on how the heterogenous microstructure influence the mechanical properties as well.

References

1. Chua, C.K. and K.F. Leong, *3D printing and additive manufacturing: principles and applications*. 2015: World Scientific Publishing.
2. Gibson, I., D.W. Rosen, and B. Stucker, *Additive manufacturing technologies*. Vol. 238. 2010: Springer.
3. Strickland, J.D., *Applications of Additive Manufacturing in the Marine Industry.* Proceedings of PRADS2016, 2016. **4**: p. 8th.
4. Patil, N., D. Pal, and B. Stucker. *A new finite element solver using numerical Eigen modes for fast simulation of additive manufacturing processes*. in *Proceedings of the Solid Freeform Fabrication Symposium, Austin, TX, Aug*. 2013.
5. Tan, X.P., et al., *Metallic powder-bed based 3D printing of cellular scaffolds for orthopaedic implants: A state-of-the-art review on manufacturing, topological design, mechanical properties and biocompatibility.* Materials Science and Engineering: C.
6. Wohlers, T., *Wohlers report 2016*. 2016: Wohlers Associates, Inc.
7. Vartanian, K. and T. McDonald, *Accelerating Industrial Adoption of Metal Additive Manufacturing Technology*. JOM, 2016. **68**(3): p. 806-810.
8. Yap, C.Y., et al., *Review of selective laser melting: Materials and applications.* Applied Physics Reviews, 2015. **2**(4): p. 041101.
9. Lewandowski, J.J. and M. Seifi, *Metal Additive Manufacturing: A Review of Mechanical Properties.* Annual Review of Materials Research, 2016. **46**(1): p. 151-186.
10. Carroll, B.E., T.A. Palmer, and A.M. Beese, *Anisotropic tensile behavior of Ti–6Al–4V components fabricated with directed energy deposition additive manufacturing.* Acta Materialia, 2015. **87**: p. 309-320.
11. Wang, P., et al., *Anisotropic Mechanical Properties in a Big-Sized Ti-6Al-4V Plate Fabricated by Electron Beam Melting*, in *TMS 2016: 145th Annual Meeting & Exhibition: Supplemental Proceedings*. 2016, John Wiley & Sons, Inc. p. 1-12.
12. Wang, Z., T.A. Palmer, and A.M. Beese, *Effect of processing parameters on microstructure and tensile properties of austenitic stainless steel 304L made by*

directed energy deposition additive manufacturing. Acta Materialia, 2016. **110**: p. 226-235.
13. Tian, Y., et al., *Rationalization of Microstructure Heterogeneity in INCONEL 718 Builds Made by the Direct Laser Additive Manufacturing Process.* Metallurgical and Materials Transactions A, 2014. **45**(10): p. 4470-4483.
14. Sridharan, N., et al., *Rationalization of anisotropic mechanical properties of Al-6061 fabricated using ultrasonic additive manufacturing.* Acta Materialia, 2016. **117**: p. 228-237.
15. Zhu, Y., et al., *The anisotropy of laser melting deposition additive manufacturing Ti–6.5Al–3.5Mo–1.5Zr–0.3Si titanium alloy.* Materials & Design, 2015. **67**: p. 538-542.
16. Dehoff, R.R., et al., *Case study: additive manufacturing of aerospace brackets.* Advanced Materials and Processes, 2013. **171**(3).
17. Sames, W.J., et al., *The metallurgy and processing science of metal additive manufacturing.* International Materials Reviews, 2016. **61**(5): p. 315-360.
18. Wu, M.-W., P.-H. Lai, and J.-K. Chen, *Anisotropy in the impact toughness of selective laser melted Ti–6Al–4V alloy.* Materials Science and Engineering: A, 2016. **650**: p. 295-299.
19. Wauthle, R., et al., *Effects of build orientation and heat treatment on the microstructure and mechanical properties of selective laser melted Ti6Al4V lattice structures.* Additive Manufacturing, 2015. **5**: p. 77-84.
20. Frazier, W.E., *Metal Additive Manufacturing: A Review.* Journal of Materials Engineering and Performance, 2014. **23**(6): p. 1917-1928.
21. Kelly, S.M. and S.L. Kampe, *Microstructural evolution in laser-deposited multilayer Ti-6Al-4V builds: Part II. Thermal modeling.* Metallurgical and Materials Transactions A, 2004. **35**(6): p. 1869-1879.
22. Wang, P., et al. *Recent Progress of Additive Manufactured Ti-6Al-4V by Electron Beam Melting*. in *Solid Freeform Fabrication 2016: Proceedings of the 26th Annual International Solid Freeform Fabrication Symposium – An Additive Manufacturing Conference*. 2016. https://sffsymposium.engr.utexas.edu/sites/default/files/2016/053-Wang.pdf.
23. Zhang, B., et al., *Study of selective laser melting (SLM) Inconel 718 part surface improvement by electrochemical polishing.* Materials & Design, 2017. **116**: p. 531-537.
24. Welsch, G., R. Boyer, and E. Collings, *Materials properties handbook: titanium alloys*. 1993: ASM international.
25. Qian, M., et al., *Additive manufacturing and postprocessing of Ti-6Al-4V for superior mechanical properties.* MRS Bulletin, 2016. **41**(10): p. 775-784.
26. Al-Bermani, S.S., et al., *The Origin of Microstructural Diversity, Texture, and Mechanical Properties in Electron Beam Melted Ti-6Al-4V.* Metallurgical and Materials Transactions A, 2010. **41**(13): p. 3422-3434.
27. Safdar, A., et al., *Evaluation of microstructural development in electron beam melted Ti-6Al-4V.* Materials Characterization, 2012. **65**: p. 8-15.
28. Gong, X., T. Anderson, and K. Chou, *Review on powder-based electron beam additive manufacturing technology.* Manufacturing Review, 2014. **1**: p. 2.
29. Murr, L.E., et al., *Microstructures and mechanical properties of electron beam-rapid manufactured Ti–6Al–4V biomedical prototypes compared to wrought Ti–6Al–4V.* Materials Characterization, 2009. **60**(2): p. 96-105.
30. Rafi, H.K., et al. *Mechanical property evaluation of Ti-6Al-4V parts made using electron beam melting*. in *Proceedings of the Solid Freeform Fabrication Symposium*. 2012.

31. Xu, W., et al., *Additive manufacturing of strong and ductile Ti–6Al–4V by selective laser melting via in situ martensite decomposition.* Acta Materialia, 2015. **85**: p. 74-84.
32. Rafi, H., et al., *Microstructures and mechanical properties of Ti6Al4V parts fabricated by selective laser melting and electron beam melting.* Journal of materials engineering and performance, 2013. **22**(12): p. 3872-3883.
33. Yap, C., et al., *Review of selective laser melting: Materials and applications.* Applied Physics Reviews, 2015. **2**(4): p. 041101.
34. Trengove, L., *William Gregor (1761–1817) discoverer of titanium.* Annals of Science, 1972. **29**(4): p. 361-395.
35. A. D. Mc Quillan, M.K.M.Q., *Titanium*. 1956, United Kingdom: Butterworths Scientific Publication.
36. Gagnon, S. *The Element Titanium*. 2017; Available from: http://education.jlab.org/itselemental/ele022.html.
37. Center, T.P. *Titanium Overview – History, Developments, and Applications*. 2017; Available from: http://titaniumprocessingcenter.com/titanium-technical-data/titanium-history-developments-and-applications/.
38. Gerd Lütjering, J.C.W., *Titanium*. Engineering Materials, Processes. 2007, Berlin: Springer Berlin Heidelberg.
39. Antonysamy, A.A., *Microstructure, Texture and Mechanical Property Evolution during Additive Manufacturing of Ti6Al4V Alloy for Aerospace Applications*. 2012, The University of Manchester: Manchester, UK.
40. George Zheng Chen, D.J.F.T.W.F., *Direct electrochemical reduction of titanium dioxide to titanium in molten calcium chloride.* Nature, 2000. **407**: p. 361-364.
41. McQuillan, A.D. and M.K. McQuillan, *Titanium.* 1959.
42. Polmear, I.J., *Light Alloys, From Traditional Alloys to Nanocrystals, Fourth Edition*. 2005, United Kingdom: Elsevier Ltd.
43. Raabe, D. *introduction to Titanium Alloys*. 2017; Available from: http://www.dierk-raabe.com/titanium-alloys/.
44. Chen, G.Z., D.J. Fray, and T.W. Farthing, *Direct electrochemical reduction of titanium dioxide to titanium in molten calcium chloride.* Nature, 2000. **407**(6802): p. 361-364.
45. Wang, P., et al., *Spatial and geometrical-based characterization of microstructure and microhardness for an electron beam melted Ti–6Al–4V component.* Materials & Design, 2016. **95**: p. 287-295.
46. Mountford, J.A., *Titanium-properties, advantages and applications solving the corrosion problems in marine service.* NACE International, 2002.
47. Bhadeshia, H., *Titanium & its Alloys.* Materials Science & Metallurgy, Cambridge University, 2005: p. 1-12.
48. Lütjering, G. and J.C. Williams, *Titanium*. Vol. 2. 2003: Springer.
49. Britton, T., F. Dunne, and A. Wilkinson. *On the mechanistic basis of deformation at the microscale in hexagonal close-packed metals*. in *Proc. R. Soc. A*. 2015. The Royal Society.
50. Britton, T., et al. *The effect of crystal orientation on the indentation response of commercially pure titanium: experiments and simulations*. in *Proceedings of the Royal Society of London A: Mathematical, Physical and Engineering Sciences*. 2010. The Royal Society.
51. Rollett, A., et al., *Recrystallization and related annealing phenomena*. 2004: Elsevier.

52. Semiatin, S., et al., *Influence on texture on beta grain growth during continuous annealing of Ti–6Al–4V.* Materials Science and Engineering: A, 2001. **299**(1): p. 225-234.
53. Fitzner, A., et al., *The effect of aluminium on twinning in binary alpha-titanium.* Acta Materialia, 2016. **103**: p. 341-351.
54. Williams, J., R. Baggerly, and N. Paton, *Deformation behavior of HCP Ti-Al alloy single crystals.* Metallurgical and Materials Transactions A, 2002. **33**(3): p. 837-850.
55. Hémery, S., P. Nizou, and P. Villechaise, *In situ SEM investigation of slip transfer in Ti-6Al-4V: Effect of applied stress.* Materials Science and Engineering: A, 2018. **709**: p. 277-284.
56. Kwasniak, P., H. Garbacz, and K. Kurzydlowski, *Solid solution strengthening of hexagonal titanium alloys: Restoring forces and stacking faults calculated from first principles.* Acta Materialia, 2016. **102**: p. 304-314.
57. Donachie, M.J., *Titanium: a technical guide*. 2000: ASM international.
58. Jayaraman, A., W. Klement Jr, and G. Kennedy, *Solid-solid transitions in titanium and zirconium at high pressures.* Physical Review, 1963. **131**(2): p. 644.
59. Matweb, A. *Titanium Ti-6Al-4V (Grade 5), Annealed*. 2017; Available from: http://asm.matweb.com/search/SpecificMaterial.asp?bassnum=MTP641.
60. Porter, D.A., K.E. Easterling, and M. Sherif, *Phase Transformations in Metals and Alloys, (Revised Reprint)*. 2009: CRC press.
61. David, S. and J. Vitek, *Correlation between solidification parameters and weld microstructures.* International Materials Reviews, 2013.
62. W. Kurz, D.J.F., *Fundamentals of Solidification 4th Edition*. 1998: CRC Press.
63. Antonysamy, A.A., *Microstructure, texture and mechanical property evolution during additive manufacturing of Ti6Al4V alloy for aerospace applications.* 2012.
64. Wang, T., et al., *Grain morphology evolution behavior of titanium alloy components during laser melting deposition additive manufacturing.* Journal of Alloys and Compounds, 2015. **632**: p. 505-513.
65. Kou, S., *Frontmatter.* Welding Metallurgy, Second Edition, 2003: p. i-xiv.
66. Kobryn, P. and S. Semiatin. *Mechanical properties of laser-deposited Ti-6Al-4V*. in *Solid Freeform Fabrication Proceedings*. 2001. Austin.
67. Kobryn, P. and S. Semiatin, *The laser additive manufacture of Ti-6Al-4V.* JOM, 2001. **53**(9): p. 40-42.
68. Kobryn, P. and S. Semiatin, *Microstructure and texture evolution during solidification processing of Ti–6Al–4V.* Journal of Materials Processing Technology, 2003. **135**(2): p. 330-339.
69. Bontha, S., et al., *Thermal process maps for predicting solidification microstructure in laser fabrication of thin-wall structures.* Journal of Materials Processing Technology, 2006. **178**(1): p. 135-142.
70. Kou, S., *Welding metallurgy.* New York, 1987: p. P. 175.
71. Walton, D. and B. Chalmers, *The origin of the preferred orientation in the columnar zone of ingots.* Transactions of the American Institute of Mining and Metallurgical Engineers, 1959. **215**(3): p. 447-457.
72. Gäumann, M., et al., *Single-crystal laser deposition of superalloys: processing–microstructure maps.* Acta Materialia, 2001. **49**(6): p. 1051-1062.
73. Zheng, C., et al., *Effect of microstructures on ballistic impact property of Ti–6Al–4V targets.* Materials Science and Engineering: A, 2014. **608**: p. 53-62.
74. Bhattacharyya, D., et al., *The role of crystallographic and geometrical relationships between α and β phases in an α/β titanium alloy.* Acta materialia, 2003. **51**(16): p. 4679-4691.

75. Brooks, C.R. and C.R. Brooks, *Heat treatment, structure and properties of nonferrous alloys*. Vol. 4. 1982: American Society for metals Metals Park, OH.
76. Al-Bermani, S.S., *An investigation into microstructure and microstructural control of additive layer manufactured Ti-6Al-4V by electron beam melting*. 2011, University of Sheffield.
77. Quail, F., M. Stickland, and T. Scanlon. *Rapid manufacturing technique used in the development of a regenerative pump impeller*. in *World Congress on Engineering*. 2009.
78. Lu, Z., et al., *Review of main manufacturing processes of complex hollow turbine blades: This paper critically reviews conventional and advanced technologies used for manufacturing hollow turbine blades.* Virtual and Physical Prototyping, 2013. **8**(2): p. 87-95.
79. ASTM, *Standard Terminology for Additive Manufacturing Technologies*, in *ASTM F2792-12a*. 2010, ASTM International: West Conshohocken, PA.
80. Bikas, H., P. Stavropoulos, and G. Chryssolouris, *Additive manufacturing methods and modelling approaches: a critical review.* The International Journal of Advanced Manufacturing Technology, 2016. **83**(1): p. 389-405.
81. Zäh, M.F. and S. Lutzmann, *Modelling and simulation of electron beam melting.* Production Engineering, 2010. **4**(1): p. 15-23.
82. Thompson, S.M., et al., *An overview of Direct Laser Deposition for additive manufacturing; Part I: Transport phenomena, modeling and diagnostics.* Additive Manufacturing, 2015. **8**: p. 36-62.
83. Bakish, R., *Introduction to electron beam technology*. 1962, New York: John Wiley & Son.
84. Syam, W.P., M.A. Mannan, and A.M. Al-Ahmari, *Rapid prototyping and rapid manufacturing in medicine and dentistry.* Virtual and Physical Prototyping, 2011. **6**(2): p. 79-109.
85. Taniguchi, N., *The energy-beam processing of materials.* 1989.
86. Al-Bermani, S.S., *An Investigation into Microstructure and Microstructural Control of Additive Layer Manufactured Ti-6Al-4V by Electron Beam Melting*, in *Department of Engineering Materials*. 2011, The University of Sheffield: England. p. 238.
87. Karunakaran, K.P., et al., *Low cost integration of additive and subtractive processes for hybrid layered manufacturing.* Robotics and Computer-Integrated Manufacturing, 2010. **26**(5): p. 490-499.
88. Hedges, M. and N. Calder, *Near-Net-Shape Rapid Manufacture and Repair by LENS®.* Rapid Prototyping, 2006. **12**(4): p. 1.
89. Muller, P., P. Mognol, and J.-Y. Hascoet, *Modeling and control of a direct laser powder deposition process for Functionally Graded Materials (FGM) parts manufacturing.* Journal of Materials Processing Technology, 2013. **213**(5): p. 685-692.
90. Dehoff, R.R. and S.S. Babu, *Characterization of interfacial microstructures in 3003 aluminum alloy blocks fabricated by ultrasonic additive manufacturing.* Acta Materialia, 2010. **58**(13): p. 4305-4315.
91. Friel, R.J. and R.A. Harris, *Ultrasonic Additive Manufacturing – A Hybrid Production Process for Novel Functional Products.* Procedia CIRP, 2013. **6**: p. 35-40.
92. Antonysamy, A.A., J. Meyer, and P.B. Prangnell, *Effect of build geometry on the β-grain structure and texture in additive manufacture of Ti6Al4V by selective electron beam melting.* Materials Characterization, 2013. **84**: p. 153-168.
93. Sun, Z., et al., *Selective laser melting of stainless steel 316L with low porosity and high build rates.* Materials & Design, 2016. **104**: p. 197-204.

94. Graff, K., M. Short, and M. Norfolk. *Very high power ultrasonic additive manufacturing (VHP UAM) for advanced materials*. in *International Conference on Additive Manufacturing*. 2010.
95. Sriraman, M.R., S.S. Babu, and M. Short, *Bonding characteristics during very high power ultrasonic additive manufacturing of copper.* Scripta Materialia, 2010. **62**(8): p. 560-563.
96. Iwasaki, K., et al., *Laser welding of titanium and dental precious alloys.* Materials Transactions, 2004. **45**(4): p. 1140-1146.
97. Heinl, P., et al., *Cellular Ti–6Al–4V structures with interconnected macro porosity for bone implants fabricated by selective electron beam melting.* Acta Biomaterialia, 2008. **4**(5): p. 1536-1544.
98. Biamino, S., et al., *Electron beam melting of Ti–48Al–2Cr–2Nb alloy: Microstructure and mechanical properties investigation.* Intermetallics, 2011. **19**(6): p. 776-781.
99. Ferrar, B., et al., *Gas flow effects on selective laser melting (SLM) manufacturing performance.* Journal of Materials Processing Technology, 2012. **212**(2): p. 355-364.
100. Sames, W.J., et al., *Thermal effects on microstructural heterogeneity of Inconel 718 materials fabricated by electron beam melting.* Journal of Materials Research, 2014. **29**(17): p. 1920-1930.
101. Zhao, X., et al., *Comparison of the microstructures and mechanical properties of Ti–6Al–4V fabricated by selective laser melting and electron beam melting.* Materials & Design, 2016. **95**: p. 21-31.
102. Wang, X. and K. Chou. *Residual stress in metal parts produced by powder-bed additive manufacturing processes*. in *proceedings of the 26th International solid freeform fabrication symposium*. 2015.
103. Syed, W.U.H., A.J. Pinkerton, and L. Li, *Combining wire and coaxial powder feeding in laser direct metal deposition for rapid prototyping.* Applied Surface Science, 2006. **252**(13): p. 4803-4808.
104. Aboulkhair, N.T., et al., *Reducing porosity in AlSi10Mg parts processed by selective laser melting.* Additive Manufacturing, 2014. **1–4**: p. 77-86.
105. Thijs, L., et al., *A study of the microstructural evolution during selective laser melting of Ti–6Al–4V.* Acta Materialia, 2010. **58**(9): p. 3303-3312.
106. Carter, L.N., et al., *The influence of the laser scan strategy on grain structure and cracking behaviour in SLM powder-bed fabricated nickel superalloy.* Journal of Alloys and Compounds, 2014. **615**: p. 338-347.
107. Zaeh, M.F. and M. Kahnert, *The effect of scanning strategies on electron beam sintering.* Production Engineering, 2009. **3**(3): p. 217-224.
108. Thijs, L., et al., *Fine-structured aluminium products with controllable texture by selective laser melting of pre-alloyed AlSi10Mg powder.* Acta Materialia, 2013. **61**(5): p. 1809-1819.
109. Thijs, L., et al., *Strong morphological and crystallographic texture and resulting yield strength anisotropy in selective laser melted tantalum.* Acta Materialia, 2013. **61**(12): p. 4657-4668.
110. Helmer, H., et al., *Grain structure evolution in Inconel 718 during selective electron beam melting.* Materials Science and Engineering: A, 2016. **668**: p. 180-187.
111. Dehoff, R.R., et al., *Site specific control of crystallographic grain orientation through electron beam additive manufacturing.* Materials Science and Technology, 2015. **31**(8): p. 931-938.
112. Spierings, A.B., et al., *Powder flowability characterisation methodology for powder-bed-based metal additive manufacturing.* Progress in Additive Manufacturing, 2016. **1**(1): p. 9-20.

113. Karapatis, N., et al. *Optimization of powder layer density in selective laser sintering*. in *Proc. of Solid Freeform Fabrication Symposium 1999*. 1999.
114. Spierings, A. and G. Levy. *Comparison of density of stainless steel 316L parts produced with selective laser melting using different powder grades*. in *Proceedings of the Annual International Solid Freeform Fabrication Symposium*. 2009. Austin, TX.
115. Dennis F. Hasson, C.R.C., *Titanium for Offshore Oil Drilling.* JOM, 1982. **34**(1): p. 23-28.
116. America, T.M.C.o., *Marine Applications of Titanium and Its Alloys, A Designer's Guide*. 1968: America.
117. Flower, H.M., *High Performance Materials in Aerospace*. 1 ed. 1995, New York: Chapman & Hall.
118. Willams, W.L., *The Science, Technology and Application of Titanium*. 1970, New York: Pergamon Press Ltd.
119. Trenter. *Co-Current Flow And Asymmetric Plates Prevent Waxing In Crude Cooling*. 2015; Available from: http://www.tranter.com/Pages/markets/oil-gas-production/offshore-crude-cooling.aspx.
120. Fabricators, N.S.M. *Services*. 2005 [cited 2015 14 March]; Available from: http://www.nsmfabs.co.uk/services.html.
121. Smith, D.A.L.D.E., *Titanium for Marine Applications.* Naval Engineers Journal, 1971. **83**(5): p. 37-44.
122. Jones, R.W.R., *Nickel-Titanium Pipe Couplings for Submarine Piping Systems*. 1975: Groton, Connecticut.
123. dddrop. *Industrial 3D printing at dddrop – ball valve*. 2017; Available from: https://www.dddrop.com/industrial-3d-printing-dddrop-ball-valve/.
124. Newman, J., *Fighting corrosion with titanium castings.* Chemical Engineering, 1979. **86**(12): p. 149-150.
125. SIMS. *Products / Impellers & Rings SIMSITE® /*. 2015 [cited 2014 14 March]; Available from: http://simsite.com/cms/impellers-rings-simsite.html.
126. Steel, N. *Marine Market*. 2015 [cited 2015 14 March]; Available from: http://www.norstl.com/markets/industrial/marine/.
127. Wang, F., et al., *Microstructure and Mechanical Properties of Wire and Arc Additive Manufactured Ti-6Al-4V.* Metallurgical and Materials Transactions A, 2013. **44**(2): p. 968-977.
128. Mok, S.H., et al., *Deposition of Ti–6Al–4V using a high power diode laser and wire, Part II: Investigation on the mechanical properties.* Surface and Coatings Technology, 2008. **202**(19): p. 4613-4619.
129. Brandl, E., et al., *Additive manufactured Ti-6Al-4V using welding wire: comparison of laser and arc beam deposition and evaluation with respect to aerospace material specifications.* Physics Procedia, 2010. **5**: p. 595-606.
130. Hrabe, N. and T. Quinn, *Effects of processing on microstructure and mechanical properties of a titanium alloy (Ti–6Al–4V) fabricated using electron beam melting (EBM), Part 2: Energy input, orientation, and location.* Materials Science and Engineering: A, 2013. **573**: p. 271-277.
131. Cain, V., et al., *Crack propagation and fracture toughness of Ti6Al4V alloy produced by selective laser melting.* Additive Manufacturing, 2015. **5**: p. 68-76.
132. Edwards, P., A. O'Conner, and M. Ramulu, *Electron beam additive manufacturing of titanium components: properties and performance.* Journal of Manufacturing Science and Engineering, 2013. **135**(6): p. 061016.

133. Baufeld, B., *Effect of deposition parameters on mechanical properties of shaped metal deposition parts.* Proceedings of the Institution of Mechanical Engineers, Part B: Journal of Engineering Manufacture, 2012. **226**(1): p. 126-136.
134. Hrabe, N. and T. Quinn, *Effects of processing on microstructure and mechanical properties of a titanium alloy (Ti–6Al–4V) fabricated using electron beam melting (EBM), part 1: Distance from build plate and part size.* Materials Science and Engineering: A, 2013. **573**: p. 264-270.
135. Qian, L., et al., *Influence of position and laser power on thermal history and microstructure of direct laser fabricated Ti–6Al–4V samples.* Materials science and technology, 2005. **21**(5): p. 597-605.
136. Zhang, B., et al., *Microstructure and mechanical properties of Inconel 625/nano-TiB2 composite fabricated by LAAM.* Materials & Design, 2016. **111**: p. 70-79.
137. Raghavan, S., et al., *Effect of different heat treatments on the microstructure and mechanical properties in selective laser melted INCONEL 718 alloy.* Materials and Manufacturing Processes, 2016: p. 1-8.
138. Takaichi, A., et al., *Microstructures and mechanical properties of Co–29Cr–6Mo alloy fabricated by selective laser melting process for dental applications.* Journal of the Mechanical Behavior of Biomedical Materials, 2013. **21**: p. 67-76.
139. Ladani, L., J. Razmi, and S.F. Choudhury, *Mechanical Anisotropy and Strain Rate Dependency Behavior of Ti6Al4V Produced Using E-Beam Additive Fabrication.* Journal of Engineering Materials and Technology, 2014. **136**(3): p. 031006.
140. Bian, L., S.M. Thompson, and N. Shamsaei, *Mechanical Properties and Microstructural Features of Direct Laser-Deposited Ti-6Al-4V.* JOM, 2015. **67**(3): p. 629-638.
141. Tammas-Williams, S., et al., *XCT analysis of the influence of melt strategies on defect population in Ti–6Al–4V components manufactured by selective electron beam melting.* Materials Characterization, 2015. **102**: p. 47-61.
142. Everton, S.K., et al., *Review of in-situ process monitoring and in-situ metrology for metal additive manufacturing.* Materials & Design, 2016. **95**: p. 431-445.
143. Seifi, M., et al., *Defect distribution and microstructure heterogeneity effects on fracture resistance and fatigue behavior of EBM Ti–6Al–4V.* International Journal of Fatigue, 2017. **94, Part 2**: p. 263-287.
144. Spierings, A.B., M. Schneider, and R. Eggenberger, *Comparison of density measurement techniques for additive manufactured metallic parts.* Rapid Prototyping Journal, 2011. **17**(5): p. 380-386.
145. ASTM, *Standard Terminology for Additive Manufacturing-Coordinate Systems and Test Methodologies*, in *ISO / ASTM52921-13*. 2013, ASTM International: West Conshohocken, PA.
146. Seifi, M., et al., *Evaluation of Orientation Dependence of Fracture Toughness and Fatigue Crack Propagation Behavior of As-Deposited ARCAM EBM Ti-6Al-4V.* JOM, 2015. **67**(3): p. 597-607.
147. Froes, F. and B. Dutta. *The Additive Manufacturing (AM) of Titanium Alloys*. in *Advanced Materials Research*. 2014. Trans Tech Publ.
148. Alcisto, J., et al., *Tensile Properties and Microstructures of Laser-Formed Ti-6Al-4V.* Journal of Materials Engineering and Performance, 2011. **20**(2): p. 203-212.
149. Simonelli, M., Y.Y. Tse, and C. Tuck, *Effect of the build orientation on the mechanical properties and fracture modes of SLM Ti–6Al–4V.* Materials Science and Engineering: A, 2014. **616**: p. 1-11.

150. Qiu, C., N.J.E. Adkins, and M.M. Attallah, *Microstructure and tensile properties of selectively laser-melted and of HIPed laser-melted Ti–6Al–4V.* Materials Science and Engineering: A, 2013. **578**: p. 230-239.
151. Vilaro, T., C. Colin, and J.D. Bartout, *As-Fabricated and Heat-Treated Microstructures of the Ti-6Al-4V Alloy Processed by Selective Laser Melting.* Metallurgical and Materials Transactions A, 2011. **42**(10): p. 3190-3199.
152. Facchini, L., et al., *Microstructure and mechanical properties of Ti-6Al-4V produced by electron beam melting of pre-alloyed powders.* Rapid Prototyping Journal, 2009. **15**(3): p. 171-178.
153. Svensson, M., U. Ackelid, and A. Ab. *Titanium alloys manufactured with electron beam melting mechanical and chemical properties*. in *Proceedings of Materials & Processes for Medical Devices Conference*. 2010.
154. Christensen, A., R. Kircher, and A. Lippincott. *Qualification of electron beam melted (EBM) Ti6Al4V-ELI for orthopaedic applications*. in *Medical Device Materials IV: Proceedings of the Materials and Processes for Medical Devices Conference*. 2008.
155. Kircher, R., A. Christensen, and K. Wurth. *Electron Beam Melted (EBM) Co-Cr-Mo Alloy for Orthopaedic Implant Applications*. in *Solid Freeform Fabrication Proceedings*. 2009.
156. Strößner, J., M. Terock, and U. Glatzel, *Mechanical and Microstructural Investigation of Nickel-Based Superalloy IN718 Manufactured by Selective Laser Melting (SLM).* Advanced Engineering Materials, 2015. **17**(8): p. 1099-1105.
157. Rosenthal, I., A. Stern, and N. Frage, *Microstructure and Mechanical Properties of AlSi10Mg Parts Produced by the Laser Beam Additive Manufacturing (AM) Technology.* Metallography, Microstructure, and Analysis, 2014. **3**(6): p. 448-453.
158. Read, N., et al., *Selective laser melting of AlSi10Mg alloy: Process optimisation and mechanical properties development.* Materials & Design (1980-2015), 2015. **65**: p. 417-424.
159. Kempen, K., et al., *Mechanical properties of AlSi10Mg produced by selective laser melting.* Physics Procedia, 2012. **39**: p. 439-446.
160. Song, C., et al., *Research on rapid manufacturing of CoCrMo alloy femoral component based on selective laser melting.* The International Journal of Advanced Manufacturing Technology, 2014. **75**(1): p. 445-453.
161. Qiu, C., et al., *Fabrication of large Ti–6Al–4V structures by direct laser deposition.* Journal of Alloys and Compounds, 2015. **629**: p. 351-361.
162. International, A., *ASTM F1472-14*, in *Standard Specification for Wrought Titanium-6Aluminum-4Vanadium Alloy for Surgical Implant Applications (UNS R56400)*. 2014: West Conshohocken, PA.
163. International, A., *ASTM F1108-14*, in *Standard Specification for Titanium-6Aluminum-4Vanadium Alloy Castings for Surgical Implants (UNS R56406)*. 2014: West Conshohocken, PA.
164. International, A., *ASTM F75-12*, in *Standard Specification for Cobalt-28 Chromium-6 Molybdenum Alloy Castings and Casting Alloy for Surgical Implants (UNS R30075)*. 2012: West Conshohocken, PA.
165. International, A., *ASTM F1537-11*, in *Standard Specification for Wrought Cobalt-28Chromium-6Molybdenum Alloys for Surgical Implants (UNS R31537, UNS R31538, and UNS R31539)*. 2011: West Conshohocken, PA.
166. Kaufman, J.G., *Properties of aluminum alloys: tensile, creep, and fatigue data at high and low temperatures*. 1999: ASM international.

167. Kirka, M.M., et al., *Mechanical behavior of post-processed Inconel 718 manufactured through the electron beam melting process.* Materials Science and Engineering: A, 2017. **680**: p. 338-346.
168. Pruitt, L.A., *Deformation, yielding, fracture and fatigue behavior of conventional and highly cross-linked ultra high molecular weight polyethylene.* Biomaterials, 2005. **26**(8): p. 905-915.
169. Schwalbe, K.-H., *On the influence of microstructure on crack propagation mechanisms and fracture toughness of metallic materials.* Engineering Fracture Mechanics, 1977. **9**(4): p. 795-832.
170. Edwards, P. and M. Ramulu, *Effect of build direction on the fracture toughness and fatigue crack growth in selective laser melted Ti-6Al-4 V.* Fatigue & Fracture of Engineering Materials & Structures, 2015. **38**(10): p. 1228-1236.
171. Lampman, S., *ASM Handbook*. Wrought Titanium and Titanium Alloys, Properties and Selection: Nonferrous Alloys and Special-Purpose Materials. Vol. 2. 1990: ASM International.
172. Cansizoglu, O., et al., *Properties of Ti–6Al–4V non-stochastic lattice structures fabricated via electron beam melting.* Materials Science and Engineering: A, 2008. **492**(1–2): p. 468-474.
173. Li, P., et al., *Critical assessment of the fatigue performance of additively manufactured Ti–6Al–4V and perspective for future research.* International Journal of Fatigue, 2016. **85**: p. 130-143.
174. Boyce, B.L. and R.O. Ritchie, *Effect of load ratio and maximum stress intensity on the fatigue threshold in Ti–6Al–4V.* Engineering Fracture Mechanics, 2001. **68**(2): p. 129-147.
175. Ding, J., R. Hall, and J. Byrne, *Effects of stress ratio and temperature on fatigue crack growth in a Ti–6Al–4V alloy.* International Journal of Fatigue, 2005. **27**(10–12): p. 1551-1558.
176. Hague, R., S. Mansour, and N. Saleh, *Material and design considerations for rapid manufacturing.* International Journal of Production Research, 2004. **42**(22): p. 4691-4708.
177. Sun, S.-H., et al., *Build direction dependence of microstructure and high-temperature tensile property of Co–Cr–Mo alloy fabricated by electron beam melting.* Acta Materialia, 2014. **64**: p. 154-168.
178. Sun, S.-H., et al., *Phase and grain size inhomogeneity and their influences on creep behavior of Co–Cr–Mo alloy additive manufactured by electron beam melting.* Acta Materialia, 2015. **86**: p. 305-318.
179. Kelly, S.M. and S.L. Kampe, *Microstructural evolution in laser-deposited multilayer Ti-6Al-4V builds: Part I. Microstructural characterization.* Metallurgical and Materials Transactions A, 2004. **35**(6): p. 1861-1867.
180. Martina, F., et al., *Microstructure of Interpass Rolled Wire + Arc Additive Manufacturing Ti-6Al-4V Components.* Metallurgical and Materials Transactions A, 2015. **46**(12): p. 6103-6118.
181. Tan, X., et al., *Graded microstructure and mechanical properties of additive manufactured Ti–6Al–4V via electron beam melting.* Acta Materialia, 2015. **97**: p. 1-16.
182. Körner, C., et al., *Tailoring the grain structure of IN718 during selective electron beam melting.* MATEC Web of Conferences, 2014. **14**: p. 08001.
183. Nassar, A.R., et al., *Intra-layer closed-loop control of build plan during directed energy additive manufacturing of Ti–6Al–4V.* Additive Manufacturing, 2015. **6**: p. 39-52.

184. Machry, T., et al., *Effect of microstructure on the tensile strength of Ti6Al4V specimens manufactured using additive manufacturing electron beam process.* Powder Metallurgy, 2016. **59**(1): p. 41-50.
185. Amine, T., J.W. Newkirk, and F. Liou, *Methodology for Studying Effect of Cooling Rate During Laser Deposition on Microstructure.* Journal of Materials Engineering and Performance, 2015. **24**(8): p. 3129-3136.
186. Jamshidinia, M., et al., *Microstructural modification of Ti–6Al–4V by using an in-situ printed heat sink in Electron Beam Melting® (EBM).* Journal of Materials Processing Technology, 2015. **226**: p. 264-271.
187. Cunningham, R., et al., *Evaluating the Effect of Processing Parameters on Porosity in Electron Beam Melted Ti-6Al-4V via Synchrotron X-ray Microtomography.* JOM, 2016. **68**(3): p. 765-771.
188. S. Raghavan, M.L.S.N., Pan Wang, Wai Jack Sin, Tao Li, Jun Wei. *Dependence of microstructure and mechanical properties on heat treat cycles of electron beam melted Ti-6Al-4V*. in *2016 Annual International Solid Freeform Fabrication Symposium - An Additive Manufacturing Conference*. 2016.
189. Amato, K.N., et al., *Microstructures and mechanical behavior of Inconel 718 fabricated by selective laser melting.* Acta Materialia, 2012. **60**(5): p. 2229-2239.
190. Song, B., et al., *Vacuum heat treatment of iron parts produced by selective laser melting: Microstructure, residual stress and tensile behavior.* Materials & Design (1980-2015), 2014. **54**: p. 727-733.
191. Brandl, E. and D. Greitemeier, *Microstructure of additive layer manufactured Ti–6Al–4V after exceptional post heat treatments.* Materials Letters, 2012. **81**: p. 84-87.
192. Yang, N., et al., *Process-structure-property relationships for 316L stainless steel fabricated by additive manufacturing and its implication for component engineering.* Journal of Thermal Spray Technology, 2017. **26**(4): p. 610-626.
193. Hrabe, N., T. Gnäupel-Herold, and T. Quinn, *Fatigue properties of a titanium alloy (Ti–6Al–4V) fabricated via electron beam melting (EBM): Effects of internal defects and residual stress.* International Journal of Fatigue, 2017. **94**: p. 202-210.
194. Lim, G., et al., *Residual Stresses in Ti-6Al-4V Parts Manufactured by Direct Metal Laser Sintering and Electron Beam Melting.* British Society of Strain Meaurement, 2017.
195. Das, S., et al., *Processing of titanium net shapes by SLS/HIP.* Materials & Design, 1999. **20**(2–3): p. 115-121.
196. Lee, D.-G., et al., *Effects of microstructural factors on quasi-static and dynamic deformation behaviors of Ti-6Al-4V alloys with widmanstätten structures.* Metallurgical and Materials Transactions A, 2003. **34**(11): p. 2541.
197. Algardh, J.K., et al., *Thickness dependency of mechanical properties for thin-walled titanium parts manufactured by Electron Beam Melting (EBM)®.* Additive Manufacturing, 2016. **12**: p. 45-50.
198. Costa, L., et al., *Rapid tooling by laser powder deposition: Process simulation using finite element analysis.* Acta Materialia, 2005. **53**(14): p. 3987-3999.
199. Gockel, J., J. Beuth, and K. Taminger, *Integrated control of solidification microstructure and melt pool dimensions in electron beam wire feed additive manufacturing of Ti-6Al-4V.* Additive Manufacturing, 2014. **1–4**: p. 119-126.
200. Vastola, G., et al., *Modeling the Microstructure Evolution During Additive Manufacturing of Ti6Al4V: A Comparison Between Electron Beam Melting and Selective Laser Melting.* JOM, 2016. **68**(5): p. 1370-1375.

201. Irwin, J., et al., *Predicting Microstructure From Thermal History During Additive Manufacturing for Ti-6Al-4V.* Journal of Manufacturing Science and Engineering, 2016. **138**(11): p. 111007-111007.
202. Jamshidinia, M., F. Kong, and R. Kovacevic, *Numerical Modeling of Heat Distribution in the Electron Beam Melting® of Ti-6Al-4V.* Journal of Manufacturing Science and Engineering, 2013. **135**(6): p. 061010-061010-14.
203. Kok, Y., et al., *Fabrication and microstructural characterisation of additive manufactured Ti-6Al-4V parts by electron beam melting.* Virtual and Physical Prototyping, 2015. **10**(1): p. 13-21.
204. Yadroitsev, I., P. Krakhmalev, and I. Yadroitsava, *Selective laser melting of Ti6Al4V alloy for biomedical applications: Temperature monitoring and microstructural evolution.* Journal of Alloys and Compounds, 2014. **583**: p. 404-409.
205. Vastola, G., et al., *Modeling and control of remelting in high-energy beam additive manufacturing.* Additive Manufacturing, 2015. **7**: p. 57-63.
206. Neira Arce, A., *Thermal modeling and simulation of electron beam melting for rapid prototyping on Ti6Al4V alloys*. 2012.
207. Lee, P.D., et al., *Multiscale modelling of solidification microstructures, including microsegregation and microporosity, in an Al–Si–Cu alloy.* Materials Science and Engineering: A, 2004. **365**(1–2): p. 57-65.
208. Voller, V.R. and C. Prakash, *A fixed grid numerical modelling methodology for convection-diffusion mushy region phase-change problems.* International Journal of Heat and Mass Transfer, 1987. **30**(8): p. 1709-1719.
209. Cheng, B., et al., *On Process Temperature in Powder-Bed Electron Beam Additive Manufacturing: Model Development and Validation.* Journal of Manufacturing Science and Engineering, 2014. **136**(6): p. 061018-061018-12.
210. Atwood, R.C. and P.D. Lee, *Simulation of the three-dimensional morphology of solidification porosity in an aluminium–silicon alloy.* Acta Materialia, 2003. **51**(18): p. 5447-5466.
211. Wang, W., P.D. Lee, and M. McLean, *A model of solidification microstructures in nickel-based superalloys: predicting primary dendrite spacing selection.* Acta Materialia, 2003. **51**(10): p. 2971-2987.
212. Rhodes, C.G. and J.C. Williams, *Observations of an interface phase in the α/β boundaries in titanium alloys.* Metallurgical Transactions A, 1975. **6**(8): p. 1670.
213. Margolin, H., E. Levine, and M. Young, *The interface phase in alpha-beta titanium alloys.* Metallurgical Transactions A, 1977. **8**(2): p. 373.
214. Rhodes, C.G. and N.E. Paton, *Formation characteristics of the α/β interface phase in Ti-6Ai-4v.* Metallurgical Transactions A, 1979. **10**(2): p. 209.
215. Zeng, L. and T.R. Bieler, *Effects of working, heat treatment, and aging on microstructural evolution and crystallographic texture of α, α′, α″ and β phases in Ti–6Al–4V wire.* Materials Science and Engineering: A, 2005. **392**(1–2): p. 403-414.
216. Murr, L.E., et al., *Metal Fabrication by Additive Manufacturing Using Laser and Electron Beam Melting Technologies.* Journal of Materials Science & Technology, 2012. **28**(1): p. 1-14.
217. Tan, X., et al., *Atom probe tomographic study of L10 martensite in a Pt-modified NiCoCrAlYTa bond coating.* Corrosion Science, 2013. **76**: p. 1-5.
218. Tarzimoghadam, Z., et al., *Microstructure design and mechanical properties in a near-α Ti–4Mo alloy.* Acta Materialia, 2015. **97**: p. 291-304.
219. Tan, X., et al., *Intergrowth of P phase with μ phase in a Ru-containing single-crystal Ni-based superalloy.* Philosophical Magazine Letters, 2012. **92**(10): p. 556-562.

220. Tan, X., et al., *Revealing martensitic transformation and α/β interface evolution in electron beam melting three-dimensional-printed Ti-6Al-4V.* Scientific reports, 2016. **6**.
221. Tan, X., et al., *An experimental and simulation study on build thickness dependent microstructure for electron beam melted Ti–6Al–4V.* Journal of Alloys and Compounds, 2015. **646**: p. 303-309.
222. Kok, Y.H., et al., *Geometry dependence of microstructure and microhardness for selective electron beam-melted Ti–6Al–4V parts.* Virtual and Physical Prototyping, 2016. **11**(3): p. 183-191.
223. Hofmann, D.C., et al., *Developing gradient metal alloys through radial deposition additive manufacturing.* Scientific reports, 2014. **4**: p. 5357.
224. Armstrong, R.W., *Engineering science aspects of the Hall-Petch relation.* Acta Mechanica, 2014. **225**(4-5): p. 1013.
225. Castany, P., et al., *Experimental study of dislocation mobility in a Ti–6Al–4V alloy.* Acta Materialia, 2007. **55**(18): p. 6284-6291.
226. Lütjering, G., J.C. Williams, and A. Gysler, *MICROSTRUCTURE AND MECHANICAL PROPERTIES OF TITANIUM ALLOYS*, in *Microstructure and Properties of Materials*. 2011, WORLD SCIENTIFIC. p. 1-77.
227. Lee, D.-G., et al., *Effects of microstructural factors on quasi-static and dynamic deformation behaviors of Ti-6Al-4V alloys with widmanstätten structures.* Metallurgical and Materials Transactions A, 2003. **34**(11): p. 2541-2548.
228. Lu, K., *Making strong nanomaterials ductile with gradients.* Science, 2014. **345**(6203): p. 1455-1456.
229. Tiley, J.S., *Modeling of Microstructure Property Relationships in Ti-6Al-4V*. 2002, The Ohio State University.
230. Matsumoto, H., et al., *Room-temperature ductility of Ti–6Al–4V alloy with α′ martensite microstructure.* Materials Science and Engineering: A, 2011. **528**(3): p. 1512-1520.
231. Facchini, L., et al., *Microstructure and mechanical properties of Ti-6Al-4V produced by electron beam melting of pre-alloyed powders.* Rapid Prototyping Journal, 2009. **15**(3): p. 171-178.
232. Schwerdtfeger, J., R.F. Singer, and C. Körner, *In situ flaw detection by IR-imaging during electron beam melting.* Rapid Prototyping Journal, 2012. **18**(4): p. 259-263.
233. Bergman, T.L. and F.P. Incropera, *Introduction to heat transfer*. 2011: John Wiley & Sons.
234. D'Souza, N., et al., *Morphological aspects of competitive grain growth during directional solidification of a nickel-base superalloy, CMSX4.* Journal of Materials Science, 2002. **37**(3): p. 481-487.
235. Wagner, A., B.A. Shollock, and M. McLean, *Grain structure development in directional solidification of nickel-base superalloys.* Materials Science and Engineering: A, 2004. **374**(1–2): p. 270-279.
236. Zhou, Y.Z., A. Volek, and N.R. Green, *Mechanism of competitive grain growth in directional solidification of a nickel-base superalloy.* Acta Materialia, 2008. **56**(11): p. 2631-2637.
237. Tourret, D. and A. Karma, *Growth competition of columnar dendritic grains: A phase-field study.* Acta Materialia, 2015. **82**: p. 64-83.
238. Tourret, D., et al., *Grain growth competition during thin-sample directional solidification of dendritic microstructures: A phase-field study.* Acta Materialia, 2017. **122**: p. 220-235.

239. Rai, A., H. Helmer, and C. Körner, *Simulation of grain structure evolution during powder bed based additive manufacturing.* Additive Manufacturing, 2017. **13**: p. 124-134.
240. Donoghue, J., et al., *The effectiveness of combining rolling deformation with Wire–Arc Additive Manufacture on β-grain refinement and texture modification in Ti–6Al–4V.* Materials Characterization, 2016. **114**: p. 103-114.
241. Zhu, Z.S., J.L. Gu, and N.P. Chen, *Transition textures induced by cyclic phase transformation in titanium sheet.* Scripta Metallurgica et Materialia, 1995. **32**(4): p. 499-504.
242. Todai, M., et al., *Effect of building direction on the microstructure and tensile properties of Ti-48Al-2Cr-2Nb alloy additively manufactured by electron beam melting.* Additive Manufacturing, 2017. **13**: p. 61-70.